

# Phase Transformations from Deformed Austenite

By  
Shiv Brat Singh  
Darwin College, Cambridge

Department of Materials Science and Metallurgy  
Pembroke Street, Cambridge, CB2 3QZ

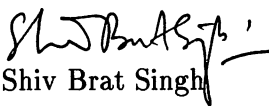
*A dissertation submitted for the degree of*  
**Doctor of Philosophy**  
*at the University of Cambridge*  
*August 1998*

# Preface

This dissertation is submitted for the degree of Doctor of Philosophy at the University of Cambridge. The investigation reported herein was carried out under the supervision of Dr H. K. D. H. Bhadeshia at the Department of Materials Science and Metallurgy between October 1995 and July 1998. Except where suitable acknowledgements and references are made to the contrary, this dissertation is the result of my own work and includes nothing which is the outcome of work done in collaboration. Neither this, nor any substantially similar dissertation has been or is being submitted for any degree, diploma or qualification at any other university or institution. This dissertation contains less than 60,000 words.

The work has been presented in following publications:

- (i) S. B. Singh and H. K. D. H. Bhadeshia, *Materials Science and Technology*, **12**, 1996, 610-612.
- (ii) S. B. Singh and H. K. D. H. Bhadeshia, *Materials Science and Engineering A*, **245A**, 1998, 72-79.
- (iii) S. B. Singh and H. K. D. H. Bhadeshia, *Materials Science and Technology*, **14**, in press.
- (iv) S. B. Singh, H. K. D. H. Bhadeshia, D. J. C. MacKay, H. Carey and I. Martin, *Ironmaking and Steelmaking*, in press.

  
Shiv Brat Singh  
August 1998



# Acknowledgements

I am indebted to the Nehru Trust for Cambridge University, India, for a scholarship and to the Committee of Vice-Chancellors and Principals, UK, for an ORS award which enabled me to undertake this research study. I also thank British Steel plc for financial support. My sincere thanks to Professor C. J. Humphreys and Professor A. H. Windle for the provision of the laboratory facilities in the Department of Materials Science and Metallurgy at the University of Cambridge.

I am very grateful to my supervisor, Dr H. K. D. H. Bhadeshia, for his inspirational guidance. His enthusiasm and encouragement have been a great motivation. I am thankful to all the members of the Phase Transformation Group for their help at various stages of the work, especially to Dr Adebayo Badmos, Francisca Caballerro, Dr Joe Robson, John Street, Mike Lord, Dr Naomi Chester and Phillipe Opdenacker. My special thanks to Dr E. Swallow and Dr P. Shipway for their help with the *Thermecmastor* experiments. Thanks also go to Ian Martin and Dr Heather Carey of Swinden Technology Centre, British Steel plc for their help.

Many thanks to The Worshipful Company of Ironmongers for sponsoring my visit to Oak Ridge National Laboratory (ORNL), USA. Dr Stan David, Dr Suresh Babu (and Anuradha) and Robby Reed provided warm hospitality and useful help for my experiments at ORNL. Their help is thankfully acknowledged.

Thanks are also due to the management of Tata Steel, India, for granting me a study leave and to Dr T. Mukherjee and Dr O. N. Mohanty for their words of encouragement before my departure from India. I also thank Professor K. Chattopadhyay for his valuable suggestions and guidance.

I take this opportunity to express my gratitude to my 'Ammi', Ashwini, for initiating me into the Cambridge life and for taking care of me for the past three years. I was lucky to find many good friends who provided a home-like atmosphere and made my stay in Cambridge a memorable one. I sincerely thank each one of them, particularly to Ajay (Mandal), Amareshda, Anuradhadi, Anil, Aninditadi, Bhaskar, Chandrasekhar, Joydeep, Maya, Parthada, PD, Sridhar and Srinivas. It is their friendship and affection that sustained me through these years.

I cannot find appropriate words to convey my sense of gratitude to my parents and uncle who have done so much bring me up to this stage. I also acknowledge with thanks the support and encouragement received from Ajay (Verma), Anjani, Baby, Bhaiya (Ramdeo), Braz, Pintu, Sunil and Teya.

# Abstract

This thesis deals with the solid-state transformation of plastically deformed austenite, with particular attention to the allotriomorphic ferrite and bainite reactions. The first three chapters are largely reviews which set the scene for the research that follows.

The deformation of austenite in circumstances where it does not recrystallise, alters its state in two respects. The total grain boundary surface per unit volume increases, as does the density of defects such as dislocations, shear bands and grain boundary steps. The overall stored energy of the austenite consequently increases on deformation.

The change in grain topology due to rolling and wire drawing operations has been calculated by applying the appropriate deformation matrix to austenite grains represented by tetrakaidecahedra. It has been possible for the first time to estimate accurately not only the change in the specific grain surface area, but also the increase in the grain edge length as a function of orientation relative to the principal deformation axes.

In the case of reconstructive transformations such as allotriomorphic ferrite, it is found that in common with much published work, the transformation is accelerated when it occurs from a plastically deformed parent phase. This is because defects are eliminated by the growth of allotriomorphic ferrite (a thermodynamic effect), and because the nucleation rate is enhanced. The latter occurs both because of an increase in the number density of nucleation sites and because the potency of the grain surfaces as heterogeneous nucleation sites is increased. It has also been discovered that there is a greater tendency for ferrite to nucleate in the deformed regions adjacent to austenite grain surfaces.

The early stages of the bainite reaction are found to be accelerated in plastically strained austenite, because of an enhanced nucleation rate. However, the overall transformation can be retarded because the deformation debris opposes the growth of the bainite plates. This is because the bainite/austenite interface is glissile and hence is hindered by obstacles in a manner akin to work hardening. The effect is commonly known as “mechanical stabilisation”.

A considerable effort was devoted to modelling new and published data on the kinetics of the bainite reaction, with the ultimate goal of explaining the detailed features of the mechanical stabilisation phenomenon. Building on previous work, a more rational model has been developed which properly addresses microstructural issues and which has a reduced number of fitting parameters. This model gives a better representation of experimental data than any previous work.

It has been proved that this kinetic model cannot explain the mechanical stabilisation phenomenon. The problem is elegantly solved once it is assumed that deformation is heterogeneous on the scale of the bainite microstructure. With this idea, it has been possible for the

first time to explain quantitatively a vast number of interesting observations on mechanical stabilisation in the context of the bainite reaction.

A neural network model has been created for predicting the mechanical properties of structural steels as a function of the rolling process parameters and the chemical composition. This is demonstrated to work well on a large quantity of experimental data and on relationships published in the literature.

The theory of bainite has been applied to the development of new steels with properties better than previously achieved. These steels cover a yield strength range of 670 to 830 MPa, have good toughness and are amenable to mass production using the control-rolling process.

# Contents

Preface .....	i
Acknowledgements .....	ii
Abstract .....	iii
Contents .....	v
List of Nomenclature .....	x
<b>1 Introduction .....</b>	<b>1</b>
1.1 Displacive Transformation .....	1
1.2 Reconstructive Transformation .....	3
1.3 Transformation Products .....	3
1.3.1 <i>Allotriomorphic and Idiomorphic Ferrite</i> .....	3
1.3.2 <i>Widmanstätten ferrite</i> .....	4
1.3.3 <i>Pearlite</i> .....	4
1.3.4 <i>Bainite</i> .....	5
1.3.5 <i>Acicular Ferrite</i> .....	6
1.3.6 <i>Martensite</i> .....	6
1.4 Summary .....	7
<b>2 Review of Bainite Kinetics .....</b>	<b>9</b>
2.1 The Thermodynamic Parameters .....	9
2.2 General Theory of Bainite Transformation .....	11
2.2.1 <i>Nucleation</i> .....	11
2.2.2 <i>Growth of the Nucleus</i> .....	14
2.2.3 <i>The Nucleation Rate</i> .....	14
2.3 Rees and Bhadeshia Model .....	15
2.4 Summary .....	19
<b>3 Stress and Strain Affected Transformations .....</b>	<b>20</b>
3.1 Introduction .....	20
3.2 Effect of Austenite Deformation on its Transformation .....	21
3.2.1 <i>Deformation in the Recrystallisation Region</i> .....	22

3.2.2	<i>Deformation in the Non-Recrystallisation Region</i> .....	22
3.3	Effect of Plastic Strain on the Bainite Transformation .....	32
3.4	Effect of Stress on the Bainite Transformation .....	35
3.5	Summary .....	38
4	Topology of Grain Deformation .....	39
4.1	Introduction .....	39
4.2	The Method .....	39
4.3	Results .....	40
4.3.1	<i>Comparison with Experimental Measurements</i> .....	42
4.4	Conclusion .....	43
5	Allotriomorphic Ferrite Formation from Deformed Austenite .....	46
5.1	Introduction .....	46
5.2	Experimental Method .....	46
5.3	Results and Discussions .....	47
5.3.1	<i>Dilatation curves</i> .....	47
5.3.2	<i>Microstructure</i> .....	47
5.4	Mathematical Modelling .....	52
5.4.1	<i>Effect of Deformation</i> .....	53
5.5	Conclusions .....	57
6	Kinetics of the Bainite Transformation Part 1: A Mathematical Model .....	58
6.1	Introduction .....	58
6.2	Limitations of the Old Model .....	58
6.3	The New Model .....	59
6.3.1	<i>Bainite Plate Volume</i> .....	59
6.3.2	<i>Autocatalysis</i> .....	59
6.3.3	<i>Overall Transformation Kinetics</i> .....	62
6.3.4	<i>Optimisation of the Model</i> .....	63
6.3.5	<i>Validation of the model</i> .....	66
6.4	Conclusions .....	66
7	Kinetics of the Bainite Transformation Part 2: Effect of Austenite Grain Size .....	68
7.1	Introduction .....	68
7.2	Nucleation Rate .....	69

7.3	The Choice of Steel .....	69
7.4	Measurement of $B_S$ .....	69
7.4.1	<i>Experiments</i> .....	69
7.4.2	<i>Results</i> .....	70
7.5	Analysis of Steven and Haynes data .....	74
7.6	Reformulation of $G_N$ .....	75
7.6.1	<i>New <math>G_N</math></i> .....	77
7.6.2	<i>Estimation of the New Constants</i> .....	78
7.7	Conclusions .....	79
8	Deformation-induced Stabilisation of Austenite Against Bainite Transformation .....	80
8.1	Experimental Procedure .....	80
8.2	Results and Discussions .....	81
8.2.1	<i>Dilatometric Measurements</i> .....	82
8.2.2	<i>Microstructural Observations</i> .....	86
8.2.3	<i>Microhardness Measurements</i> .....	87
8.2.4	<i>Conversion of Dilatometric Data</i> .....	96
8.3	Mathematical Model for Mechanical Stabilisation .....	99
8.4	Model Predictions .....	102
8.4.1	<i>Effect of Strain</i> .....	103
8.4.2	<i>Effect of Grain size</i> .....	107
8.4.3	<i>Effect of Transformation Temperature</i> .....	113
8.5	Conclusions .....	114
9	Transformation Strain Recovery During Stress-affected Cyclic Transformation .....	115
9.1	Introduction .....	115
9.2	Experimental Method .....	115
9.3	Results and Discussions .....	116
9.3.1	<i>The Transformation Strain</i> .....	118
9.3.2	<i>The Microstructure</i> .....	121
9.4	Conclusions .....	122
10	Estimation of Bainite Plate Thickness in Low-alloy Steels .....	123
10.1	Introduction .....	123
10.2	Data .....	125
10.3	The Technique .....	127
10.4	The Analysis .....	128

10.5	Network Training .....	130
10.6	Application of the Model .....	131
10.6.1	<i>Effect of Temperature</i> .....	134
10.6.2	<i>Effect of Driving Force</i> .....	134
10.6.3	<i>Effect of Austenite Strength</i> .....	136
10.7	Conclusions .....	136
11	Neural Network Analysis of Steel Plate Processing .....	138
11.1	Introduction .....	138
11.2	The Database .....	138
11.3	Network Training .....	139
11.3.1	<i>The Yield Strength</i> .....	139
11.3.2	<i>The Ultimate Tensile Strength</i> .....	142
11.4	Application of the Models .....	144
11.4.1	<i>Carbon Concentration</i> .....	146
11.4.2	<i>Manganese Concentration</i> .....	149
11.4.3	<i>Silicon Concentration</i> .....	151
11.4.4	<i>Microalloying Additions</i> .....	152
11.4.5	<i>Rolling Parameters</i> .....	155
11.4.6	<i>Optimisation of YS/UTS Ratio</i> .....	156
11.4.7	<i>Other Published Data</i> .....	157
11.5	Conclusions .....	158
12	Control–Rolled Bainitic Steels .....	163
12.1	Introduction .....	163
	Part One: Si–Mn–Mo Steels .....	164
12.2	Experiments .....	164
12.2.1	<i>Testing</i> .....	165
12.3	Results .....	165
	Part Two: MABS and BABS .....	171
12.4	Alloy Design .....	171
12.4.1	<i>Neural Network Analysis of Rolled Bainitic Steel Plates</i> .....	173
12.4.2	<i>Testing the Models</i> .....	174
12.5	Rolling and Testing .....	179
12.6	Results .....	180
12.7	Conclusions .....	182
13	Conclusions and Suggestions .....	186

Appendix 1   MAP Documentation ..... 189

          A.1   Program MAP\_STEEL\_SPEEDNEW ..... 189

Appendix 2   Data for Neural Network Analysis  
              of Steel Plate Processing ..... 195

References ..... 200



# List of Nomenclature

$a$	length of the edges of a tetrakaidecahedron
$a_b$	thickness of bainite sub-unit
$a'_b$	thickness of bainite sub-unit when the austenite is deformed
$a_\alpha$	lattice parameter of ferrite at any temperature
$a_\alpha^o$	lattice parameter of ferrite at room temperature
$a_\gamma$	lattice parameter of austenite at any temperature
$a_\gamma^o$	lattice parameter of austenite at room temperature
$A$	surface area of a tetrakaidecahedron after deformation
$A_o$	surface area of a tetrakaidecahedron before deformation
$Ae_3$	equilibrium $\gamma/\gamma + \alpha$ phase boundary
$Ae'_3$	paraequilibrium $\gamma/\gamma + \alpha$ phase boundary
$Ar_3$	austenite to ferrite transformation-start temperature during cooling
$b$	principal distortion (ratio of the final to initial length of the unit vector) along the $x$ axis. Alternatively, magnitude of the Burgers vector
$B_d$	highest temperature at which bainite can form under the influence of an externally applied stress
$B_S$	bainite-start temperature
$c$	principal distortion along the $z$ axis
$d$	principal distortion along the $y$ axis
$\underline{d}$	vector describing the shear component of an invariant-plane strain shape deformation
$d_\alpha$	ferrite grain size
$e_\alpha$	linear thermal expansion coefficient of ferrite
$e_\gamma$	linear thermal expansion coefficient of austenite
$G_N$	universal nucleation function specifying the minimum free energy change required to obtain a detectable rate of nucleation of Widmanstätten ferrite or bainite
$G^*$	activation energy for nucleation
$h$	Planck constant
$h_i$	hyperbolic transfer function of the neural network
$I$	nucleation rate per unit volume
$I_b$	total nucleation rate of bainite including the effect of autocatalysis
$I_B$	total nucleation rate of ferrite on austenite grain boundaries
$I_B^f$	nucleation rate of ferrite on the grain boundary faces
$I_{T_h}$	nucleation rate at the $T_h$ temperature
$k_B$	Boltzmann constant
$K_1^f$	fraction of grain boundary face sites which nucleate ferrite
$K_2^f$	shape factor which depends on the shape of the nucleus on grain faces

$\ell$	total edge length of the tetrakaidecahedron after deformation
$\ell^i$	total edge length of a deformed tetrakaidecahedron along the principal axis $i$
$\ell_o^i$	total edge length of an undeformed tetrakaidecahedron along the principal axis $i$
$\ell_o$	total edge length of the tetrakaidecahedron before deformation
$\bar{L}$	mean lineal intercept length for grain size measurement
LPE	log predictive error
$M_d$	highest temperature at which martensite can form under the influence of an externally applied stress
$M_S$	martensite-start temperature
$N_V^o$	initial density of nucleation sites of bainite
$N_V^t$	density of nucleation sites of bainite at time $t$
$N_V^T$	total density of nucleation sites of bainite including the autocatalytic nucleation
$N_s^f$	number density of ferrite nucleation sites on grain faces
$p$	amount of reduction during deformation
$q$	frequency term defining the rate at which sites become nuclei
$Q$	activation energy for atoms crossing the austenite/ferrite interface
$R$	universal gas constant
$s$	shear component of an invariant-plane strain shape deformation
$S$	deformation matrix
$S_V$	grain boundary area per unit volume
$S_V^{db}$	surface area per unit volume of the deformation bands
$S_V^o$	initial grain boundary area per unit volume
$S_V^T$	total surface area per unit volume of defects including grain boundaries and deformation bands
$t$	time
$T$	absolute temperature
$T_e$	test energy
$T_h$	the highest temperature at which displacive transformation can take place
$T_{nr}$	recrystallisation stop temperature
$T_o$	temperature at which austenite and ferrite of the same composition have the same free energy
$T_o'$	same as $T_o$ but allowing for 400 J mol <sup>-1</sup> of stored energy of bainite
$u$	volume of bainite sub-unit
$v$	volume fraction
$v_\alpha$	volume fraction of ferrite
$\bar{w}_c$	mean carbon concentration of the alloy in weight percent
$w_c^\alpha$	weight percent of carbon in the ferrite
$w_c^\gamma$	weight percent of carbon in the austenite
$w_i$	concentration of element $i$ in weight percent
$w_{ij}^{(1)}, w_{ij}^{(2)}$	weights in neural network model
$W$	stored energy of deformation

$W_S$	Widmanstätten ferrite–start temperature
$\bar{x}$	average mole fraction of carbon in an alloy
$x_i$	concentration of element $i$ in mole fraction
$x_j$	inputs of neural network
$x_m^\alpha$	mole fraction of carbon in ferrite nucleus for maximum free energy change
$x_{min}$	minimum value of input $x_j$
$x_{max}$	maximum value of input $x_j$
$x_j^N$	normalised value of input $x_j$
$x^{\alpha\gamma}$	mole fraction of carbon in ferrite in equilibrium or paraequilibrium with austenite
$x^{\gamma\alpha}$	mole fraction of carbon in austenite in equilibrium or paraequilibrium with ferrite
$\alpha$	ferrite
$\alpha_1$	growth rate of allotriomorphic ferrite
$\beta$	autocatalysis factor for bainite nucleation
$\gamma$	austenite
$\delta$	interatomic spacing
$\Delta a_\alpha^c$	expansion of ferrite lattice due to dissolved carbon
$\Delta G$	general term representing Gibbs free energy change or the driving force
$\Delta G_m$	maximum molar free energy change for nucleation
$\Delta G_m^o$	initial value ( $\xi = 0$ ) of $\Delta G_m$
$\Delta G_{MECH}$	mechanical driving force
$\Delta G_v$	free energy change per unit volume for nucleation
$\Delta G^{\gamma \rightarrow \alpha}$	free energy change for austenite to ferrite transformation without any composition change
$\Delta G^{\gamma \rightarrow \gamma' + \alpha}$	free energy change associated with the equilibrium decomposition austenite into a mixture of carbon–enriched austenite and ferrite
$\Delta T$	undercooling
$\eta$	aspect ratio of discs of ferrite allotriomorphs
$\theta_b$	maximum volume fraction of bainite possible at any temperature
$\theta_i^{(1)}, \theta^{(2)}$	biases of the neural network analysis
$\epsilon$	dilatation normal to habit plane
$\varepsilon$	true strain
$\phi_S$	extent of stabilisation
$\lambda_1, \lambda_2$	constants defining bainite autocatalysis factor $\beta$
$\mu$	shear modulus
$\nu$	collision frequency of atoms
$\rho_d$	dislocation density
$\rho_d^o$	dislocation density of annealed material
$\rho_d^t$	dislocation density after $t$ seconds of recovery
$\tau$	shear stress along the shear direction

$\tau_d$	dislocation line energy per unit length
$\tau_{max}$	maximum shear stress on habit plane
$\sigma_A$	applied stress
$\sigma_N$	normal stress on habit plane
$\sigma_y^\gamma$	yield strength of austenite
$\sigma_{\gamma\alpha}$	austenite–ferrite nucleus interface energy
$\sigma_\nu$	estimated noise level of the data
$\xi$	volume fraction divided by the equilibrium or limiting volume fraction
$\xi_\alpha$	extent of allotriomorphic ferrite reaction

## Chapter One

# Introduction

Deformation is an important step in the processing of steels. Although primarily aimed at imparting a change in shape, it also governs the course of microstructural evolution which, together with the chemical composition, determines the final properties of the product.

In the past, processes like controlled rolling and thermomechanical control processing (TMCP) have been developed which combine heat treatment with mechanical deformation [Morrison and Chapman, 1976; Tanaka, 1995]. This not only eliminates the need for post-working heat treatment, but also results in a superior product [Tanaka 1995]. It involves controlling the development of microstructure by adjusting the deformation schedule (controlled rolling) and by resorting to accelerated cooling after rolling (TMCP).

Products with leaner chemistry but meeting the property requirements have been developed based on TMCP. This has considerable advantage over conventional products containing larger concentrations of solute elements. Weldability is improved on account of the lower ‘carbon equivalent’ and moreover, TMCP totally or partially eliminates the need for the addition of costly microalloying elements.

These developments have necessitated a more profound understanding of the effect of deformation of austenite ( $\gamma$ ) on its transformation behaviour. Austenite has a face-centred cubic (fcc) crystal structure. Upon cooling, it may transform to a variety of body-centred cubic (bcc) products by two fundamentally different mechanisms, reconstructive or displacive. The transformations in steels and their mechanisms have been extensively reviewed in the published literature [Christian and Edmonds, 1984; Bhadeshia, 1985; Bhadeshia and Christian, 1990]. Nevertheless, they are explained briefly in this chapter to provide the background for the work presented in the thesis.

### 1.1 Displacive Transformation

A displacive transformation is accomplished by a homogeneous deformation of the parent phase (Figure 1.1a, b). The resultant shape deformation causes elastic or plastic strains in the surrounding matrix when the transformation occurs under constraint. This reduces the total driving force available for transformation and therefore the product is constrained to grow in the form of a thin plate which minimises the strain energy of the shape deformation. The atoms move in a coordinated manner across the interface and as such there is no change in the chemical composition. The absence of solute partitioning further reduces the free energy change. An essential feature of this mechanism is the existence of an atomic correspondence

between the parent and the product phase so that given vectors, planes and unit cells of one structure are related to corresponding vectors, planes and unit cells of the other structure in a particular way [Bhadeshia, 1992]. The interface between the parent and the product phase is coherent or semi-coherent. The interface dislocations can move conservatively which leave the interface glissile and capable of moving without diffusion.

In some substitutionally alloyed systems, where diffusion occurs much more readily than in iron, a shape change can be accompanied by a change in chemical composition by very short range atom movements. Such a transformation has been called ‘diffusional–displacive’ transformation [Christian, 1994; Christian, 1997]. A further possibility arises for interstitial alloys where the difference in the diffusion coefficients of interstitial and substitutional atoms can be many orders of magnitude [Christian, 1962]. Interstitial atoms may, in this case, diffuse over relatively long distances whereas the substitutional lattice is deformed into the new crystal structure. Thus there is a lattice correspondence but no atomic correspondence [Bhadeshia, 1992].

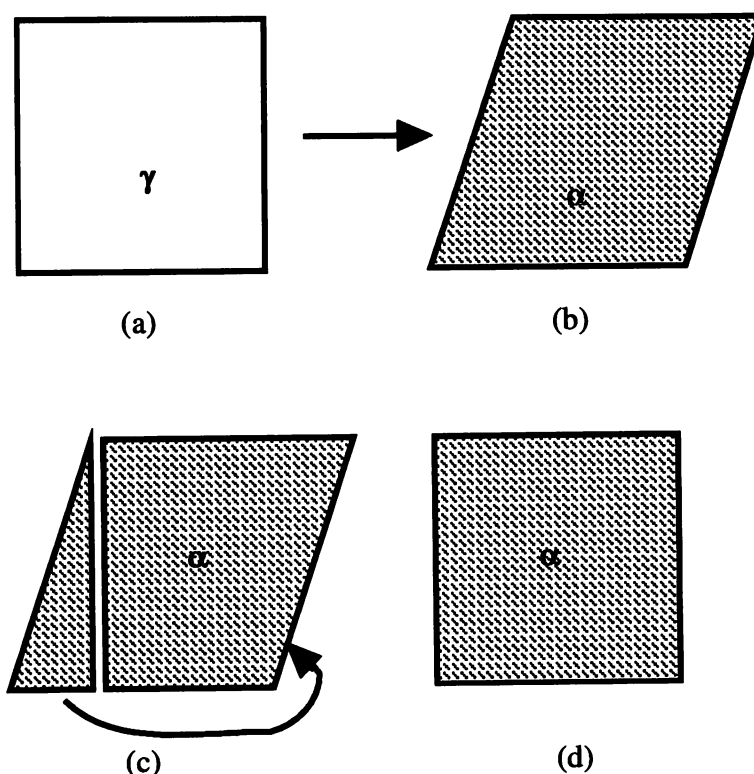


Figure 1.1: A schematic interpretation of the displacive and reconstructive transformations. Steps (a) to (b) represent displacive transformation while steps (a) to (d) represent reconstructive transformation. The mass transport illustrated in (c) eliminates the shape change due to shear [Bhadeshia, 1992].

## 1.2 Reconstructive Transformation

Reconstructive transformation takes place by the thermally activated, uncoordinated movement of atoms across the interface. This entails breaking the old bonds and formation of new ones. The flow of matter is sufficient to prevent any shape deformation with a shear component. This ensures the minimisation of strain energy, leaving only the volume change effects. This phenomenon is illustrated schematically in Figure 1.1. In this phenomenological representation, the displacive transformation is followed by diffusion which minimises the change in shape, though in practice all the processes must occur simultaneously as the transformation interface advances. All elements, including iron, must diffuse over relatively large distances during the transformation to minimise <sup>the</sup>  $\gamma$  strain energy [Bhadeshia, 1992]. This does not necessarily mean any bulk partitioning of substitutional elements during transformation; for example in pure metals, the reconstructive phase transition does not entail a composition change.

Figure 1.1 also highlights the essential difference between the two mechanisms of transformations. The reconstructive transformation is analogous to the process of plastic deformation followed by recrystallisation and the displacive transformation to that of plastic deformation only. The difference being that there is no change in crystal structure during plastic deformation or recrystallisation. It is expected therefore that the deformation of austenite can have quite different effects on the two types of transformations.

Thus, a study of the effect of deformation of austenite on its transformation is important from an industrial as well as from a fundamental point of view and this was the purpose of the work presented in this thesis.

Before proceeding to discuss the effects of deformation of austenite, the variety of transformation products that may form during cooling of austenite are briefly described.

## 1.3 Transformation Products

Depending on the driving force available for transformation at a given temperature, austenite can transform to allotriomorphic ferrite, Widmanstätten ferrite, pearlite, bainite or martensite by one of the two mechanisms described above.

### 1.3.1 Allotriomorphic and Idiomorphic Ferrite

Allotriomorphic ferrite is the first phase to form on cooling austenite below the  $A_{e3}$  temperature (the highest temperature at which both austenite and ferrite can coexist under equilibrium conditions). The ferrite nucleates on austenite grain boundaries. The transformation takes place by a reconstructive mechanism which requires the diffusion of all the atoms. However, in a system like Fe-C-X (where X denotes a substitutional solute such as Mn, Si, Ni *etc.*), the diffusivity of interstitial carbon is several orders of magnitude higher than that of X. This gives rise to two situations to maintain the flux balance of all the species for a given interface velocity while simultaneously ensuring that local equilibrium is maintained at the interface for all the solute atoms [Kirkaldy, 1958; Coates, 1973]:

- (1) At low supersaturations and small driving force, the carbon concentration of austenite

at the interface is nearly the same as the bulk alloy composition. The activity of carbon is then almost constant in austenite. This reduces the flux of carbon to an extent which allows a considerable redistribution of substitutional X atoms into austenite. This is called partitioning local equilibrium (PLE) because there is appreciable partitioning of substitutional solute atoms.

(2) At high supersaturations, only a small amount of X is partitioned into austenite which gives rise to a sharp concentration gradient of X ahead of interface. The flux of X can then match the flux of carbon atoms. This mode of growth is termed negligible partitioning local equilibrium (NPLE).

At still lower temperatures, the diffusion of substitutional solute atoms is so slow that it cannot partition at all. The Fe/X ratio is the same in both the phases. The ferrite growth rate is controlled by the diffusion of interstitial C atoms which, subject to the constraint that the Fe/X ratio must be the same everywhere, attains local equilibrium at the interface. The ferrite in this case is said to grow by a paraequilibrium mechanism. The highest temperature at which this becomes possible is designated as the  $Ae'_3$  temperature.

Idiomorphic ferrite also forms by the same mechanism as the grain boundary or allotriomorphic ferrite but it nucleates within the austenite grains on particles which are usually non-metallic.

### 1.3.2 Widmanstätten ferrite

Widmanstätten ferrite plates nucleate on austenite grain boundaries or on pre-existing ferrite allotriomorphs. The transformation occurs at a temperature below that of allotriomorphic ferrite but above bainite. The mechanism of transformation is displacive but the available driving force at this relatively high temperature is not enough to sustain growth without carbon partitioning. The substitutional atoms do not partition. The paraequilibrium growth rate is therefore controlled by carbon diffusion in austenite [Bhadeshia and Christian, 1990]. The cooperative, back to back growth of two mutually accommodating variants ensures that the strain energy of transformation is minimised to about  $50 \text{ J mol}^{-1}$ , thus allowing the transformation to proceed at a relatively small driving force [Bhadeshia, 1981]. Widmanstätten ferrite has a wedge morphology. It is frequently observed in welds but is less common in wrought products.

### 1.3.3 Pearlite

Pearlite forms from austenite by a reconstructive mechanism and involves the cooperative growth of ferrite and cementite, resulting in an apparently lamellar mixture. Nodules of pearlite nucleate on austenite grain boundaries, austenite-ferrite interfaces or on inclusions. Pearlite is nucleated by ferrite in a hypo-eutectoid steels or by cementite in hyper-eutectoid steels. Pearlite grows in the form of nodules which consist of interpenetrating single crystals of ferrite and of cementite. The growth of pearlite in plain carbon steels is controlled by the diffusion of carbon in the austenite ahead of the interface [Mehl and Hagel, 1956]. A large volume fraction of pearlite in the microstructure has a significant effect on the yield and tensile strengths of



steel. The strength depends on the interlamellar spacing which in turn depends on the cooling rate and the transformation temperature.

#### 1.3.4 Bainite

Bainite forms by displacive mechanism. The growth of bainite is accompanied by an invariant-plane strain shape deformation with a large shear component. The strain energy of the shape deformation has been calculated and measured to be about  $400 \text{ J mol}^{-1}$  [Bhadeshia, 1981]. Though carbon diffusion takes place during paraequilibrium nucleation, the growth is diffusionless [Bhadeshia, 1992]. This makes it impossible for the transformation to take place above the  $T_o$  temperature at which both austenite and ferrite of the same composition have the same free energy. Nucleation usually occurs at austenite grain surfaces.

Compared to martensite, bainite grows at relatively high temperatures when the austenite is weak and undergoes plastic deformation to relieve the large strain associated with the shape change. The resulting local increase in dislocation density hinders the motion of glissile transformation interface. The growth of the plate is eventually stifled by the build up of dislocation debris so that each plate is usually much smaller than the austenite grain size. The reaction progresses further by the nucleation of new plates, also known as sub-units, particularly at the tips of the existing ones. This results in a sheaf-like structure [Hehemann, 1970; Bhadeshia, 1992]. Since the driving force for the bainite transformation is smaller than for martensite and because of the plastic deformation caused by the shape change, bainite plates grow at a rate much slower than martensite plates. Direct experimental measurements [Bhadeshia, 1984] and the analysis of available kinetic data [Ali and Bhadeshia, 1989], however, show that the bainite plate growth rate is orders of magnitude faster than can be expected from paraequilibrium carbon diffusion-controlled growth.

It has been confirmed experimentally that substitutional atoms do not diffuse during bainite transformation [Bhadeshia and Waugh, 1982]. The role of carbon is somewhat different. Even though the plate first forms without partitioning, the excess carbon escapes into the residual austenite immediately after transformation. The next plate of bainite then grows from carbon-enriched austenite with a lower driving force. This continues until the carbon concentration of austenite reaches  $T_o$  when the driving force for diffusionless transformation drops to zero and the reaction stops. The locus of  $T_o$  temperatures as a function of carbon concentration on the Fe-C phase diagram is called the  $T_o$  curve, Figure 1.2. The curve is shifted to still lower temperatures to account for  $400 \text{ J mol}^{-1}$  of the stored energy due to the shape deformation; the locus is then designated as the  $T'_o$  curve. The phenomenon is known as “incomplete reaction phenomenon” because the reaction stops before the austenite reaches its equilibrium concentration given by the  $Ae_3$ . The maximum volume fraction of bainite ( $\theta_b$ ) that can form at any temperature increases with decreasing temperature.

Bainite can be distinguished into the upper and lower bainite morphologies, Figure 1.3. Upper bainite forms at higher temperatures where the carbon can diffuse rapidly. The time taken for the decarburisation of a supersaturated ferrite plate is smaller than that required for precipitation of carbide within the plate. The excess carbon of the supersaturated ferrite

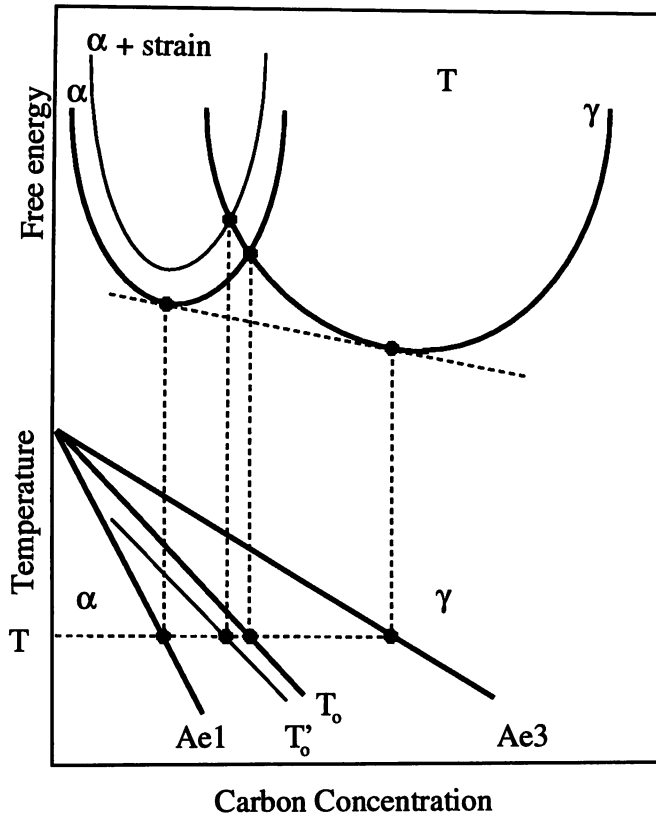


Figure 1.2: A schematic illustration of  $T_0$  curve and the incomplete reaction phenomenon. Diffusionless transformation is impossible if the carbon concentration of austenite exceeds the  $T_0$  curve [Bhadeshia, 1992].

is therefore rejected into the adjacent austenite. Cementite may eventually precipitate out of the enriched residual austenite. As the transformation temperature is lowered, the diffusion of carbon becomes slower and some of the carbon is precipitated as fine carbide particles inside the ferrite plates. The remaining carbon escapes into the austenite and may precipitate as inter-plate carbide. This gives the lower bainite morphology.

### 1.3.5 Acicular Ferrite

Acicular ferrite is similar to bainite, but they are microstructurally different in that the bainite plates nucleate on grain boundaries and grow in the form of sheaves of parallel plates whereas acicular ferrite plates nucleate intragranularly on non-metallic inclusions and grow radially in many different directions. The resulting chaotic microstructure gives a better toughness because cleavage cracks are deflected more frequently at the plate boundary.

### 1.3.6 Martensite

Martensite nucleates and grows without diffusion. The highest temperature at which martensite transformation becomes possible is termed the  $M_s$  temperature. Martensite in steels can be hard and brittle when it is supersaturated with carbon. This necessitates a tempering treatment to give ferrite and finely dispersed carbides with good strength and toughness.

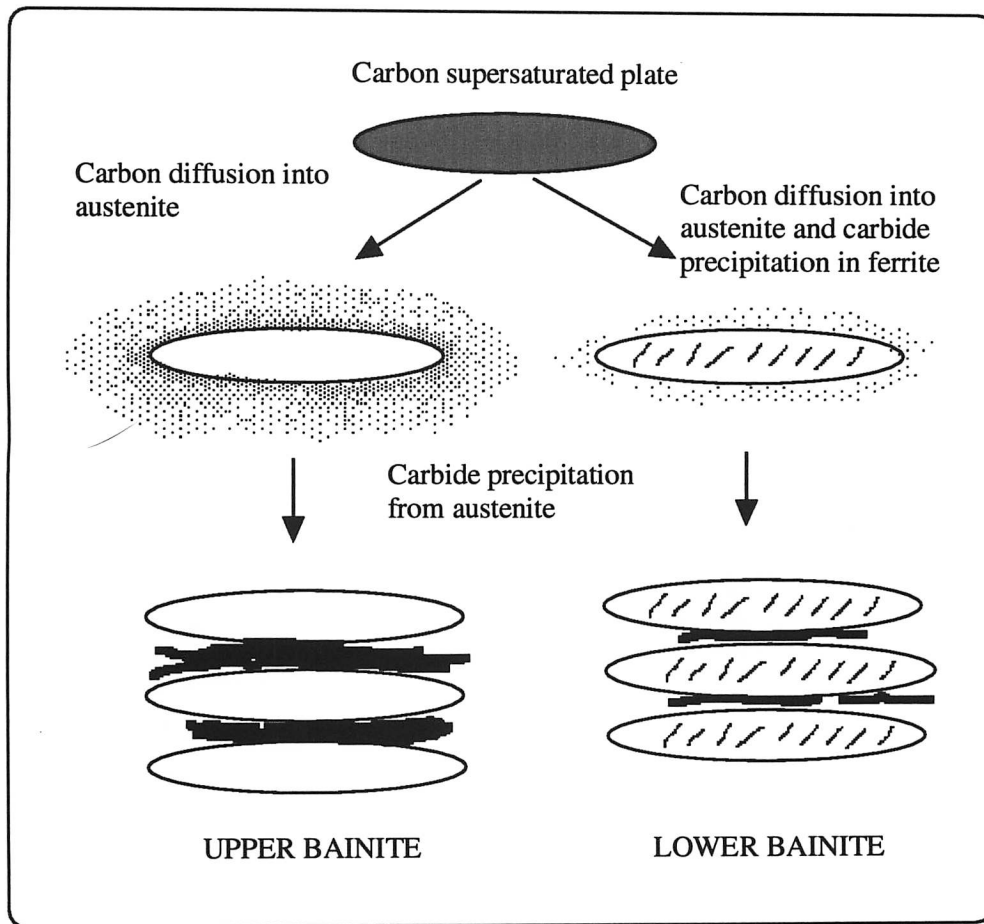


Figure 1.3: A schematic description of the transition from upper to lower bainite [Bhadeshia, 1992].

#### 1.4 Summary

The reconstructive and displacive mechanisms of phase transformation have been discussed. A flow chart summarising the characteristics of the different transformation products and their mechanisms is shown in Figure 1.4. The relative amounts of different phases described above and hence the final properties of the product depend on chemical composition, state of austenite before transformation (including effects of deformation, if any) and cooling conditions.

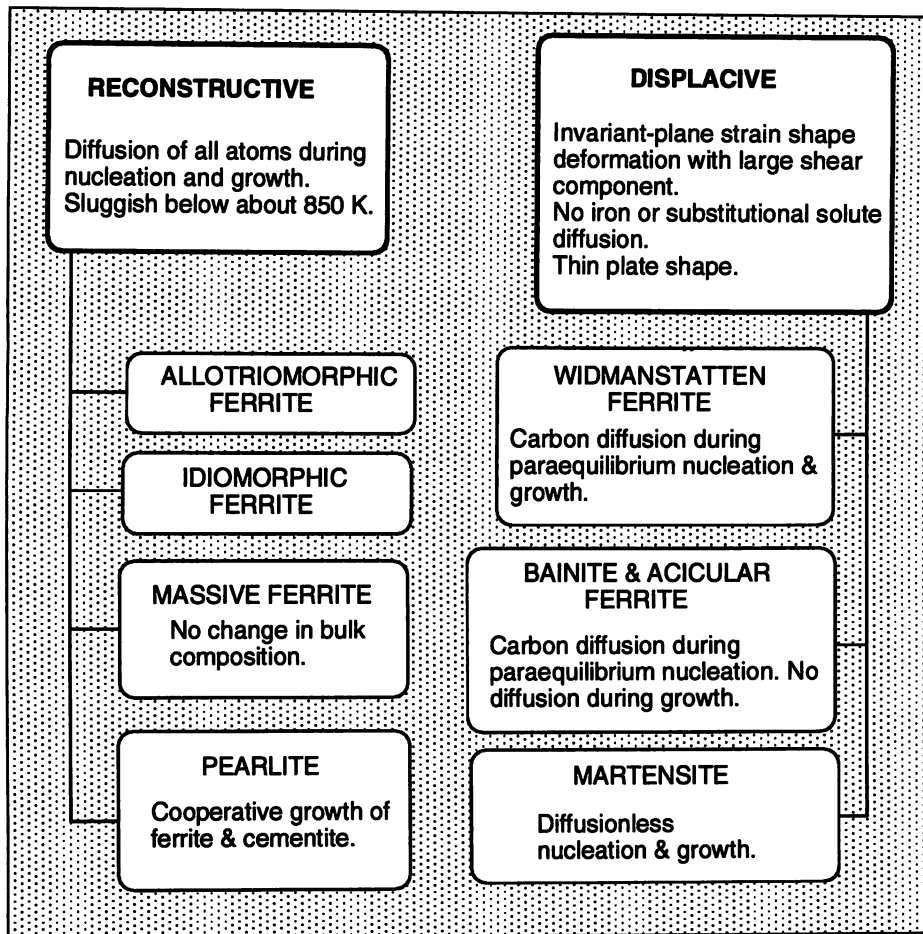


Figure 1.4: A flow chart summarising various transformations in steels and their mechanism [Bhadeshia, 1992].

## Chapter Two

# Review of Bainite Kinetics

A brief review of the general theory of the bainite transformation is presented. This is followed by a description of a mathematical model for the kinetics of bainite transformation as proposed by Rees and Bhadeshia [1992].

### 2.1 The Thermodynamic Parameters

Before undertaking a review of the theory of the bainite transformation, the thermodynamic terms relevant to this discussion will be illustrated geometrically.

Consider austenite of composition  $\bar{x}$  at temperature  $T_1$  (Figure 2.1a). Its free energy ( $G$ ) can decrease if it decomposes into a mixture of ferrite and carbon-enriched austenite. The decrease in free energy associated with the decomposition is the largest when compositions of the ferrite and the austenite are  $x^{\alpha\gamma}$  and  $x^{\gamma\alpha}$  respectively. These values are obtained by drawing a tangent which is common to the free energy curves of both the phases.  $x^{\alpha\gamma}$  and  $x^{\gamma\alpha}$  are given by the points where the common tangent touches the respective free energy curves. The free energy change associated with the equilibrium decomposition of one mole of austenite,  $\Delta G^{\gamma \rightarrow \gamma' + \alpha}$ , can thus be obtained by a common tangent construction, Figure 2.1a. It can be shown that the free energy change for the formation of one mole of ferrite is given by  $\Delta G_1$ , which is  $\Delta G^{\gamma \rightarrow \gamma' + \alpha}$  divided by  $(x^{\gamma\alpha} - \bar{x})/(x^{\gamma\alpha} - x^{\alpha\gamma})$ , the ferrite mole fraction.

The amount of the product formed during nucleation is very small and as such has little influence on the composition of the residual austenite. In the limiting case, it can be said that the points representing the composition of the initial austenite and the residual austenite coincide with each other so that the line AB becomes a tangent to the austenite free energy curve at the original composition  $\bar{x}$ , Figure 2.1b. The free energy change accompanying the formation of one mole of ferrite nuclei of composition  $x_\alpha$  is then given by  $\Delta G_2$ . The value of  $\Delta G_2$  depends on the choice of the ferrite nucleus composition and attains a maximum value of  $\Delta G_m$  when the nucleus composition is  $x_m^\alpha$ . As shown in Figure 2.1b, this is obtained by drawing a tangent to the ferrite free energy curve which is parallel to the tangent AB [Hillert, 1953].

Finally, the free energy change for the diffusionless transformation,  $\Delta G^{\gamma \rightarrow \alpha}$ , is obtained as the difference in the free energies of austenite and ferrite at the appropriate composition, Figure 2.1c.

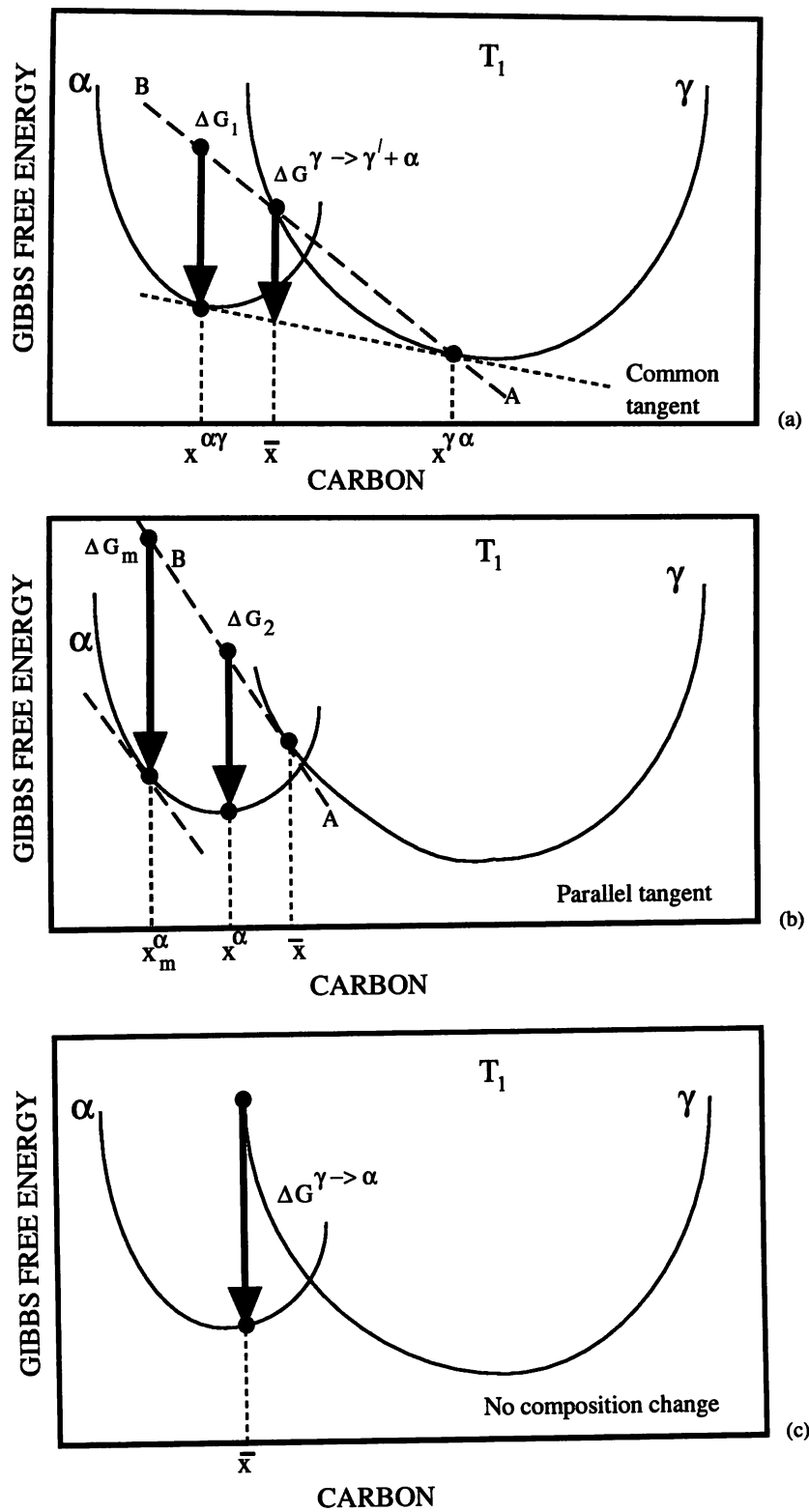


Figure 2.1: Geometrical illustration of the chemical free energy changes associated with nucleation and growth of ferrite from austenite of composition  $\bar{x}$ , after Bhadeshia [1992].

## 2.2 General Theory of Bainite Transformation

A time–temperature–transformation (TTT) diagram for steels consists essentially of two C–curves, one for high temperature reconstructive transformations to allotriomorphic ferrite and pearlite and the other for displacive transformations to Widmanstätten ferrite and bainite which occur at comparatively lower temperatures (Figure 2.2). In steels where the transformation is very fast, the two curves overlap so that only a single curve may be detected in routine experiments.

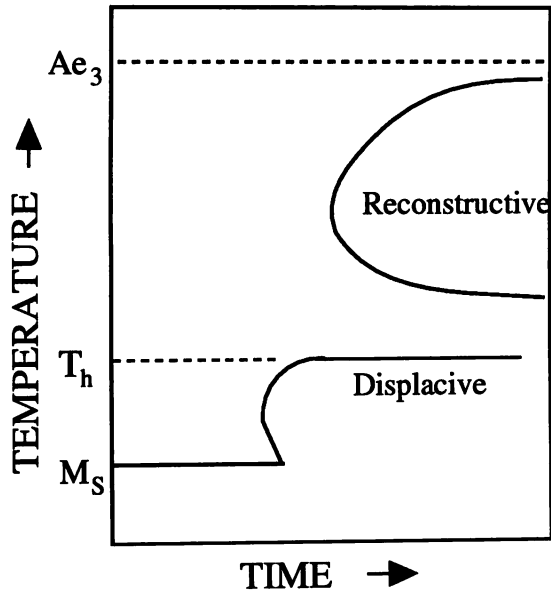


Figure 2.2: A schematic TTT diagram showing the two C–curves and the  $T_h$  temperature [Bhadeshia, 1992].

### 2.2.1 Nucleation

The lower C–curve has a characteristic flat top which represents the highest temperature  $T_h$  at which displacive transformation to ferrite can take place. This transformation–start temperature must be controlled by nucleation which is more difficult than growth, because of the disproportionate amount of energy spent in creating a new interface around a small particle. An analysis of the magnitude of the free energy change available at  $T_h$  provides useful clues to the mechanism of transformation and gives an indication of the amount of driving force necessary for nucleation to occur at a detectable rate [Bhadeshia, 1981].

Steven and Haynes [1956] have measured  $T_h$  temperatures for a wide range of low–alloy steels, all of which exhibited two distinct C–curves. For each of these steels, the driving force available at  $T_h$  was calculated assuming two possible nucleation mechanisms – (i) nucleation without the partitioning of any of the solute atoms including carbon ( $\Delta G^{\gamma \rightarrow \alpha}$ ) and (ii) nucleation with paraequilibrium carbon partitioning ( $\Delta G_m$ ) [Bhadeshia, 1981]. The results of the analysis are plotted in Figure 2.3 and reveal some important facts. Firstly, the nucleation of

Widmanstätten ferrite or bainite occurs with the partitioning of carbon atoms since the alternative hypothesis of diffusionless nucleation would lead to an increase in the free energy for some of the cases illustrated (Figure 2.3a). Secondly, all the points, whether they correspond to Widmanstätten ferrite or to bainite lie on the same straight line in Figure 2.3b. It can therefore be concluded that both phases originate from the same nucleus which develops into bainite or Widmanstätten ferrite depending on certain growth criteria which will be discussed later.

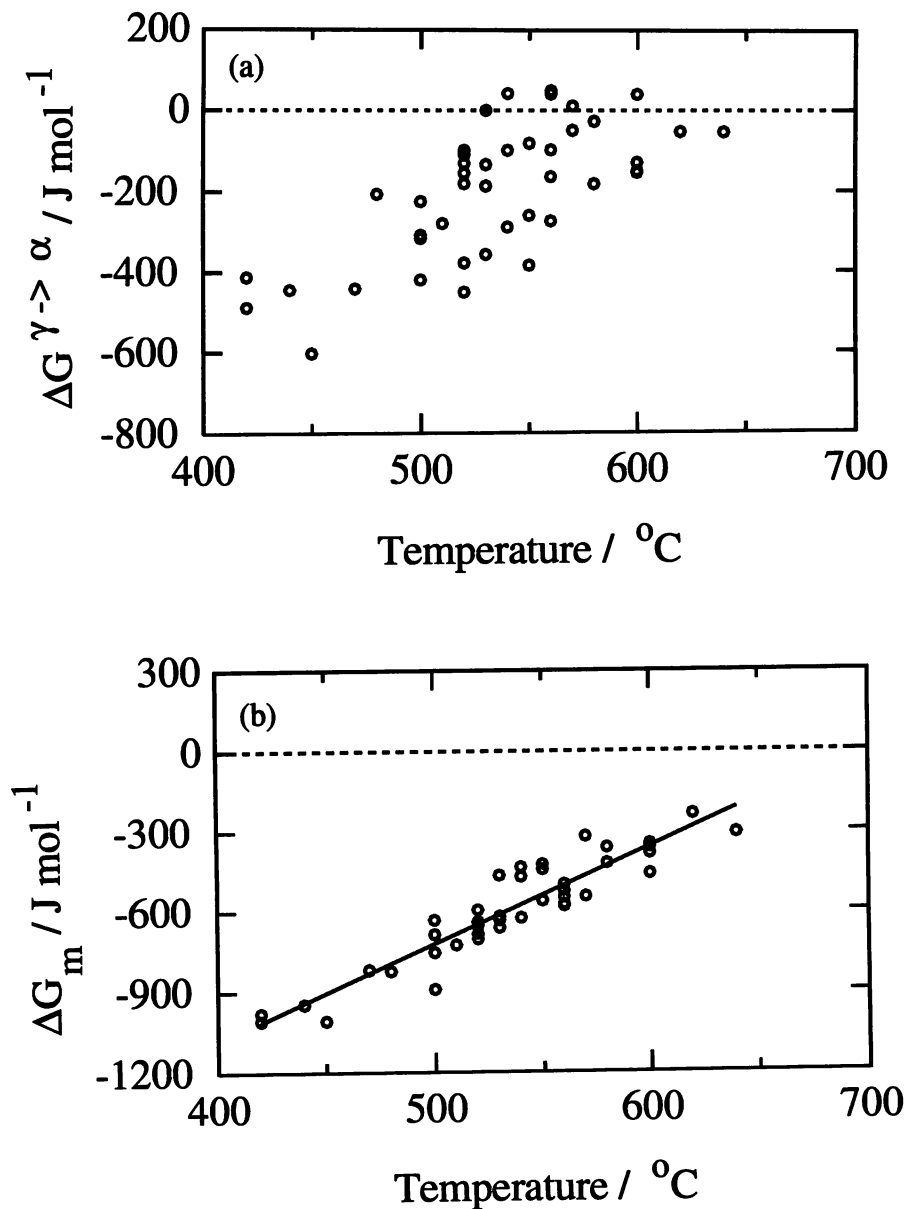


Figure 2.3: The driving force for nucleation for a variety of steels at their respective  $T_h$  temperatures [Bhadeshia, 1981]. The driving force was calculated assuming (a) diffusionless nucleation ( $\Delta G^{\gamma \rightarrow \alpha}$ ) and (b) paraequilibrium redistribution of carbon ( $\Delta G_m$ ).



Figure 2.3b also shows that the driving force at which nuclei start to form at a detectable rate varies linearly with the temperature  $T_h$ :

$$G_N = B_1 T_h - B_2 \quad \text{J mol}^{-1} \quad (2.1)$$

where  $G_N$  is defined as the minimum free energy change required to obtain a detectable amount of Widmanstätten ferrite or bainite. For the best fit line, the values of  $B_1$  and  $B_2$  have been found to be  $3.637 \text{ J mol}^{-1} \text{ K}^{-1}$  and  $2540 \text{ J mol}^{-1}$  respectively when  $T_h$  is expressed in  $^{\circ}\text{C}$  [Ali and Bhadeshia, 1990].  $G_N$  is known as the “universal nucleation function” and is applicable to all low-alloy steels. Nucleation of Widmanstätten ferrite or bainite becomes possible at a temperature at which the actual driving force for nucleation,  $\Delta G_m$  (negative), becomes less than that given by the  $G_N$  function.

Although the above treatment appears empirical, it has been interpreted in terms of martensite nucleation theory [Bhadeshia, 1981; Bhadeshia, 1992]. The nucleation rate per unit volume depends on the activation energy  $G^*$ :

$$I \propto \nu \exp\{-G^*/RT\} \quad (2.2)$$

where  $\nu$  is the attempt frequency factor,  $R$  is the gas constant and  $T$  the absolute temperature. Equation 2.2 can be written as

$$-G^* \propto BT \quad \text{where} \quad B = R \ln\{I/\nu\} \quad (2.3)$$

The highest temperature at which displacive transformation can take place (*i.e.*,  $T_h$ ) corresponds to the temperature at which nucleation rate becomes detectable. This value of the nucleation rate should be constant and independent of steel composition. Thus, for all steels, the rate of nucleation of displacive ferrite at their respective  $T_h$  temperatures is the same. Therefore,  $B$  is constant when  $I$  is evaluated at  $T = T_h$ . This gives

$$-G^* \propto T_h \quad (2.4)$$

We now proceed to justify this relationship in terms of nucleation theory. The nucleation of martensite occurs by the dissociation of arrays of dislocations [Olson and Cohen, 1976]. For this case, the activation energy is expected to be directly proportional to the driving force [Magee, 1970; Raghavan and Cohen, 1971] so that

$$-G^* \propto \Delta G_m \quad (2.5)$$

If it is assumed that Widmanstätten ferrite and bainite nucleate by a similar mechanism then a combination of equations 2.4 and 2.5 gives  $\Delta G_m \propto T_h$  and since at  $T_h$ ,  $\Delta G_m = G_N$ , it follows that  $G_N \propto T_h$  which is precisely the relationship illustrated in Figure 2.3b and expressed by equation 2.1.

It is also to be noticed that in the classical nucleation theory where a new phase forms by a random structural and composition fluctuation in the parent phase,  $G^* \propto \Delta G_m^{-2}$ . Such a relation cannot explain the behaviour obtained for Widmanstätten ferrite and bainite.

### 2.2.2 Growth of the Nucleus

It was pointed out earlier that both Widmanstätten ferrite and bainite grow from the same nucleus and that the nucleation rate becomes appreciable when

$$\Delta G_m \leq G_N \quad (2.6)$$

The nucleus can develop into Widmanstätten ferrite (*i.e.*,  $T_h = W_S$ ) if the driving force for paraequilibrium growth exceeds the stored energy of Widmanstätten ferrite which has been estimated to be  $50 \text{ J mol}^{-1}$  [Bhadeshia, 1981]

$$\Delta G^{\gamma \rightarrow \gamma' + \alpha} \leq -50 \text{ J mol}^{-1} \quad (2.7)$$

Alternatively, if the driving force for diffusionless growth is sufficient to allow for  $400 \text{ J mol}^{-1}$  of the stored energy of bainite then transformation to bainite takes place and  $T_h$  is identified with the bainite-start temperature  $B_S$ ,

$$\Delta G^{\gamma \rightarrow \alpha} \leq -400 \text{ J mol}^{-1} \quad (2.8)$$

It should be noted that for all the steels included in the analysis of Figure 2.3 and equation 2.1, the transformation-start temperature ( $T_h$ ) was controlled by the nucleation criterion.  $\Delta G^{\gamma \rightarrow \gamma' + \alpha}$  was less than  $-50 \text{ J mol}^{-1}$  at  $T_h$  in all the cases so that the growth criterion for Widmanstätten ferrite was satisfied for all steels.

The concept elucidated above is illustrated in Figure 2.4. The Widmanstätten ferrite-start temperature,  $W_S$ , or the bainite-start temperature,  $B_S$ , is defined as the highest temperature at which both the nucleation and the growth criteria for the respective phase are first satisfied.

### 2.2.3 The Nucleation Rate

At any temperature the rate of nucleation per unit volume is related to the activation energy by an Arrhenius type equation:

$$I = B_3 \exp \left\{ -\frac{G^*}{RT} \right\} \quad (2.9)$$

where  $B_3$  is a constant related to the density of potential nucleation sites. Expanding  $G^*$  to account for its linear dependence on the driving force, we get

$$I = B_3 \exp \left\{ -\frac{B_4 + B_5 \Delta G_m}{RT} \right\} \quad (2.10)$$

where  $B_4$  and  $B_5$  are constants. At  $T = T_h$ ,  $\Delta G_m = G_N$ ; the nucleation rate,  $I_{T_h}$ , is then given by:

$$I_{T_h} = B_3 \exp \left\{ -\frac{B_4 + B_5 G_N}{RT_h} \right\} \quad (2.11)$$

Dividing equation 2.10 by equation 2.11 and rewriting it in terms of the undercooling below  $T_h$

$$I = I_{T_h} \exp \left\{ -\frac{B_4 \Delta T}{RT T_h} - \frac{B_5}{R} \left( \frac{\Delta G_m}{T} - \frac{G_N}{T_h} \right) \right\} \quad (2.12)$$

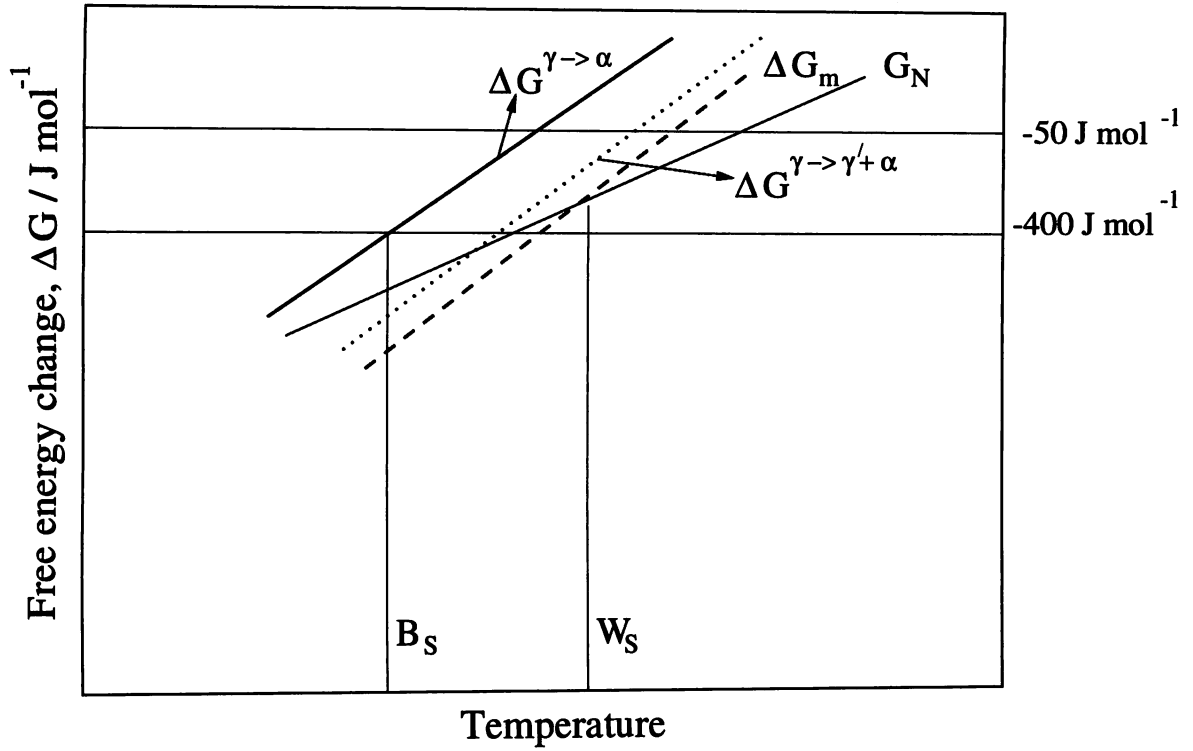


Figure 2.4: Diagram illustrating the definition of  $W_S$  and  $B_S$  temperatures based on available driving force for nucleation and growth, [Bhadeshia, 1981].

where,  $\Delta T = T_h - T$  is the undercooling.

Consider two steels A and B. The ratio of the rates at which ferrite nucleates by a displacive mechanism at their respective transformation-start temperatures,  $T_h^A$  and  $T_h^B$ , is [Rees and Bhadeshia, 1992]:

$$\frac{I_{T_h^A}}{I_{T_h^B}} = \exp \left\{ - \frac{(B_4 - B_2 B_5)(T_h^A - T_h^B)}{RT_h^A T_h^B} \right\} \quad (2.13)$$

At their respective  $T_h$  temperatures all steels have an identical nucleation rate;  $I_{T_h^A} = I_{T_h^B} = I_{T_h}$ . This gives  $B_4 = B_2 \times B_5$ . The nucleation rate is therefore written as:

$$I = B_3 \exp \left\{ - \frac{B_4}{RT} - \frac{B_4 \Delta G_m}{B_2 RT} \right\} \quad (2.14)$$

### 2.3 Rees and Bhadeshia Model

The above theory was applied by Bhadeshia [1982a] to model the kinetics of the bainite transformation. The model was subsequently modified by Rees and Bhadeshia [1992]. The model is limited to upper bainite and to steels where carbide precipitation is prevented by alloying with elements like silicon.

The bainite plates first nucleate on austenite grain boundaries. The initial nucleation rate is given by equation 2.14. The density of nucleation sites,  $B_3$ , is related to the austenite grain

size

$$B_3 = (\bar{L}B'_3)^{-1} \quad (2.15)$$

where  $\bar{L}$  is the mean lineal intercept length and  $B'_3$  is an empirical constant.

The dislocation debris generated by the shape deformation stops plate growth even before it encounters an austenite grain boundary. The transformation proceeds further by autocatalytic nucleation of new plates at the tips of the old ones [Oblak and Hehemann, 1967]. This results in a sheaf-like structure, Figure 2.5. The plates, once nucleated, grow very rapidly to consume a fixed volume of austenite before they are halted [Barford and Owen, 1961; Oblak and Hehemann, 1967; Bhadeshia and Edmonds, 1979]. The overall transformation kinetics are thus controlled by nucleation rather than by growth. The nucleation rate due to autocatalysis was assumed to be proportional to the existing bainite volume fraction [Bhadeshia, 1982a]. The total nucleation rate per unit volume was written as

$$I_b = I(1 + \beta\theta_b\xi) \quad (2.16)$$

where  $\beta$  is an autocatalysis constant and  $\xi$  is the volume fraction of bainite ( $v$ ) normalised with respect to the maximum fraction,  $\theta_b$ , possible at a given temperature

$$\xi = v/\theta_b \quad (2.17)$$

The austenite is enriched in carbon as the reaction progresses, reducing the driving force. The free energy for nucleation,  $\Delta G_m$ , was allowed to vary linearly with the extent of reaction from its initial value of  $\Delta G_m^o$  to the final value of  $G_N$  according to

$$\Delta G_m = \Delta G_m^o - \xi(\Delta G_m^o - G_N) \quad (2.18)$$

The form of equation 2.18 assumes that the nucleation and growth criteria of transformation fail simultaneously so that  $\Delta G_m = G_N$  when  $\xi = 1$ .

The autocatalysis factor  $\beta$  was modelled as a function of the carbon content of the steel:

$$\beta = \lambda_1(1 - \lambda_2\bar{x}) \quad (2.19)$$

where  $\lambda_1$  and  $\lambda_2$  are empirical constants and  $\bar{x}$  is the mean carbon concentration of the steel in mole fraction. Thus autocatalysis is less effective in higher carbon steels where a significant build up of carbon at the transformation interface inhibits nucleation of new plates. When the steels are considered individually,  $\beta = \lambda_1$  for that steel.

Consider austenite of volume  $V^\gamma$  undergoing transformation to bainite. The extended volume of bainitic ferrite that forms between time  $\tau$  and  $\tau + d\tau$  is given as

$$dV_e = I_b V^\gamma u d\tau \quad (2.20)$$

where  $u$  is the volume of a bainite plate. The change in real volume is related to the corresponding change in extended volume by [Christian, 1975]

$$dV = (1 - \xi) dV_e \quad (2.21)$$

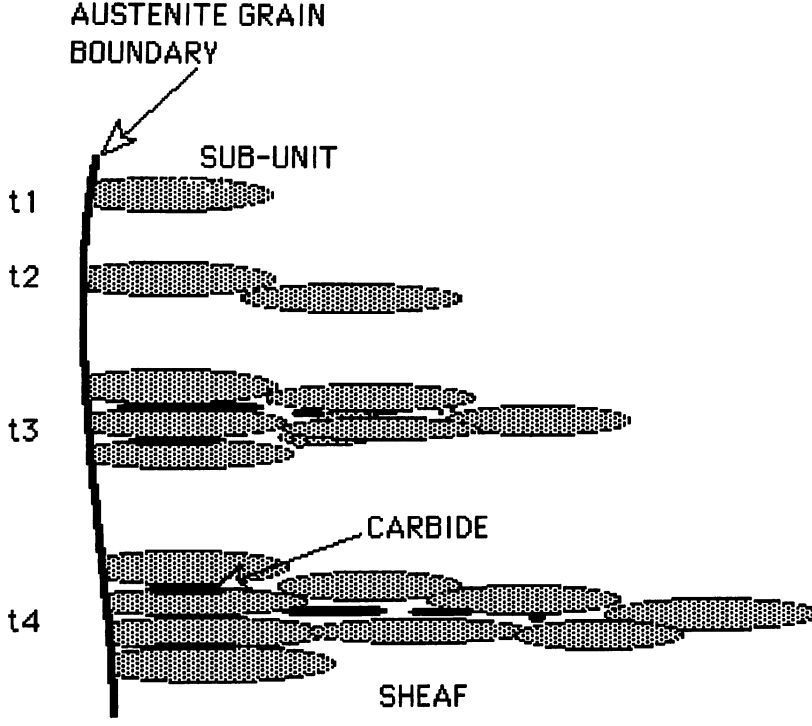


Figure 2.5: Schematic illustration of the sheaf structure of bainite, after Bhadeshia [1992].

This gives

$$dV = (1 - \xi) V^\gamma u I_b d\tau \quad (2.22)$$

Writing this in terms of bainite volume fraction  $v$  while remembering that  $v = \theta_b \xi$ , we get

$$\theta_b d\xi = (1 - \xi) u I_b d\tau \quad (2.23)$$

Substituting for nucleation rate  $I$  gives the differential equation for the overall transformation rate

$$d\xi = \frac{u B_3}{\theta_b} (1 - \xi) (1 + \beta \theta_b \xi) \times \exp \left[ -\frac{B_4}{RT} \left( 1 + \frac{\Delta G_m^o}{B_2} \right) + \Gamma_2 \xi \right] d\tau \quad (2.24)$$

where  $\Gamma_2$  is given by

$$\Gamma_2 = \frac{B_4 (\Delta G_m^o - G_N)}{B_2 RT} \quad (2.25)$$

Equation 2.24 was solved analytically to give the time to form a certain volume fraction of bainite [Rees and Bhadeshia, 1992].

The above model has four empirical constants, namely  $B'_3$ ,  $B_4$ ,  $\lambda_1$  and  $\lambda_2$ . The model was optimised using the bainite transformation kinetics data due to Bhadeshia [1982a] to determine the best fit values of these empirical constants. The chemical compositions of the steels used in the analysis are given in Table 2.1. The best fit values of the constants after optimisation are given in Table 2.2.

Alloy	C	Si	Mn	Ni	Cr	Mo	V
Fe-Mn-Si-C	0.22	2.03	3.0	0.00	0.00	0.00	0.00
Fe-Ni-Si-C	0.39	2.05	0.00	4.08	0.00	0.00	0.00
300 M	0.44	1.74	0.67	1.85	0.39	0.83	0.09

Table 2.1: The composition (wt.%) of the steels used for the optimisation of Rees and Bhadeshia model [1992]. The bainite transformation kinetics of these alloys were first studied by Bhadeshia [1982a].

Dataset	$B'_3/u, \text{m}^{-1}\text{s}$	$B_4, \text{J mol}^{-1}$	$\lambda_1$	$\lambda_2$
Fe-Mn-Si-C	$3.876 \times 10^7$	1.925	4.756	0.00
Fe-Ni-Si-C	$2.028 \times 10^7$	$2.907 \times 10^4$	90.822	0.00
300 M	$1.231 \times 10^7$	$3.767 \times 10^4$	141.66	0.00
Combined data	$3.390 \times 10^7$	$2.065 \times 10^4$	139.00	25.46

Table 2.2: The best fit values of the empirical constants of Rees and Bhadeshia model [1992].

Alloy	C	Si	Mn	Ni	Cr	P	S	N
A	0.27	1.98	2.18	0.02	1.90	0.015	0.012	0.0054
B	0.27	2.01	2.16	2.07	–	0.015	0.011	0.0049
C	0.46	2.10	2.15	0.02	–	0.014	0.013	0.0062
D	0.44	2.13	2.14	0.02	0.5	0.014	0.011	0.0079
E	0.10	1.77	2.12	2.00	0.02	0.013	0.012	0.0053
F	0.26	1.85	2.10	0.02	–	0.015	0.013	0.0086
G	0.26	1.93	2.04	0.02	1.02	0.015	0.010	0.0069
H	0.10	1.63	1.99	0.03	1.97	0.013	0.011	0.0080

Table 2.3: The composition (wt.%) of the alloys used for the study of bainite transformation kinetics by Chang [1995].

Chang [1995] has also studied the bainite transformation kinetics of a number of high silicon steels (Table 2.3). The data were analysed according to the theory presented above. The best fit values of the constants deduced by Chang [1995] are shown in Table 2.4.

Dataset	$B'_3/u, \text{ m}^{-1}\text{s}$	$B_4, \text{ J mol}^{-1}$	$\lambda_1$	$\lambda_2$
A	$2.473 \times 10^7$	$1.613 \times 10^4$	16.578	0.00
B	$2.720 \times 10^7$	$5.967 \times 10^3$	7.337	0.00
C	$3.079 \times 10^7$	$2.207 \times 10^{-2}$	4.657	0.00
D	$1.639 \times 10^8$	$1.030 \times 10^4$	71.067	0.00
E	$1.974 \times 10^6$	$2.729 \times 10^{-1}$	2.577	0.00
F	$3.953 \times 10^6$	$6.414 \times 10^2$	4.139	0.00
G	$1.576 \times 10^7$	$7.455 \times 10^3$	21.550	0.00
H	$5.908 \times 10^6$	$8.171 \times 10^3$	48.421	0.00
Combined data	$1.277 \times 10^8$	$1.582 \times 10^{-2}$	335.69	45.05

Table 2.4: The best fit values of the empirical constants when optimisation was done on Chang's alloys, A–H [Chang, 1995].

## 2.4 Summary

The theory of bainite transformation as proposed by Bhadeshia [1981] has been reviewed. A mathematical model to predict the bainite transformation kinetics based on this theory has been discussed. There are a number of difficulties with the theory which will be highlighted and discussed in context in chapter six.

## Chapter Three

# Stress and Strain Affected Transformations

### 3.1 Introduction

A number of industrial processes such as plate rolling, rod rolling and forging are used to fabricate steel beginning with an ingot, slab, billet or a blank. Though each process differs in technical detail, the underlying metallurgical principles are the same. Rolling deformation is probably the most commonly used and will be described here. The feed stock is heated in a furnace to a temperature which depends on the chemical composition but is usually in the range 1100–1250 °C. The microstructure then becomes fully austenitic. After removing the scales, the feed stock is subjected to deformation in the roll gap. The deformation is carried out in a number of steps, called passes, in a reversing or continuous mill with a predetermined amount of thickness reduction in each pass. Finally, after the required thickness has been achieved the product is allowed to cool freely in air or is subjected to accelerated cooling using air or water sprays.

For a given chemical composition, the final microstructure and hence the mechanical properties depend on the microstructure of austenite before it begins to transform, and on the rate of cooling. It is possible to control the time–temperature–deformation sequence (the ‘rolling schedule’) to leave the austenite in a state which will induce it to transform into the required microstructure upon cooling. Thermomechanical control processing (TMCP) is used widely in the steel industry for austenite “conditioning”. It consists of controlled rolling and accelerated cooling in a four stage process which is shown in Figure 3.1. Stage 1 rolling is carried out under conditions where the austenite can recrystallise readily. The coarse grains of austenite produced during the high temperature heat treatment are refined by repeated deformation and recrystallisation. There is a limit to the degree of austenite grain refinement that can be achieved in this way and an additional possibility is to leave the austenite in a cold–deformed state before cooling it to induce ferrite transformation. This is stage 2 of TMCP which leads to elongated austenite grains thus providing more nucleation sites for ferrite. Deformation bands and other such defects which act as ferrite nucleation sites are also introduced within the austenite grains. All of these factors enhance the ferrite nucleation rate and the final microstructure is greatly reduced in scale. Microalloying elements such as Nb, V, Ti *etc*, when present, play an important role. The solute atoms and the strain–induced precipitates of carbide and/or carbonitrides of these elements retard the recrystallisation of austenite and further augment the ferrite nucleation rate. The precipitates also provide additional strengthening.



Rolling is sometimes continued into the two phase  $\gamma + \alpha$  region which is stage 3 of TMCP. Besides a continuation of the processes in stage 2, the deformation in this stage introduces plastic strain in the ferrite. Subsequent recovery processes in the ferrite produce a sub-grain structure which is another source of strength in these steels. Stage 4 of TMCP consists of interrupted accelerated cooling in a suitable temperature range. This increases the supercooling at which transformation takes place and a highly refined microstructure can be obtained. In steels with adequate hardenability, bainite and martensite can be obtained during cooling. The relative quantity of the different phases depends on the steel composition, the rolling schedule and the cooling rate.

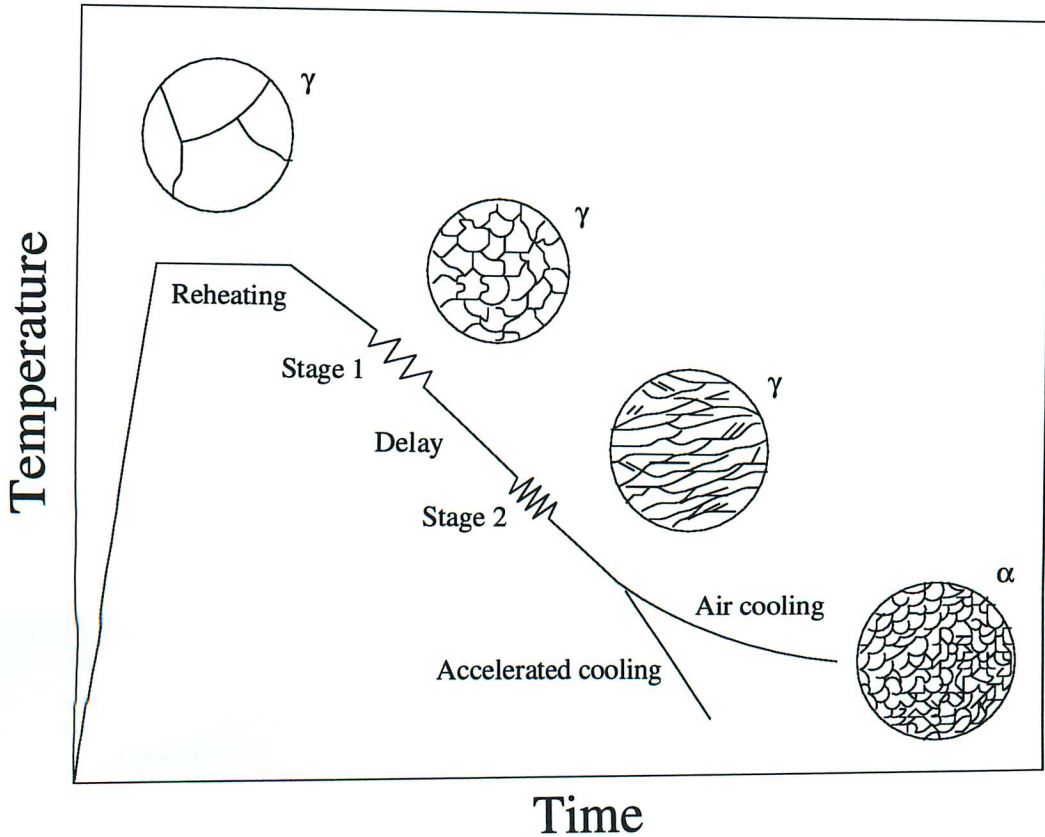


**Figure 3.1:** A schematic and simplistic time-temperature-deformation schedule for thermomechanical control processing (TMCP).

### 3.2 Effect of Austenite Deformation on its Transformation

Plastic deformation significantly alters the structural state of austenite. How this influences transformation behaviour depends on the mechanism of ferrite formation. Attention is focused here on allotriomorphic ferrite and bainite which are the key phases in structural steels, and conveniently, are good representatives of the reconstructive and displacive mechanisms of growth. The effect of plastic deformation on the transformation of austenite to other phases has been reported elsewhere: Umemoto *et al.* [1983] (pearlite); Shipway and Bhadeshia [1997] (Widmanstätten ferrite); Yang *et al.* [1995] (acicular ferrite); Raghavan [1992] (martensite).

### 3.2.1 Deformation in the Recrystallisation Region

The austenite is deformed at temperatures above which it can recrystallise during or after deformation. A smaller austenite grain size leads to a greater grain surface area per unit volume, and hence a larger number density of nucleation sites. This results in a higher austenite to ferrite transformation temperature during cooling ( $Ar_3$ ) and a smaller ferrite grain size. The growth of austenite grains after recrystallisation can be avoided by appropriate microalloying [Amin and Pickering, 1982a; Santella and DeArdo, 1982].

### 3.2.2 Deformation in the Non-Recrystallisation Region

The austenite is deformed below its recrystallisation temperature. There are many effects of this relatively low temperature deformation as discussed below.

#### 3.2.2.1 Change in the Grain Shape

Deformation below the recrystallisation temperature results in a flattening of the austenite grains, a phenomenon known as pancaking. The change from an equiaxed to a pancaked microstructure is accompanied by an increase in the grain boundary area per unit volume. Many attempts have been made to quantify the increase in the boundary area as a function of deformation strain. Some of these relationships are based purely on geometrical considerations whereas others are derived empirically.

Speich *et al.* [1984] took the grains to be cubic and calculated the grain boundary area per unit volume,  $S_V$ , which after plane-strain deformation is given by (Figure 3.2)

$$S_V = \frac{2}{\bar{L}} \left( 1 + c + \frac{1}{c} \right) \quad (3.1)$$

where  $c$  is the ratio of the final to the initial lengths of the sides of the cube and  $\bar{L}$  is the initial grain size expressed as the mean intercept length.

Umemoto *et al.* [1983] estimated the change in the austenite grain surface area per unit volume by representing the grains as spheres, each of unit radius. Plane-strain deformation changes a sphere into an ellipsoid (Figure 3.3) with axes 1,  $(1 - p)$  and  $1/(1 - p)$ , where  $p$  is the reduction given by  $p = 1 - c$ . The surface area per unit volume of the ellipsoidal grain was found to be

$$S_V = \int_{-1/(1-p)}^{1/(1-p)} \left[ \left\{ 4x \int_0^{\pi/2} \sqrt{1 - (2p - p^2) \sin^2 \theta} d\theta \right\} \times \sqrt{\frac{x^2(1-p)^6}{1 - x^2(1-p)^2} + 1} \right] dx \quad (3.2)$$

which can be compared against the initial surface area per unit volume ( $S_V^0$ ) of the spherical grains which is  $4\pi$ . The increase in  $S_V$  as calculated according to equation 3.2 is shown in Figure 3.4 [Umemoto *et al.*, 1983].

The other published relationships between  $S_V$  and deformation are empirical [*e.g.* Ouchi *et al.*, 1982]. It is possible to measure the grain boundary area metallographically. According to Underwood [1968],  $S_V$  is given by

$$S_V = 0.429(N_L)_{\parallel} + 2.571(N_L)_{\perp} - (N_L)_l \quad (3.3)$$

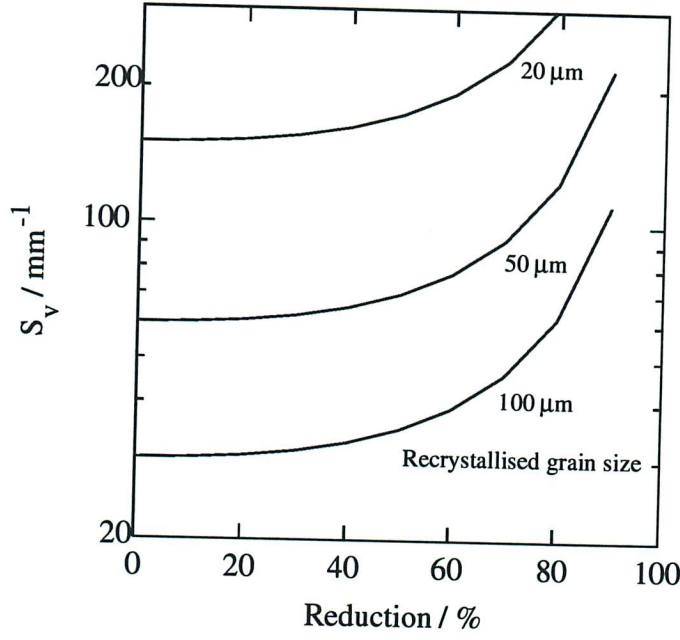


Figure 3.2: The increase in surface area per unit volume of a cube-shaped grain structure as a result of plane-strain deformation [Speich *et al.*, 1984].

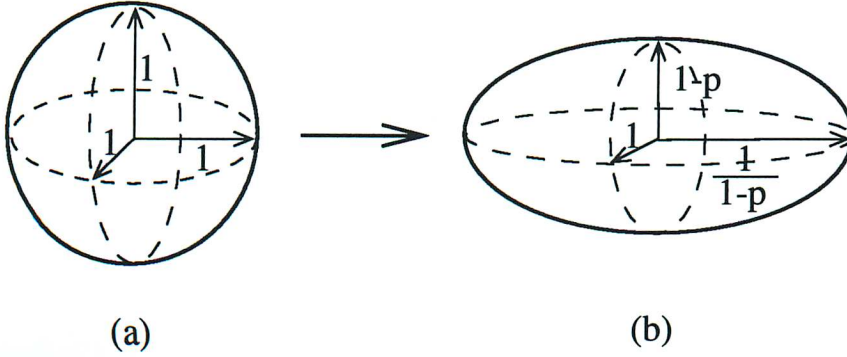


Figure 3.3: The change in shape from (a) sphere to (b) ellipsoid due to a plane-strain reduction of  $p$ . After Umemoto *et al.* [1983].

where  $(N_L)_\parallel$ ,  $(N_L)_\perp$  and  $(N_L)_\perp$  are the number of intercepts with grain boundaries of unit length of test lines along the longitudinal, transverse and through thickness directions respectively. The equation takes into account the anisotropy in the grain shape caused by deformation. Ouchi *et al.* [1982] found empirically that the measured  $S_V$  varied linearly with plane-strain reduction of more than 0.1 (Figure 3.5):

$$S_V = \frac{2}{L} [1.67(p - 0.1) + 1] \quad (3.4)$$

For  $p < 0.1$ , the increase in surface area is taken to be negligible so that  $S_V \simeq S_V^0$ , where  $S_V^0$  is the grain boundary surface area per unit volume before deformation.



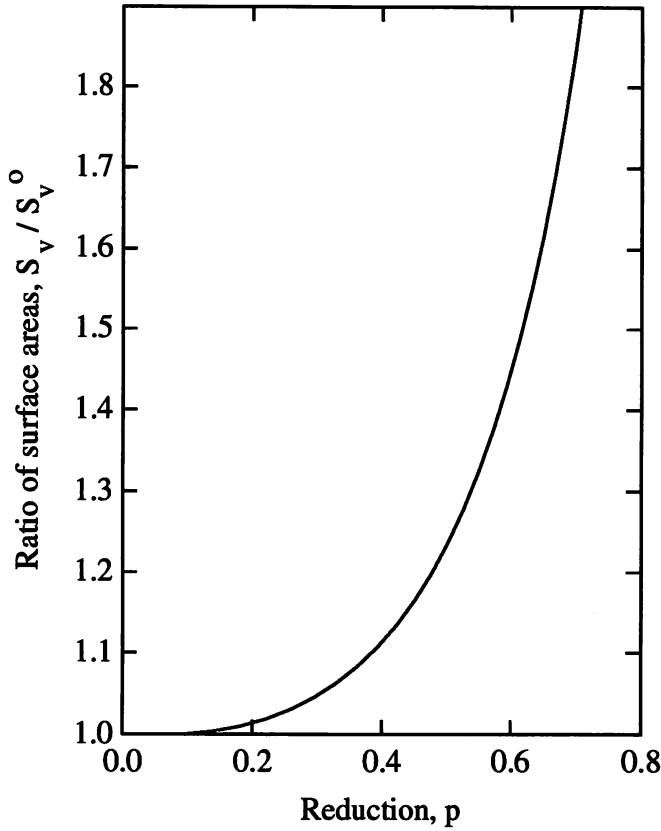


Figure 3.4: The ratio of surface area of a sphere before and after a rolling reduction  $p$  [Umemoto *et al.*, 1983].

### 3.2.2.2 Comparison with Measurements

Sandberg and Roberts [1982] have systematically studied the effect of deformation of austenite in the non-recrystallisation region on ferrite transformation for a number of microalloyed steels. They also used the Underwood's method (equation 3.3) to experimentally measure the austenite grain boundary area for a range of unconstrained deformation strains starting from two recrystallised austenite grain sizes of  $50\text{ }\mu\text{m}$  and  $75\text{ }\mu\text{m}$ . The calculated values of  $S_v$  according to the three equations discussed above are compared against the measured values in Figure 3.6. Ouchi's linear equation overestimates the increase in grain boundary area upon deformation whereas that of Speich *et al.* underestimates it. The equation based on the deformation of sphere proposed by Umemoto *et al.* gives reasonable agreement with the measurements. It should be noted that the experiments of Ouchi *et al.* were carried out under plane-strain conditions (rolling) whereas those of Sandberg and Roberts involved uniaxial compression; the calculations for  $S_v$  were all done assuming plane-strain deformation.

Though the three models for  $S_v$  give different values, it is obvious that the  $S_v$  does not rise enormously with levels of strains usually employed during commercial rolling or other deformation processes. For example, the sphere model of Umemoto *et al.* [1983] predicts that the boundary area increases by only 25% with a 50% reduction. The experimental measurements of Ouchi *et al.* [1982] and of Sandberg and Roberts [1982] also indicate that a 50% deformation

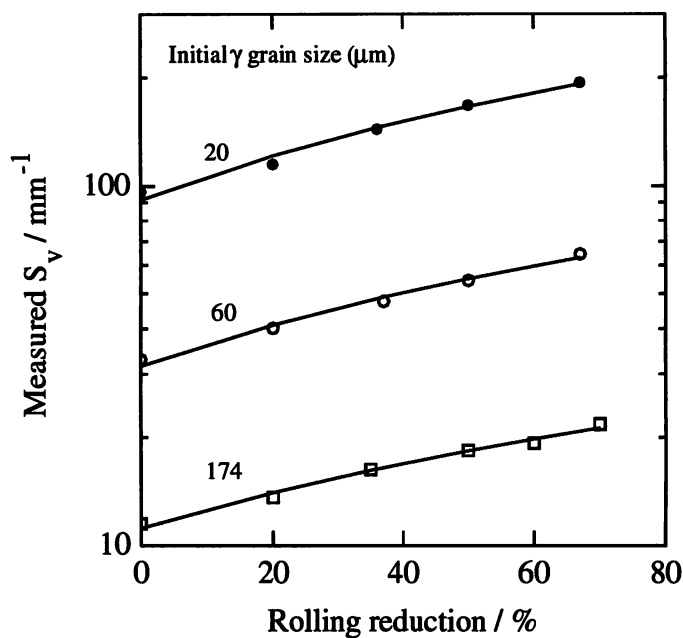


Figure 3.5: The increase in grain boundary surface area per unit volume as a function of rolling reduction below the recrystallisation temperature of austenite. The figure illustrates the linear relationship between  $S_v$  and  $p$  suggested by Ouchi *et al.* [1982].

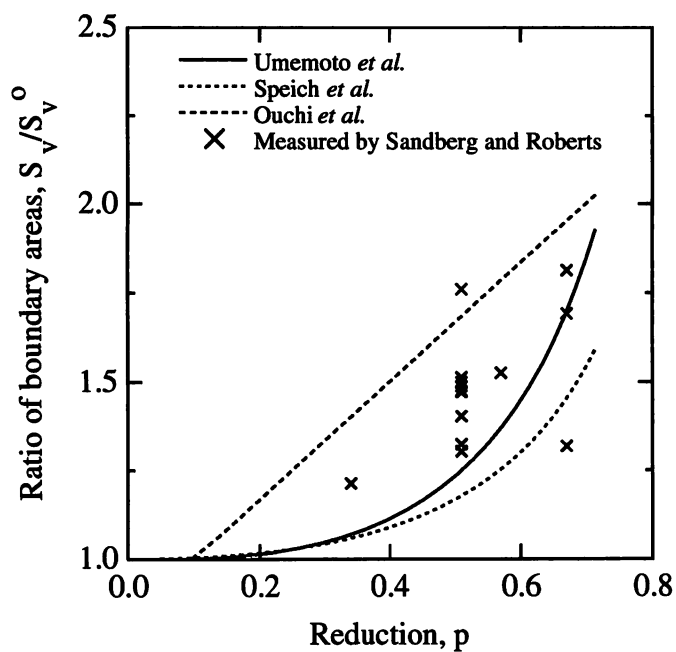


Figure 3.6: A comparison of measured and calculated increase in austenite grain boundary area as a result of deformation. The measurements were done by Sandberg and Roberts [1982].

raises the boundary area by only about 50%. This small increase in  $S_V$  alone cannot account for a very fine ferrite grain size which is obtained when the transformation occurs from deformed austenite [Roberts *et al.*, 1980; Sandberg and Roberts, 1982; Amin and Pickering, 1982b]. For the same value of  $S_V$ , the ferrite grain size formed from deformed and unrecrystallised austenite was found to be smaller than that from recrystallised austenite, Figure 3.7 [Kozasu *et al.*, 1976]. Clearly, the effect of deformation of austenite in the non-recrystallisation region is more than just an increase in the grain boundary area which greatly enhances the ferrite nucleation rate.

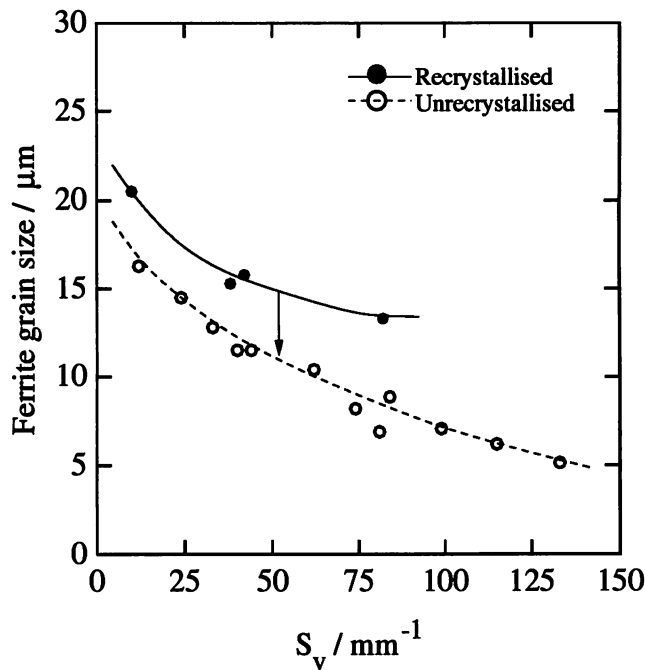


Figure 3.7: Relationship between the ferrite grain size and the austenite grain boundary area ( $S_V$ ) for recrystallised and unrecrystallised austenite grains. For the same  $S_V$ , a finer ferrite grain structure is obtained if the austenite is in an unrecrystallised state [Kozasu, 1976].

### 3.2.2.3 Enhanced Nucleation on Deformed Austenite Grain Boundaries

The deformation of austenite not only increases  $S_V$ , but has also been reported to increase the nucleation potency of the grain surface [Walker and Honeycombe, 1978; Roberts *et al.*, 1980; Amin and Pickering, 1982b; Sandberg and Roberts, 1982; Umemoto and Tamura, 1986]. This effect, however, does not occur at relatively small strains [Priestner, 1975]. Based on their experimental measurements, Umemoto and Tamura [1986] estimated that a rolling deformation of 30% and 50% increased the ferrite nucleation rate per unit area of grain surface by a factor of 740 and 4200 respectively. The reason for such a large increase in ferrite nucleation rate on austenite grain boundary is not very clear. It has been argued by Sandberg and Roberts [1982] that the austenite grain boundaries develop serrations and bulges as a result of strain-induced

boundary migration. Metallographic evidence for the presence of austenite grain boundary bulges has been provided by Roberts *et al.* [1980]. Invoking the hypothesis of Lee and Aaronson [1975], they suggested that bulges provide readily available sites for the nucleation of faceted ferrite grains which is possible only on a 'puckered' boundary [Lee and Aaronson, 1975]. The activation energy for the nucleation of faceted ferrite on bulges was estimated by Sandberg and Roberts [1982] to be much lower than that for the corresponding unfaceted ferrite. Besides, the density of such sites is also high as they are spread all over the deformed grain boundary [Sandberg and Roberts, 1982]. The combined effect of these two factors is to enhance the grain boundary nucleation rate. Similarly, Umemoto and Tamura [1986] have suggested that a large number of grain boundary ledges are formed as a result of deformation. The activation energy for nucleation is smaller on these ledges, augmenting the grain boundary nucleation rate.

Amin and Pickering [1982b] have discounted the above theory of nucleation on grain boundary bulges. They did not observe bulging in many cases and yet the ferrite nucleation rate in the vicinity of the deformed austenite grain boundary was found to be higher [also see discussion to Roberts *et al.*, 1980]. Instead, they proposed that the deformed austenite grains exhibit higher lattice mismatch because of greater lattice distortion and a higher dislocation density near the deformed grain boundaries.

An increase in the grain boundary nucleation rate has also been observed in microalloyed steels [Amin and Pickering, 1982b] or in steels containing other carbide forming elements such as Cr and Mo [Walker and Honeycombe, 1978]. In such cases, as will be discussed later, strain induced precipitates play an important part.

### 3.2.2.4 Intragranular Nucleation Sites

Apart from enhancing the ferrite nucleation rate on the austenite grain boundaries, deformation also induces certain nucleation sites within the austenite grains. These sites can be deformation bands, incoherent annealing twins, sub-grain boundary and second phase particles.

Deformation bands are regions of intense localised shear. These deformation bands can act as ferrite nucleation sites inside the austenite grains because of the higher energy (higher dislocation density) associated with them [Walker and Honeycombe, 1978; Umemoto and Tamura, 1986; Inagaki, 1986; Feng *et al.*, 1990]. The distribution of deformation bands amongst the grains tends to be rather irregular. It depends on the grain size and the amount of deformation. While the bands are rarely observed for a low amount of deformation ( $\leq 30\%$ ), the band distribution becomes more uniform with large deformations ( $\geq 50\%$ ) [Tanaka *et al.*, 1982]. Ouchi *et al.* [1982] have suggested that the density of deformation bands,  $S_V^{db}$ , in unrecrystallised austenite is linearly dependent on the amount of reduction above 30%:

$$S_V^{db} = 63(p - 0.3) \quad \text{mm}^{-1} \quad (3.5)$$

Umemoto and Tamura [1986] assumed a slightly different parabolic relationship between the deformation band density and the true plastic strain ( $\epsilon$ )

$$S_V^{db} = 30 \epsilon^2 \quad \text{mm}^{-1} \quad (3.6)$$

where  $\varepsilon = -\ln(1 - p)$ .

The deformation band density calculated according to these two equations is compared with that measured by Sandberg and Roberts [1982] in Figure 3.8. For normal rolling reductions both the equations give similar results, though the parabolic relationship of Umemoto and Tamura [1986] gives marginally better fit. At higher reductions, the equation proposed by Ouchi *et al.* [1982] gives a reasonable density whereas the parabolic relationship gives an unrealistic value.

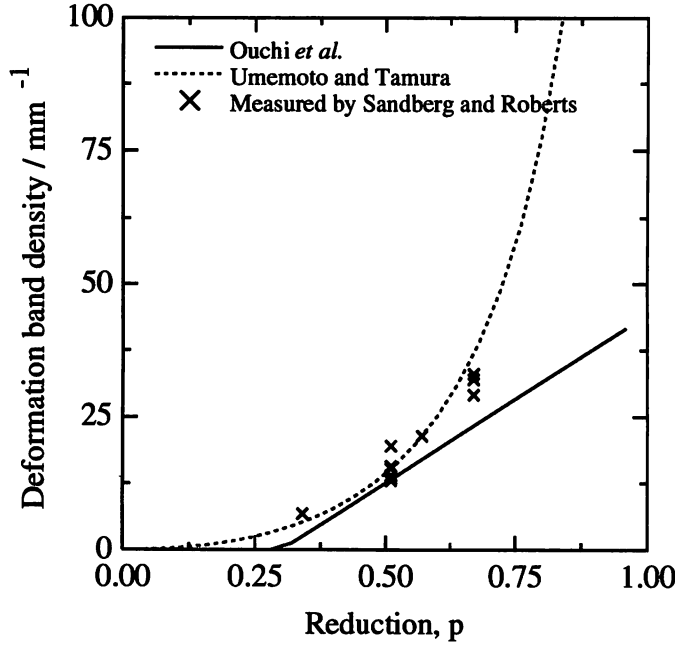


Figure 3.8: The variation of deformation band density with reduction  $p$ . The values calculated according to equations proposed by Ouchi *et al.* [1982] and by Umemoto and Tamura [1986] are compared against the measured values reported by Sandberg and Roberts [1982].

The deformation bands increase the total surface area effectively available for the heterogeneous nucleation of ferrite. It is generally assumed that the nucleation potency of the deformation bands is the same as austenite grain boundaries [Ouchi *et al.*, 1982; Speich *et al.*, 1984; Umemoto and Tamura, 1986]. The total interfacial area per unit volume ( $S_V^T$ ) available for ferrite nucleation is therefore given by summing the areas of deformed grain boundaries and deformation bands

$$S_V^T = S_V + S_V^{db} \quad (3.7)$$

However, all the deformation bands are not equally potent because of variable energies associated with them [Amin and Pickering, 1982b]. They found that higher energy bands which nucleated ferrite were usually associated with larger rolling reductions. Moreover, the recovery of dislocation structure within the deformation bands may decrease its potential for ferrite nucleation [Amin and Pickering, 1982b]. Thus, a slow cooling which provides time for



the recovery of dislocation structure within the deformation band reduces its potency for ferrite nucleation.

Inagaki [1986] has measured the ferrite nucleation rate on different sites at two isothermal transformation temperatures and with two starting austenite grain sizes. For the smaller austenite grain size, ferrite nucleated predominantly on the austenite grain boundary even after deformation; nucleation on deformation bands was not observed. However, with a coarse austenite grain size, deformation did induce ferrite nucleation on the deformation bands and at a lower isothermal transformation temperature, the nucleation rate on deformation bands was found to be much higher than on the grain boundaries (Figure 3.9). It has been suggested that at lower transformation temperatures the activation energy for nucleation is smaller and hence the probability of nucleation on intragranular sites such as deformation bands is much higher [Tanaka, 1995; Inagaki, 1986]. It is also possible that at lower temperatures the recovery of the dislocation structure is slower and consequently sufficient driving force is available for nucleation.

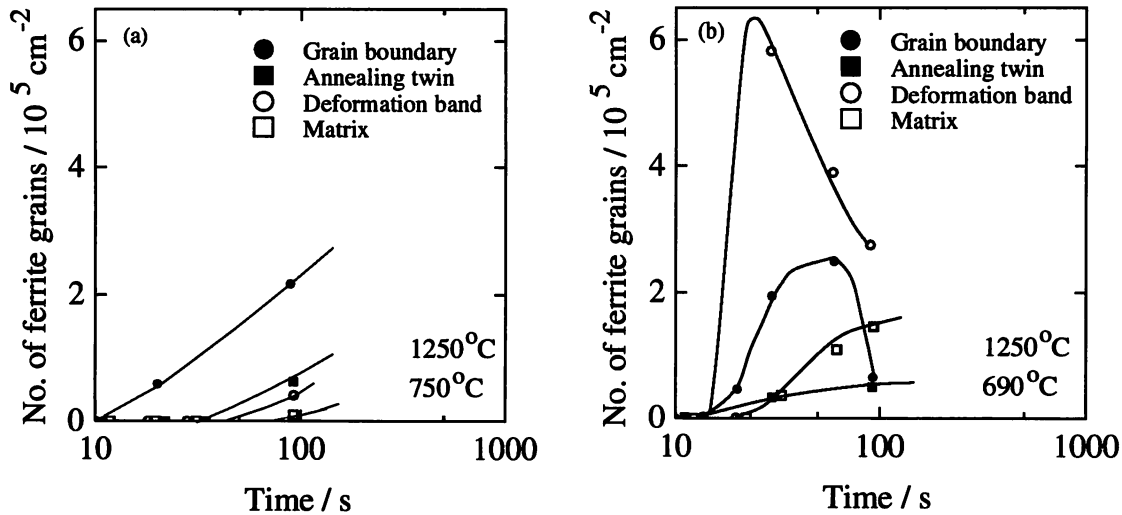


Figure 3.9: Effect of deformation and isothermal transformation temperature on ferrite nucleation at different sites. The samples were austenitised at  $1250^\circ\text{C}$  and rolled to 56% reduction at  $830^\circ\text{C}$  before isothermal transformation at (a)  $750^\circ\text{C}$  and (b)  $690^\circ\text{C}$  [Inagaki, 1986].

Inagaki's observations that ferrite nucleation on deformation bands is dependent on the initial austenite grain size and the transformation temperature invalidates the assumption underlying equation 3.7 that the nucleation potencies of deformation bands and austenite grain boundaries are the same under all conditions. Nevertheless, it is a simple and useful approximation in many cases and is used widely for modelling the ferrite transformation [Ouchi *et al.*, 1982; Speich *et al.*, 1984; Umemoto and Tamura, 1986; Tanaka, 1995; Parker, 1997].

Annealing twins are substantially coherent and therefore not effective as nucleation sites. They can lose their coherency due to deformation in which case ferrite nucleation becomes

possible on the resultant high-energy incoherent interfaces [Tanaka, 1995]. Ferrite nucleation on annealing twin has been observed by Inagaki (Figure 3.9) [1986] and by Speich *et al.* [1984].

Direct microstructural evidence for ferrite nucleation on sub-grain boundaries has been presented by Walker and Honeycombe [1978]. Amin and Pickering [1982b] have also presented indirect proof of nucleation <sup>on</sup> sub-grain boundaries. They observed extensive intragranular ferrite nucleation even in the absence of deformation bands and second phase particles and concluded that the nucleation must have taken place on sub-grain boundaries. The occurrence of a mixed ferrite grain structure has also been interpreted in terms of this effect. Recovery of the deformation structure produces a network of sub-grain boundaries. It has been postulated that strain is not uniformly distributed within the grain and that it is localised in the neighbourhood of the grain boundaries [Amin and Pickering, 1982b]. This gives rise to a higher density of sub-boundaries in the vicinity of the grain boundary than away from it. Ferrite nucleation takes place on the original and sub-grain boundaries. If microalloying or other precipitate forming elements are present, precipitates may form on this network [Walker and Honeycombe, 1978; Amin and Pickering, 1982b]. The precipitates inhibit ferrite growth allowing for fresh nucleation and may themselves act as nucleation sites. It is pertinent to note here that in some cases, cold working of iron is also reported to produce a banded region along the grain boundary where the density of sub-grains is higher [Hutchinson, 1974; Bay and Hansen, 1980].

Roberts *et al.* [1980] point out that the interfacial energy of sub-grain boundaries is too small for them to be able to act as ferrite nucleation sites. However, at large supercoolings, the activation energy required for nucleation is relatively small and ferrite nucleation on sub-grain boundaries may be possible.

All the factors listed above are expected to substantially promote intragranular nucleation. This has been observed in many cases particularly at lower transformation temperatures or under accelerated cooling conditions when recovery is minimised [Morrison and Chapman, 1976; Amano *et al.*, 1986; Abe *et al.*, 1988].

#### 3.2.2.5 Stored Energy of Deformed Austenite

A certain fraction of the energy spent for deformation is stored in austenite in the form of an increased density of dislocations and other defects. In the absence of recovery and recrystallisation, the austenite remains in a state of higher energy. The free energy change associated with the deformed-austenite to ferrite transformation is thus larger than that during a corresponding transformation from recrystallised austenite. This should, in principle, raise the  $A_{e3}$  temperature and increase the equilibrium carbon concentration of austenite at a given temperature. Consequently, the amount of ferrite in equilibrium with austenite at any temperature must also increase. Some experimental results reported by Yada *et al.* [1986] and by Matsumara and Yada [1987] indicate strain-induced austenite to ferrite transformation above the equilibrium  $A_{e3}$  temperature. It was inferred by Yada *et al.* [1986] that 1 to 11% of the deformation energy is utilised for transformation, the rest presumably being dissipated as heat.

The activation energy for nucleation is inversely proportional to the square of driving force

available for transformation [Christian, 1975]. The stored energy of deformation increases the driving force and thereby reduces the activation energy for nucleation. This results in an increase in the nucleation rate and the  $Ar_3$  temperature. The stored energy of deformation should also cause an increase in the growth rate of ferrite [Umemoto and Tamura, 1986; Parker, 1997].

### 3.2.2.6 Effect of Microalloying Elements

In plain C–Mn–Si steels, deformation causes only a marginal increase of 35–40 °C in the transformation temperature [Ouchi *et al.*, 1982]. A much higher increase has been reported by Ouchi *et al.* [1982] and by Collins *et al.* [1988] for Nb containing steels even at a slow cooling rate. However, other workers have reported a smaller increase for such steels under similar cooling conditions [Abe *et al.*, 1986; Liu *et al.*, 1995; Yamamoto *et al.*, 1995; Khlestov *et al.*, 1996]. In Nb containing steels, such a sharp rise in the  $Ar_3$  temperature has been attributed to the formation of strain induced Nb(CN) precipitates [Ouchi *et al.*, 1982]. Nb in solution in austenite lowers its transformation temperature [Morrison, 1963; Abe *et al.*, 1986; Huang *et al.*, 1993]. Thomas and Michal [1982] have suggested that in low Nb alloys, Nb remains in solution during cooling and segregates to the austenite boundaries lowering the grain boundary energy. The activation energy required for ferrite nucleation is therefore increased. Thus, even though Nb does not appreciably alter the chemical free energy change associated with ferrite formation, it lowers the ferrite nucleation rate [Ouchi *et al.*, 1982]. A similar argument holds for other elements such as Mo and V [Essadiqi and Jonas, 1989]. Essadiqi and Jonas [1989] measured the ferrite nucleation rate as a function of temperature and found that at the same undercooling the nucleation rate in plain carbon steel was higher than in steels alloyed with only Mo or with Mo, Nb and V. When austenite is deformed, strain induced precipitates of carbides and/or nitrides (*e.g.*, Nb(CN)) are formed on or around austenite grain boundaries depleting the grain boundary of dissolved solute atoms [Morrison and Chapman, 1976; Amin and Pickering, 1982b]. The nucleation rate on the grain boundary then increases sharply because the solute atoms are no longer available for segregation. Precipitates themselves may act as potent nucleation sites accelerating the transformation, probably further aided by a carbon depleted region around the precipitates [Thomas and Michal, 1982; Jung *et al.*, 1995]. The net result is a dramatic rise in the  $Ar_3$  temperature.

Even in undeformed austenite, precipitation of Nb(CN) is known to accelerate the ferrite formation [Thomas and Michal, 1982; Jung *et al.*, 1995].

A further effect of the presence of microalloying elements is retardation of the recovery processes by strain induced precipitates; the defects are retained in austenite and they accelerate transformation as described above [Feng *et al.*, 1990].

Thus in microalloyed steels, it appears that the extent of rise in transformation temperature depends on carbide precipitation which in turn depends on alloy chemistry and the deformation schedule. If extensive precipitation precedes transformation then a sharp rise in the transformation temperature is observed.

### 3.3 Effect of Plastic Strain on the Bainite Transformation

We have seen that the deformation of austenite accelerates ferrite transformation which forms by a reconstructive mechanism. Bainite and martensite on the other hand form by a displacive mechanism of transformation which involves a coordinated movement of atoms during the glide of glissile interfaces. Such movements cannot be sustained against strong obstacles such as grain boundaries. Thus, martensite or bainite cannot cross grain boundaries. Defects such as dislocations also hinder the progress of any glissile interface in much the same way that ordinary slip is made more difficult by the presence of dislocation forests.

It follows that displacive transformations can be suppressed by prestraining the parent phase which has the effect of enhancing the matrix defect density. This effect is known as mechanical stabilisation and is well established for martensitic transformation [Raghavan, 1992]. Prior deformation of metastable austenite at temperatures sufficiently above  $M_s$  lowers the transformation temperature and the amount of martensite formed at any subsequent temperature is reduced [Christian, 1975; Raghavan, 1992]. The detailed effect of plastic strain on displacive transformation is more complex than the simple stabilisation described above. Although the crystallographic discontinuities in the austenite, caused by strain, clearly interfere with the progress of plates of transformation product, the same discontinuities can provide heterogeneous nucleation sites [Fiedler *et al.*, 1955]. There is therefore an enhancement of nucleation on defects but at the same time a hindrance to growth.

The literature available on the mechanical stabilisation of austenite against bainitic transformation indicates results similar to that for martensite though there are some apparent inconsistencies. Interference with other reactions such as the formation of allotriomorphic ferrite prior to bainite transformation or precipitation of carbides during transformation make the interpretation of results difficult. Difficulties may also arise if the transformation is allowed to proceed under stress. The effect of stress on displacive transformation will be considered separately.

Vlad [1986] has reported that during continuous cooling of a low-alloy steel, the austenite to bainite transformation was retarded when the austenite was deformed prior to transformation. This could be the mechanical stabilisation effect, but at least a part of the retardation can be explained by an accelerated decomposition of deformed austenite to allotriomorphic ferrite. The carbon enrichment of residual austenite stabilises it against bainite transformation. Hot rolling experiments carried out by Davenport [1977] on alloys with a hardenability high enough to avoid the formation of allotriomorphic ferrite provide more appropriate evidence of mechanical stabilisation. The austenite deformed to a larger extent transformed to bainite at a lower temperature during continuous cooling. Similar results were obtained by Zhang and Boyd [1996] on a 0.11C–1.6Mn–0.09 Nb–0.01Ti–0.003B steel at a cooling rate of  $10^\circ\text{C s}^{-1}$  which was fast enough to avoid the formation of allotriomorphic ferrite even from the deformed austenite. A decrease in the bainite transformation temperature during continuous cooling is however not always observed. Smith and Siebert [1971] found an increase of as much as  $100^\circ\text{C}$  in the bainite-start temperature of low-carbon Mo–B steels when austenite was

deformed before transformation. The bainite-start curves tended to become flat with austenite deformation. They also observed a deformation-induced increase in the martensite-start temperature of 30 to 50 °C. The investigators, in this case, do not rule out the possibility of strain-induced precipitation of carbides of molybdenum at the deformation temperature. The precipitation obviously affects subsequent reactions. A closer examination of the CCT curves presented by Smith and Siebert [1971] reveal that prior deformation does lower the bainite transformation temperature in some cases. In some other cases in the same study, a low amount of deformation accelerated the bainite transformation while a large deformation retarded it.

A rise in the bainite transformation temperature during continuous cooling caused by austenite deformation has also been reported by other investigators [Huang *et al.*, 1993; Yamamoto *et al.*, 1995]. Yamamoto *et al.* [1995] have shown that for the same austenite grain boundary area per unit volume, the bainite transformation temperature was higher when the transformation was preceded by austenite deformation. It was suggested that the increase is caused by the stored energy of deformation. This explanation does not appear reasonable given that bainite forms by a displacive mechanism. If a defect cannot hinder or halt the progress of glissile interface it gets incorporated into the product phase. Thus the defect density is the same in the matrix and the product phase and no additional benefit accrues to the phase transformation in terms of energy because of deformation. In ausformed bainite the dislocation density has been found to be much higher than in the conventional bainite [Edwards and Kenon, 1978; Irani, 1967]. This is quite unlike reconstructive ferrite transformation or recrystallisation where long-range diffusion sweeps away the deformed regions and the product is strain free.

Direct evidence for mechanical stabilisation comes from isothermal transformation to bainite. Freiwillig *et al.* [1976] reported that when austenite is deformed prior to transformation, the initial rate of bainite formation increased though the total amount of bainite that formed at any temperature decreased; the incubation period before the start of transformation was found to be significantly lower. Even when the deformation was applied during isothermal transformation, the reaction rate was found to increase with a concomitant reduction in the volume fraction of bainite. A decrease in the incubation period as a result of austenite deformation was also observed by Edwards and Kennon [1974]. In their study the effect of deformation was more pronounced on upper bainite; the effect on lower bainite was rather modest. Similar results were obtained by Tsuzaki *et al.* [1989]. They found that ausforming accelerated the lower bainite reaction only marginally whereas the upper bainite reaction was greatly accelerated. They also showed that stabilisation was apparent only at the lower transformation temperature. The amount of upper bainite at high temperature was unaffected by ausforming. The probable reason for this behaviour is that the isothermal transformation to upper bainite was carried out at the temperature of deformation itself. The strain rate of deformation was a mere  $0.1 \text{ s}^{-1}$ . It is possible that the transformation was affected by the applied stress also. This has to be viewed in the light of the experiments of Bhattacharya and Kehl [1955]. They showed that the rate of bainite reaction increased when transformation took place under the

influence of stress; the acceleration was more pronounced when the applied stress exceeded the yield stress of the steel. They further showed that removal of stress after some transformation has taken place does not decrease the reaction rate. This suggests that the effect of stress is to stimulate nucleation rather than growth. As will be considered in the next section, stress may also increase the volume fraction of bainite at any temperature. In short, the results of Tsuzaki *et al.* on upper bainite could be because of the concurrent effect of stress on transformation; the reaction might have started during deformation itself.

Other results available in literature, with a few exceptions, are in agreement with the general trend outlined above [Umemoto *et al.*, 1986; Fujiwara *et al.*, 1995; Kasper *et al.*, 1994, Shipway and Bhadeshia, 1995a]. Umemoto *et al.* [1986] found that deformation above 500 °C had little effect on bainite transformation in medium-carbon Ni/Ni-Cr, Si-free steels. Deformation below 500 °C substantially accelerated the transformation. Stabilisation was observed in some cases. Based on microstructural observations and microhardness measurements across non-uniformly deformed samples Shipway and Bhadeshia [1995a] also concluded that deformation of austenite stabilises it against bainite transformation. Results reported by Konopleva and McQueen [1996] on medium-carbon, Cr-Ni-Mo steels are rather complicated. They indicate that for a given deformation temperature, the rate of reaction and the amount of bainite depend on the transformation temperature. At transformation temperatures above 400 °C, deformation accelerates the reaction and is accompanied by an increase in the bainite volume fraction. Below this temperature, the reaction is decelerated and the amount of bainite is lowered. At 400 °C however, initial acceleration is followed by a reduction in the eventual amount of bainite. The interpretation of results in this case is made difficult by the presence of carbide forming Cr in substantial quantity. The kinetics of bainite transformation has to be considered in conjunction with the carbide precipitation kinetics which too is affected by deformation. Precipitation of carbides alters the matrix composition which in turn influences the bainite transformation kinetics. A deceleration in the initial rate of reaction was also reported by Yang and coworkers [1996] for a medium-carbon, Mn-Si steel. The chemical compositions of the bainitic steels studied in literature are given in Table 3.1.

An acceleration of the bainite reaction is also observed when austenite undergoes plastic deformation because of transformation stresses. Bainite transformation is therefore also observed at temperatures below  $M_s$  in some steels [Howard and Cohen, 1948; Ericsson *et al.*, 1976]. Martensite is the first phase to form at these temperatures. The austenite is deformed because of the martensite transformation. The transformation strain then induces bainite transformation at an accelerated rate. Similarly, partial transformation to lower bainite enhances the rate of upper bainite reaction [Hehemann, 1970]. Elimination of transformation strains by an annealing treatment in the bay region removes the acceleration, Figure 3.10. It is, however, not clear why the annealing treatment leads to reduction in the bainite volume fraction.

Reference	C	Si	Mn	Ni	Cr	Mo	Nb	B	Other
Hehemann, 1970	0.31	0.30	0.76	3.07	1.22	0.49	–	–	–
Smith and Siebert, 1971	0.10	0.33	0.87	–	–	0.24	–	0.0021	–
Smith and Siebert, 1971	0.10	0.34	0.88	–	–	0.39	–	0.0027	–
Smith and Siebert, 1971	0.10	0.35	0.88	–	–	0.66	–	0.0031	–
Smith and Siebert, 1971	0.20	0.30	0.87	–	–	0.38	–	0.0025	–
Edwards and Kennon, 1974	0.85	–	1.39	–	0.59	–	–	–	0.53W
Freiwillig <i>et al.</i> , 1976	0.43	0.18	0.38	0.12	3.51	–	–	–	0.15Cu
Freiwillig <i>et al.</i> , 1976	0.86	0.20	0.39	0.05	3.74	–	–	–	0.05Cu
Freiwillig <i>et al.</i> , 1976	1.02	0.19	0.40	0.15	3.56	–	–	–	0.15Cu
Davenport, 1977	0.13	0.30	1.45	1.38	1.48	0.40	0.10	–	0.7Cu
Umemoto <i>et al.</i> , 1986	0.50	–	–	3.60	1.45	–	–	–	–
Vlad, 1986	0.04	1.34	1.07	0.03	0.02	$\leq 0.01$	–	–	–
Vlad, 1986	0.09	1.33	1.20	0.02	0.59	0.40	–	–	–
Vlad, 1986	0.51	1.68	0.78	0.05	0.04	–	–	–	–
Vlad, 1986	0.69	0.26	0.86	0.06	0.19	–	–	–	–
Tsuzaki <i>et al.</i> , 1989	0.59	2.01	1.02	–	–	–	–	–	–
Huang <i>et al.</i> , 1993	0.03	0.16	1.39	–	–	–	0.045	0.0020	0.022Ti
Fujiwara <i>et al.</i> , 1995	0.18	0.20	1.37	0.62	–	–	0.014	0.0008	0.012Ti
Fujiwara <i>et al.</i> , 1995	0.10	0.20	1.34	0.62	–	–	0.015	0.0013	0.012Ti
Fujiwara <i>et al.</i> , 1995	0.08	0.20	1.38	0.60	–	–	0.016	0.0009	0.011Ti
Shipway and Bhadeshia, 1995	0.45	2.08	2.69	–	–	–	–	–	–
Yamamoto <i>et al.</i> , 1995	0.04	0.20	2.94	–	–	–	0.028	0.0002	0.023Ti
Yamamoto <i>et al.</i> , 1995	0.04	0.20	2.95	–	–	–	–	0.0003	0.002Ti
Yamamoto <i>et al.</i> , 1995	0.18	0.21	1.72	–	–	0.25	0.039	0.0003	0.011Ti
Konopleva and McQueen, 1996	0.55	0.24	0.54	1.45	0.70	–	–	–	–
Konopleva and McQueen, 1996	0.35	1.04	0.03	5.10	1.13	0.17	–	–	–
Konopleva and McQueen, 1996	0.43	0.33	0.78	1.50	0.87	–	–	–	–
Yang <i>et al.</i> , 1996	0.43	2.02	3.00	–	–	–	–	–	–
Zhang and Boyd, 1996	0.10	–	1.60	–	–	–	0.09	0.0030	0.01

Table 3.1: The compositions (wt.%) of the bainitic steels studied in the reported literature for mechanical stabilisation effects.

### 3.4 Effect of Stress on the Bainite Transformation

The total shape change accompanying transformation can have two components, dilatational and shear. The displacive mechanism of phase transformation is quite similar to plastic deformation. The basic difference being that during a phase transformation, a shape change is accompanied also by a change in the crystal structure. It follows from here that any applied stress will interact with the progress of transformation. When transformation proceeds under stress, the total driving force can be partitioned into a ‘mechanical driving force’ and the

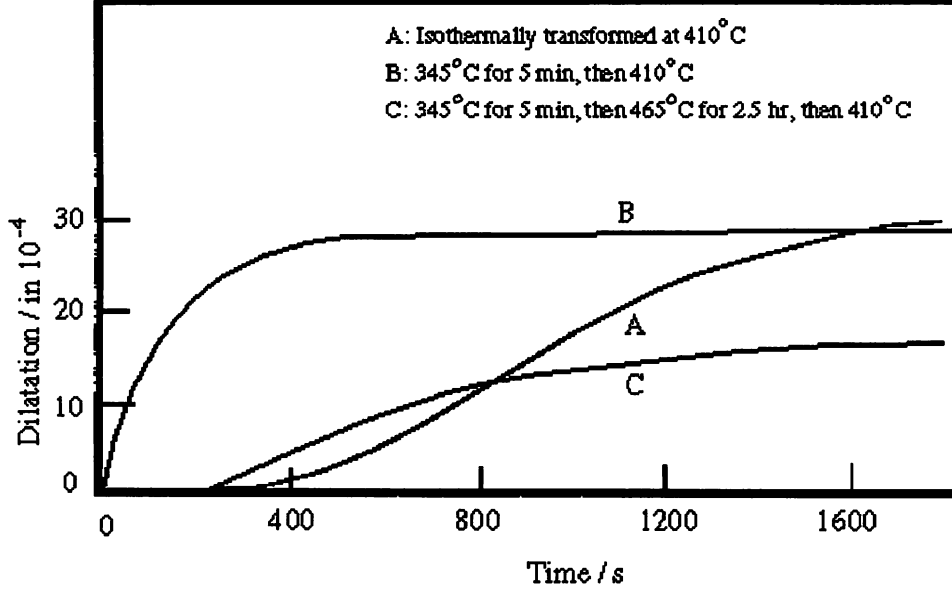


Figure 3.10: The influence of internally generated transformation strains on the rate of bainite transformation at 410 °C in a Fe-0.31C-0.3 Si-0.76Mn-3.07Ni-1.2Cr-0.49Mo wt.% alloy. Curve A corresponds to isothermal transformation to upper bainite; for curve B the sample was first partially transformed to lower bainite which resulted in an acceleration of upper bainite reaction at 410 °C; curve C highlights how annealing out the transformation strains by a treatment in the bay region removes the acceleration [Hehemann, 1970].

chemical driving force [Patel and Cohen, 1953]. The movement of <sup>a</sup>glissile interface is effectively a combined deformation and transformation process. The mechanical driving force may then be added to the chemical free energy change to obtain the total driving force available for transformation. The mechanical driving force ( $\Delta G_{MECH}$ ) is taken to be equivalent to the work done by the externally applied stress in achieving the required shape deformation and is given by

$$\Delta G_{MECH} = \sigma_N \epsilon + \tau s \quad (3.8)$$

where  $\sigma_N$  is the normal stress on the habit plane,  $\tau$  is the shear stress component on the habit plane, parallel to the direction of shear displacement, Figure 3.11.  $\epsilon$  and  $s$  are the dilatational and the shear components of the shape deformation respectively.

The shear component of shape strain is zero for reconstructive transformation. Only the hydrostatic component of the applied stress interacts with the comparatively small dilatational component. Consequently, the effect of applied stress is not very large and the change in transformation temperature depends on whether the stress is tensile or compressive. The shear component is large for displacive transformations in steels [Bhadeshia, 1995] and so the mechanical driving force component is significant. Moreover, the system has a freedom to choose from a menu of 24 available crystallographic variants of the transformation products so that the work done by the shear stress is always expected to be positive whereas that due



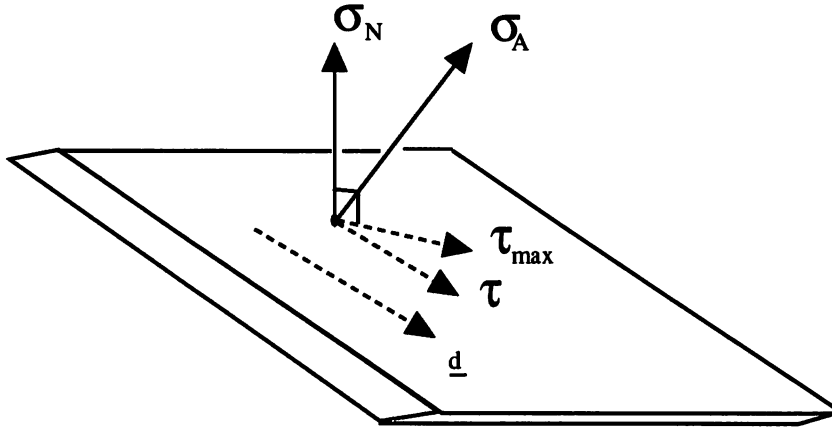


Figure 3.11: Resolution of an applied tensile stress,  $\sigma_A$ , into its normal and shear components which act on the habit plane. The vector  $\underline{d}$  indicates the direction of the shear displacement of the shape deformation.  $\tau_{max}$  is the maximum shear stress on the habit plane;  $\tau$  is the resolved component of  $\tau_{max}$  along  $\underline{d}$ . The net displacement vector of the invariant-plane strain shape deformation includes a dilatational component also and hence is slightly different from  $\underline{d}$  [Bhadeshia, 1995].

to normal component depends on the sign of  $\sigma_N$ . Since the dilatational component is much smaller than the shear component, the overall effect of the applied stress is dominated by its shear component [Patel and Cohen, 1953].

The driving force for a displacive transformation occurring under the influence of a uniaxial stress is higher than when the transformation occurs in the absence of any superimposed stress. The transformation can then take place at temperatures where it does not occur spontaneously. This is irrespective of whether the applied stress is compressive or tensile since the shear component always remains favourable; the contribution of the normal component, even if negative, being negligibly small due to a small dilatational component. However, a hydrostatic stress has no shear component and as such it interacts with only the dilatational component of the shape change. A hydrostatic compressive stress, as a result, would cause a decrease in the transformation temperature [Patel and Cohen, 1953].

Stress can induce martensitic transformation at temperatures above  $M_S$ . The highest temperature at which stress can induce martensitic transformation is termed <sup>the</sup>  $M_d$  temperature [Wayman and Bhadeshia, 1996]. At temperatures higher than  $M_d$ , the applied stress, limited as they are by the yield stress of the parent phase, can not provide enough driving force to aid the chemical driving force.

The applied stress can also favour the formation of those variants which best comply with the stress and thus change the appearance of the microstructure.

Similar experiments have not been carried out for bainite, though Bhadeshia [1992] has presented 'circumstantial evidence' and a theoretical model to show that under stress, similar

to martensite, bainite transformation can also be induced at temperatures above  $B_S$  (the bainite-start temperature). It has been shown that at temperatures sufficiently above  $B_S$ , no amount of deformation causes the austenite to transform to bainite [Drozdo *et al.*, 1962]. This temperature has been interpreted [Bhadeshia, 1992] to be above  $B_d$ . The difficulty in experimental observation of a  $B_d$  temperature stems from the fact that the austenite is weaker at the relatively high temperatures at which bainite forms. The amount of stress required to induce bainite transformation at such high temperatures may not be sustained by the austenite, resulting in extensive plastic deformation. This can also accelerate the reconstructive transformations which is otherwise sluggish at these temperatures.

Acceleration of bainitic transformation under stress has, however, been observed in a number of cases [Drozdo *et al.*, 1962; Bhattacharya and Kehl, 1955; Shipway and Bhadeshia, 1995b; Mutiu *et al.*, 1977] and the volume fraction of bainite formed at a particular temperature has been found to increase with stress [Shipway and Bhadeshia, 1995b; Cottrell, 1945]. Cottrell [1945] further showed that the effect of stress diminished as the bainite-start temperature was approached. This can be attributed to the contribution of the mechanical driving force to the total driving force. The acceleration is more rapid at stresses in excess of the yield strength [Bhattacharya and Kehl, 1955; Mutiu *et al.*, 1977] and may be due to strain induced nucleation as in the case of martensite [Wayman and Bhadeshia, 1996].

### 3.5 Summary

The effect of stress and strain on austenite transformation has been reviewed with particular emphasis on allotriomorphic ferrite and bainite.

The deformation of austenite accelerates the ferrite transformation. During continuous cooling, the transformation temperature may increase by about 35–40 °C when the austenite is deformed. The acceleration of transformation is due to pancaking of the austenite grains and also due to the introduction of other defects such as deformation bands, incoherent annealing twins and sub-grain boundaries which act as ferrite nucleation sites. The defects introduced as a result of deformation effectively raise the energy of austenite making it less stable to ferrite transformation. In microalloying steels, the loss of solutes to strain induced precipitates may drastically accelerate the rate of transformation and this may cause a sharp rise in the  $A_{r3}$  temperature.

The available literature indicates that the effect of prior deformation of austenite on bainite transformation is complicated because of its contradictory effects on nucleation and growth. Deformation stimulates nucleation but hinders the growth of bainite plates. This leads to rather conflicting results. While some investigators have reported an increase in the bainite transformation temperature during continuous cooling others found a decrease. Similarly, some isothermal experiments show that the deformation of austenite accelerates the bainite transformation whereas others show a deceleration. In alloys containing carbide-forming elements, it is difficult to correctly interpret the results because of secondary precipitation reactions. Consistent with its displacive mechanism, the progress of <sup>the</sup> bainitic transformation is strongly affected by any applied stress.

## Chapter Four

# Topology of Grain Deformation

### 4.1 Introduction

The development and manufacture of steel by controlled rolling is a very complicated process. There is, therefore, considerable research throughout the world to produce kinetic models dealing with the transformation of deformed austenite, as an aid to the design of steels [Speich *et al.*, 1984; Umemoto *et al.*, 1983; Essadiqi and Jonas, 1989; Hodgson and Gibbs, 1992]. One of the most important factors in any kinetic theory is the number density of the nucleation sites, *i.e.*, the austenite grain surface area, the edge length and the number of corners per unit volume. These parameters may be altered by plastic deformation. Homogeneous deformation leads to an increase in the grain surface and grain edge per unit volume but there is no change in the number of grain corners per unit volume. Since surfaces, edges and corners are all heterogeneous nucleation sites, any change in their number density must be taken into account in the kinetic model.

In the last chapter, we presented two geometrical methods used for estimating grain boundary surface area as a function of deformation strain. They make the simple assumption that initially, the grains are either cubical in shape [Speich *et al.*, 1984] or in the form of a sphere [Umemoto *et al.*, 1983]. The grains are certainly not in the shape of a cube. Whereas a sphere is a closer approximation, it is not a shape which is space-filling and spheres do not have edges or corners. Calculations are presented here for the changes in surface and edge densities as a function of strain for grains which are initially in the form of Kelvin's space-filling tetrakaidecahedra. This is probably the most realistic simple shape for equiaxed grains [Christian, 1975].

### 4.2 The Method

The deformation of a shape as complicated as a tetrakaidecahedron can be considered by representing each corner with a vector whose origin is conveniently chosen. The deformation itself can be described by a  $3 \times 3$  deformation matrix [Bhadeshia, 1987], which operates on each vector in turn to generate a set of new vectors defining the new shape. Thus, a vector  $\mathbf{u}$  becomes a new vector  $\mathbf{v}$  as a consequence of a homogeneous deformation  $\mathbf{S}$ :

$$\begin{aligned}\mathbf{v} &= \mathbf{S}\mathbf{u} \\ &= \begin{pmatrix} b & 0 & 0 \\ 0 & d & 0 \\ 0 & 0 & c \end{pmatrix} \begin{pmatrix} u_1 \\ u_2 \\ u_3 \end{pmatrix}\end{aligned}\tag{4.1}$$

where  $u_i$  are the components of  $\mathbf{u}$ , and  $b$ ,  $d$  and  $c$  are the principal distortions (ratios of the final to initial lengths of unit vectors along the principal axes). Therefore,  $\ln\{b\}$ ,  $\ln\{d\}$  and  $\ln\{c\}$  are the true strains along the three principal axes of the deformation. Since all practical deformations involve only shears, there is no change in volume so that the determinant of  $\mathbf{S}$  must be unity. It follows that  $bcd = 1$ . Rolling involves plane-strain deformation with  $d = 1$  and  $bc = 1$ .

### 4.3 Results

A tetrakaidecahedron has 14 faces consisting of 8 hexagons and 6 squares (Figure 4.1). The resulting 36 edges each have a length  $a$ . The edges can be represented by just six non-parallel vectors whose components with respect to an origin defined at a corner are listed in Table 4.1, both before and after the deformation described by equation 4.1.

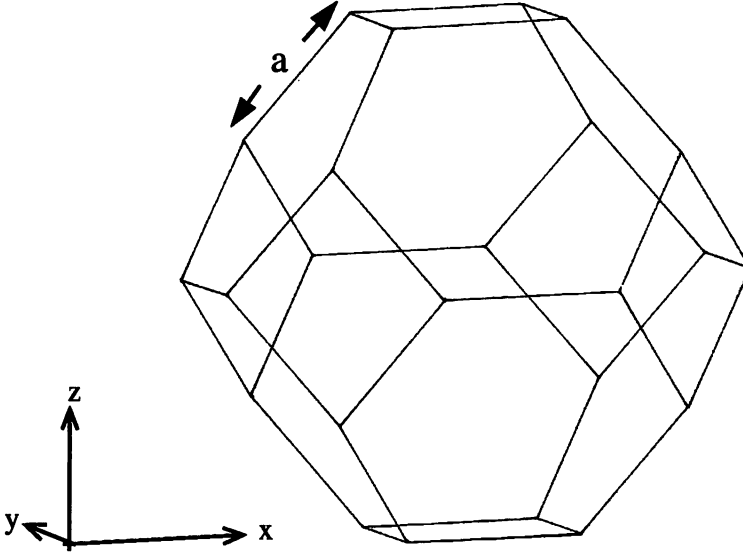


Figure 4.1: The shape of tetrakaidecahedron. The coordinate axes illustrated are orthogonal with each basis vector of length  $a$ .

The surface area and edge length can easily be calculated using the vectors given in Table 4.1. Bearing in mind that  $d = 1/bc$  in order to retain a constant volume, the ratio  $A/A_0$  of the surface area of the deformed to the undeformed tetrakaidecahedron is given by

$$\frac{A}{A_0} = \frac{b + 3(b\sqrt{1 + 2b^2c^4} + \sqrt{b^2 + 2c^2}) + c\sqrt{2(1 + b^4c^2)}}{3bc(2\sqrt{3} + 1)} \quad (4.2)$$

Similarly, the ratio of the total edge length of the deformed to undeformed tetrakaidecahedron is:

$$\frac{\ell}{\ell_0} = \frac{1 + b^2c + 2\sqrt{1 + b^4c^2 + 2b^2c^4}}{6bc} \quad (4.3)$$

Vector	Before deformation			After deformation		
1	$a$	0	0	$ab$	0	0
2	0	$a$	0	0	$ad$	0
3	$-\frac{a}{2}$	$-\frac{a}{2}$	$\frac{a}{\sqrt{2}}$	$-\frac{ab}{2}$	$-\frac{ad}{2}$	$\frac{ac}{\sqrt{2}}$
4	$\frac{a}{2}$	$-\frac{a}{2}$	$\frac{a}{\sqrt{2}}$	$\frac{ab}{2}$	$-\frac{ad}{2}$	$\frac{ac}{\sqrt{2}}$
5	$\frac{a}{2}$	$\frac{a}{2}$	$\frac{a}{\sqrt{2}}$	$\frac{ab}{2}$	$\frac{ad}{2}$	$\frac{ac}{\sqrt{2}}$
6	$-\frac{a}{2}$	$\frac{a}{2}$	$\frac{a}{\sqrt{2}}$	$-\frac{ab}{2}$	$\frac{ad}{2}$	$\frac{ac}{\sqrt{2}}$

Table 4.1: The six vectors which completely define the edges of the tetrakaidecahedron and their components after the deformation S.

For the case of plane-strain deformation ( $b = 1/c$ ), equations 4.2 and 4.3 simplify to:

$$\frac{A}{A_o} = \frac{1 + 3(\sqrt{1 + 2c^2} + \sqrt{1 + 2c^4}) + c\sqrt{2(1 + c^2)}}{3c(2\sqrt{3} + 1)} \quad (4.4)$$

$$\frac{\ell}{\ell_o} = \frac{1 + c + 2\sqrt{1 + c^2 + 2c^4}}{6c} \quad (4.5)$$

The ratios for plane-strain deformation are illustrated in Figure 4.2a, as a function of strain along the rolling direction. A negative value of the strain implies an anti-rolling deformation beginning with an equiaxed grain structure. The increase in the edge length is approximately the same as that in the surface area. The increase is roughly symmetrical for the positive and negative values of strain. Comparison with the results of Umemoto *et al.* [1983] in Figure 4.2b shows that the increase in area is larger when a tetrakaidecahedron is deformed as opposed to the deformation of a sphere. This is not surprising since a sphere has a minimum surface to volume ratio in three dimensions. In order to enable a valid comparison, the volumes of the tetrakaidecahedron and sphere have been set to be equal for the calculations presented in Figure 4.2b. Therefore, the length of the edges of the tetrakaidecahedron ( $a$ ) is set at unity and the radius of the sphere at 1.392652.

Another type of deformation common in the processing of steel is wire drawing or rod rolling, characterised by  $b = c$ . For such cases, equations 4.2 and 4.3 can be reduced to:

$$\frac{A}{A_o} = \frac{1 + 3(\sqrt{3} + \sqrt{1 + 2c^6}) + \sqrt{2(1 + c^6)}}{3c(2\sqrt{3} + 1)} \quad (4.6)$$

$$\frac{\ell}{\ell_o} = \frac{1 + c^3 + 2\sqrt{1 + 3c^6}}{6c^2} \quad (4.7)$$

The results for this are illustrated in Figure 4.3, where the strain on the horizontal axis is along the radial direction (*i.e.*, normal to the drawing direction). A positive strain therefore implies an anti-drawing operation but always beginning with an equiaxed grain structure.

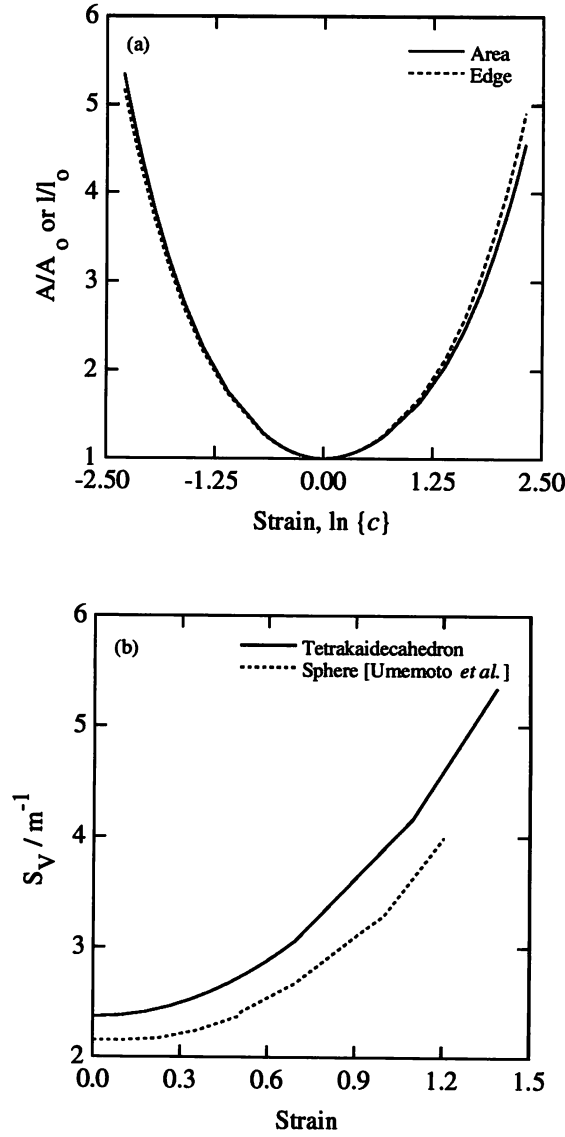


Figure 4.2: (a) Increase in the surface area and the edge length of a tetrakaidecahedron as a function of strain along the rolling direction, during plane-strain deformation. A negative value of strain implies an anti-rolling operation. (b) Comparison of the surface area per unit volume ( $S_V$ ) for the tetrakaidecahedron and sphere of the same volume.  $a = 1$  m for the tetrakaidecahedron; the corresponding radius of the sphere is 1.393 m.

Figure 4.4 shows the shape of the tetrakaidecahedron after a plane-strain deformation and after a wire drawing type of deformation. These were generated from the coordinates of the vertices of the original tetrakaidecahedron using equation 4.1.

#### 4.3.1 Comparison with Experimental Measurements

The increase in the grain boundary area due to deformation calculated here is compared against the values measured by Ouchi *et al.* [1982] and by Sandberg and Roberts [1982] in Figure 4.5. The measurements were made according to the Underwood's equation (equation 3.3). Con-

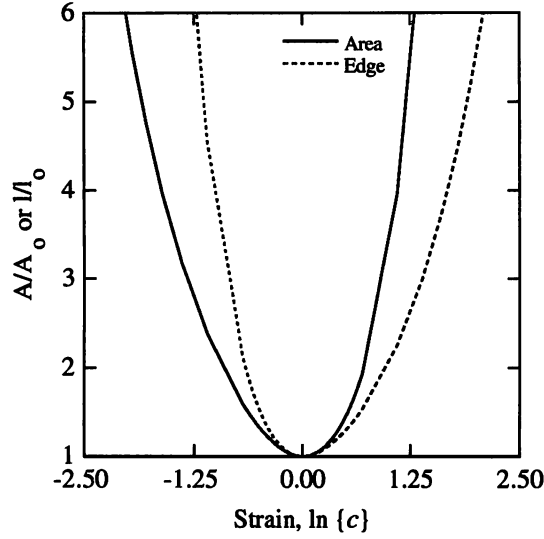


Figure 4.3: The increase in the surface area and the edge length of a tetrakaidecahedron as a function of strain along the radial direction, during a wire drawing operation. A positive value of strain implies an anti-drawing operation.

sistent with their respective experimental techniques, the calculations were performed for the plane-strain condition for Ouchi's rolling results and wire drawing condition for the measurements of Sandberg and Roberts done on uniaxially compressed samples. Figure 4.5 shows good agreement between the calculated and the measured values, though there is a tendency for slight underprediction. It should also be noted that in both the cases, the authors have not indicated the errors in their measurements.

#### 4.4 Conclusion

Rigorous relationships have been derived for the increase in the surface area and edge length when equiaxed grains, idealised as space-filling tetrakaidecahedra, are homogeneously deformed. This information should be of use in the modelling of transformation kinetics for reactions which are heterogeneously nucleated. The results improve on a previous model which was based on the deformation of a sphere. Comparison with experimental measurements showed good agreement.

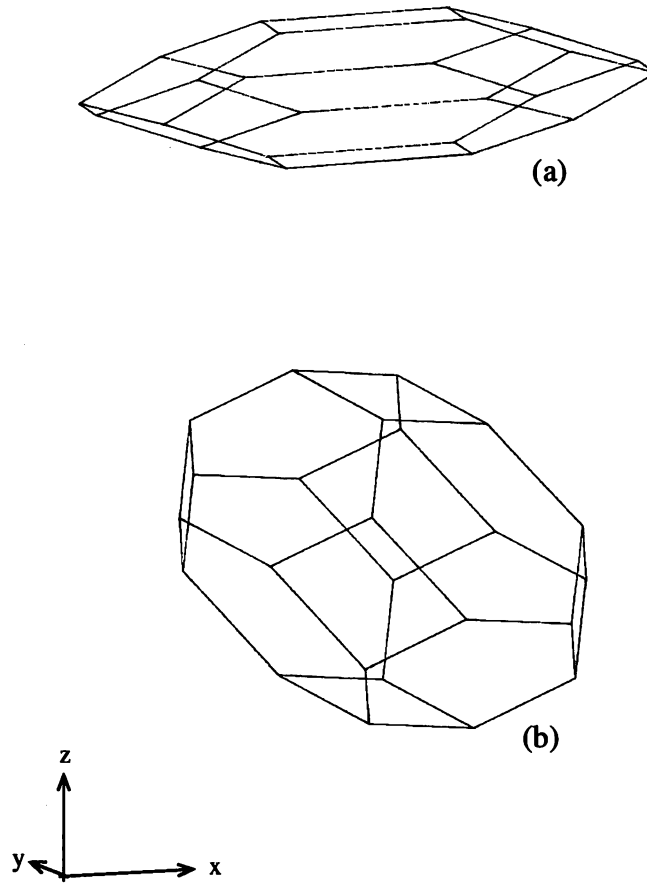


Figure 4.4: The calculated shape of the tetrakaidecahedron after (a) plane-strain deformation; (b) after wire drawing. The strain relative to the undeformed shape is 0.693 in each case, but Figure 4.4a has been uniformly scaled down in size by a factor of 2 relative to Figure 4.4b.



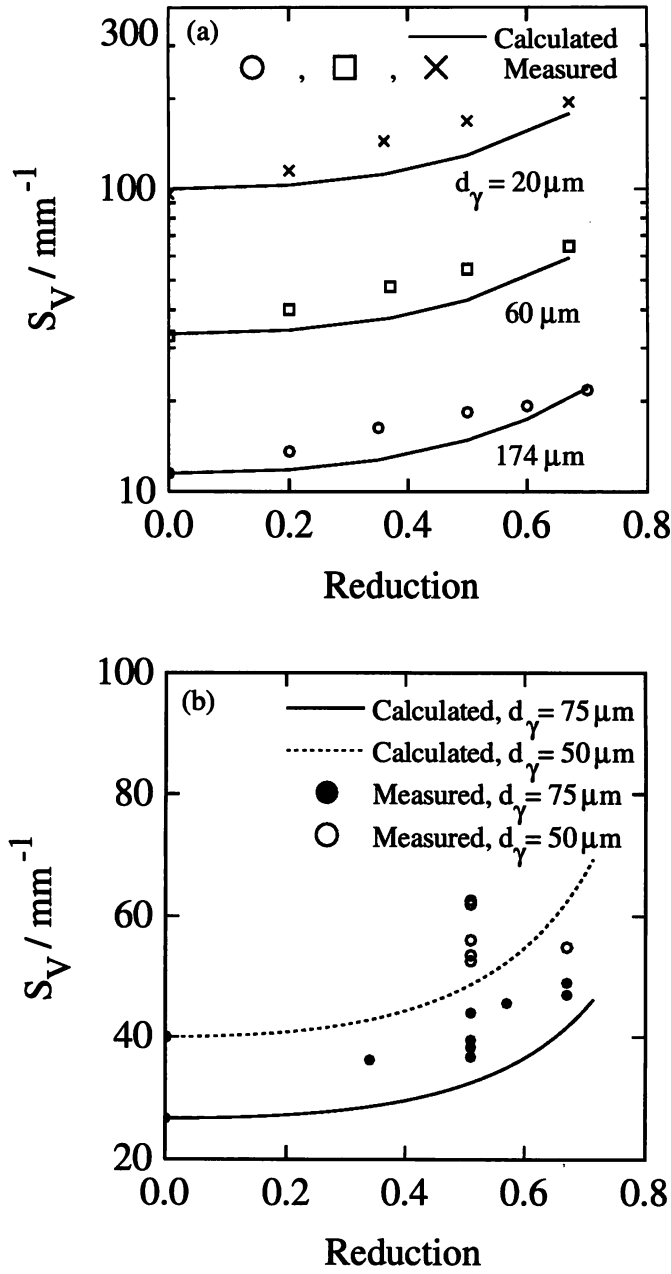


Figure 4.5: Calculated variation of austenite grain boundary area per unit volume with deformation and its comparison with the experimental measurements reported in literature. (a) For plane-strain deformation [Ouchi *et al.*, 1982] and (b) uniaxial compression tests [Sandberg and Roberts, 1982]. The deformation experiments were done starting with a variety of recrystallised austenite grain sizes.

## Chapter Five

# Allotriomorphic Ferrite Formation from Deformed Austenite

### 5.1 Introduction

The allotriomorphic ferrite transformation occurs at a faster rate when the austenite is in a deformed state [Walker and Honeycombe, 1978; Amin and Pickering, 1982; Sandberg and Roberts, 1982; Speich *et al.*, 1984; Umemoto and Tamura, 1986; Inagaki, 1986]. The reasons cited in literature can be summarised as: an increase in the austenite grain boundary area per unit volume and hence in the number density of nucleation sites, the stored energy of deformation, heterogeneous nucleation of ferrite on deformation-induced defects and increase in the nucleation potency of the deformed austenite grain boundaries. The latter effect is supposed to arise because plastic strain causes the formation of steps and bulges on the grain boundaries thus increasing the area density of heterogeneous nucleation sites [Sandberg and Roberts, 1982; Umemoto and Tamura, 1986]. Keeping this in mind, experiments were conducted to study the effect of deformation on ferrite nucleation at the austenite grain boundaries. An existing model for allotriomorphic ferrite transformation has been modified to estimate the transformation-start temperature of ferrite during continuous cooling ( $A_{r3}$ ) of deformed austenite.

### 5.2 Experimental Method

The chemical composition of the alloy chosen for the study was Fe-0.12C-1.96Si-3.0Mn-0.26Mo (wt.%). With its high hardenability, the alloy transforms very slowly to ferrite, thus allowing controlled experiments.

Long cylindrical samples (6.34 mm  $\times$  108 mm) with suitable threads at both the ends were machined from the rolled plates. Thermal and/or mechanical treatments were performed in Gleeble 1500 thermomechanical simulator. The samples were resistance heated to the austenitising temperature of 1200 °C and then held there for 5 minutes. A chromel-chromel/alumel thermocouple was used to measure and control the temperature. The hot zone was confined to 15 mm along the length of the sample. After austenitising, the samples were cooled to the deformation temperature and pulled in tension at a stroke rate of about 3 mm s<sup>-1</sup>. The deformation caused necking within the central heated zone in all the samples. The specimens were then cooled to the isothermal transformation temperature at 25 °C s<sup>-1</sup> as shown in Figure 5.1 and held there for 1 hour and then cooled to the ambient temperature. The change in

sample diameter was monitored using a strain gauge. All the experiments were repeated with undeformed austenite.

The heat treated samples were sectioned along the deformation axis, ground and polished for microstructural examination.

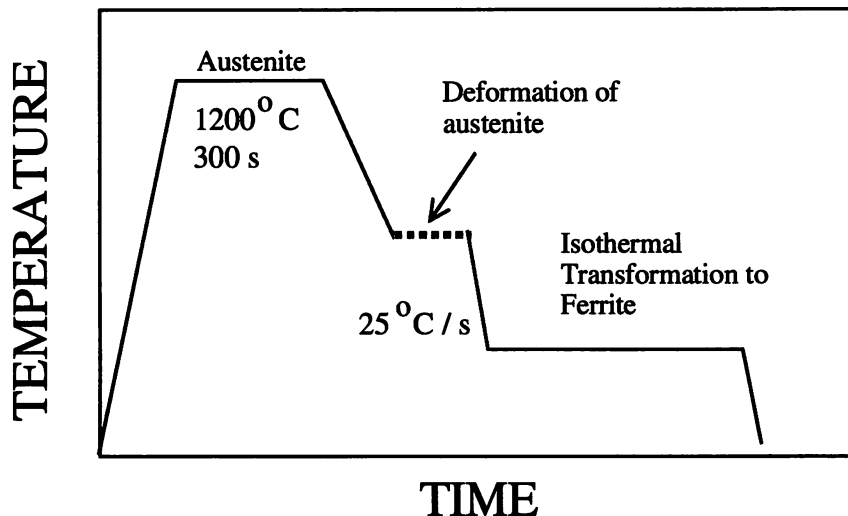


Figure 5.1: Schematic illustration of the thermomechanical test cycle.

### 5.3 Results and Discussions

The true stress–true strain curve of the alloy deformed at 800 °C is shown in Figure 5.2. As confirmed by metallography, this deformation temperature was low enough to prevent recrystallisation. The subsequent transformation therefore occurred with austenite in a deformed state.

#### 5.3.1 Dilatation curves

It was confirmed, by monitoring the change in length as a function of temperature, that transformation did not occur during cooling from the austenite condition to the isothermal reaction temperature. The isothermal dilatation curves of the samples transformed at 680 °C and 650 °C with and without any deformation at 800 °C are shown in Figure 5.3. In both cases, deformation not only accelerates the transformation but also leads to an increase in the quantities of the product phase.

#### 5.3.2 Microstructure

The microstructures of the samples transformed at 680 °C and 650 °C for 1 hour without any prestrain are shown in Figures 5.4a and c. The austenite grain boundaries are decorated with allotriomorphic ferrite.

The pancaked grain structure of the austenite is clearly evident in the samples which were deformed at 800 °C prior to transformation, Figures 5.4b and d. Apart from an exaggerated formation of ferrite on grain boundaries, there is also copious nucleation of ferrite *in the vicinity*

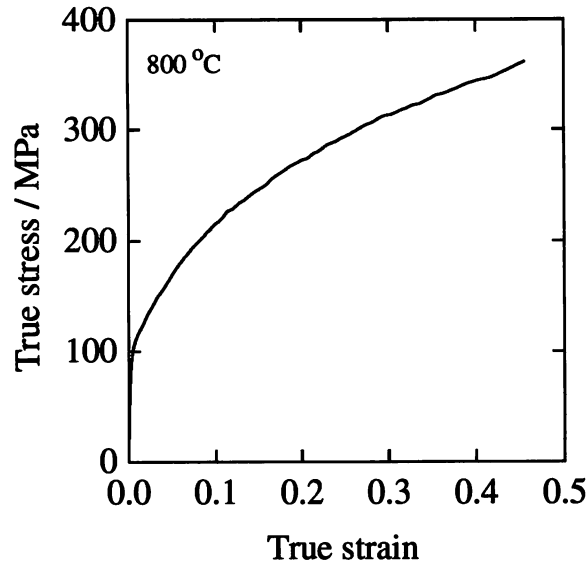


Figure 5.2: The true stress–true strain curve of the steel for deformation at 800 °C.

of the austenite grain boundaries (Figure 5.5). This is in contrast to the undeformed samples where ferrite nucleation was confined to the austenite grain boundaries. The number of ferrite grains along the austenite grain boundary trace was counted for the samples isothermally transformed at 680 °C for one hour with and without any prior deformation. The number was  $22 \pm 7$  grains per millimetre of the grain boundary trace for the undeformed sample and  $46 \pm 5$  grains per millimetre for the sample deformed at 800 °C before transforming at 680 °C. 200 grains were counted in each case. For the deformed sample, only the grains along the grain boundary plane were counted; the grains in the second or third layers were not counted. This proves that deformation increases the number of grain boundary sites per unit area.

The deformation of austenite has the effect of inducing ferrite nucleation not only on the grain boundaries but also in the proximity of the grain boundary regions. In the undeformed austenite, each nucleus grows into both the adjacent grains restricted only by impingement with other grain boundary nucleated ferrite grains. The layer of ferrite is therefore monocrystalline or at the most bicrystalline in a direction normal to the austenite grain boundary. On the other hand, multiple rows of ferrite grains were observed around the grain boundaries when the transformation occurred from deformed austenite. In some cases upto 6 ferrite grains were observed in a direction normal to the grain boundary trace (Figure 5.5). For the sample deformed at 800 °C and transformed at 680 °C, the average number of grains in a direction normal to the grain boundary trace was counted to be 3. Intragranularly nucleated grains, particularly on the deformation bands were also observed. The enhanced nucleation leads to an increase in the volume fraction of ferrite at any time when compared with transformation from undeformed austenite (Figure 5.3).

Similar microstructures were observed for the samples deformed at 850 °C and 700 °C

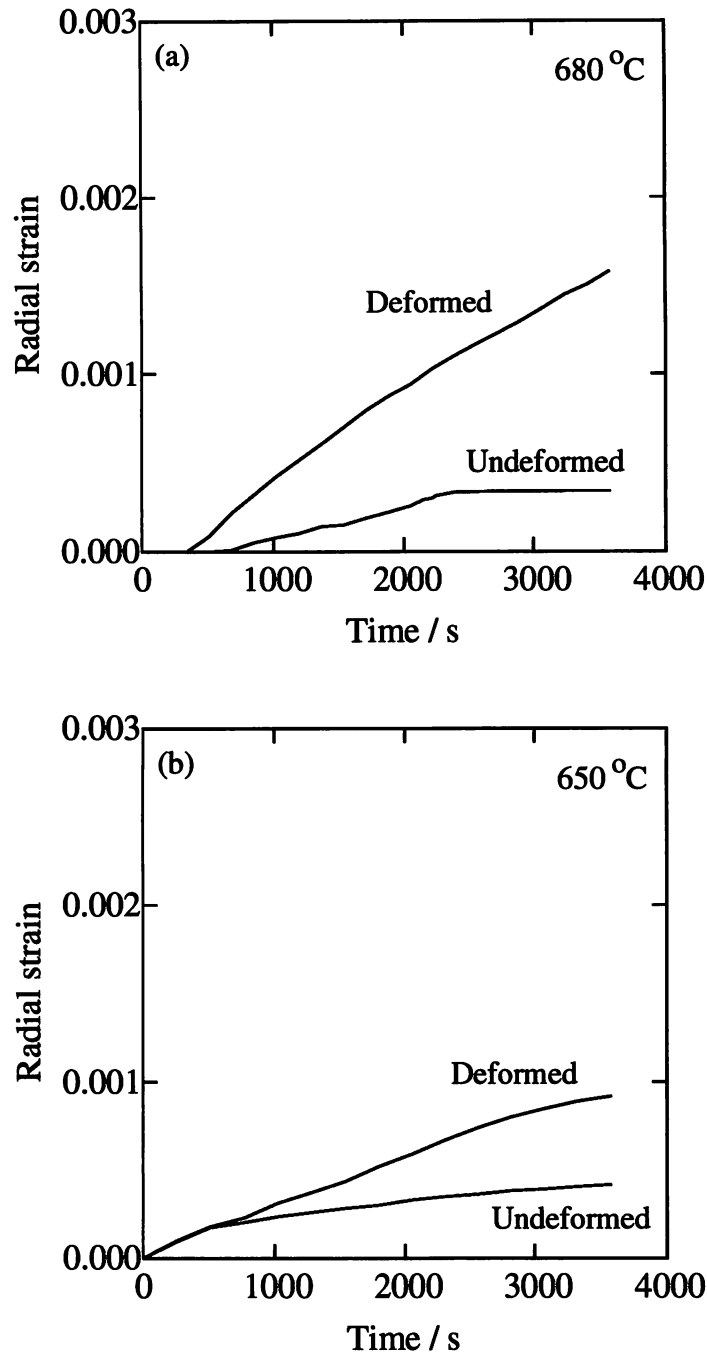


Figure 5.3: The effect of deformation on ferrite transformation kinetics. (a) 680 °C and (b) 650 °C.

before transforming at 680 °C (Figure 5.6).

It is thought that the recovery of dislocations produces a sub-grain structure which provides nucleation sites for ferrite [Amin and Pickering, 1982b]. Amin and Pickering [1982b] argued that the sub-grains are much finer near the grain boundary than away from it because of the strain gradient normal to the boundary. This results in an enhanced nucleation near the grain boundaries. Moreover, the density of dislocations due to pile up is much higher near

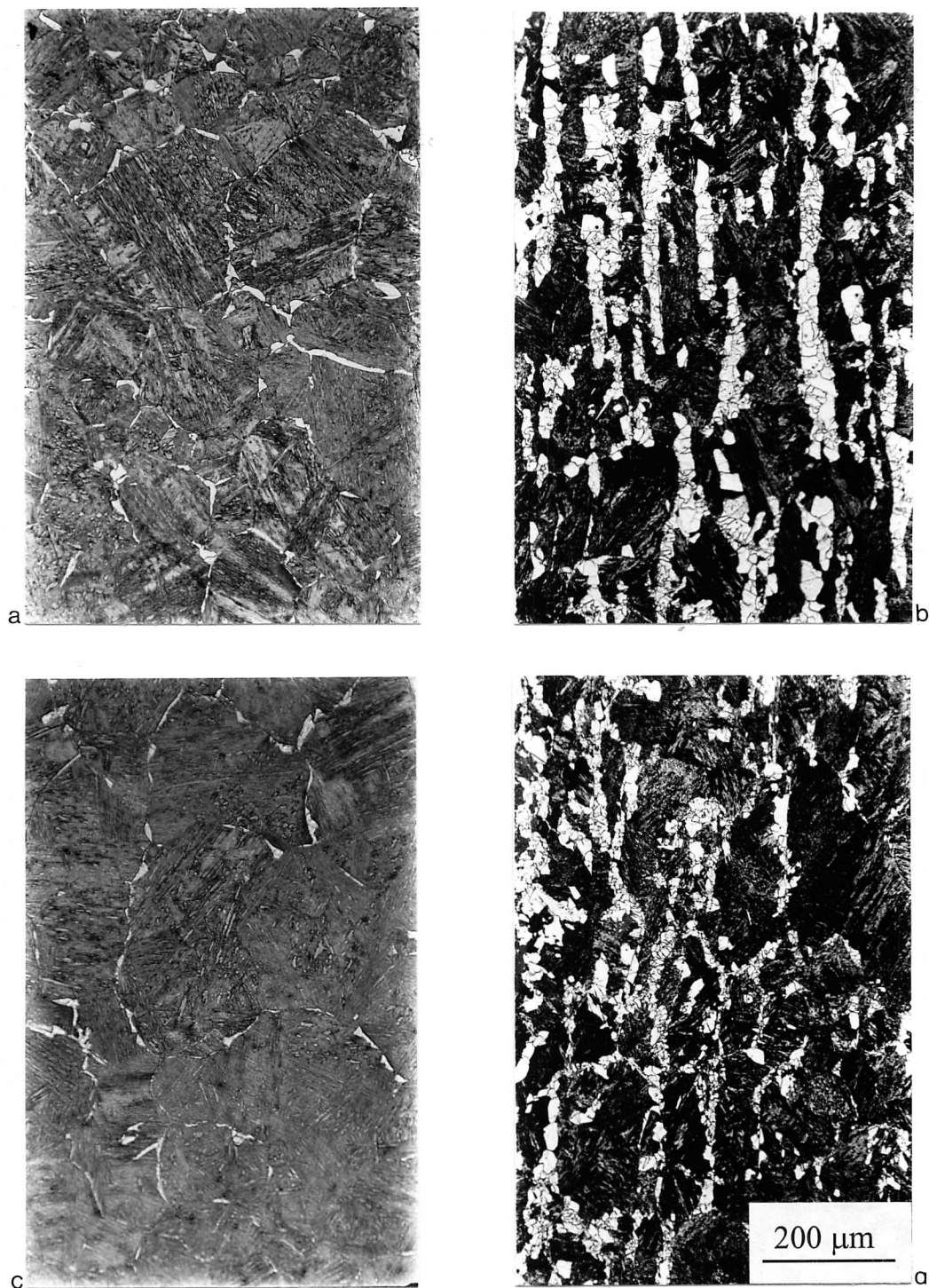


Figure 5.4: Microstructures showing the effect of deformation on ferrite nucleation. The isothermal transformation temperature was: (a and b) 680 °C and (c and d) 650 °C. Micrographs (a and c) are from undeformed samples while (b and d) are from samples deformed at 800 °C. Austenitisation was at 1200 °C for 5 minutes in each case; the isothermal transformation time was 1 hour.

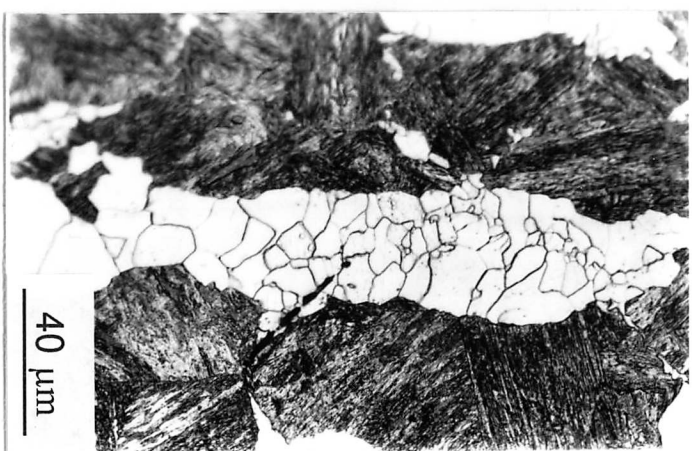
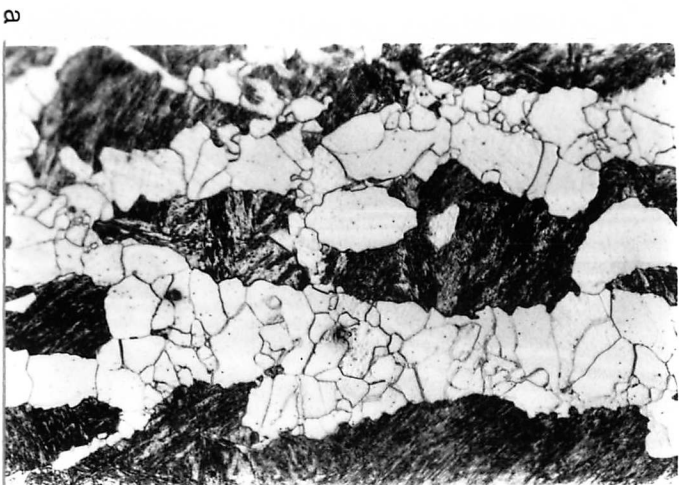


Figure 5.5: The microstructure of the samples deformed at 800 °C and then transformed for 1 hour at (a) 680 °C and (b) 650 °C.



Figure 5.6: The microstructure of the samples transformed at 680 °C for 1 hour after deformation at (a) 850 °C and (b) 700 °C.

the grain boundaries which can catalyse ferrite nucleation.

In samples with pancaked austenite grains, the ferrite nucleated more frequently on the boundaries along the deformation direction than along the transverse direction. This can be explained by considering the deformation of tetrakaidecahedra as described in the previous chapter. A tensile deformation along the principal axis  $y$  will result in elongation along  $y$  but contraction along the other two principal axes,  $x$  and  $z$ . If  $\varepsilon$  is the true plastic strain and  $\ell_o^i$  and  $\ell^i$  are the total edge lengths of the grains along the direction  $i$  (where  $i = x, y, z$ , the principal axes of deformation) before and after the deformation, then their ratio can be calculated to be:

$$\frac{\ell^y}{\ell_o^y} = \exp(\varepsilon) \quad \text{and} \quad \frac{\ell^x}{\ell_o^x} = \exp(-\varepsilon/2) \quad \text{or} \quad \frac{\ell^z}{\ell_o^z} = \exp(-\varepsilon/2) \quad (5.1)$$

This gives

$$\frac{\ell^y}{\ell^x} = \exp(1.5\varepsilon) \quad (5.2)$$

Thus the total edge length along the direction of deformation is much larger than in the normal directions. This explains the propensity for the formation of ferrite along the longitudinal grain boundaries.

#### 5.4 Mathematical Modelling

The purpose here was to interpret the experimental results using an austenite to ferrite transformation model developed by Bhadeshia *et al.* [1987] by incorporating the perceived effects of deformation. The model relies on Avrami's theory [1939] as modified by Cahn [1956] to account for nucleation on grain boundaries [Christian, 1975]. The allotriomorphs of ferrite were modelled as discs growing from the austenite grain boundaries under diffusion control. The volume fraction of ferrite normalised relative to its equilibrium fraction,  $\xi_\alpha$ , at any time  $t$  is given by [Bhadeshia, 1987]:

$$\xi_\alpha = 1 - \exp\left[-S_V \alpha_1 t^{1/2} \left\{ \int_0^1 1 - \exp\left\{-\frac{\pi}{2} I_B \eta^2 \alpha_1^2 t^2 (1 - \phi^4)\right\} d\phi \right\}\right] \quad (5.3)$$

where  $S_V$  is the austenite grain boundary area per unit volume,  $\alpha_1$  is the one dimensional parabolic growth rate constant,  $I_B$  is the nucleation rate on austenite grain boundaries,  $\eta$  is the aspect ratio of the discs,  $\phi = y/\alpha_1 t^{1/2}$  and  $y$  = distance between austenite grain boundary and an arbitrary plane parallel to the boundary.

The possible heterogeneous nucleation sites for allotriomorphic ferrite are grain boundary faces, edges and corners. However, at sufficiently large undercoolings only the face sites make a significant contribution to the total nucleation rate since the number density of other two sites is much lower and may be neglected. Thus, one can write

$$I_B \simeq I_B^f \quad (5.4)$$

where  $I_B^f$  is the nucleation rate on the grain boundary faces. Following classical nucleation theory, the steady state rate of nucleation on grain boundary faces is given by [Christian, 1975;



Reed and Bhadeshia, 1992]:

$$I_B^f = N_s^f \frac{k_B T}{h} \exp \left\{ -\frac{(G^* + Q)}{RT} \right\} \quad (5.5)$$

where  $N_s^f$  is the number density of face sites per unit area of grain boundary which support nucleation,  $k_B$  and  $h$  are the Boltzmann and Planck constant respectively,  $G^*$  is the activation energy for ferrite nucleation on grain faces and  $Q$  is the activation energy required for crossing the austenite/ferrite interface. Christian [1975] defined  $N_s^f$  as:

$$N_s^f = \frac{K_1^f}{\delta^2} \quad (5.6)$$

where  $K_1^f$  is an empirical constant representing the fraction of face sites which actually act as nuclei and  $\delta$  is the interatomic spacing taken as 2.5 Å.

Ignoring the strain energy of nucleus, the activation free energy for nucleation can be written as:

$$G^* = \frac{\sigma_{\gamma\alpha}^3}{\Delta G_v^2} K_2^f \quad (5.7)$$

where  $\sigma_{\gamma\alpha}$  is the austenite–ferrite nucleus interface energy per unit area,  $\Delta G_v$  is the magnitude of the chemical free energy change per unit volume associated with the nucleation of ferrite from austenite and  $K_2^f$  is a shape factor which depends on the shape of the nucleus which forms on the boundary faces.

$K_1^f$  and  $K_2^f$  have been determined by fitting to experimental data [Reed and Bhadeshia, 1992].

#### 5.4.1 Effect of Deformation

Deformation enhances the number density of nucleation sites for at least two reasons. It leads to grain elongation and introduces deformation bands. For simplicity, it can be assumed that the ferrite nucleating potency of both these sites are same. Thus, the total surface area per unit volume of defects,  $S_V^T$ , can be given as the sum of the elongated grain boundary area per unit volume ( $S_V$ ) and the surface area per unit volume of the deformation bands ( $S_V^{db}$ ). The deformation band density depends on the magnitude of the applied strain  $\epsilon$  [Umemoto and Tamura, 1986].

$$S_V^T = S_V + S_V^{db}, \quad S_V^{db} = 30 \epsilon^2 \text{ mm}^{-1} \quad (5.8)$$

A part of the work done during deformation is stored in austenite in the form of an increased defect density. Its effect on transformation was discussed in chapter three. The activation energy for ferrite nucleation should therefore be modified to include the stored energy term  $W$ .

$$G^* = \frac{\sigma_{\gamma\alpha}^3}{(\Delta G_v - W)^2} K_2^f \quad (5.9)$$

##### 5.4.1.1 Calculation of Stored Energy

The stored energy of deformation can be calculated in two ways, either from the work of deformation or from the density of dislocations generated by deformation. The total work

done in achieving a certain strain can be calculated from the area under the stress–strain curve and then a fraction of the total work can be assumed to be stored inside the material. If  $\bar{\sigma}_i$  and  $\varepsilon_i$  are the mean flow stress and the strain respectively for the  $i$ th pass then the total energy stored after  $n$  passes below the recrystallisation temperature can be given by:

$$W = \sum_{i=1}^n \alpha_s \bar{\sigma}_i \varepsilon_i \quad (5.10)$$

The parameter  $\alpha_s$  gives the fraction of the work done which is stored and is taken as 0.1 [Liu and Karjalainen, 1996], the remainder is dissipated as heat.

Liu *et al.* [1996] have proposed a modified equation for stored energy, according to which:

$$W = \sum_{i=1}^n \frac{2}{3} [(\bar{\sigma}_R)_i - (\bar{\sigma}_T)_i] \varepsilon_i \quad (5.11)$$

where  $n$  is the number of passes below the recrystallisation temperature,  $\bar{\sigma}_R$  is the actual mean flow stress below the recrystallisation temperature and  $\bar{\sigma}_T$  was identified as the ‘temperature dependent part of the mean flow stress’. However, it was defined as an empirical flow stress calculated from extrapolation of the stresses above the recrystallisation temperature, Figure 5.7.

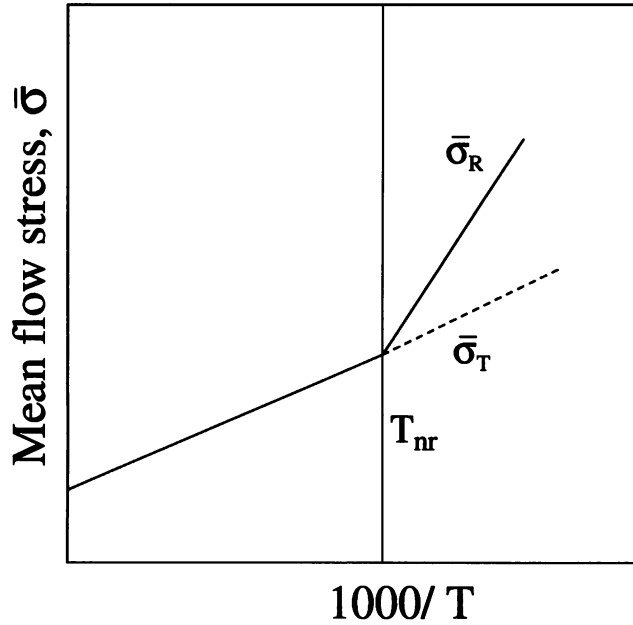


Figure 5.7: Schematic illustration of the variation of mean flow stress with temperature to define the terms  $\bar{\sigma}_R$  and  $\bar{\sigma}_T$  used in equation 5.11 [Liu *et al.*, 1996].  $T_{nr}$ , the no recrystallisation temperature, is the temperature below which recrystallisation is not possible for specified conditions.

The dislocation density of austenite generated by deformation can be computed from the measured flow stress of the material for the given strain. The flow stress  $\sigma$  is related to the

dislocation density  $\rho_d$  by [Mukherjee, 1975]:

$$\sigma = \alpha_m M \mu_T b \rho_d^{0.5} \quad (5.12)$$

where  $\alpha_m$  is a constant, taken to be equal to 0.15,  $\mu_T$  is the shear modulus at the temperature of deformation,  $b$  is the magnitude of the Burgers vector and  $M$  is the Taylor factor.

Yoshie *et al.* [1987] have proposed an empirical formulation for the calculation of dislocation density in deformed austenite. They also proposed an equation for the static recovery which takes place during the interpass time (the time gap between two successive passes). The dislocation density just after the deformation was given by:

$$\rho_d = B_y / C_y [1 - \exp(-C_y \varepsilon)] + \rho_d^o \exp(-C_y \varepsilon) \quad (5.13)$$

where  $B_y$  and  $C_y$  are constants and  $\rho_d^o$  is the dislocation density in the annealed condition.  $B_y$  was assumed to depend on temperature and  $C_y$  on temperature, strain rate and the austenite grain size. The annihilation of dislocations through static recovery was expressed as:

$$\rho_d^t = (\rho_d - \rho_d^o) \exp(-D_y t) + \rho_d^o \quad (5.14)$$

where  $\rho_d^t$  is the dislocation density at any time  $t$  after the deformation and  $D_y$  is a constant dependent on temperature, strain rate and the austenite grain size.

The constants were determined by fitting flow curve data to the above equations with the knowledge that the flow stress is proportional to the square root of the dislocation density,  $\sigma \propto \rho_d^{0.5}$ .

For the calculation of stored energy from the dislocation density, the dislocation line energy per unit length ( $\tau_d$ ) is required. An approximate value of  $\tau_d$  can be obtained from [Cottrell, 1961]:

$$\tau_d \simeq \frac{\mu b^2}{2} \quad (5.15)$$

where  $\mu$  is the shear modulus of the material. The additional stored energy is then given by:

$$W = \tau_d (\rho_d - \rho_d^o) \quad (5.16)$$

#### 5.4.1.2 Comparison with Experimental Measurements

Liu *et al.* [1995] have studied the effect of deformation on austenite to ferrite transformation temperature during continuous cooling ( $Ar_3$ ) of a 0.1C, 1.32Mn, 0.3Si, 0.028Nb (wt.%) steel. The deformation was carried out in 13 passes in the temperature range of 1150 °C to 910 °C at intervals of 20 °C. The strain in each pass was 0.3. Reheating was done at 1250 °C. The as-reheated and the recrystallised austenite grain sizes were measured to be 156  $\mu$ m and 27  $\mu$ m respectively. The recrystallisation stop temperature ( $T_{nr}$ ) was 950 °C. The transformation temperature was detected by monitoring the variation of stress with temperature.

For the above experimental conditions with two passes below the recrystallisation temperature (at 930 °C and 910 °C), the dislocation density as calculated from the equations of

Yoshie *et al.* [1987] was estimated to be  $2.29 \times 10^{15} \text{ m}^{-2}$ . Taking  $b = 2.5 \times 10^{-10} \text{ m}$  and  $\mu = 8.1 \times 10^{10} \text{ J m}^{-3}$ , the dislocation line energy can be computed to be  $2.5 \times 10^{-9} \text{ J m}^{-1}$ . This gives an estimated stored energy of  $5.7 \times 10^6 \text{ J m}^{-3}$  or  $41 \text{ J mol}^{-1}$ .

Using equation 5.11 and the measured flow stress values, Liu *et al.* [1996] calculated the stored energy to be  $37 \text{ J mol}^{-1}$  for the above experimental conditions. Considering the case of a 0.1C, 1.42Mn, 0.31Si wt.% steel, Parker [1997] estimated the stored energy to be  $3.0 \times 10^6 \text{ J m}^{-3}$  and  $8.8 \times 10^6 \text{ J m}^{-3}$  for strains of 0.2 and 0.4 respectively. Equation 5.10 was used for the purpose. Different methods thus give similar values for the stored energy.

Taking a stored energy value of  $41 \text{ J mol}^{-1}$ , the  $Ar_3$  temperature of the steel (0.1C, 1.32Mn, 0.3Si, wt.%) was calculated as a function of cooling rate. The experimentally measured transformation temperatures with and without the deformation are compared against the respective calculated temperatures in Figure 5.8. The predictions also take into account the increased defect density of the deformed austenite (equation 5.8). The elongated grain boundary area was calculated as in the previous chapter. The predicted temperature is higher than the experimental value at all the cooling rates. This is because the effect of Nb was ignored in the calculations. It has been shown that Nb retards the kinetics of allotriomorphic ferrite formation [Thomas and Michal, 1982; Abe *et al.*, 1986; Huang *et al.*, 1993]. Considering this, the agreement between the measured and the calculated values is good. At the slowest cooling rate, deformation has only a small effect on the  $Ar_3$  temperature and this was thought to be the result of a higher degree of recovery at a slower cooling rate [Liu *et al.*, 1995].

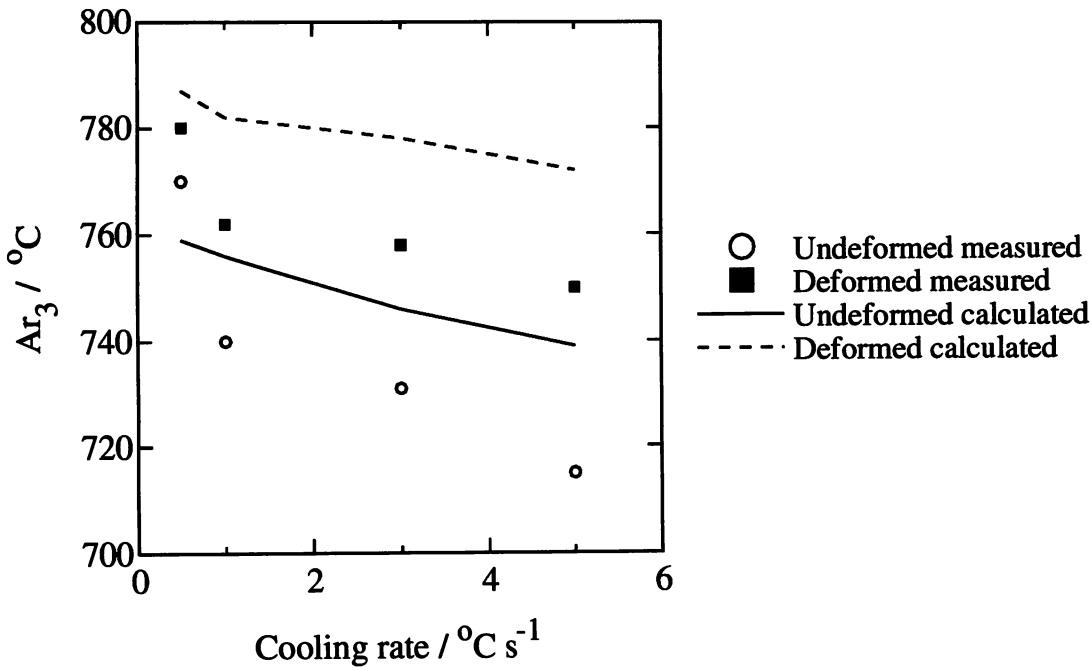


Figure 5.8: Comparison of the calculated and the measured ferrite transformation-start temperature during continuous cooling ( $Ar_3$ ) of a Fe-0.1C-1.32Mn-0.3Si-0.028Nb (wt.%) steel. The measurements were done by Liu *et al.* [1995].

## 5.5 Conclusions

The effect of deformation of austenite on its transformation to allotriomorphic ferrite has been studied. Deformation was found to accelerate the transformation by stimulating ferrite nucleation on the austenite grain boundaries and their adjacent regions. Intragranular nucleation of ferrite was also observed.

The transformation-start temperature during continuous cooling of a low carbon steel has been calculated with and without the deformation of austenite. An existing model for allotriomorphic ferrite was modified for the purpose to take into account the stored energy of deformation. The predicted trends agree reasonably with the measurements.

## Chapter Six

# Kinetics of the Bainite Transformation

## Part 1: A Mathematical Model

### 6.1 Introduction

A mathematical model to predict the bainite transformation kinetics proposed by Rees and Bhadeshia [1992] was discussed in chapter two. The work described in this chapter is a further development of that theory with a reduced level of empiricism.

### 6.2 Limitations of the Old Model

The Rees and Bhadeshia model described earlier has a number of empirical assumptions. The bainite plate volume,  $u$ , is not considered explicitly. Measurements of bainite plate thickness indicate that it varies with the composition of the steel and with the transformation temperature [Ohmori *et al.*, 1971; Sandvik and Nevalainen, 1981; Chang and Bhadeshia, 1996]. The model does not take into account this variation and treats the plate thickness as an empirical constant along with the site density. The effect of autocatalytic nucleation is modelled empirically in equation 2.16. The optimised value of the autocatalysis factor  $\beta$  is unrealistically high in some cases (*e.g.*, it is 141 for alloy 300M) which is not consistent with the observed sheaf structure [Bhadeshia and Edmonds, 1979]. With such a high value of  $\beta$ , the sheaf would tend to fan outwards from the initial austenite grain boundary nucleation sites, whereas in practice it thins away from the boundary. The observed structure indicates that each plate can nucleate only about 3 or 4 new plates by autocatalysis.

Another inconsistency with the autocatalysis factor is that when all the alloys are considered together,  $\beta$  is assumed to decrease linearly with increasing carbon concentration of the steel (equation 2.19). However, as illustrated in Figure 6.1, when the data for individual alloys are treated separately, the optimum values of  $\beta$  indicate exactly the opposite trend. This is particularly true for the alloys listed in Table 2.1. The best fit value of the empirical constant  $B_4$  varies by 6 orders of magnitude from alloy to alloy which does not seem justified (Tables 2.2 and 2.4). The treatment in equation 2.13 implies that  $B_4$  should be independent of alloy composition.

The assumption in equation 2.18 that the chemical free energy change associated with nucleation ( $\Delta G_m$ ) varies linearly with the extent of reaction  $\xi$  from its initial value  $\Delta G_m^o$  to  $G_N$  is, in general, not justified, as shown in Figure 6.2. It may, however, be true in a few special cases (Figure 6.2c).

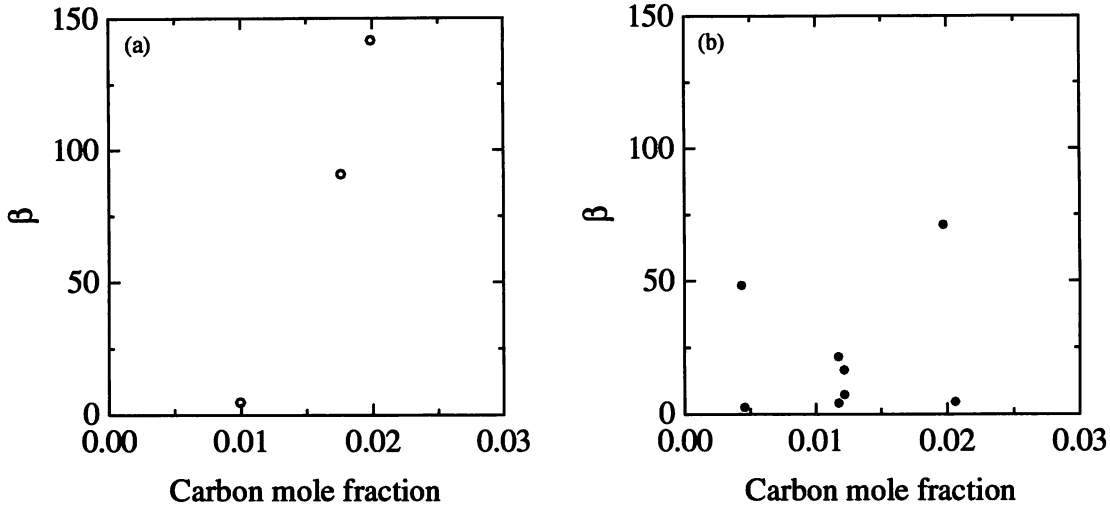


Figure 6.1: Plot of autocatalysis factor  $\beta$  as a function of mole fraction carbon when the data for the alloys are optimised individually. (a) Bhadeshia's alloys, as listed in Table 2.1 and (b) Chang's alloys listed in Table 2.3.

### 6.3 The New Model

#### 6.3.1 Bainite Plate Volume

There is no physical model which can predict the bainite plate thickness, given the steel composition and the transformation temperature. In the present work therefore, a quantitative model was developed using neural network analysis with inputs which have physical meaning. The experimental data on the thickness of bainite plates in high-silicon steels published by Chang and Bhadeshia [1996] were used for the purpose of training the network. The details are described in chapter ten.

The plate thickness predicted by the neural network model was used as an input to the kinetics model. The predicted thicknesses at different transformation temperatures for the three alloys used in the Rees and Bhadeshia work (Table 2.1) and for alloys B and D (Table 2.3) are shown in Figure 6.3. The thicknesses for the other alloys in the series A–H (Table 2.3) were measured experimentally and constituted the training data for the analysis. For a given alloy, the predicted plate thickness increases with transformation temperature which is consistent with the established trend [Bhadeshia, 1992].

Considering an oblate spheroid shape of a bainite plate with a constant radius to thickness ratio over the entire transformation range, the volume of the plate can be modelled as being proportional to the cube of its thickness,  $a_b$

$$u = \alpha_p a_b^3, \quad \alpha_p = \text{constant} \quad (6.1)$$

#### 6.3.2 Autocatalysis

An attempt was made to formulate the effect of autocatalysis on the total nucleation rate based on the actual mechanism of the development of the sheaf structure. Let  $N_V^o$  be the

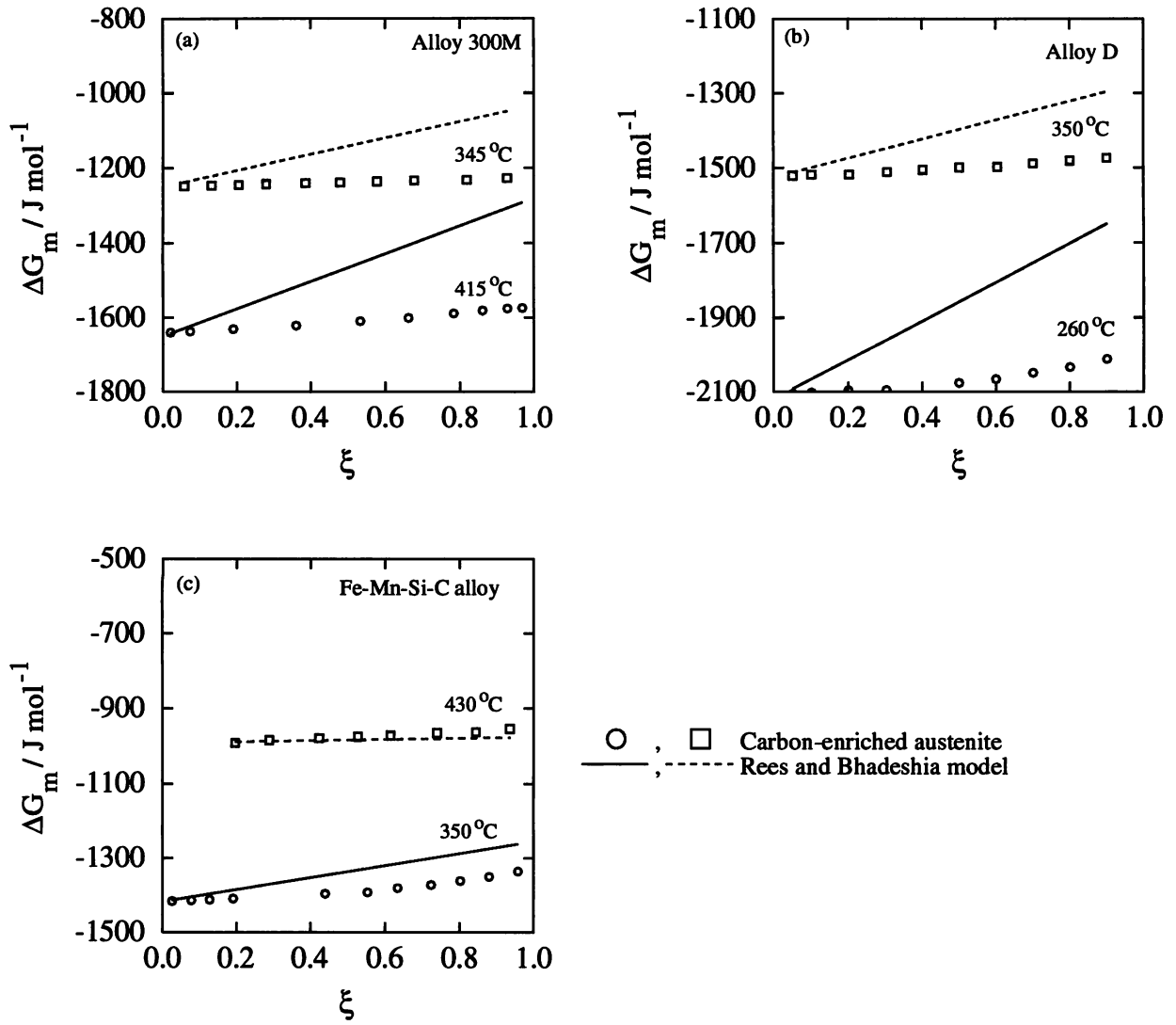


Figure 6.2: The variation in the driving force for nucleation,  $\Delta G_m$ , with the extent of bainite transformation  $\xi$ . The values calculated considering carbon enrichment of the residual austenite are compared against those calculated according to equation 2.18 suggested by Rees and Bhadeshia [1992]. (a) Alloy 300M (Table 2.1), (b) alloy D (Table 2.3) and (c) Fe-Mn-Si-C alloy (Table 2.1). The method of calculating  $\Delta G_m$  has been described elsewhere [Hillert, 1953; Bhadeshia, 1982b].

initial density of potential nucleation sites and  $I$  the initial nucleation rate per unit volume on the austenite grain boundaries.  $I$  is given by

$$I = N_V^o \nu \exp\left(-\frac{G^*}{RT}\right) \quad (6.2)$$

where frequency factor  $\nu = k_B T / h$  and  $k_B$  is the Boltzmann constant, other terms have their usual meaning. In extended space, the total number of plates per unit volume after time  $\tau$  is then  $I\tau$ . Each of these plates is capable of nucleating  $\beta$  new plates due to autocatalysis. The



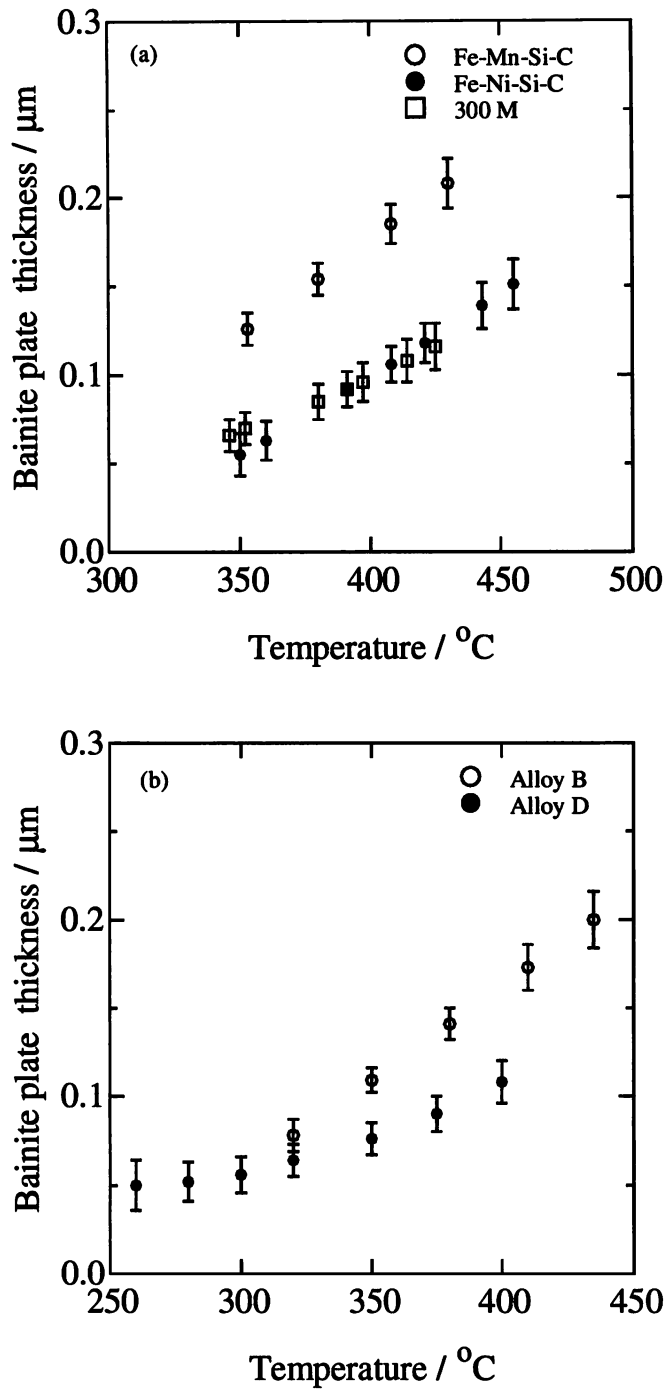


Figure 6.3: Bainite plate thickness predicted using the neural network model described in chapter ten. (a) Alloys in the Rees and Bhadeshia study (Table 2.1) and (b) alloys B and D (Table 2.3). The error bars represent  $\pm 1\sigma$  limits.

total extended density of nucleation sites at time  $\tau$  can thus be written as

$$N_V^T = N_V^o + \beta I \tau \quad (6.3)$$

$\beta$  was considered to vary linearly with the initial carbon concentration of the steel, as in the old model (equation 2.19):

$$\beta = \lambda_1 (1 - \lambda_2 \bar{x}) \quad (6.4)$$

where  $\lambda_1$  and  $\lambda_2$  are empirical constants and  $\bar{x}$  is the mean carbon concentration of the steel in mole fraction. The net nucleation rate,  $I_b$ , including the effect of autocatalysis is now time dependent and can be written as

$$I_b = N_V^T \nu \exp\left(-\frac{G^*}{RT}\right) \quad (6.5)$$

Combination of equation 6.5 with equations 6.2 and 6.3 gives

$$I_b = I \left[ 1 + \beta \tau \nu \exp\left(-\frac{G^*}{RT}\right) \right] \quad (6.6)$$

### 6.3.3 Overall Transformation Kinetics

Consider austenite of volume  $V^\gamma$  which is transforming to bainite. The extended volume of bainitic ferrite that forms between time  $\tau$  and  $\tau + d\tau$  is given as

$$dV_e = I_b V^\gamma u d\tau \quad (6.7)$$

where  $u$  is the volume of a bainite plate. The change in real volume is related to the corresponding change in extended volume by [Christian, 1975]

$$dV = (1 - \xi) dV_e \quad (6.8)$$

This gives

$$dV = (1 - \xi) V^\gamma u I_b d\tau \quad (6.9)$$

Writing this in terms of bainite volume fraction  $v$  while remembering that  $v = \theta_b \xi$ , we get

$$\theta_b d\xi = (1 - \xi) u I_b d\tau \quad (6.10)$$

On substituting the values of  $I_b$  and  $I$ , rearranging and integrating, we get:

$$\frac{\theta_b}{u N_V^o \nu} \int_0^\xi \frac{d\xi}{\exp\left(-\frac{G^*}{RT}\right) (1 - \xi)} = \int_0^t \left[ 1 + \beta \tau \nu \exp\left(-\frac{G^*}{RT}\right) \right] d\tau \quad (6.11)$$

The initial number density of nucleation sites,  $N_V^o$ , is directly proportional to the austenite grain boundary area per unit volume ( $S_V^o$ ) which in turn is inversely proportional to the grain

size represented by mean lineal intercept length  $\bar{L}$  [Rees and Bhadeshia, 1992; Underwood, 1968]. The nucleation site density was therefore written as:

$$N_V^o = \frac{B_3'}{\bar{L}} \quad (6.12)$$

Consistent with martensite nucleation theory [Olson and Cohen, 1976], the activation energy for nucleation,  $G^*$ , is given by:

$$G^* = B_4 \left\{ 1 + \frac{\Delta G_m}{B_2} \right\} \quad (6.13)$$

It will now be assumed that at a fixed temperature,  $\Delta G_m$  remains constant over the entire extent of transformation, *i.e.*, from  $\xi = 0$  to  $\xi = 1$ . In reality, the value of  $\Delta G_m$  varied by a maximum of about 7–8% of its initial value with  $\xi$  for the alloys considered. The neglect of this small variation is not expected to introduce any serious error in the calculations. With this assumption, equation 6.11 can be integrated analytically to give

$$\beta t^2 \nu \exp(-G^*/RT) + 2t + (C/\nu) \exp(G^*/RT) \ln(1 - \xi) = 0 \quad (6.14)$$

where the constant  $C$  is

$$C = \frac{2\theta_b \bar{L}}{a_b^3 B_3''} \quad \text{and} \quad B_3'' = \alpha_p B_3' \quad (6.15)$$

Equation 6.14 can be solved to give

$$t = \frac{-1 + \sqrt{1 - C\beta \ln(1 - \xi)}}{\beta \nu \exp(-G^*/RT)} \quad (6.16)$$

The second root of equation 6.14 was neglected because it gives a negative value of  $t$ .

#### 6.3.4 Optimisation of the Model

The new model also has four empirical constants,  $B_3''$ ,  $B_4$ ,  $\lambda_1$  and  $\lambda_2$ . Optimisation of the model was carried out to find the best fit values of these constants. The isothermal transformation data already available for steels in Tables 2.1 and 2.3 were used for the purpose. As in the earlier work of Rees and Bhadeshia, optimisation involved the minimisation of a prediction error represented by  $\sum [\ln(t_p) - \ln(t_m)]^2$ , where  $t_p$  and  $t_m$  denote the predicted and the measured reaction times respectively.

The degree of agreement between the experimental and predicted reaction times for the alloys in Tables 2.1 and 2.3 optimised separately and together is shown in Figure 6.4. While the agreement is excellent for Bhadeshia alloys (Table 2.1), it is not so good for Chang's alloys (Table 2.3). Nevertheless, the mean prediction error (prediction error/number of observations) for Chang's alloys showed marked improvement from 1.224 for the old model to 0.811 for the new model. The corresponding improvement for the Bhadeshia alloys was marginal, from 0.101 to 0.093. The composition of the Chang's alloys varies over a wider range. The discrepancy between the experimental and measured times may arise because of the simplistic assumption that the bainite plate thickness to radius ratio is constant for all alloys at all the temperatures. In the case of martensite, the plate thickness to radius ratio is found to vary with the extent of

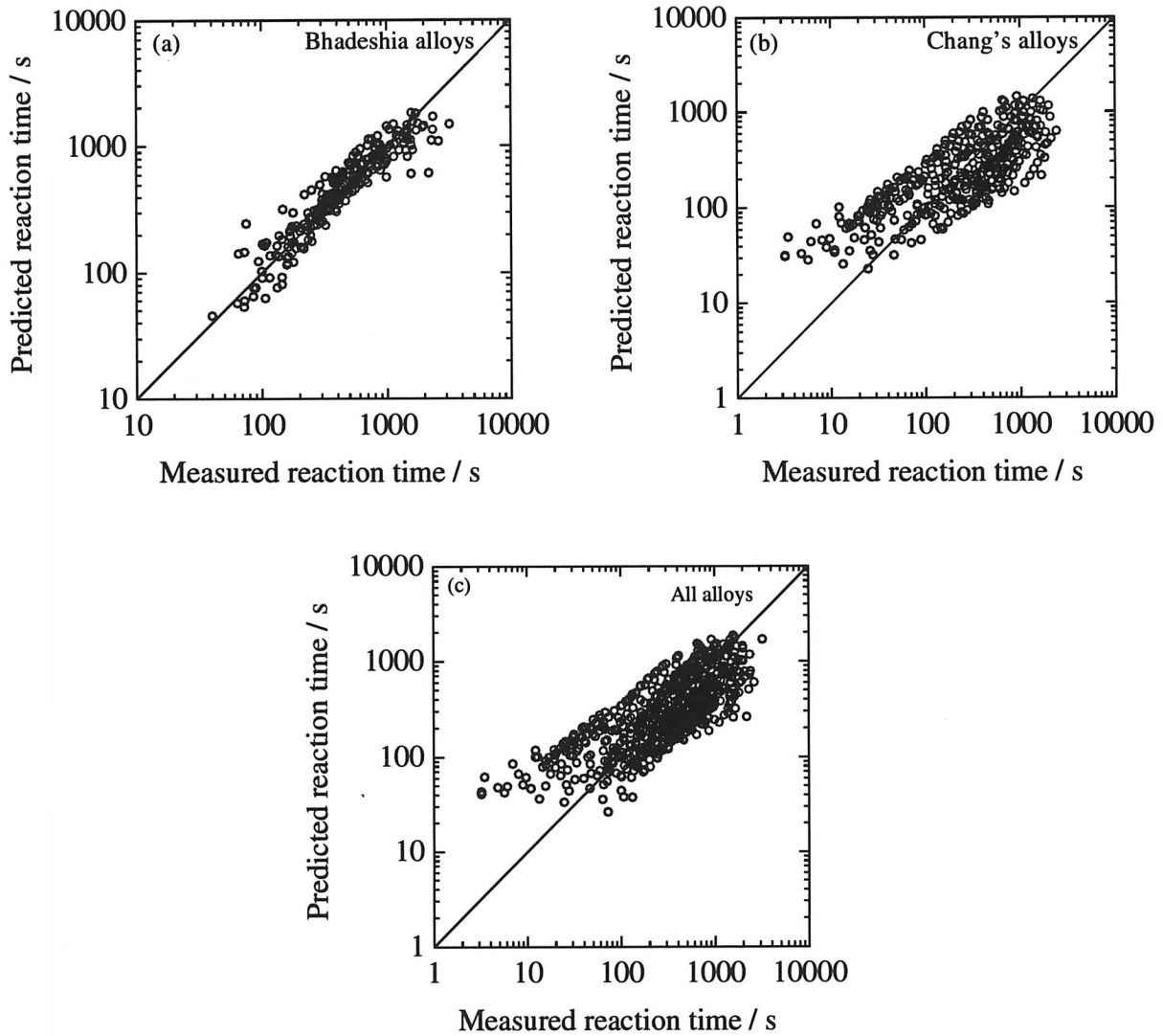


Figure 6.4: Level of agreement between the experimental and predicted reaction times when optimisation was carried out with (a) Bhadeshia alloys (Table 2.1) (b) Chang's alloys (Table 2.3) and (c) all these alloys taken together.

the transformation during isothermal treatment [Ghosh and Raghavan, 1986]. Such variation, if any, has not been allowed for in the present model.

The best fit values of the constants for individual alloys as well as for all the alloys taken together are shown in Table 6.1. Though  $B_3''$  varies somewhat, unlike the previous work, the value of  $B_4$  is found to be nearly constant for all the alloys. The autocatalysis factor varied from 1.4 to 3.5 which is compatible with the observed sheaf microstructure. The value of  $\beta$  for the individual alloys is also consistent with the assumption that autocatalysis is difficult in higher carbon steels. Figure 6.5 shows a plot of the optimum values of  $\beta$  for the individual alloys. The equation of the best fit line through these points is:

$$\beta = -102.43 \bar{x} + 3.8 \quad (6.17)$$

Comparing equation 6.17 with equation 6.4, the values of  $\lambda_1$  and  $\lambda_2$  can be calculated to be 3.8 and 26.96 respectively. In close agreement with this, the best fit values of  $\lambda_1$  and  $\lambda_2$  after considering all the alloys together are 4.9 and 45.16 respectively (Table 6.1).

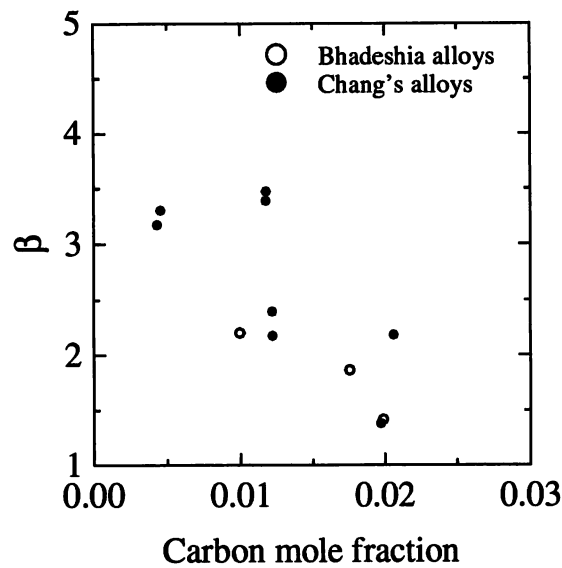


Figure 6.5: The variation of the autocatalysis factor ( $\beta$ ) of the individual steels with their carbon content after optimisation of the new model.

Dataset	$B_3'', \text{ m}^{-2}$	$B_4, \text{ J mol}^{-1}$	$\lambda_1$	$\lambda_2$
Fe-Mn-Si-C	$3.845 \times 10^{-25}$	$4.469 \times 10^4$	2.203	0.00
Fe-Ni-Si-C	$1.945 \times 10^{-22}$	$8.407 \times 10^4$	1.865	0.00
300 M	$2.432 \times 10^{-23}$	$7.147 \times 10^4$	1.416	0.00
A	$4.746 \times 10^{-23}$	$7.269 \times 10^4$	2.394	0.00
B	$5.574 \times 10^{-23}$	$6.721 \times 10^4$	2.177	0.00
C	$1.675 \times 10^{-26}$	$1.633 \times 10^4$	2.184	0.00
D	$6.063 \times 10^{-26}$	$3.832 \times 10^4$	1.379	0.00
E	$5.283 \times 10^{-23}$	$4.858 \times 10^4$	3.305	0.00
F	$3.615 \times 10^{-22}$	$6.357 \times 10^4$	3.475	0.00
G	$2.860 \times 10^{-23}$	$6.128 \times 10^4$	3.389	0.00
H	$1.049 \times 10^{-22}$	$5.474 \times 10^4$	3.174	0.00
Combined data	$3.845 \times 10^{-25}$	$3.805 \times 10^4$	4.932	45.158

Table 6.1: The best fit values of the empirical constants after optimisation of the new model.

### 6.3.5 Validation of the Model

In this work, the isothermal bainite transformation kinetics of an Fe-0.12C-2.03Si-2.96Mn (wt.%) alloy was measured at four temperatures after austenitisation at 1200 °C for 180 s. The austenite grain size was  $135 \pm 11 \mu\text{m}$ . Other details are given in chapter eight. The measured reaction time for a given volume fraction is compared with the corresponding predicted value in Figure 6.6. The agreement is reasonably good. For comparison, the predictions of the old model are also given in Figure 6.6. It is clear that the predictions of the new model are in better agreement with the experiments.

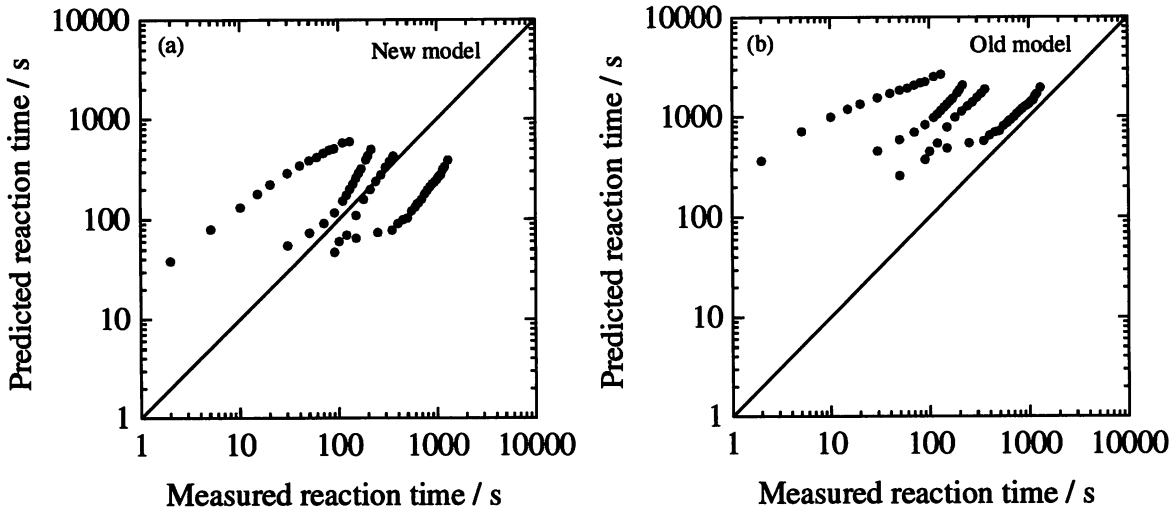


Figure 6.6: Comparison of the experimental and predicted bainite transformation kinetics of an Fe-0.12C-2.03Si-2.96Mn (wt.%) alloy. Austenitisation was carried out at 1200 °C for 180 s; the austenite grain size was  $135 \pm 11 \mu\text{m}$ .

The model was subjected to further interrogation to ensure that it can reproduce some of the known trends. A decrease in transformation temperature accelerates the transformation [e.g., Bhadeshia, 1982a]. On the other hand, enriching the steel with some alloying additions retards the kinetics. As shown in Figure 6.7, the present model correctly reproduces both these effects. Addition of Mn to a leaner alloy slows down the bainite transformation.

## 6.4 Conclusions

An existing model for bainite transformation kinetics has been modified. The bainite plate thickness, as calculated using a neural network model was an input to the kinetics model. The autocatalytic nucleation of ferrite plates is modelled in a way which is consistent with the observed sheaf microstructure. These modifications led to some improvement over the previous model.

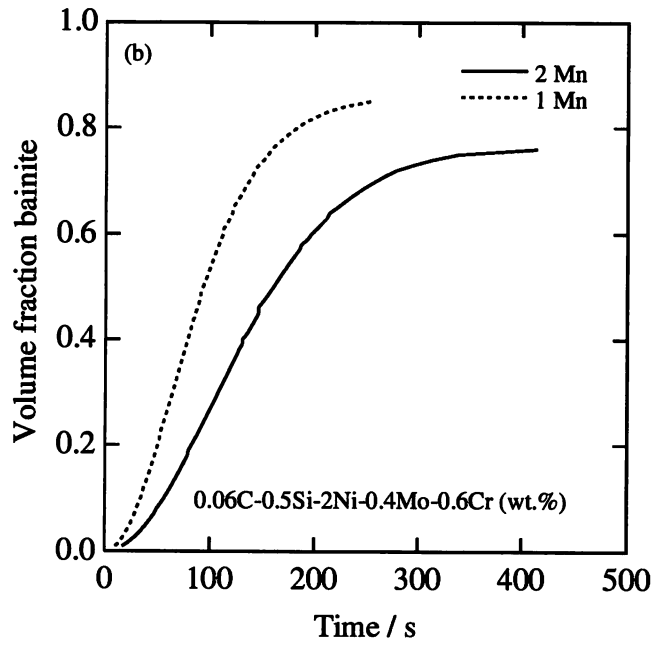
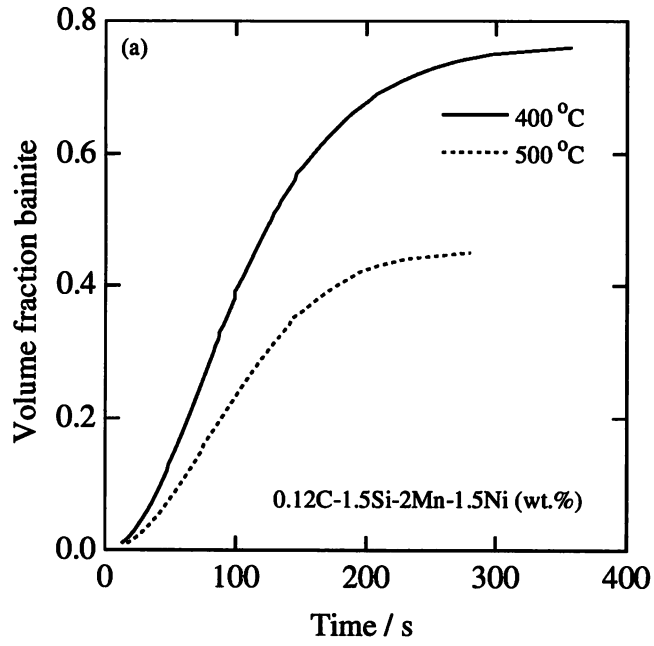


Figure 6.7: The influence of (a) reaction temperature and (b) Mn addition on the predicted bainite transformation kinetics. The initial austenite grain was taken to be  $50 \mu\text{m}$  in both the cases. The results highlight the ability of the model to correctly predict the trends expected with respect to the effect of temperature and Mn addition.

## Chapter Seven

# Kinetics of the Bainite Transformation

## Part 2: Effect of Austenite Grain Size

### 7.1 Introduction

Bainite is known to nucleate on austenite grain boundaries. It is therefore to be expected that the austenite grain size will have an effect on its transformation kinetics. However, autocatalytic nucleation of bainite also plays an important role in the overall transformation kinetics. Hence the role of austenite grain boundaries may not be as significant as in the case of allotriomorphic ferrite and pearlite. This is often cited as the reason why elements like boron, which segregate to the austenite grain boundaries, have little influence on bainite transformation even though they greatly retard the allotriomorphic ferrite transformation [Irvine *et al.*, 1957; Pickering, 1978].

Conflicting results on the effect of austenite grain size on the rate of bainite transformation are reported in literature. In some cases, interpretation is made difficult by the presence of undissolved carbide particles, quenching stresses *etc.* Davenport *et al.* [1941] found no change in the rate of bainite transformation of a 0.37C–0.77Mn–0.98Cr (wt.%) steel when the austenite grain size was varied from ASTM 7–8 to 2–3. Graham and Axon [1959] have reported that when the austenitisation treatment is long enough to dissolve all the carbides, an increase in the grain size lowers the incubation period for the formation of lower bainite in a Fe–0.97C wt.% alloy. The time required for the transformation to reach completion was unaffected. By contrast, other investigators have observed a deceleration in the rate of bainite transformation with an increase in the austenite grain size. Thus, Barford and Owen [1961] discovered that the time to form up to 25% of upper or lower bainite is directly proportional to the grain diameter. No measurements were made for higher volume fractions. Similarly, Ali [1991] found an acceleration in the rate of transformation as the austenitising temperature was reduced. In one case in that study, the austenitising temperature had little effect on the bainite kinetics. It was suggested that the rate of reaction was so rapid that the grain size effect could not be resolved experimentally.

While all the results discussed so far focus on the effect of grain size on the reaction kinetics at a given temperature, no data are available for its influence on the  $B_S$  temperature as defined in chapter two and this was the purpose of the work reported in the present chapter.



## 7.2 Nucleation Rate

In the last chapter, the bainite nucleation rate was expressed as (equations 6.2 and 6.12):

$$I = \frac{B'_3}{\bar{L}} \frac{k_B T}{h} \exp \left\{ -\frac{B_4}{RT} - \frac{B_4 \Delta G_m}{B_2 RT} \right\} \quad (7.1)$$

Clearly, the nucleation rate depends on the austenite grain size. Moreover, at  $T = T_h$ ,  $\Delta G_m = G_N = B_1 T_h - B_2$ , the nucleation rate at  $T_h$  can thus be written as:

$$I_{T_h} = \frac{B'_3}{\bar{L}} \frac{k_B T_h}{h} \exp \left\{ -\frac{B_4 B_1}{R B_2} \right\} \quad (7.2)$$

For  $I_{T_h}$  to be constant [Bhadeshia, 1981],  $T_h$  must depend on  $\bar{L}$ , the austenite grain size. We now present some experimental evidence for the effect of grain size on bainite-start temperature, *i.e.*, when  $T_h = B_S$ .

## 7.3 The Choice of Steel

Some care has to be exercised when selecting a steel for this study. The steel should not contain carbide forming elements such as Cr, Mo, *etc.* to avoid any complications arising out of undissolved carbides. It should have a high Si concentration to prevent the precipitation of cementite during the bainite transformation. To reveal the effect of grain size, the composition of the steel should be such that the bainite-start temperature ( $B_S$ ) is controlled by nucleation rather than by growth.

Considering these factors, a steel with composition (wt.%) Fe-0.27C-2.01Si-2.16Mn-2.07Ni was selected for the study. The calculated thermodynamic parameters, driving force for nucleation ( $\Delta G_m$ ) and for diffusionless growth ( $\Delta G^{\gamma \rightarrow \alpha}$ ) together with the  $G_N$  function, are plotted in Figure 7.1 [Bhadeshia and Edmonds, 1980; Bhadeshia, 1982b]. Though the growth of bainite becomes feasible at 456 °C, nucleation is not possible above 418 °C which is therefore identified as the nucleation limited bainite-start temperature ( $T_h$  or  $B_S$ ) for this steel. The calculated TTT diagram shown in Figure 7.2 indicates that the alloy has adequate hardenability to prevent allotriomorphic ferrite or pearlite.

## 7.4 Measurement of $B_S$

### 7.4.1 Experiments

Samples 8 mm diameter and 12 mm in length were machined from rolled plates of the above steel. They were sealed in a quartz tube with a partial pressure of pure argon and homogenised at 1200 °C for two days before quenching in water.

Experiments were carried out in a *Thermecmator Z* thermomechanical simulator with an attached laser dilatometer to monitor the diameter change. The details of the experimental technique are given in the next chapter. The samples were induction heated at 10 °C s<sup>-1</sup> to the austenitising temperature. Two austenitising treatments, 3 minutes at 950 °C and 15 minutes at 1300 °C, were carried out to yield widely different austenite grain sizes. After

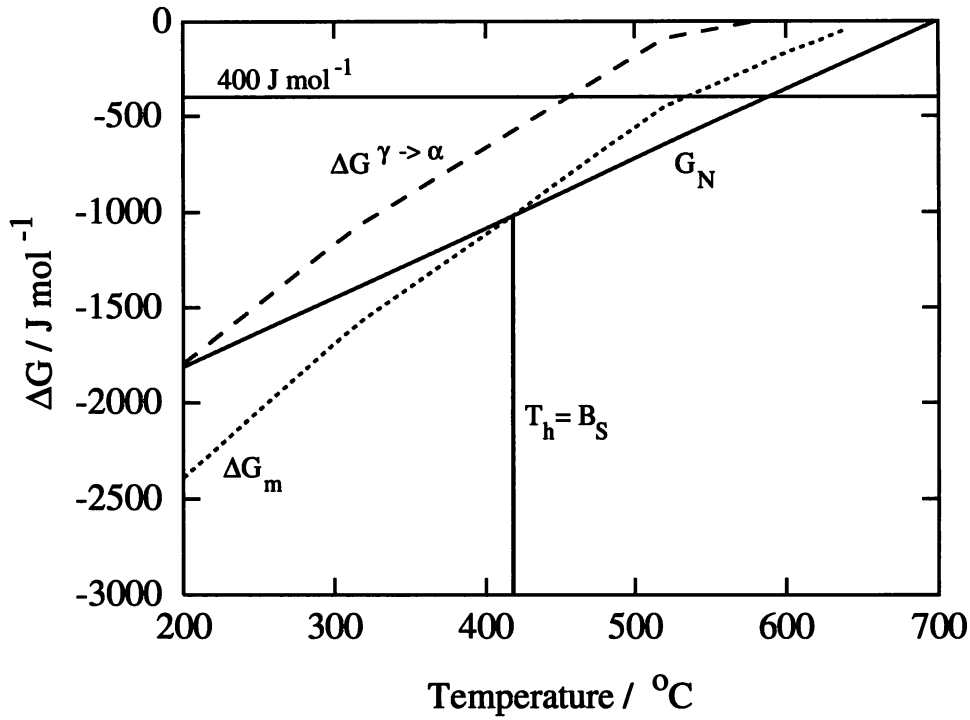


Figure 7.1: The calculated thermodynamic parameters of the Fe-0.27C-2.01Si-2.16Mn-2.07Ni (wt.%) alloy used in this study [Bhadeshia and Edmonds, 1980; Bhadeshia, 1982b].

austenitisation, the samples were cooled rapidly to 500 °C to prevent any high temperature transformation products. The cooling was continued at a much slower rate from 500 °C to the end of transformation. The cooling rate was varied from 0.2 °C s<sup>-1</sup> to 0.05 °C s<sup>-1</sup> in this temperature range. The heat treatment is illustrated in Figure 7.3.

#### 7.4.2 Results

The dilatometric curves for the two austenitising heat treatments are shown in Figure 7.4. The austenite grain size for 1300 °C austenitisation was measured to be 268±26 μm and that for the 950 °C austenitisation was 47±6 μm. It was confirmed that the microstructure consisted of bainite in all the cases. No high temperature transformation products were observed. The transformation-start temperatures on these dilatometric curves therefore correspond to the beginning of the bainite reaction. As examples, the microstructures of the samples cooled at 0.1 °C s<sup>-1</sup> after the two austenitising treatments are shown in Figure 7.5.

The measured transformation-start temperatures as a function of the cooling rate for the two conditions are plotted in Figure 7.6. An increase in the austenitising temperature led to a decrease in the transformation-start temperature at all the cooling rates. For austenitisation at 950 °C, the transformation-start temperature was almost the same at both the cooling rates. The corresponding  $T_h$  temperature can be taken to be 462 °C. On the other hand, the transformation-start temperature showed a small variation with the cooling rate for the high temperature austenitisation. The temperature increased slightly on slowing down the cooling

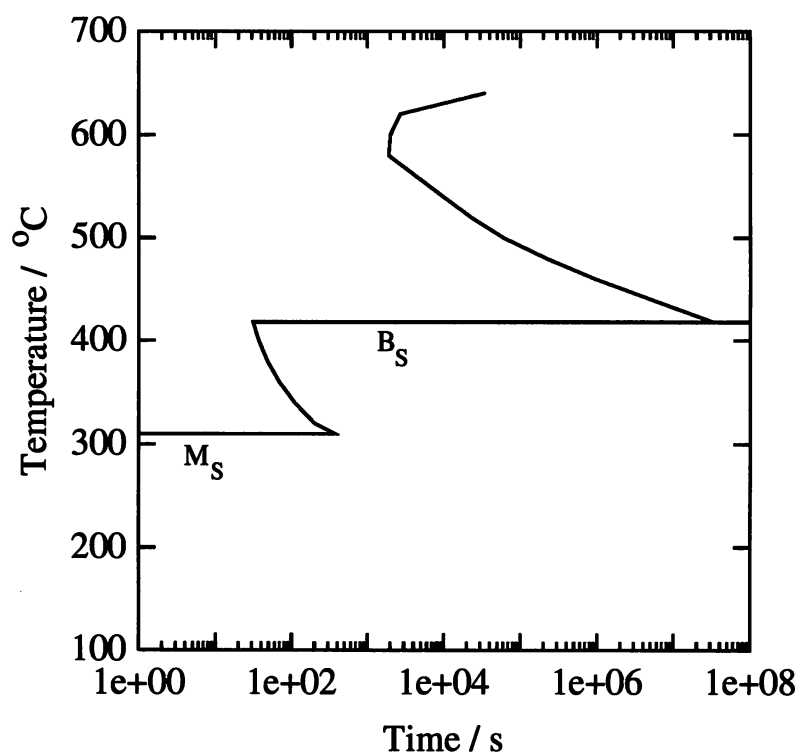


Figure 7.2: The calculated TTT diagram of the alloy Fe-0.27C-2.01Si-2.16Mn-2.07Ni (wt.%), [Bhadeshia, 1982b].

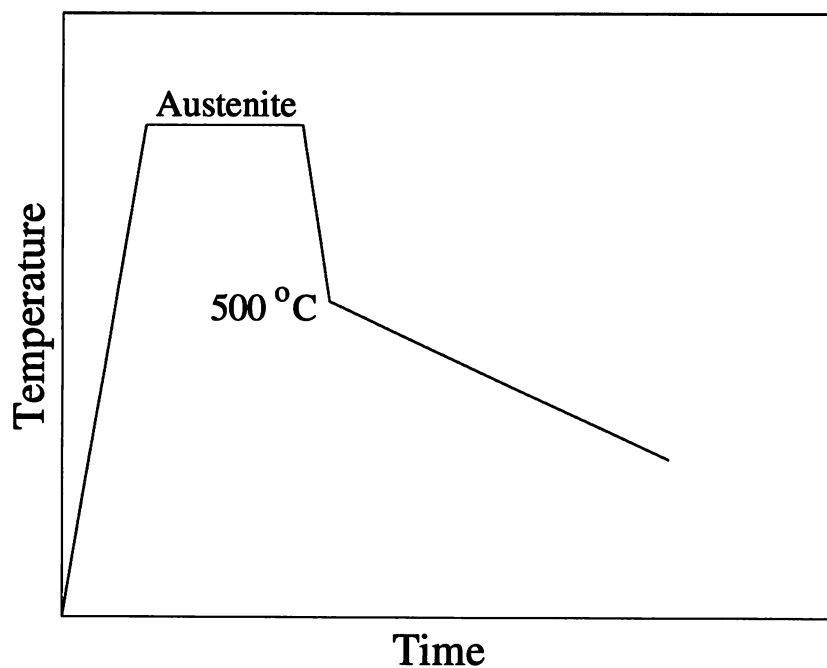


Figure 7.3: Schematic illustration of the heat treatment cycle. Austenitisation was carried out either at 950 °C for 3 minutes or at 1300 °C for 15 minutes.

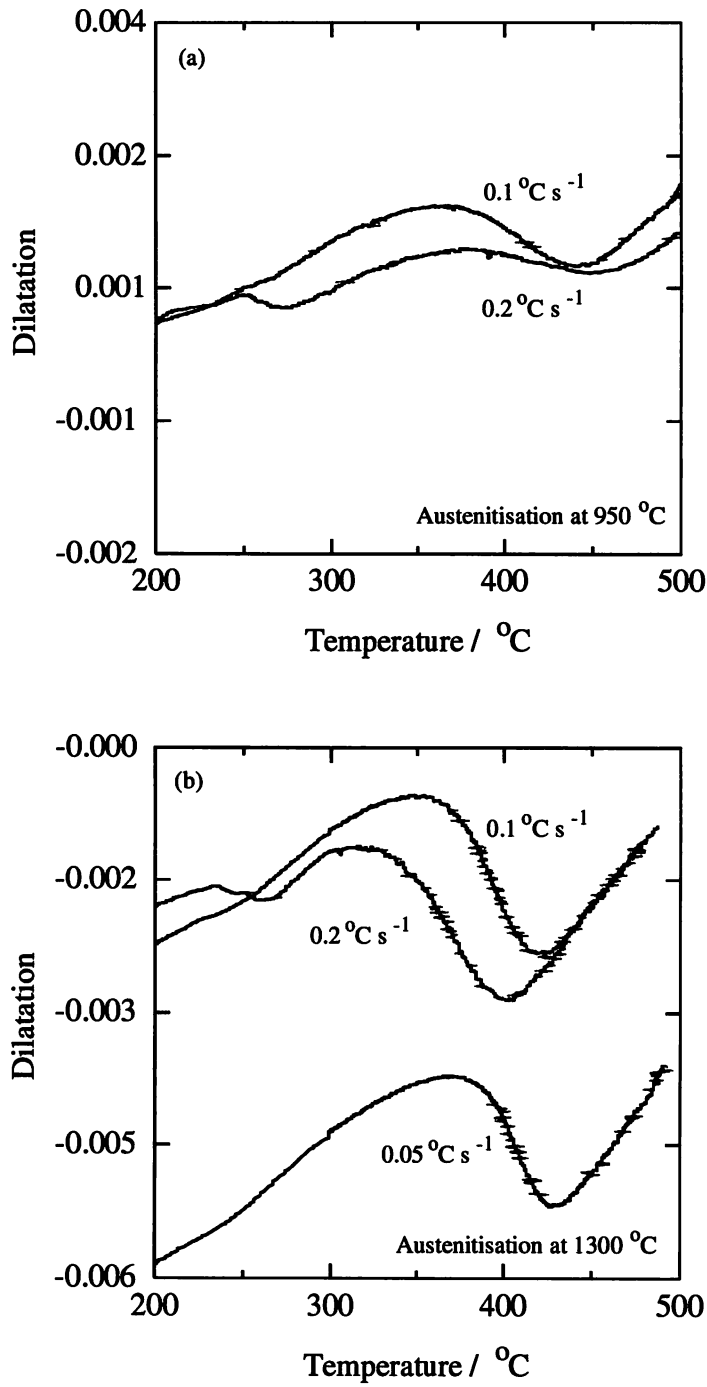
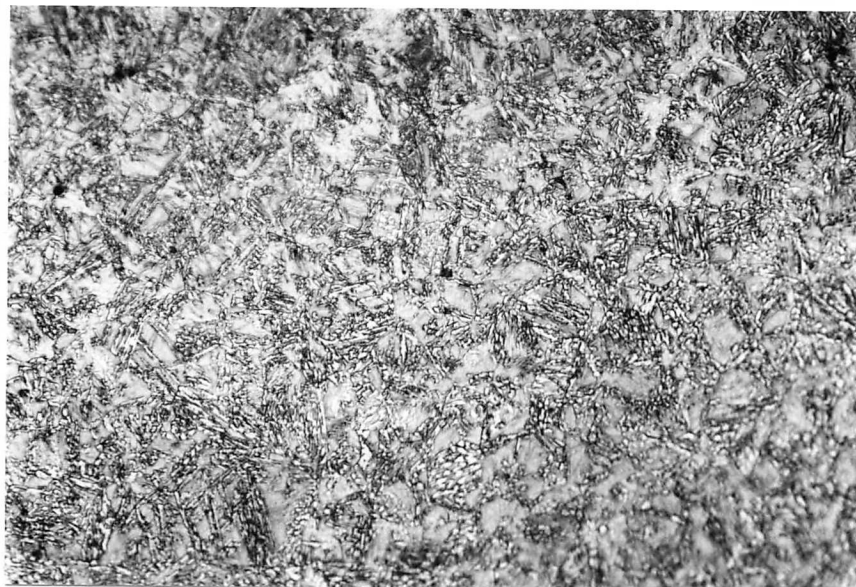


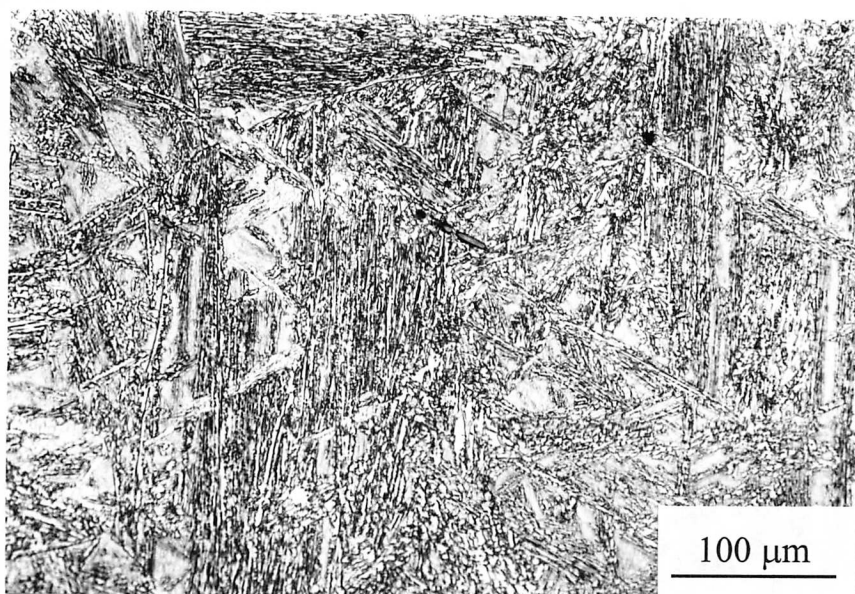
Figure 7.4: The dilatation curves at different cooling rates for the two austenitising conditions, (a) 950 °C for 3 minutes and (b) 1300 °C for 15 minutes.

rate from 0.2 °C s<sup>-1</sup> to 0.1 °C s<sup>-1</sup>, but a further decrease in the cooling rate to 0.05 °C s<sup>-1</sup> did not alter the transformation-start temperature. This temperature, namely 433 °C, can be taken as the  $T_h$  temperature for 1300 °C austenitising heat treatment.

From the above results it can be inferred that, as predicted, the  $T_h$  temperature for bainite transformation does depend on the austenite grain size.



d



b

Figure 7.5: The bainitic microstructure at a cooling rate of  $0.1^{\circ}\text{C s}^{-1}$ . Austenitisation was done at (a)  $950^{\circ}\text{C}$  for 3 minutes and (b)  $1300^{\circ}\text{C}$  for 15 minutes.

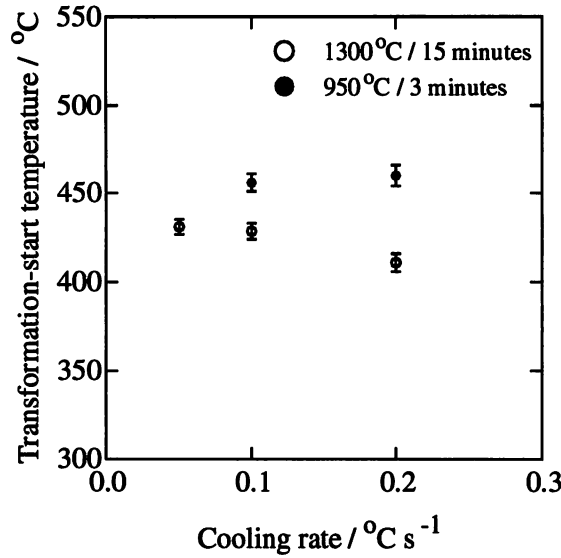


Figure 7.6: The measured transformation–start temperature at different cooling rates under the two austenitising conditions.

## 7.5 Analysis of Steven and Haynes data

Further evidence for the influence of the austenite grain size on the  $T_h$  temperature was obtained by reanalysing the Steven and Haynes [1959] data. A plot of the calculated free energy change associated with paraequilibrium nucleation at the measured start temperature  $T_h$  was given in chapter two and is reproduced here in Figure 7.7. Each point represents a unique steel composition. The plot shows considerable scatter, the maximum deviation from the fitted  $G_N$  line being  $\pm 30^\circ\text{C}$ . It was believed that some of this might be explained by the variation in the starting austenite grain size for these measurements. The data are therefore plotted in Figure 7.8 by segregating them according to the initial austenite grain sizes.

Precise measurements of the austenite grain size were not done in the study of Steven and Haynes. The data are divided into two sets according to the available ASTM grain size numbers. In one group, all steels with initial grain sizes ASTM 6–7, 6–8 and ASTM 7 are considered whereas in the other group all data with grain sizes ASTM 8 and ASTM 8–9 are treated together. Linear regression analysis was performed on each set of data, fitting an equation of the form  $G_N = B_1 T - B_2$ . The values of the constants  $B_1$  and  $B_2$  with  $T$  expressed in  $^\circ\text{C}$  together with the correlation coefficients  $r^2$  are given in Table 7.1. For comparison, the values of these constants when all the grain sizes are considered together are also given in Table 7.1.

Separating the Steven and Haynes data into two groups according to grain size gives a better linear fit (the correlation coefficient improves, Table 7.1). This indicates that the free energy change at which the nucleation rate becomes detectable depends on the grain boundary area and complements the earlier conclusion that the  $T_h$  temperature should depend on the austenite grain size. At low temperatures, the  $G_N$  for the coarse grains lies below that for the

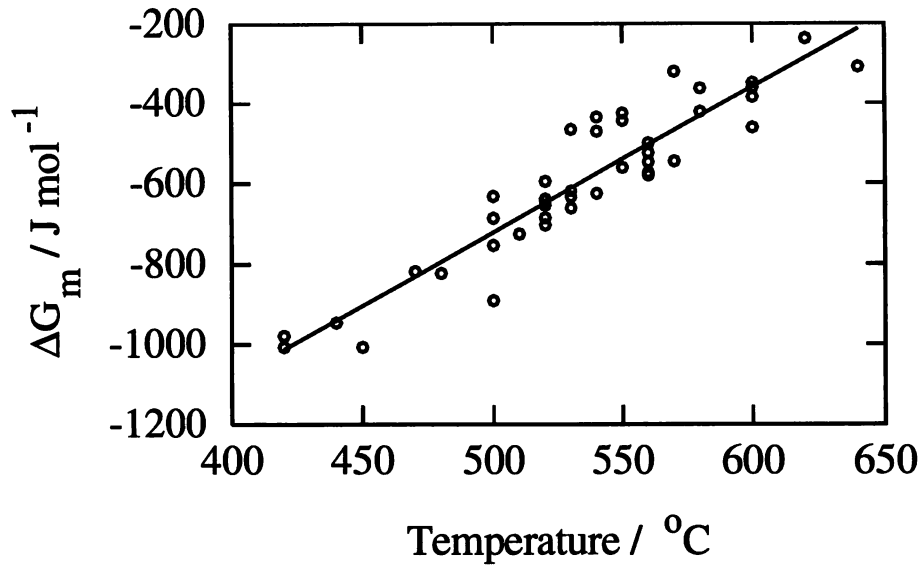


Figure 7.7: The driving force for paraequilibrium nucleation of ferrite ( $\Delta G_m$ ) for a variety of steels at their respective  $T_h$  temperatures [Bhadeshia, 1981].

fine grains, signifying that for a coarse grain size a greater free energy change is required to achieve an appreciable nucleation rate. It should be noted that although separation of the data into the grain size ranges is convincing, the scatter is significantly large to cause an overlap at temperatures above 468 °C.

Grain size ASTM no.	$B_1$ J mol <sup>-1</sup> K <sup>-1</sup>	$B_2$ J mol <sup>-1</sup>	$r^2$
6-7, 7, 6-8	3.676 ±0.3	2542 ±171	0.882
8, 8-9	3.099 ±0.2	2272 ±161	0.934
All	3.637 ±0.2	2540 ±120	0.865

Table 7.1: The values of the coefficients in the  $G_N$  function. The regression analysis was performed by separating the Steven and Haynes data into two groups of coarse and fine grain sizes as well as on all the data taken together. The standard errors of the coefficients are also given.

## 7.6 Reformulation of $G_N$

The above results warrant a modification of  $G_N$ , the universal nucleation function. It was argued earlier that the top of the lower C-curve of the TTT diagram is controlled by nucleation. The corresponding temperature,  $T_h$ , was identified as the temperature at which the nucleation rate of Widmanstätten ferrite or bainite becomes detectable. It was shown that at  $T_h$ ,  $\Delta G_m = G_N$ . Since  $T_h$  depends on the austenite grain size, the  $G_N$  should also be a function of the

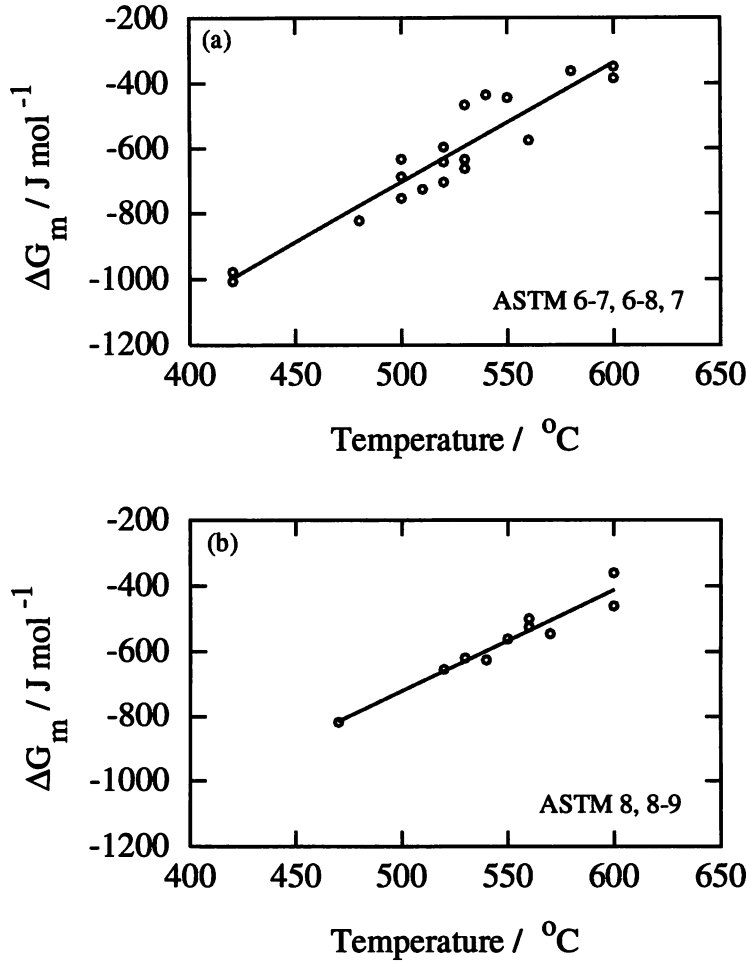


Figure 7.8: Effect of grain size on the universal nucleation function  $G_N$ . The Steven and Haynes data [1959] were separated into two groups according to the initial austenite grain size.

austenite grain size. This is equivalent to saying that the free energy change necessary before a detectable rate of nucleation can be obtained depends on the total austenite grain boundary area available for nucleation; a higher driving force should be required for a coarser grain size.

In the original Rees and Bhadeshia model, the pre-exponential term,  $B_3$ , in the nucleation rate equation was taken to be independent of temperature (equations 2.14 and 2.15). In classical nucleation theory, this term includes a frequency factor term which in turn depends on temperature (equations 2.2 and 6.2). Thus at a constant grain size,  $I_{T_h}$  is proportional to the  $T_h$  temperature (equation 7.2). This requires further modification of  $G_N$  to include an additional temperature term so that  $I_{T_h}$  becomes independent of  $T_h$ .



### 7.6.1 New $G_N$

In view of the above results,  $G_N$  was rewritten as:

$$G_N = C_1 T \ln \left\{ \frac{C_2 \bar{L}}{T} \right\} - C_3 \quad (7.3)$$

where  $C_1, C_2$  and  $C_3$  are the new constants. Following the same procedure as in section 2.2 (equations 2.2 through 2.5), it can be shown that the form of  $G_N$  is consistent with the theory of martensite nucleation. The nucleation rate  $I$  is related to the austenite grain size  $\bar{L}$ , the frequency factor  $\nu = k_B T/h$  and the activation energy  $G^*$ :

$$I \propto \frac{1}{\bar{L}} \frac{k_B T}{h} \exp\{-G^*/RT\} \quad (7.4)$$

Equation 7.4 can be written as

$$-G^* \propto T \ln \left( \frac{I \bar{L} h}{k_B T} \right) \quad (7.5)$$

At  $T = T_h$ ,  $I = I_{T_h}$ , which is a constant. This gives

$$-G^* \propto T_h \ln \left( \frac{B \bar{L}}{T_h} \right) \quad \text{where} \quad B = I_{T_h} h / k_B \quad (7.6)$$

Widmanstätten ferrite and bainite nucleate by a mechanism which is similar to that of martensite; the activation energy for nucleation is directly proportional to the available driving force [Magee, 1970; Raghavan and Cohen, 1971; Olson and Cohen, 1976]:

$$-G^* \propto \Delta G_m \quad (7.7)$$

Combining equation 7.7 with equation 7.6, we get

$$\Delta G_m \propto T_h \ln \left( \frac{B \bar{L}}{T_h} \right) \quad (7.8)$$

At  $T_h$ ,  $\Delta G_m = G_N$ , therefore we can write:

$$G_N \propto T_h \ln \left( \frac{B \bar{L}}{T_h} \right) \quad (7.9)$$

which justifies the form of new  $G_N$  in equation 7.3.

Similarly, it can be shown that the ratio of the ferrite nucleation rates of two steels A and B at their respective  $T_h$  temperatures,  $T_h^A$  and  $T_h^B$ , is (section 2.2):

$$\frac{I_{T_h^A}}{I_{T_h^B}} = \frac{T_h^A}{T_h^B} \frac{\bar{L}_B}{\bar{L}_A} \exp \left\{ \frac{(B_4 - C_3 B_5) (T_h^A - T_h^B) - B_5 C_1 T_h^A T_h^B \ln (T_h^B \bar{L}_A / T_h^A \bar{L}_B)}{R T_h^A T_h^B} \right\} \quad (7.10)$$

where  $\bar{L}_A$  and  $\bar{L}_B$  are the initial austenite grain sizes of the alloys A and B respectively.

The condition  $I_{T_h^A} = I_{T_h^B} = I_{T_h}$  can be satisfied if  $B_4 = C_3 \times B_5$  and  $B_5 \times C_1 = -R$ . The new  $G_N$  function is now consistent with the original assumption that the ferrite nucleation

rate at  $T_h$  temperature is independent of alloy composition, the austenite grain size as well as the  $T_h$  temperature.

### 7.6.2 Estimation of the New Constants

The precise determination of the constants  $C_1$ ,  $C_2$  and  $C_3$  requires extensive experiments much like the ones reported by Steven and Haynes [1959] but where the initial austenite grain size is also varied systematically. In the absence of such results,  $C_1$  and  $C_3$  were calculated at first by ignoring the grain size effect.  $G_N$  was written as a function of temperature only

$$G_N = C_1 T \ln(1/T) - C_3 \tag{7.11}$$

As before, the transformation–start temperatures ( $T_h$ ) measured by Steven and Haynes [1959] were used for fitting the above function. The free energy change accompanying ferrite nucleation with paraequilibrium carbon partitioning was calculated for each  $T_h$  temperature [Bhadeshia, 1982b]. The result is shown in Figure 7.9. Expressing  $T$  in °C, the values of  $C_1$  and  $C_3$  were found to be -0.50065 and 2278 respectively. The correlation coefficient ( $r^2$ ) was 0.865 which is same as when  $G_N = B_1 T - B_2$  was fitted to the data (Table 7.1).

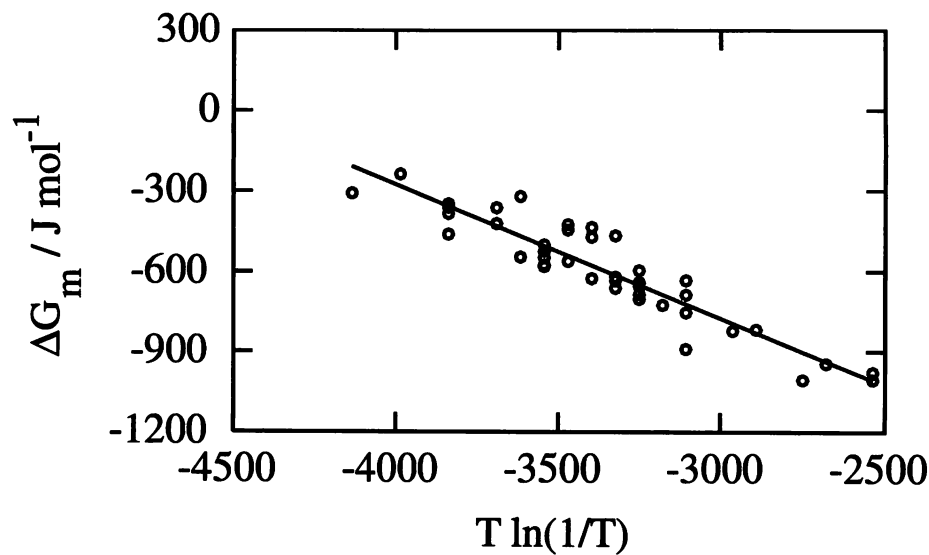


Figure 7.9: Fitting the Steven and Haynes data to the new nucleation function,  $G_N$ . The effect of grain size on  $G_N$  was ignored. The temperature is in °C.

A rough estimate of  $C_2$  together with  $C_1$  and  $C_3$  can be done if the initial austenite grain size for the Steven and Haynes measurements is taken into account. For the sake of simplicity, the austenite grain size was assumed to be ASTM 7 (nominal grain diameter = 32  $\mu\text{m}$ ) in all the cases. As in the last chapter, the constants were determined by optimisation. The error term was expressed as the square of the difference between the calculated and the predicted values of the nucleation free energy,  $(\Delta G_m - G_N)^2$ . Iteration was stopped when no appreciable

improvement in the error term could be achieved. With  $T$  in °C and grain size  $\bar{L}$  in  $\mu\text{m}$ , the optimum values of the constants  $C_1$ ,  $C_2$  and  $C_3$  were found to be -0.471065, 0.02136 and 2275 respectively. The correlation coefficient ( $r^2$ ) was calculated to be 0.865. The values of  $C_1$  and  $C_3$  thus calculated are similar to the ones when the grain size effect on  $G_N$  is ignored (equation 7.11).

#### 7.6.2.1 Evaluation of $B_4$

In chapter six, the constant  $B_4$  was calculated empirically by optimising the bainite kinetics model with the experimental transformation kinetics data. When all the steels were considered together its value was found to be  $3.805 \times 10^4$ . It can now be calculated from the constants in the new  $G_N$  function. Earlier it was shown that  $B_4 = C_3 \times B_5$  and  $B_5 \times C_1 = -R$ ; these conditions hold even if the  $G_N$  is written as a function of temperature only as in equation 7.11. Using  $C_1 = -0.50065$  and  $C_3 = 2278$  gives  $B_5 = 16.606$  and  $B_4 = 3.783 \times 10^4$ . The two values of  $B_4$  (calculated from optimising the bainite kinetics model in chapter six and calculated from the new  $G_N$ ) are in excellent agreement.

Alternatively, the nucleation rate can be written as

$$I = \frac{B'_3}{\bar{L}} \frac{k_B T}{h} \exp \left\{ \frac{C_3 + \Delta G_m}{C_1 T} \right\} \quad (7.12)$$

so that the equation does not have the additional empirical constant  $B_4$ .

## 7.7 Conclusions

It has been argued that the temperature corresponding to the top of the lower C-curve of the TTT diagram which gives the Widmanstätten ferrite or the bainite transformation–start temperature ( $T_h$ ) should depend on the austenite grain size. This has been experimentally proved for bainite transformation taking the example of an Fe-0.27C-2.01Si-2.16Mn-2.07Ni (wt.%) alloy. Further evidence has been provided by analysing the data reported in literature. The universal nucleation function  $G_N$  has been modified in the light of this result. The function now takes into account the grain size effect. The dependence of  $G_N$  on temperature has also been modified.

With the new  $G_N$  function, the number of empirical constants in the bainite kinetics model described in chapter six can be reduced from 4 to 3.

## Chapter Eight

# Deformation-induced Stabilisation of Austenite Against Bainite Transformation

Experiments have been carried out to study the effect of plastic deformation on the transformation of austenite to bainite. The results have been interpreted by modifying the kinetic theory to take account of mechanical stabilisation and other effects associated with deformation defects in the austenite.

### 8.1 Experimental Procedure

The alloy used for this work was Fe-0.12C-2.03Si-2.96Mn (wt.%), where the silicon suppresses the precipitation of cementite from austenite. Carbide-free upper bainite can therefore be obtained, allowing the observation of transformation without interference from subsidiary reactions.

Cylindrical samples (8 mm diameter, 12 mm length) were machined from the alloy after homogenisation at 1200 °C for two days whilst sealed in a quartz tube containing pure argon. These samples are suitable for experiments using an adapted *Thermecmator Z* thermomechanical simulator (Figure 8.1). The machine is capable of performing a large variety of thermal and/or mechanical cycles which can be pre-programmed. The sample temperature is monitored using a spot-welded Pt-PtRh (type *R*) thermocouple. The samples were induction heated to 1200 °C at 10 °C s<sup>-1</sup> in a vacuum ( $4 \times 10^{-2}$  mbar) and held there for 180 s before cooling to the deformation temperature at 25 °C s<sup>-1</sup>. The samples were then deformed in compression to a predetermined strain at an average strain rate of 1 s<sup>-1</sup>. They were then cooled rapidly to a selected isothermal transformation temperature as illustrated in Figure 8.2 using helium as the quenching gas. The alloy has sufficient hardenability to avoid any transformation before this isothermal treatment. A number of strains and isothermal transformation temperatures were studied. The isothermal transformation was allowed to progress without any externally applied stress. The specimens were finally helium-quenched to ambient temperature after the completion of isothermal transformation to bainite.

The sample temperature, diameter and the load were measured and stored as a function of time using a data acquisition system. A laser transducer having an accuracy of  $\pm 1 \mu\text{m}$  was used for diameter measurement.

The compression of cylindrical samples tends to be inhomogeneous, as described elsewhere in detail [Shipway and Bhadeshia, 1995a]. In the present study, thin mica sheets were used at

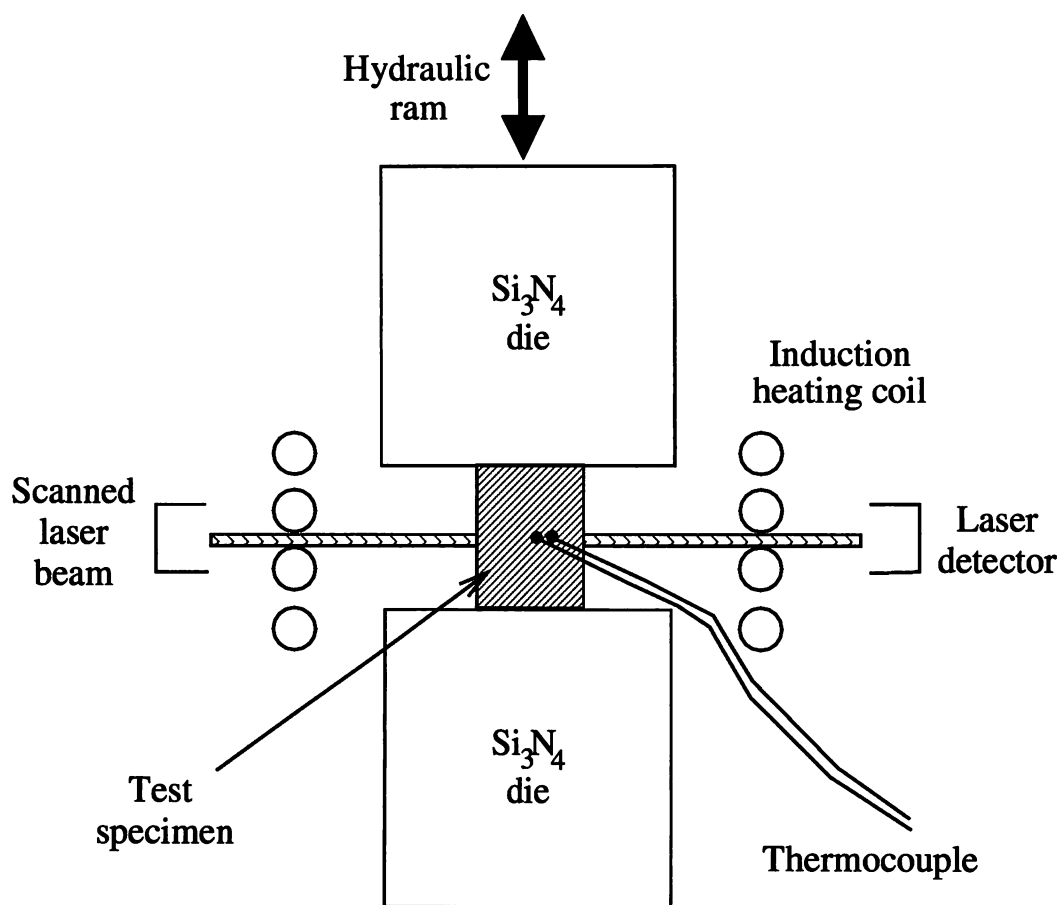


Figure 8.1: A schematic diagram of the *Thermecmaster Z* specimen chamber, after Parker [1997].

the sample/die interface to minimise barrelling. The dilatometric data reported here represent changes in sample diameter due to the formation of bainite. They were measured using the laser transducer directed half way along the length of each sample. Different samples can therefore be compared, but the absolute magnitudes of the measured transformation strains reflect the average degree of transformation in the cross-section at half sample height.

After the above thermomechanical treatment, the samples were sectioned longitudinally, ground, polished and etched in 2% nital for microstructural observations. Vickers microhardness tests were conducted using a *Leitz miniload* tester at a load of 4.903 N. The load was selected to allow a sufficiently large number of indentations per sample and at the same time sampling a reasonably large area of the microstructure per indentation to give an average hardness. The indentations were taken along the compression axis at intervals of 500  $\mu\text{m}$ .

## 8.2 Results and Discussions

The calculated phase boundaries and the TTT diagram of the steel studied are shown in Figure 8.3. The method used for the calculations has been described elsewhere [Bhadeshia and Edmonds, 1980; Bhadeshia, 1982b]. The alloy clearly has sufficient hardenability to avoid the

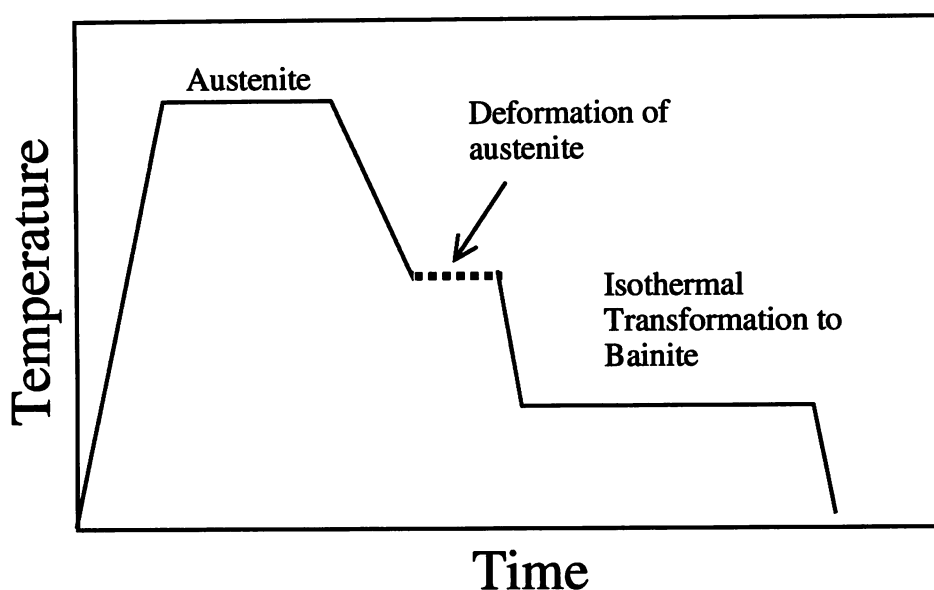


Figure 8.2: Schematic illustration of the heat treatment and the deformation schedule. All austenitising treatments were at 1200 °C for 180 s.

formation of products other than bainite during the heat treatment. The  $B_S$  temperature of the alloy was calculated to be 515 °C. No transformation was observed at 520 °C even after holding for 5400 seconds. It can thus be concluded that the  $B_S$  temperature is below 520 °C, a result consistent with Figure 8.3.

The variation of nominal stress with true strain at 700 °C is shown in Figure 8.4.

### 8.2.1 Dilatometric Measurements

The dilatation curves for different isothermal temperatures are shown in Figure 8.5. The magnitude of the transformation strain increases as the isothermal reaction temperature is lowered. This is in keeping with the incomplete reaction phenomenon so that more bainite is formed as the temperature is reduced below the bainite-start temperature. A method to convert the dilatation data into the corresponding volume fraction of bainite will be discussed later in the chapter.

Figure 8.6 shows the effect of prior deformation of austenite at 700 °C on subsequent transformation to bainite. “Prestrain” accelerates the formation of bainite but the total amount of transformation is reduced. This is because there is an increase in the nucleation rate but each nucleus then transforms a smaller volume of austenite when it is plastically deformed. The dislocations introduced by deformation block the motion of the austenite/bainite interface so that the plate growth is halted at a size which is smaller than would be the case in the undeformed austenite.

The results illustrated in Figure 8.6b are from experiments at a lower isothermal transformation temperature. The driving force for bainitic transformation is therefore larger, so it is not surprising that the maximum extent of transformation observed is larger for both levels of strain.

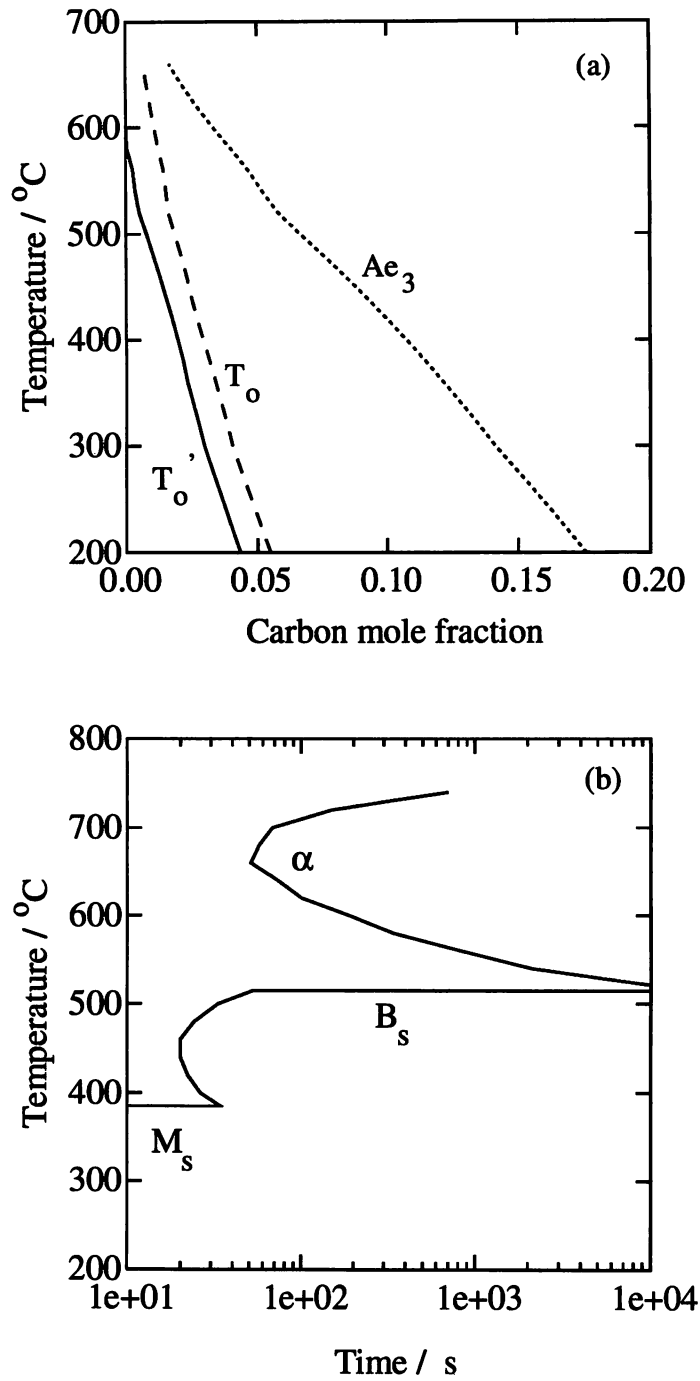


Figure 8.3: The calculated (a) phase diagram and (b) TTT diagram of the Fe-0.12C-2.03Si-2.96Mn wt.% alloy studied [Bhadeshia and Edmonds, 1980; Bhadeshia, 1982b].

Further data are summarised in Figure 8.7. Prestrain is seen to have a smaller effect at lower transformation temperatures. The applied strain is much less effective in restricting the growth of bainite plates at lower temperatures because of the larger chemical driving force available for the growth of bainite. Indeed, for transformation at 400 °C, it is evident that the increase in nucleation rate caused by prestrain overrides the decrease in plate size so that

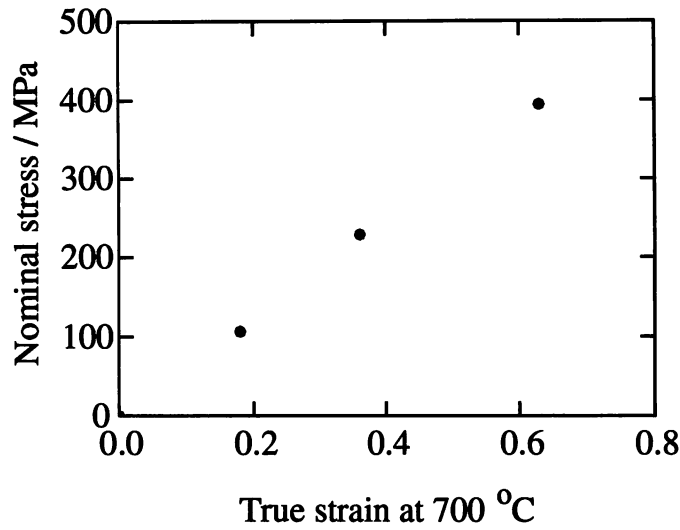


Figure 8.4: The variation of nominal stress with strain for a fully austenitic sample at 700 °C.

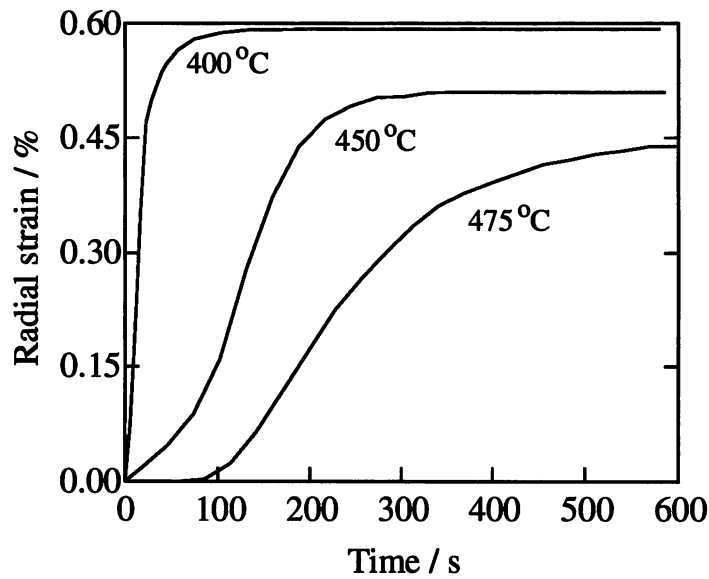


Figure 8.5: Change in radial strain during isothermal bainite transformation at different temperatures.

the net extent of transformation is increased in the deformed austenite. At all other bainite formation temperatures, the extent of reaction clearly decreases with increasing prestrain, though the changes observed are smaller as the isothermal transformation temperature is reduced. Bhadeshia and Shipway [1995a] also arrived at the same conclusion, although they did not report any quantitative data.

#### 8.2.1.1 The $M_S$ Temperature

It was possible, for the higher bainite transformation temperatures, to measure the martensite-start temperature ( $M_S$ ) of the residual austenite (*i.e.*, the carbon-enriched austenite that is not



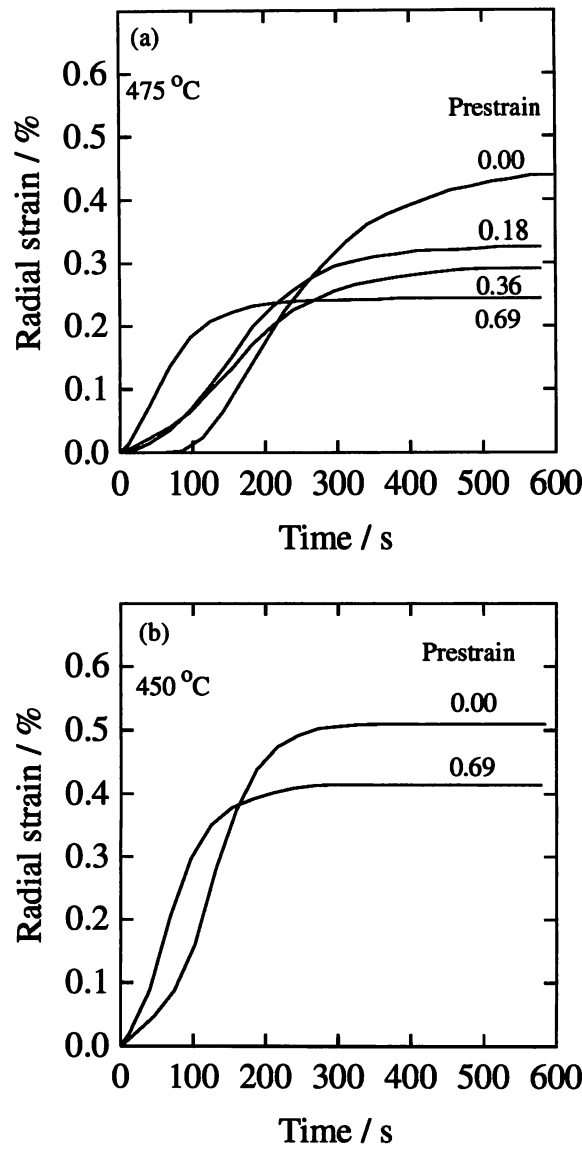


Figure 8.6: The change in radial strain during isothermal transformation to bainite at (a) 475 °C and (b) 450 °C, as a function of time and prestrain at 700°C.

transformed to bainite), as the samples cooled to ambient temperature. The  $M_S$  temperature of the residual austenite depends on two factors: the change in the carbon concentration caused by the formation of bainite and the effect of prestrain with respect to mechanical stabilisation of both bainite and martensite.

As expected, Figure 8.8 shows that in all cases, the measured  $M_S$  temperature is reduced relative to the sample without any bainite or prestrain. The greater the quantity of bainite, the higher is the carbon enrichment of residual austenite which therefore has a lower  $M_S$ . Prestrain initially causes an increase in  $M_S$  as the extent of bainitic transformation is reduced (Figure 8.7). However, it then decreases with increasing prestrain because the martensite itself becomes mechanically stabilised.

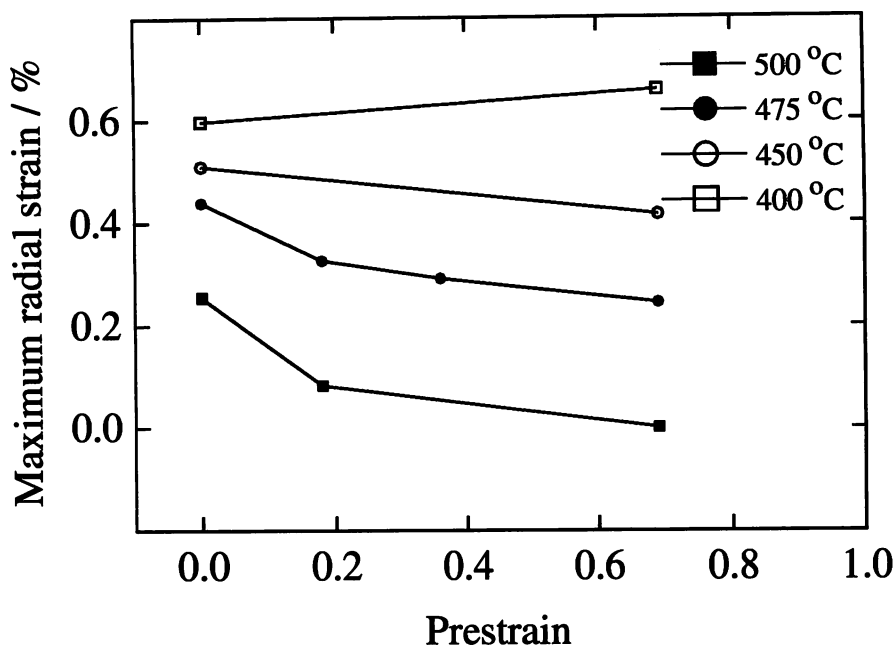


Figure 8.7: The maximum observed radial strain as a function of the prestrain and isothermal transformation temperature.

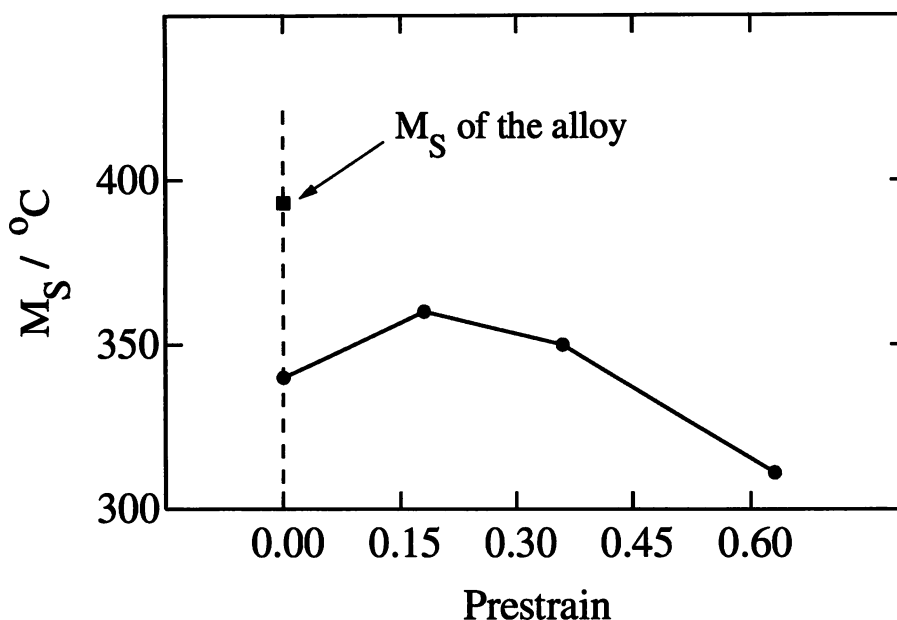


Figure 8.8: The measured martensite-start temperature of the austenite left untransformed after the completion of bainite reaction at 475 °C, as a function of prestrain.

### 8.2.2 Microstructural Observations

The classical sheaf-like bainitic microstructure developed from undeformed austenite at isothermal temperatures of 500 °C, 475 °C, 450 °C and 400 °C is shown in Figures 8.9 and 8.10. The amount of bainite increases as the transformation temperature is lowered. Microstruc-

tural observations of deformed samples confirm the dilatometric results presented above. The micrographs of the samples deformed at 700 °C and transformed to bainite are presented in Figures 8.11–8.17. At each isothermal temperature (except at 400 °C), the prior deformation of austenite is seen clearly to reduce the amount of bainite. The larger the prestrain, smaller is the quantity of bainite. It was pointed out earlier that compressive deformation is inhomogeneous because of the tendency of the sample to barrel. Thus, less bainite is formed at the more heavily deformed sample centre than at the edge. The effect of transformation temperature is also clearly reflected in the microstructures that developed. At 500 °C, deformation causes a large reduction in the amount of bainite. Hardly any bainite forms for a prestrain of 0.69 during transformation at 500 °C. The effect is not so severe as the transformation temperature is progressively lowered.

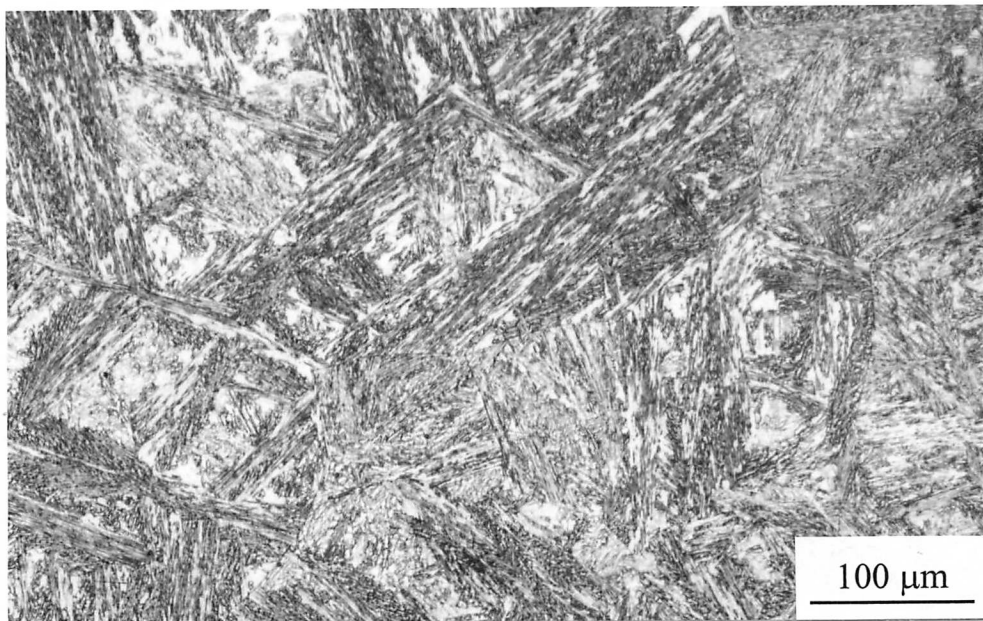
Apart from a reduction in the amount of bainite, deformation also changes the general appearance of the microstructure. Consistent with an increased nucleation rate and restricted growth of bainite, the microstructure becomes more refined. The classical sheaf morphology was not developed at large prestrains. Some earlier studies showed similar results [Davenport, 1977; Fujiwara *et al.*, 1995; Yang *et al.*, 1995; Kalish *et al.*, 1965; Bhadeshia and Shipway, 1995a]. One obvious reason for the increased nucleation rate is the increase in the grain boundary area caused by deformation below the recrystallisation temperature as described in chapter 5, three and four. It is also possible that deformation introduces other intragranular nucleation sites [Yamamoto *et al.*, 1995; Yang *et al.*, 1995; Kalish *et al.*, 1965]. Intragranular nucleation was also observed in the present study (*e.g.*, Figure 8.15b).

### 8.2.3 Microhardness Measurements

Hardness data provided further evidence for the mechanical stabilisation effect. A decrease in the fraction of bainite with a concomitant increase in the fraction of martensite should lead to a corresponding increase in the hardness. Deformed samples, with a lower amount of bainite, should therefore be harder. This is precisely what is observed, as illustrated in Figure 8.18, for the samples deformed at 700 °C and transformed at 475 °C. Part of the hardness rise must however be attributed to the higher dislocation density of deformed samples since it is well established that bainite inherits the defect structure of austenite [Irani, 1967] and to the reduced size of the bainite plates [Bhadeshia, 1992; Edwards and Kennon, 1978]. The higher hardness at the sample centre compared to that towards the edge is due to the strain gradient along the compression axis and the resultant variation in the amount of bainite [Shipway and Bhadeshia, 1995a].

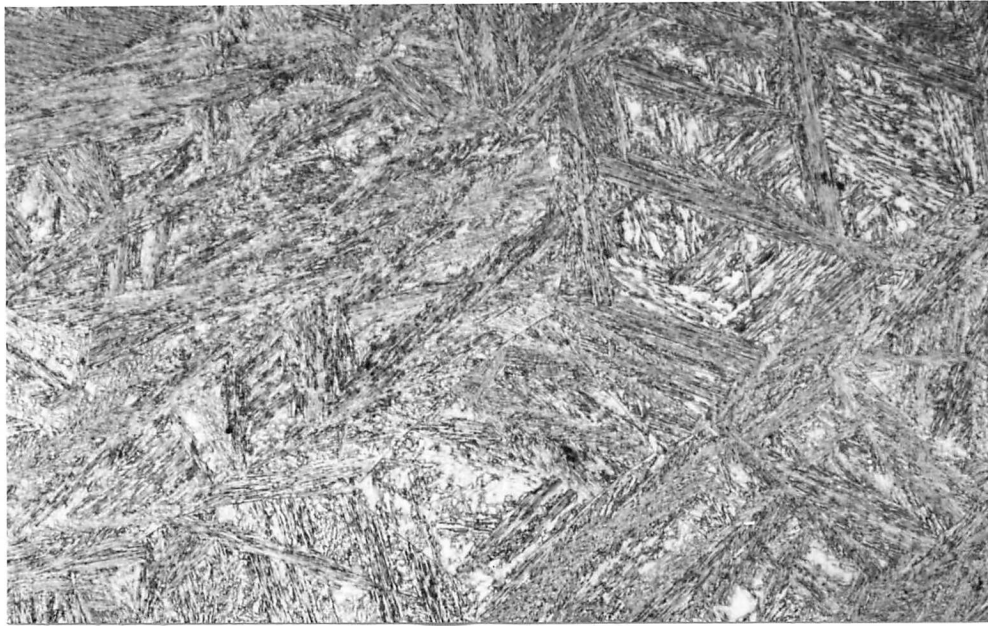


a

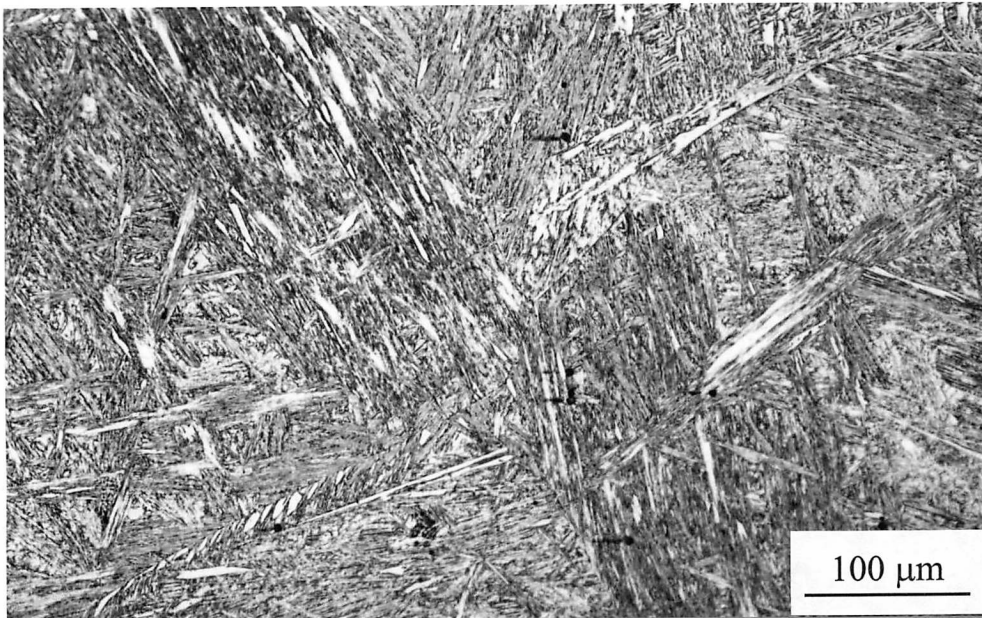


b

Figure 8.9: Optical microstructure of Fe-0.12C-2.03Si-2.96Mn (wt.%) alloy after completion of the bainite transformation at (a) 500 °C and (b) 475 °C.

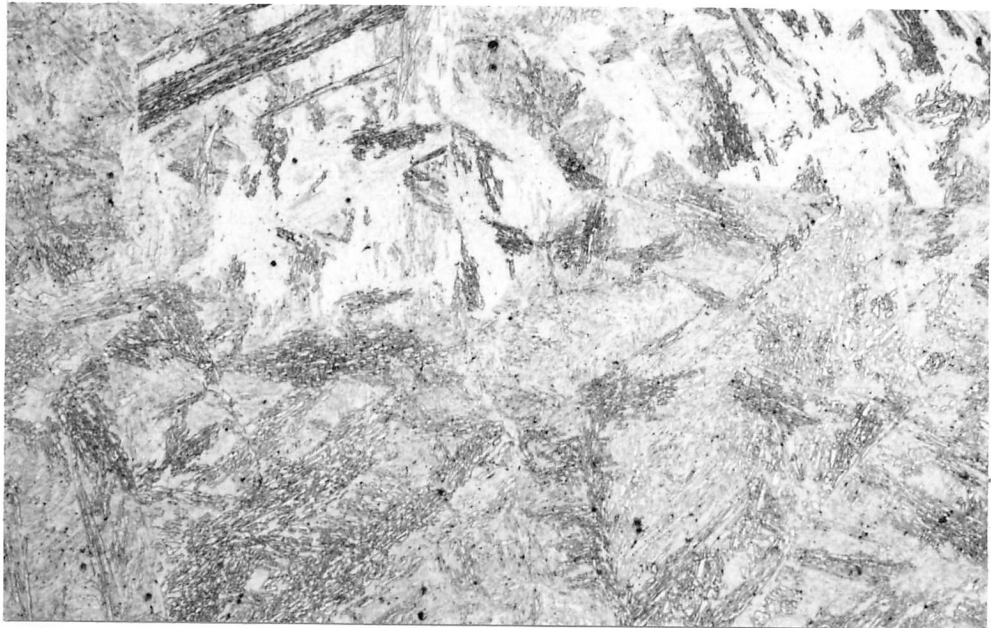


a



b

Figure 8.10: Optical microstructure of Fe-0.12C-2.03Si-2.96Mn (wt.%) alloy after completion of the bainite transformation at (a) 450 °C and (b) 400 °C.



a



b

Figure 8.11: Microstructure of the sample transformed at 500 °C after uniaxial compression at 700 °C to a longitudinal strain of 0.18; (a) is from the edge region and (b) from the central region of the sample.

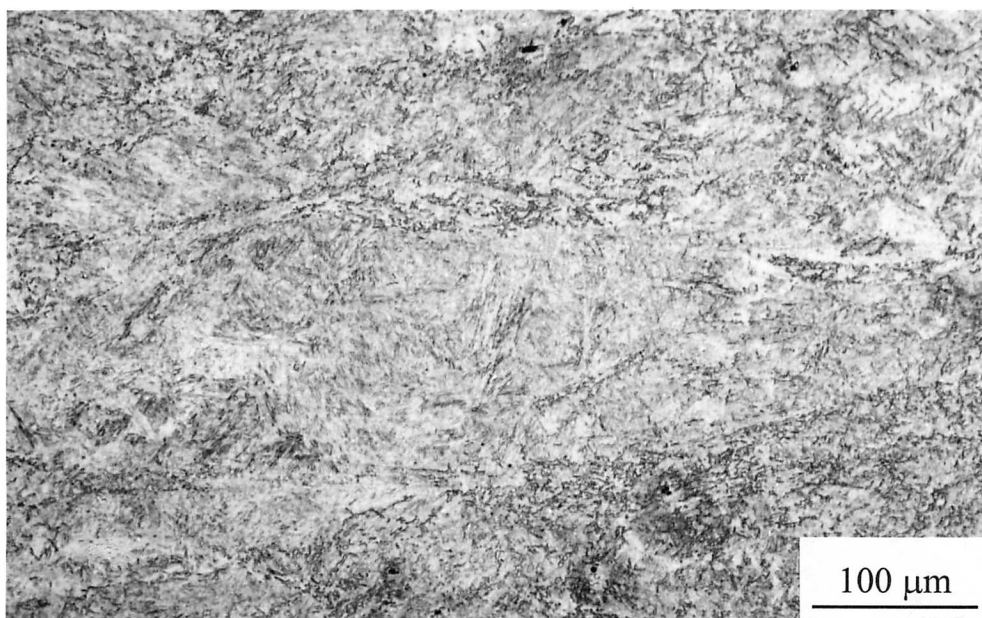
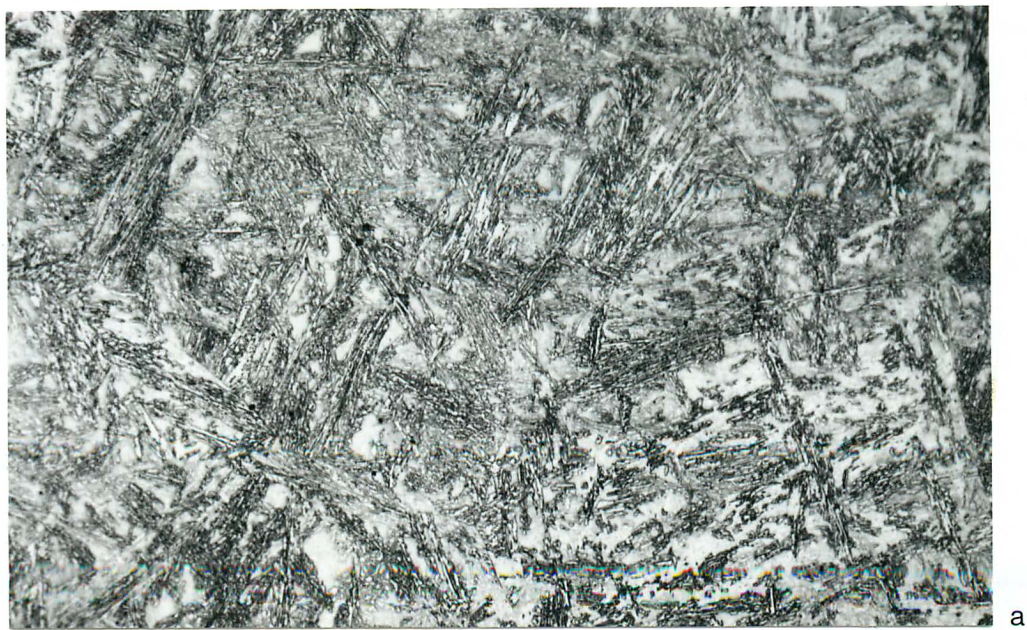


Figure 8.12: Microstructure of the sample transformed at 500 °C after uni-axial compression at 700 °C to a longitudinal strain of 0.69. The micrograph is from the central region of the sample.





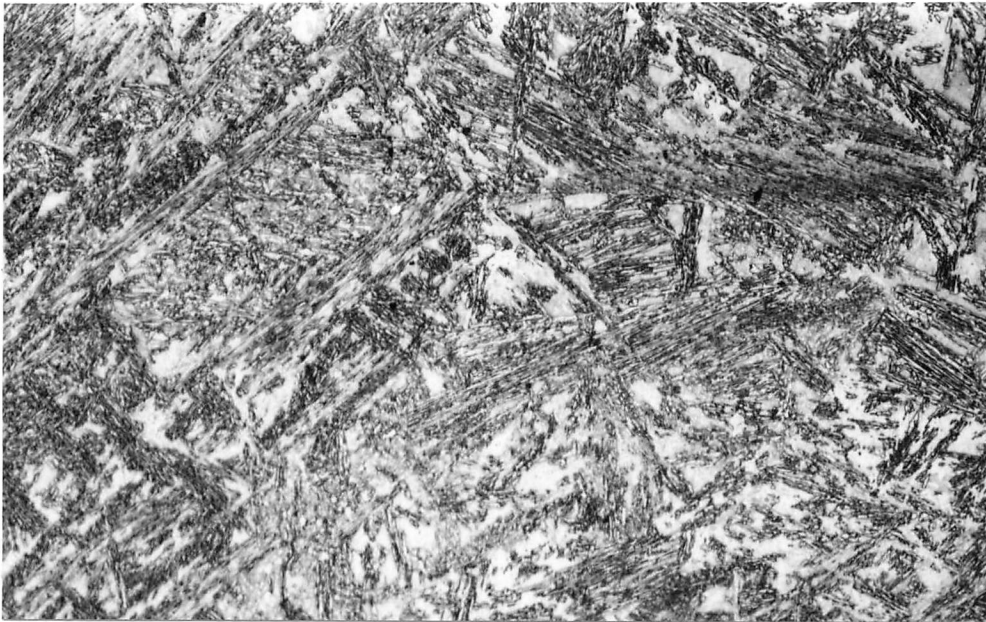
a



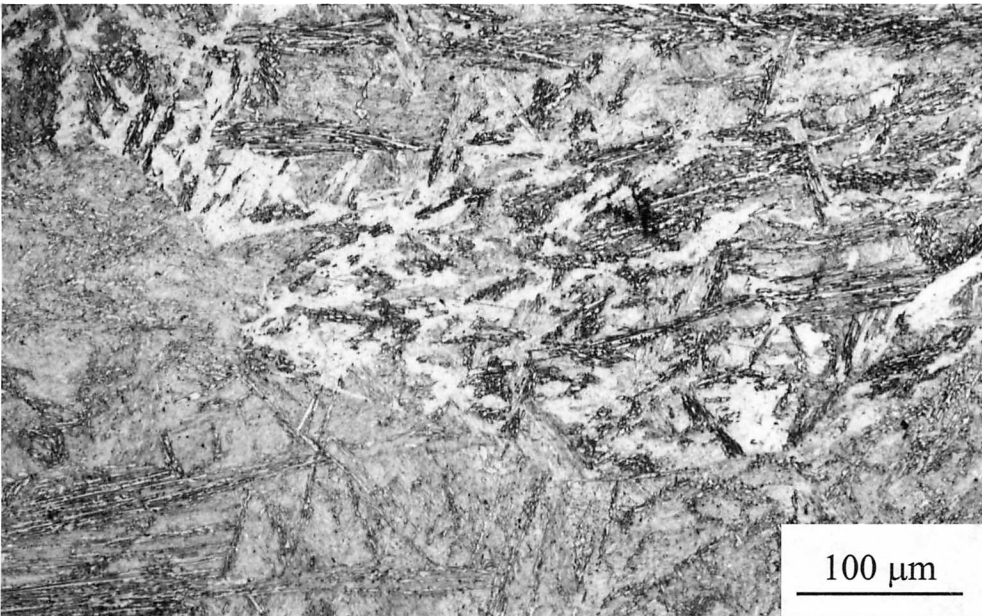
b

Figure 8.13: The effect of uniaxial compression at 700 °C on the development of bainitic microstructure at 475 °C. The longitudinal strain was 0.18; (a) is from the edge region and (b) from the central region of the sample.





a



b

Figure 8.14: Microstructure after uniaxial compression at 700 °C. The longitudinal strain was 0.36. Isothermal transformation was carried out at 475 °C. (a) is from the edge region and (b) from the central region.

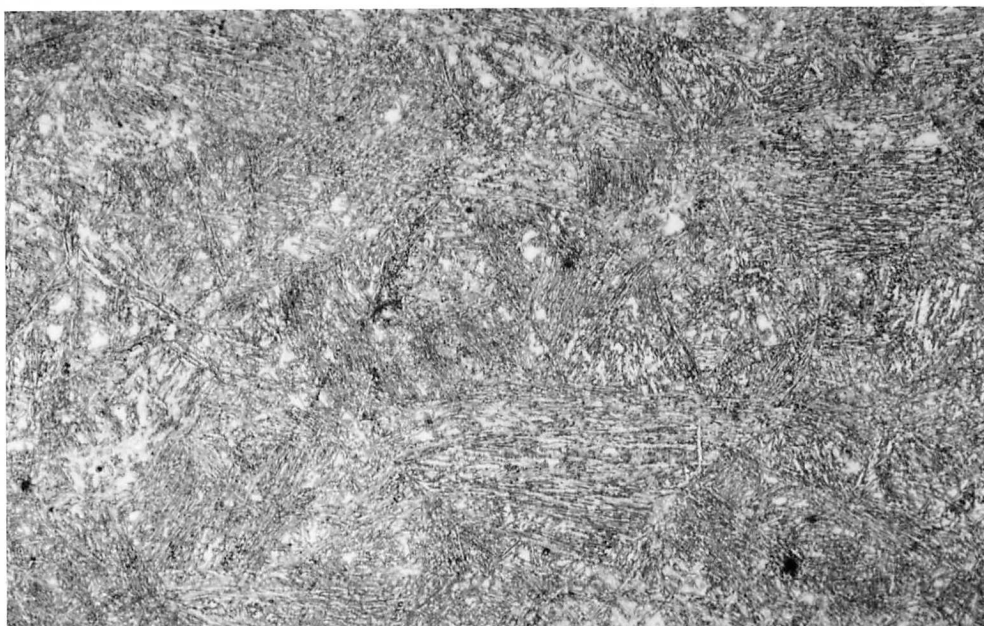


a

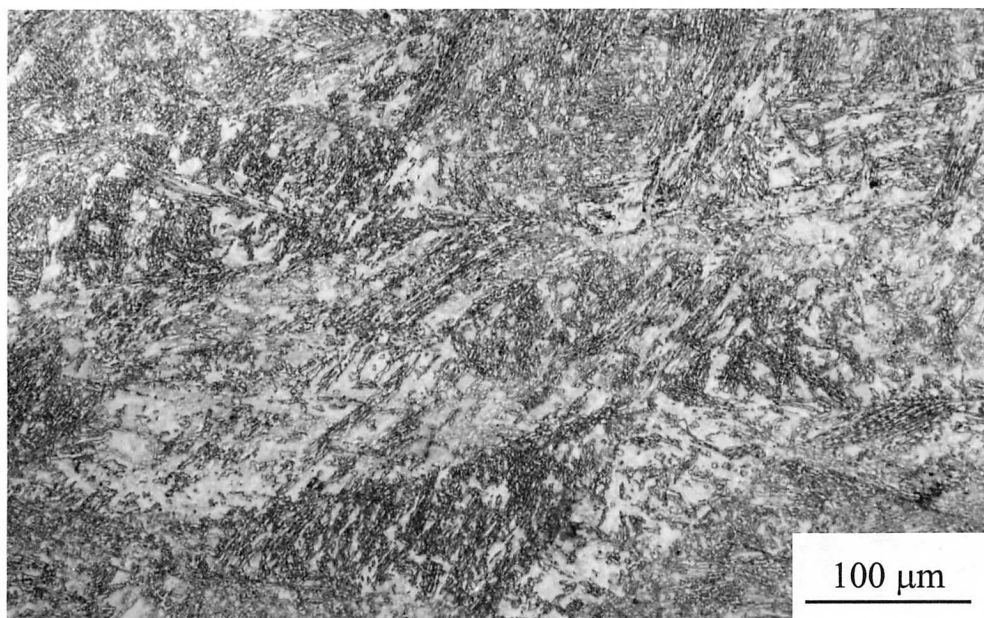


b

Figure 8.15: Microstructure after uniaxial compression at 700 °C. The longitudinal strain was 0.69. Isothermal transformation was carried out at 475 °C. (a) is from the edge region and (b) from the central region.



a



b

Figure 8.16: Microstructure of the sample deformed in compression at 700 °C to a longitudinal strain of 0.69 and then transformed at 450 °C. (a) is from the edge region and (b) from the central region.

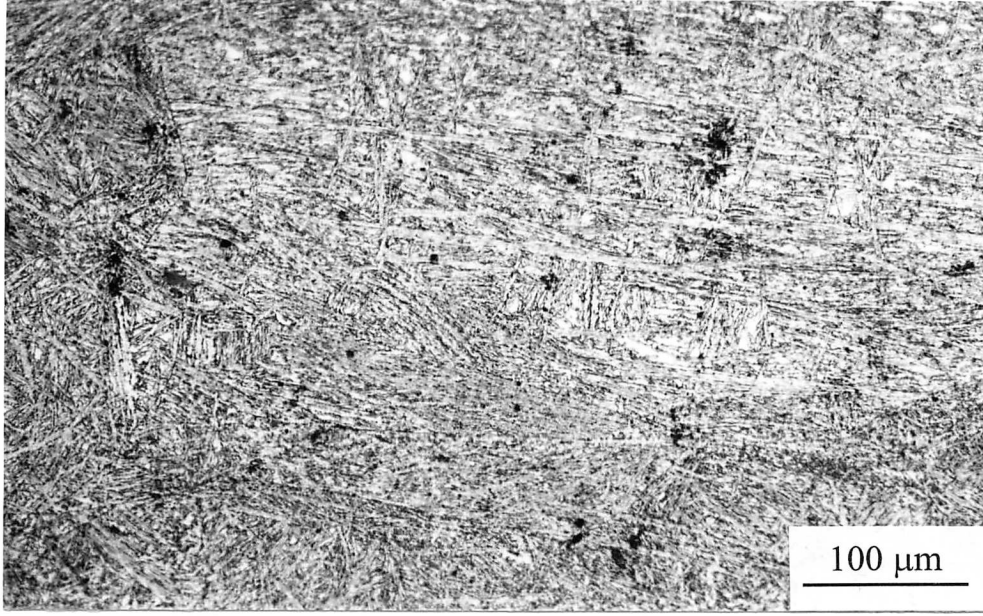


Figure 8.17: Microstructure of the sample compressed uniaxially at 700 °C to a longitudinal strain of 0.69 and then transformed to bainite at 400 °C.

#### 8.2.4 Conversion of Dilatometric Data

The dilatation data described above can be converted into the corresponding volume fraction of ferrite transformed [Bhadeshia, 1982a]. The method is applicable only when there is no carbide precipitation. When the ferrite volume fraction is  $v_\alpha$ , the relative length change,  $\Delta L/L$ , is given as:

$$\frac{\Delta L}{L} \simeq \frac{2v_\alpha a_\alpha^3 + (1 - v_\alpha) a_\gamma^3 - a_\gamma^3}{3a_\gamma^3} \quad (8.1)$$

where  $a_\alpha$  and  $a_\gamma$  are the lattice parameters of ferrite and austenite respectively at the transformation temperature  $T$ . The lattice parameter of a phase at any temperature depends on its thermal expansion coefficient and the chemical composition. Austenite is enriched in carbon during the bainite transformation which needs to be taken into account. If  $e_\alpha$  and  $e_\gamma$  are the linear thermal expansion coefficients of ferrite and austenite respectively then [Dyson and Holmes, 1970; Bhadeshia *et al.*, 1991]

$$a_\alpha = \left[ a_\alpha^o + \Delta a_\alpha^c + \sum_{i=1}^n C_i x_i \right] [1 + e_\alpha (T - 298)] \quad (8.2)$$

$$\text{and } a_\gamma = \left[ a_\gamma^o + C_{j(j=1)} w_c^\gamma + \sum_{j=2}^n C_j w_j \right] [1 + e_\gamma (T - 298)] \quad (8.3)$$

where  $a_\alpha^o$  and  $a_\gamma^o$  are the lattice parameters of the unalloyed ferrite and austenite at the room temperature and are taken to be 2.8664 Å and 3.573 Å respectively.  $\Delta a_\alpha^c$  is the expansion of ferrite lattice due to dissolved carbon.  $C_i$  and  $C_j$  are the coefficients which give the effect

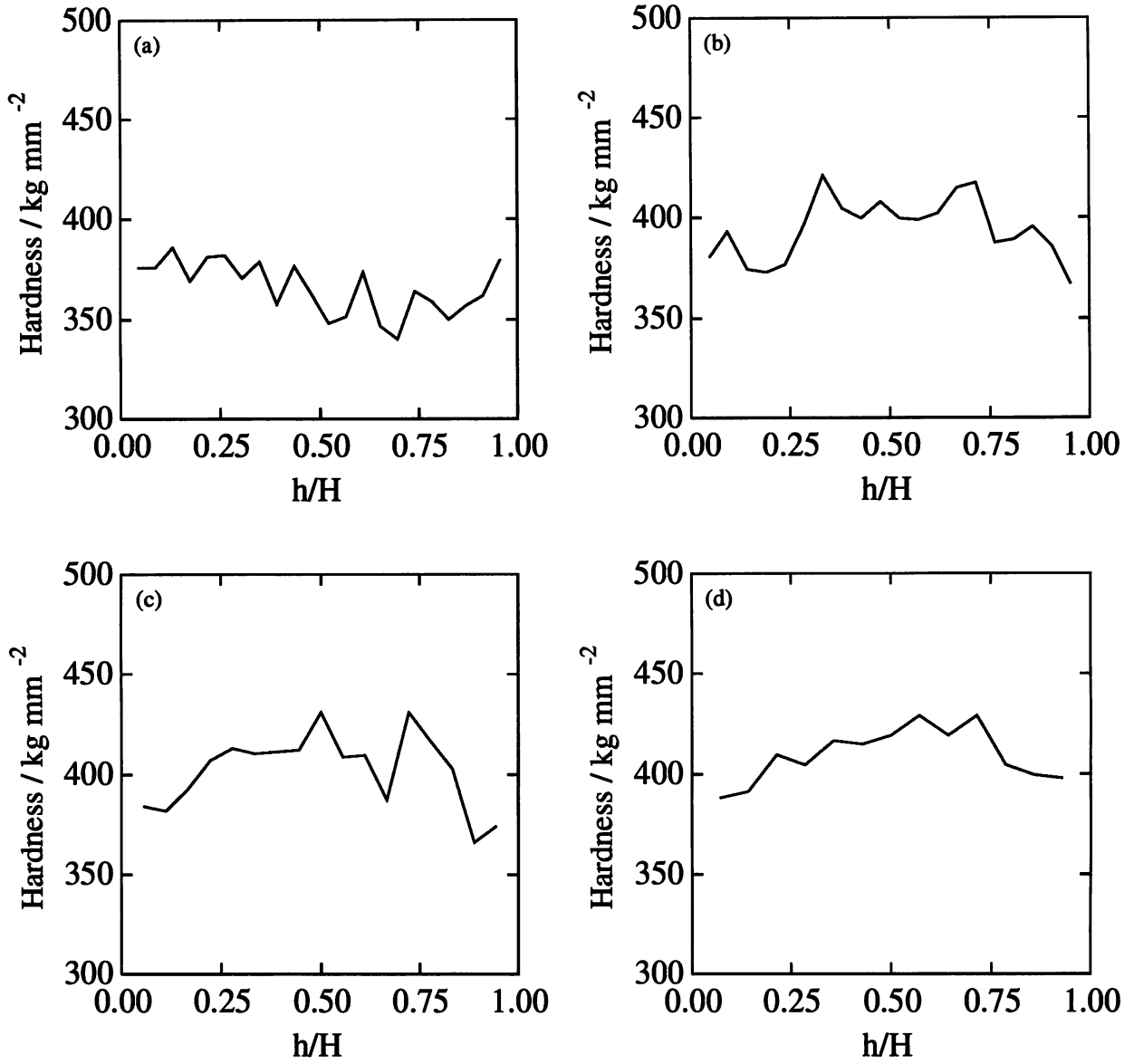


Figure 8.18: Hardness profiles of the samples compressed uniaxially at 700°C to various levels of strain and then isothermally transformed at 475 °C. The strains are (a) 0.0 (b) 0.18 (c) 0.36 (d) 0.69.  $H$  = sample height,  $h$  = distance from the sample edge parallel to the compression axis.

of the alloying elements on the lattice parameters of ferrite and austenite.  $x_i$  and  $w_i$  are the alloying element concentrations in mole fraction and weight percent respectively.  $w_c^\gamma$  is the wt.% of carbon in the residual austenite at any stage of transformation. Considering the mass balance for carbon and allowing for difference in the densities of ferrite and austenite,  $w_c^\gamma$  can be evaluated approximately as:

$$w_c^\gamma = \bar{w}_c + \frac{v_\alpha a_\gamma^3 (\bar{w}_c - w_c^\alpha)}{2a_\alpha^3 (1 - v_\alpha)} \quad (8.4)$$

where  $\bar{w}_c$  is the mean carbon concentration of the alloy and  $w_c^\alpha$  is the concentration of carbon in the ferrite. The term  $a_\gamma^3/2a_\alpha^3$  represents the ratio of the densities of ferrite and austenite



which, for simplicity, was assumed to depend on the atomic weight of iron only. The set of equations is solved iteratively to give  $v_\alpha$ ,  $w_c^\gamma$  and  $a_\gamma$  at any time during the transformation.

The room temperature ferrite lattice parameter of the alloy under study has been measured to be  $2.873 \pm 0.002 \text{ \AA}$  [Ali, 1991]. This value was calculated to be  $2.867 \text{ \AA}$  from equation 8.2 which is in good agreement with the measured value.

#### 8.2.4.1 Measurement of Thermal Expansion Coefficients

The thermal expansion coefficients needed for the analysis were measured. To measure the expansion coefficient of ferrite, a water quenched sample was tempered at  $600^\circ\text{C}$  to ensure a ferritic microstructure; small amount of cementite, if any, precipitated during tempering can be ignored. The sample was then cooled slowly at  $1^\circ\text{C s}^{-1}$ . For austenite, the sample was heated to  $1200^\circ\text{C}$  and then cooled slowly at  $5^\circ\text{C s}^{-1}$ ; the data in the temperature range  $1000$  to  $500^\circ\text{C}$  were used for the calculation of  $e_\gamma$ . The measured length change data (Figure 8.19) were fitted to a second order polynomial of temperature, with correlation coefficients ( $r^2$ ) of more than 0.99 in both cases. The analysis gives:

$$e_\alpha = 7.03494 \times 10^{-9}(T - 273) + 1.22097 \times 10^{-5} \text{ K}^{-1} \quad (8.5)$$

$$e_\gamma = 4.19764 \times 10^{-9}(T - 273) + 2.03923 \times 10^{-5} \text{ K}^{-1} \quad (8.6)$$

#### 8.2.4.2 Volume Fraction of Bainite

The calculated volume fractions of bainite under different test conditions are shown in Table 8.1. From the  $T'_0$  curve in the phase diagram for the alloy shown earlier, the maximum fraction of bainite that can form at  $500^\circ\text{C}$ ,  $475^\circ\text{C}$ ,  $450^\circ\text{C}$  and  $400^\circ\text{C}$  is calculated to be 0.32, 0.53, 0.64 and 0.74 respectively. This is in good agreement with the amount experimentally observed. The carbon concentration of the residual austenite when the bainite reaction ceases during the isothermal treatment at these temperatures is compared with the calculated  $T_0$  and  $T'_0$  curves in Figure 8.20. The points lie close to the  $T'_0$  curve. These calculations confirm the incomplete reaction phenomenon now well established for bainite and also that the strain energy accompanying bainite plate formation is around  $400 \text{ J mol}^{-1}$  [Bhadeshia, 1981]. It can also be concluded that the  $B_S$  temperature of the alloy is  $515^\circ\text{C}$ .

The extent of stabilisation ( $\phi_S$ ) at a given transformation temperature with prestrain can be represented as follows:

$$\phi_S = 1 - \frac{\text{maximum fraction with strain}}{\text{maximum fraction without strain}} \quad (8.7)$$

The variation of  $\phi_S$  with the amount of prestrain at  $700^\circ\text{C}$  at different temperatures is illustrated in Figure 8.21. Of particular interest are the results obtained at an isothermal transformation temperature of  $500^\circ\text{C}$  ( $B_S - 15^\circ\text{C}$ ). At a large enough value of strain (0.69), a very small amount of bainite was observed to form ( $\sim 100\%$  stabilisation). It is possible that at higher strains or lower supercoolings no bainite will be formed.

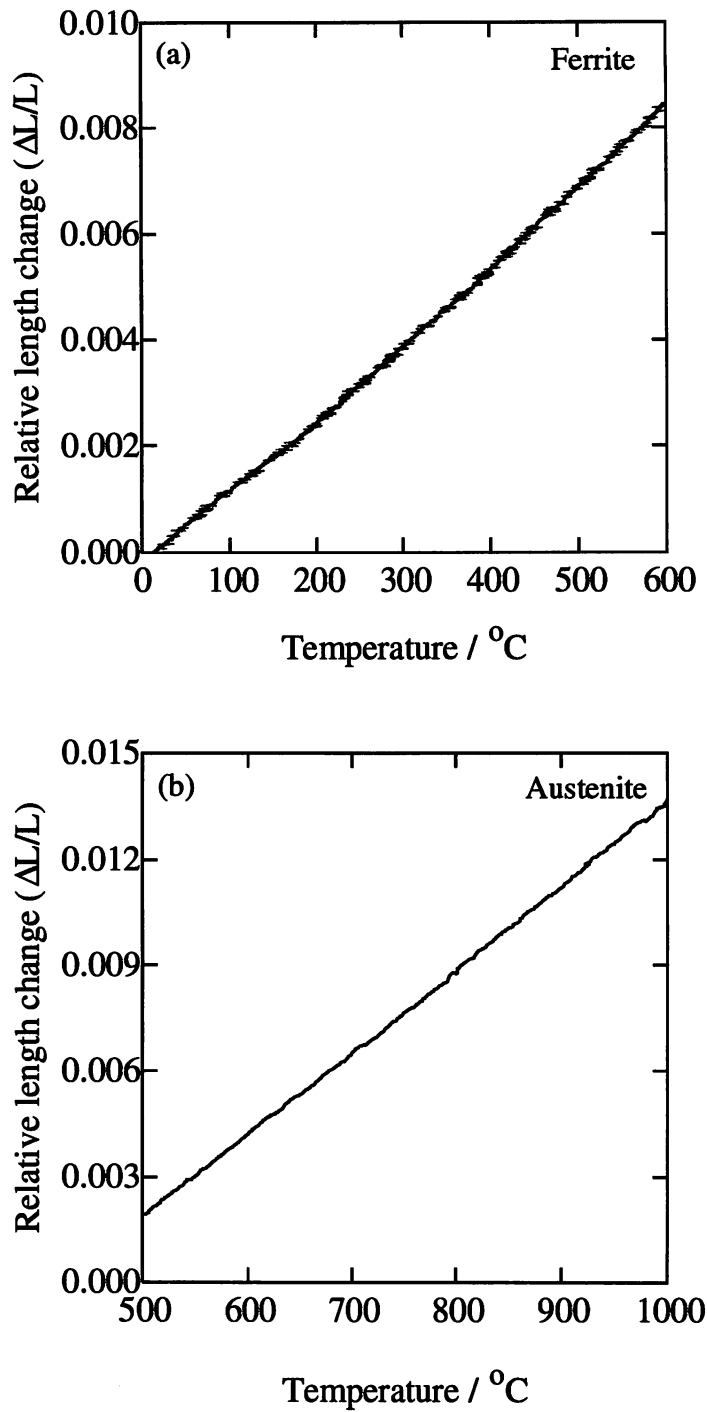


Figure 8.19: The length change data used for the measurement of the linear expansion coefficients of (a) ferrite and (b) austenite.

### 8.3 Mathematical Model for Mechanical Stabilisation

A model to predict the bainite transformation kinetics was presented in chapter six. This has been modified to take into account the influence of deformation. The experimental results for the effect of deformation can be summarised as follows:

- (i) transformation is initially accelerated in deformed austenite

Temperature °C	Strain (at 700 °C)	Measured bainite fraction	Calculated bainite fraction
500	0	0.34	0.32
	0.18	0.12	
	0.69	~ 0	
475	0	0.59	0.53
	0.18	0.45	
	0.36	0.43	
	0.69	0.36	
450	0	0.69	0.64
	0.69	0.58	
400	0	0.76	0.74
	0.69	0.84	

Table 8.1: The volume fraction of bainite as calculated from the measured dilatation data under different test conditions. The fraction calculated from the  $T'_o$  line is also given.

- (ii) the total amount of bainite that can be obtained at any isothermal transformation temperature is reduced relative to that in the undeformed austenite
- (iii) deformation is more effective in stabilising the austenite against the bainite transformation at low supercoolings below  $B_S$ .

The transformation is first accelerated because of the increase in the number density of nucleation sites. Plastic deformation not only increases the amount of grain surface per unit volume but also causes a significant increase in the number of other defects (dislocations, deformation bands). Bainite is known to nucleate on deformation bands and dislocation cell boundaries [Yamamoto *et al.*, 1995; Fujiwara *et al.*, 1995; Bai *et al.*, 1998]. Microstructural observations confirmed the intragranular nucleation of bainite. As in chapters three and five, the total surface area of the defects capable of nucleating bainite ( $S_V^T$ ) was taken to be

$$S_V^T = S_V + S_V^{db}, \quad S_V^{db} = 30 \varepsilon^2 \text{ mm}^{-1} \quad (8.8)$$

where  $S_V$  is the grain boundary area per unit volume of the deformed grains,  $S_V^{db}$  is the deformation band density and  $\varepsilon$  is the strain. The austenite grain boundary area after deformation (uniaxial compression in this case) was calculated as in chapter four.

A further effect of deformation is to reduce the size of bainite plates so that each nucleus transforms a smaller amount of austenite when the latter is deformed prior to transformation. Thus at a fixed transformation temperature, the amount of bainite that can form tends to decrease.



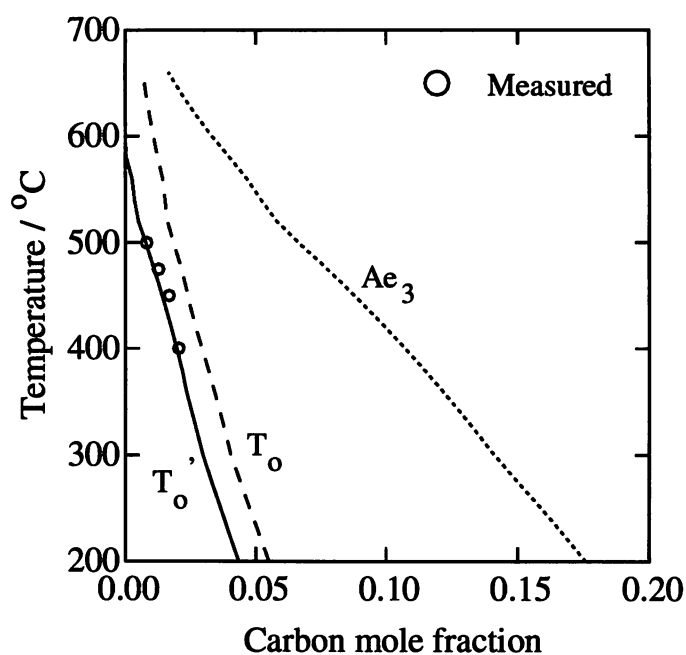


Figure 8.20: The carbon concentration of the residual austenite after completion of the isothermal bainite transformation. The calculated  $T_0$  and  $T'_0$  curves are also shown for comparison. The figure illustrates the classical behaviour known as the incomplete reaction phenomenon.

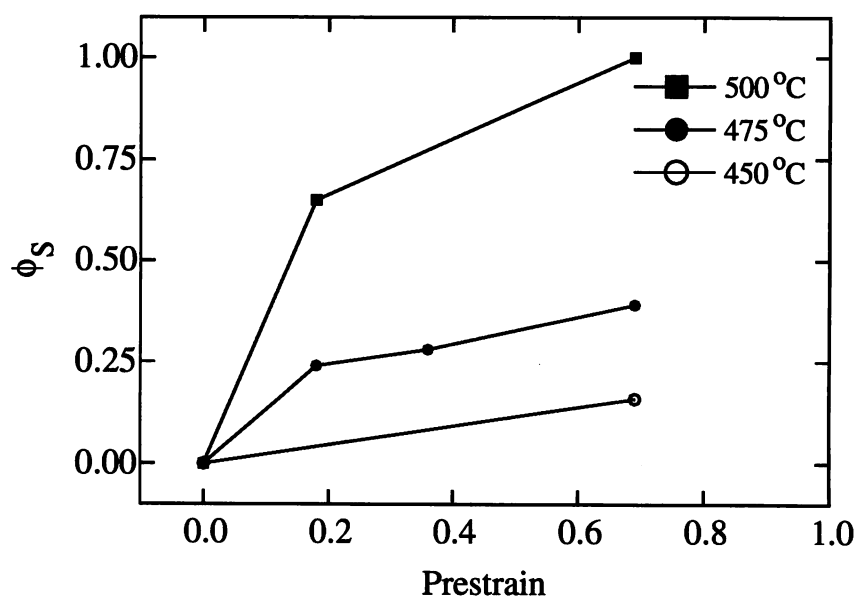


Figure 8.21: Fraction of austenite stabilised at different isothermal transformation temperatures as a result of prestrain at 700 °C.

In the bainite kinetics model described in chapter six, the initial density of nucleation sites was taken to be constant throughout the transformation. If the supply of nucleation sites is unlimited then there is no reason why the deformation of austenite should lead to a reduction in the maximum amount of bainite that can form, although the microstructure will be refined.

It can therefore be concluded that the density of nucleation sites is not constant but decreases as the reaction progresses. Eventually, the nucleation sites are exhausted and the reaction stops even before the thermodynamic limit is attained. Accordingly, it was assumed that the density of nucleation sites decays exponentially with reaction time  $t$  [Christian, 1975]

$$N_V^t = N_V^o \exp(-qt) \quad (8.9)$$

where  $N_V^t$  is the nucleation site density at any time  $t$  and  $q$  is a frequency term which gives the rate at which individual sites become nuclei.  $N_V^o$  is the initial ( $t = 0$ ) site density. Also, when  $q = 0$ ,  $N_V^t = N_V^o$  for all times so that this reduces to the earlier version of the model. The total nucleation rate including the effect of autocatalysis is written as (equation 6.6)

$$I_b = I \left[ 1 + \beta t \nu \exp\left(-\frac{G^*}{RT}\right) \right] \quad (8.10)$$

where all the terms have their usual meaning.  $I$  is now given by

$$I = N_V^t \nu \exp\left(-\frac{G^*}{RT}\right) \quad (8.11)$$

Following the procedure detailed in chapters two and six, it can be shown that

$$\frac{\theta_b \bar{L}}{u B'_3 \nu} \int_0^\xi \frac{d\xi}{\exp\left(-\frac{G^*}{RT}\right) (1 - \xi)} = \int_0^t \left[ \exp(-qt) + \beta \nu t \exp(-qt) \exp\left(-\frac{G^*}{RT}\right) \right] dt \quad (8.12)$$

Once again ignoring the small variation of  $\Delta G_m$  with  $\xi$ , the above equation can be integrated to give

$$\xi = 1 - \exp[-f(t)] \quad (8.13)$$

where

$$f(t) = \frac{a_b^3 \alpha_p B'_3}{\theta_b \bar{L} q^2} \nu \exp(-G^*/RT) \left[ q \{1 - \exp(-qt)\} + \beta \nu \exp(-G^*/RT) \{1 - \exp(-qt)(qt+1)\} \right] \quad (8.14)$$

The terms  $a_b$ ,  $\alpha_p$  and  $B'_3$  are as defined in chapter six.

#### 8.4 Model Predictions

The experimental data from Fe-0.12C-2.03Si-2.96Mn (wt.%) alloy were used to test the model predictions. The austenite grain size after austenitisation at 1200 °C for 180 s was measured to be  $135 \pm 11 \mu\text{m}$ . The predicted kinetics at 500 °C, 475 °C and 450 °C without any prior deformation are shown in Figure 8.22 with four different values of  $q$ . The case of  $q \rightarrow 0$  is equivalent to the model discussed in chapter six. In comparison with this, the predicted value of the maximum volume fraction of bainite shows a small reduction when  $q$  is high (0.003). Lower values of  $q$  have little effect on the predicted maximum volume fraction, though the transformation rate is marginally retarded. Furthermore, the effect of exhaustion of nucleation sites on the maximum volume fraction is more pronounced at lower temperatures where the

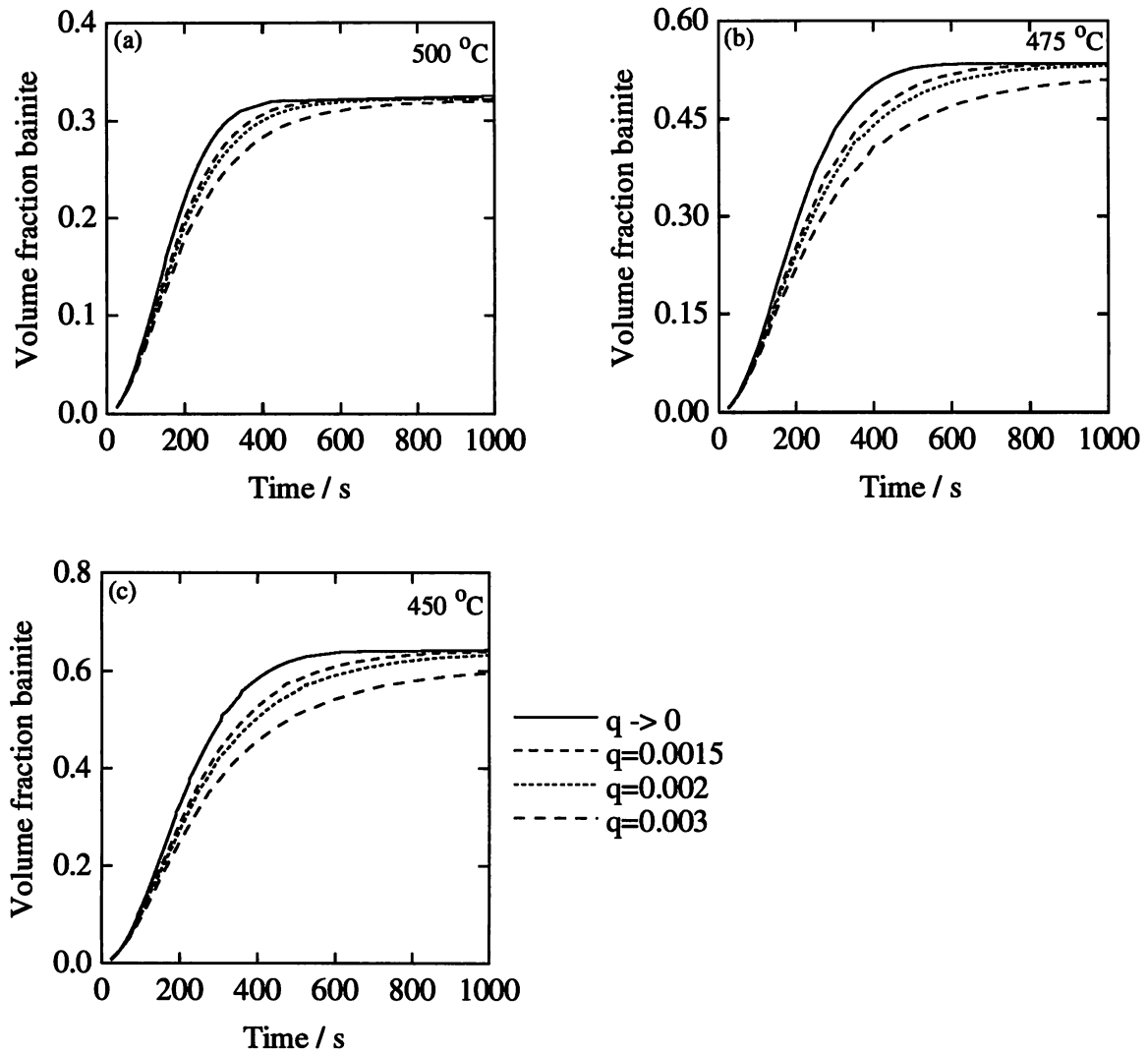


Figure 8.22: The predicted isothermal kinetics of Fe-0.12C-2.03Si-2.96Mn (wt.%) alloy with four different value of  $q$ . (a) 500 °C, (b) 475 °C and (c) 450 °C.

driving force for transformation is higher. The optimum value of  $q$  was taken to be 0.002 and used for all subsequent predictions.

#### 8.4.1 Effect of Strain

The bainite plate thickness of the above alloy as calculated using the neural network model at different transformation temperatures is shown in Figure 8.23. Prestrain is well known to reduce plate thickness but the effect has not been quantified as yet [Fujiwara *et al.*, 1995; Bai *et al.*, 1998; Yang *et al.*, 1996]. Therefore, the bainite plate thickness in deformed austenite was set empirically to give the best possible fit with experimental data. Some investigators have reported that the length of the bainite plates also decreases in deformed austenite [Fujiwara *et al.*, 1995; Bai *et al.*, 1998]. Fujiwara *et al.* [1995] further showed that the length of the plates is directly proportional to the calculated sub-grain size when the austenite is heavily deformed.

It is not clear whether this implies a change in the aspect ratio of the plates. In the absence of detailed information, the aspect ratio was taken to be constant so that a decrease in the plate thickness would automatically reduce its length.

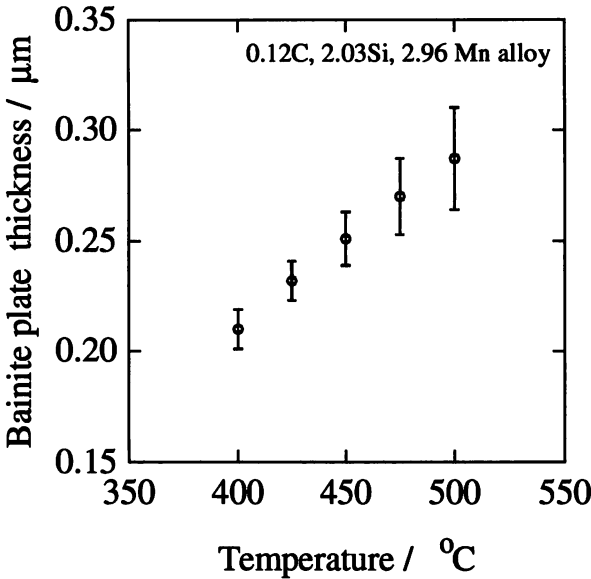


Figure 8.23: The bainite plate thickness of the Fe-0.12C-2.03Si-2.96Mn (wt.%) alloy at different isothermal transformation temperatures as calculated using the neural network model (chapter ten).

The calculated kinetics at 475 °C for different levels of austenite prestrain are shown in Figure 8.24. The predictions take into account the increase in nucleation site density and the reduction in the bainite plate thickness due to the prestrain. The bainite plate thickness was allowed to vary linearly with the logarithm of strain,  $a'_b = a_b(-0.137 \ln \varepsilon + 0.326)$ , where  $a'_b$  and  $a_b$  are the plate thicknesses corresponding to deformed and undeformed austenite respectively.

The model can correctly predict the amount of bainite formed at a given strain. However, it fails to predict the initial acceleration in the transformation experimentally observed at all the strains studied. It was simply not possible to simultaneously reproduce the initial acceleration together with the final reduction in the bainite volume fraction with *any combination* of the values of  $q$  and  $a'_b$ . The lowering of the bainite plate thickness to match the final volume fraction more than compensated for the increase in the nucleation site density throughout the reaction so that the predicted kinetics for the case of deformed austenite was always slower than that for the undeformed one. It is possible to predict an acceleration with a very moderate decrease in the plate thickness, but in such cases the maximum volume fraction is predicted to be higher for the deformed samples. This can be proved analytically. If  $d\xi$  is the normalised volume fraction of bainite that forms in undeformed austenite between time  $t$  and  $t + dt$ , then it was shown earlier (chapters two and six) that:

$$\theta_b d\xi = (1 - \xi) u I_b dt \tag{8.15}$$

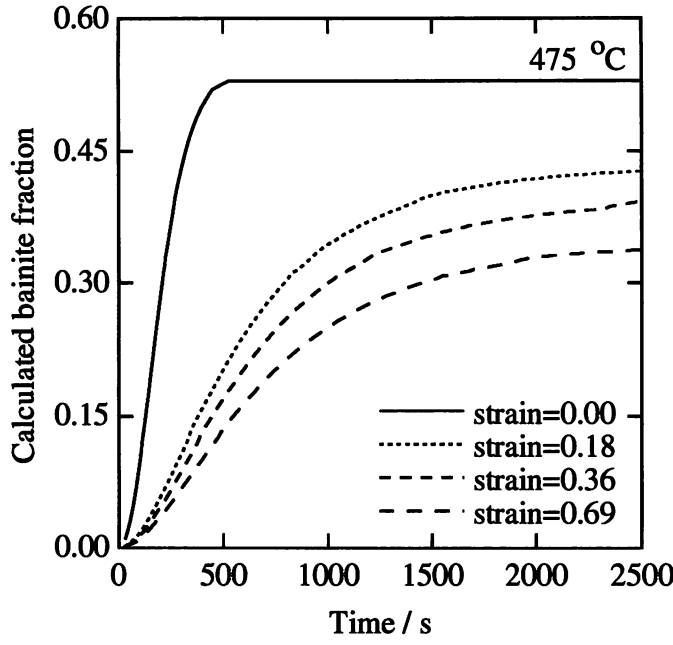


Figure 8.24: The calculated transformation kinetics of bainite at 475 °C when the austenite is deformed. The predicted kinetics take into account the increased nucleation sites due to deformation and the reduction in the bainite plate thickness.

or

$$\frac{d\xi}{(1-\xi)} = \frac{u}{\theta_b} I_b dt \quad (8.16)$$

Integrating between the limits

$$\int_0^\xi \frac{d\xi}{(1-\xi)} = \frac{u}{\theta_b} \int_0^t I_b dt \quad (8.17)$$

This gives:

$$-\ln(1-\xi) = \frac{u}{\theta_b} \int_0^t I_b dt \quad (8.18)$$

Similarly, if  $\xi'$  is the normalised volume fraction of bainite in deformed austenite after time  $t$ , then

$$-\ln(1-\xi') = \frac{u'}{\theta_b} \int_0^t I'_b dt \quad (8.19)$$

where  $u'$  and  $I'_b$  are the bainite plate volume and the nucleation rate respectively when the austenite is deformed.  $u'$  can be related to  $u$ , the plate volume when the austenite is undeformed, according to:

$$u' = u(\phi_1 - \phi_2 \ln \varepsilon)^3 \quad (8.20)$$

where  $\phi_1$  and  $\phi_2$  are constants which describe the effect of strain on the plate volume (for the calculations shown in Figure 8.24,  $\phi_1 = 0.326$  and  $\phi_2 = 0.137$ ).

Assuming that the driving force for nucleation ( $\Delta G_m$ ) is independent of  $\xi$ , it can be shown that

$$\frac{\int_0^t I'_b dt}{\int_0^t I_b dt} = \frac{N'_V}{N_V} \quad (8.21)$$

where  $N'_V$  and  $N_V$  are the nucleation site densities for deformed and undeformed austenite respectively. The nucleation site density is proportional to the density of defects which can nucleate bainite, hence

$$\frac{N'_V}{N_V} = \frac{S_V^T}{S_V^o} \quad (8.22)$$

where  $S_V^o$  is the austenite grain boundary area per unit volume for the undeformed austenite and  $S_V^T$  is as defined in equation 8.8. Dividing equation 8.19 by equation 8.18, we get:

$$\frac{\ln(1 - \xi')}{\ln(1 - \xi)} = (\phi_1 - \phi_2 \ln \varepsilon)^3 \frac{S_V^T}{S_V^o} \quad (8.23)$$

which is independent of time. For the calculations presented in Figure 8.24,  $\ln(1 - \xi')/\ln(1 - \xi)$  is indeed a constant at a given strain. Thus, if the maximum volume fraction of bainite with the austenite in a deformed state is smaller when compared with an undeformed austenite, it is *impossible* to predict an acceleration at any stage of the reaction. An acceleration in the initial stages of the reaction would be accompanied by an increase on the volume fraction of bainite for the deformed austenite.

These discrepancies can be understood if it is assumed that the applied strain is not homogeneously distributed on a microscopic scale. Except at very large deformations, the strain will be heterogeneous on a microscopic scale. The strain is localised to certain regions which become stabilised. Other regions are relatively strain free and the bainite plates can be coarser as in the normal circumstances, unhindered by the defects induced by the applied deformation. This leads to the conclusion that *the plate thickness should exhibit a bimodal size distribution*.

There is experimental evidence to support this conclusion. The inhomogeneous distribution of strain at the microscopic level and its consequence on the bainite transformation has been described by Freiwillich *et al.* [1976]. The experimental results of Tsuzaki *et al.* [1989] where stabilisation was observed only at the lower transformation temperature in a Fe-0.59C-2.01Si-1.02Mn (wt.%) steel has been explained as being the result of non-uniform distribution of the applied strain [Bhadeshia, 1992]. This was also reflected in the microstructure that developed.

An experiment was carried out to provide further confirmation of the non-uniformity of stabilisation. After austenitisation at 1200 °C, the sample (Fe-0.12C-2.03Si-2.96Mn, wt.%) was deformed at 700 °C by a longitudinal strain of 0.36. The deformation was followed by a partial isothermal transformation to bainite at 475 °C for 184 seconds; the sample was quenched before the transformation could reach completion. Other experimental conditions were exactly the same as reported earlier. The microstructure is shown in Figures 8.25 and 8.26. While

the sheaves appear to be fairly thick at places, very fine transformed regions can also be seen. This indicates that the stabilisation is not uniform.

This phenomenon can be modelled by partitioning the austenite into two discrete fractions, one comprising of the regions of easy transformation (represented by fraction  $Z$ ) and the other where stabilisation is achieved (fraction  $1 - Z$ ). The transformation is accelerated in the former fraction because of the enhancement in the nucleation site density whereas it is retarded in the stabilised fraction due to a lower plate thickness. The overall rate is obtained by taking the weighted average of the two regions. The calculations for a strain of 0.69 and at a transformation temperature of 475 °C with  $Z = 0.65$  are shown in Figure 8.27. The value of  $Z$  was selected so as to give a good fit with the experimental data. The bainite plate thickness in the stabilised part ( $a'_b$ ) was set to 0.06  $\mu\text{m}$ . The resultant transformation curve when those for the strained as well as the strain-free fractions are combined together follows the experimentally observed trend.

Figure 8.28 shows similar calculations but for a strain of 0.18. It was assumed that at a lower strain, the stabilisation takes effect in a smaller volume fraction of austenite than at a higher strain. Thus,  $Z$  was set to 0.8 and the bainite plate thickness in the stabilised fraction to 0.09  $\mu\text{m}$ . The resultant kinetics does not show any acceleration in this case. The calculated transformation curve for the fraction which is not stabilised (this involved calculating the kinetics by taking into account the increase in the nucleation site density only) exhibits only marginal acceleration over the curve for the undeformed austenite. The actual acceleration experimentally observed for a strain of 0.18 (Figure 8.6a) is higher than even this curve which does not allow for stabilisation effects. This probably signifies that deformation induces more nucleation sites for bainite than the ones taken into consideration by the model. For example, it has been shown that nucleation of bainitic ferrite can take place on sub-grain boundaries of the deformed austenite [Fujiwara *et al.*, 1995]. It is also worth recalling here that in the experiments reported above, the diameter was monitored at a cross section where the actual strain was more than the nominal applied strain. This makes one-to-one comparison between the experiments and the calculations difficult.

The predicted transformation curves at 475 °C with different values of prestrain for which experiments were carried out are shown in Figure 8.29. Apart from the initial stages at low strain, the curves can reproduce the observed trend.

#### 8.4.2 Effect of Austenite Grain Size

Some of the results reported in literature are in apparent contradiction to the results presented here. They do not indicate an initial acceleration of the bainite transformation when the austenite is deformed. Using Fe-0.43C-2.02Si-3.0Mn (wt.%) steel, Yang *et al.* [1996] found that deformation retarded the bainite transformation even in the initial stages at all the strains studied. The maximum deformation employed was 40% (strain=0.51). The austenitisation in this work was carried out at 950 °C for 10 minutes. Though the actual austenite grain size has not been reported, from the bainite micrographs presented it appears to be around 25  $\mu\text{m}$  or less. The calculated transformation curves for this steel at 350 °C for a prestrain of

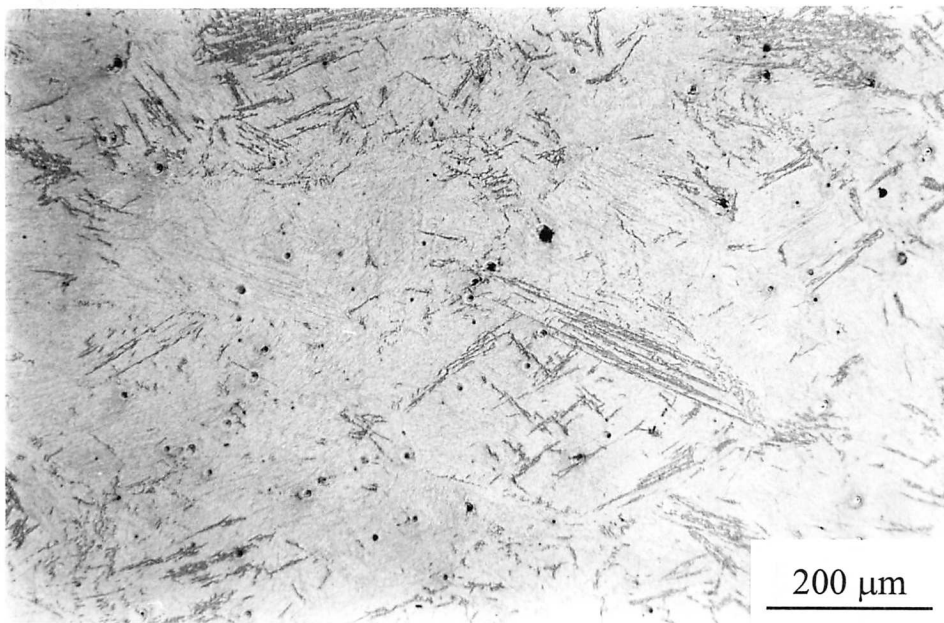


Figure 8.25: The microstructure of the sample deformed at 700 °C (longitudinal strain=0.36) and partially transformed to bainite at 475 °C showing non-uniformity of stabilisation as a consequence of inhomogeneous distribution of strain at the microscopic level. The micrographs are from around the central region of the deformed sample.



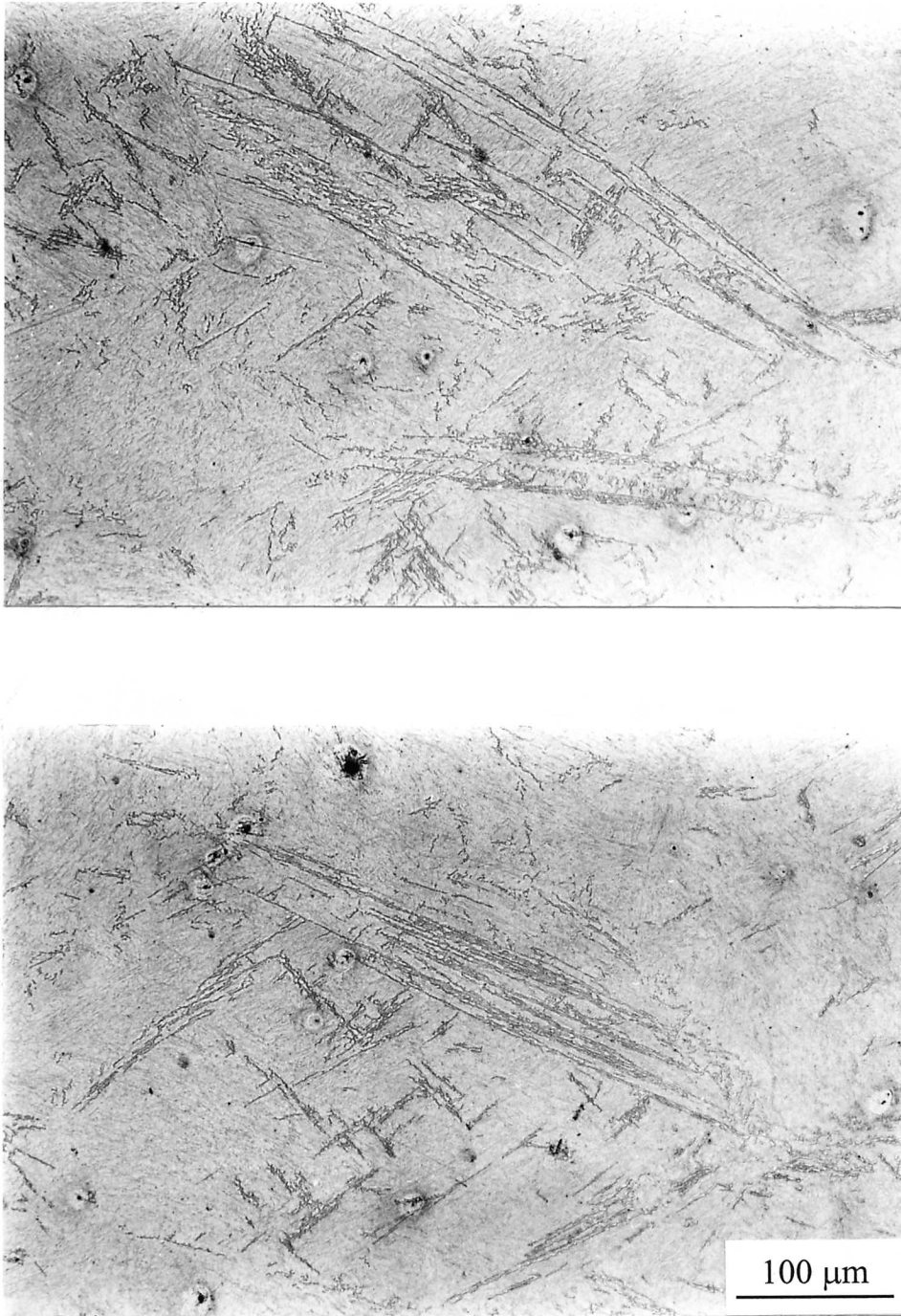


Figure 8.26: The microstructure of the sample deformed at 700 °C (longitudinal strain=0.36) and partially transformed to bainite at 475 °C showing non-uniformity of stabilisation as a consequence of inhomogeneous distribution of strain at the microscopic level. The micrographs are from around the central region of the deformed sample.

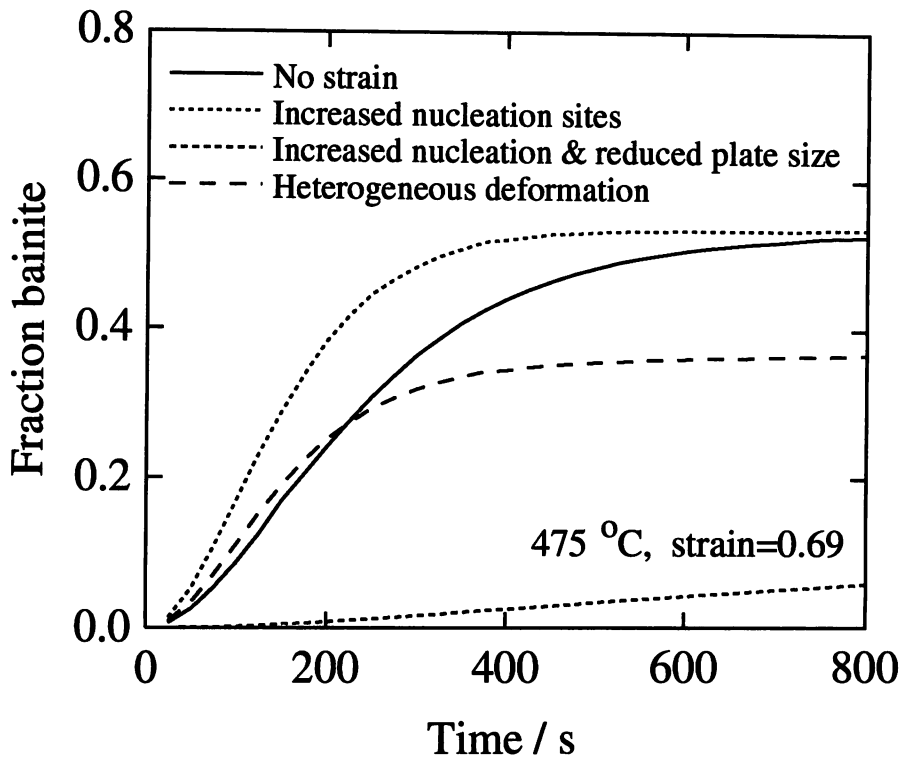


Figure 8.27: The predicted transformation kinetics of bainite at 475 °C following a prestrain of 0.69. The calculations take into account the heterogeneous nature of the stabilisation with  $Z = 0.65$ .

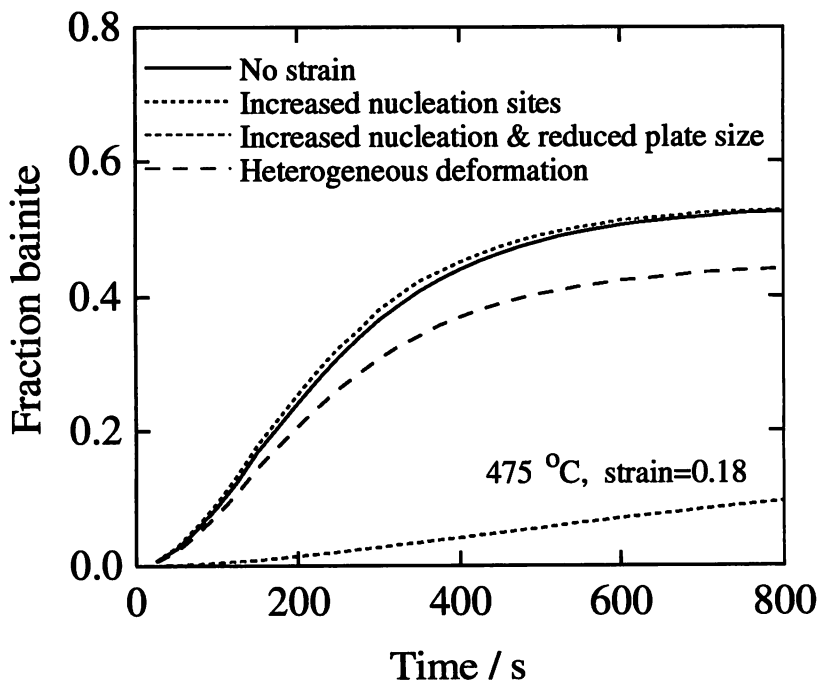


Figure 8.28: The predicted transformation curves of bainite at 475 °C for a prestrain of 0.18.

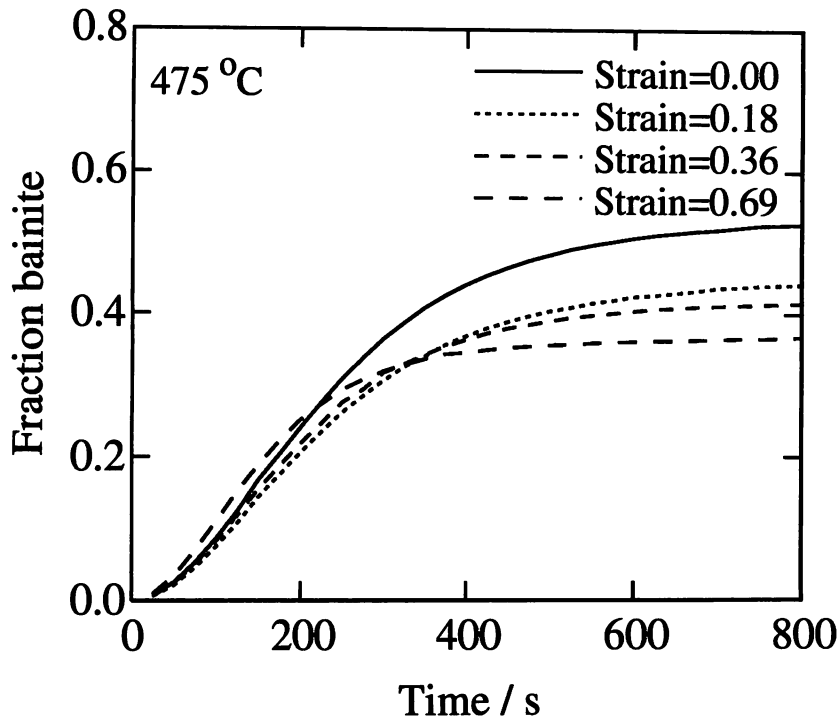


Figure 8.29: The transformation curves of bainite of the Fe-0.12C-2.03Si-2.96Mn (wt.%) steel at 475 °C as a function of prestrain.

0.22 (20% deformation) and 0.51 are shown in Figure 8.30. To match the maximum volume fraction,  $Z$  was set to 0.78 and 0.68 respectively for these strains. The bainite plate thickness for this alloy was calculated to be  $0.088 \mu\text{m}$  at  $350^\circ\text{C}$  and was varied with strain as in earlier calculations. The predictions are in good agreement with the experimental results and a deceleration is predicted throughout the transformation. This appears to be due to a very small prior austenite grain size. When the austenite grains are fine, the total austenite grain boundary area available for nucleation is already very high and the additional nucleation sites induced by deformation do not cause any dramatic increase in the transformation rate.

The predicted transformation kinetics of Fe-0.12C-2.03Si-2.96Mn (wt.%) steel at  $475^\circ\text{C}$  when the initial austenite grain size is taken as  $40 \mu\text{m}$  is presented in Figure 8.31. The calculations were done for strains of 0 and 0.69; all other parameters were kept same as earlier. It can be seen that the transformation is retarded at all stages when a fine-grained austenite is deformed. Figure 8.31 also shows that for a relatively small austenite grain size ( $40 \mu\text{m}$ ), the acceleration in transformation when only the increased nucleation site density is considered is rather small. In comparison, this acceleration is larger when the grain size is  $135 \mu\text{m}$  (Figure 8.27).

The grain size effect can also explain the continuous cooling results reported in literature. While Zhang and Boyd [1996] found a decrease in the transformation-start temperature of bainite during continuous cooling when the austenite was deformed, Yamamoto *et al.* [1995] found an increase. The cooling rates were sufficiently high to avoid the formation of allotriomorphic ferrite. This is because the starting austenite grain size in the experiments of Zhang and Boyd

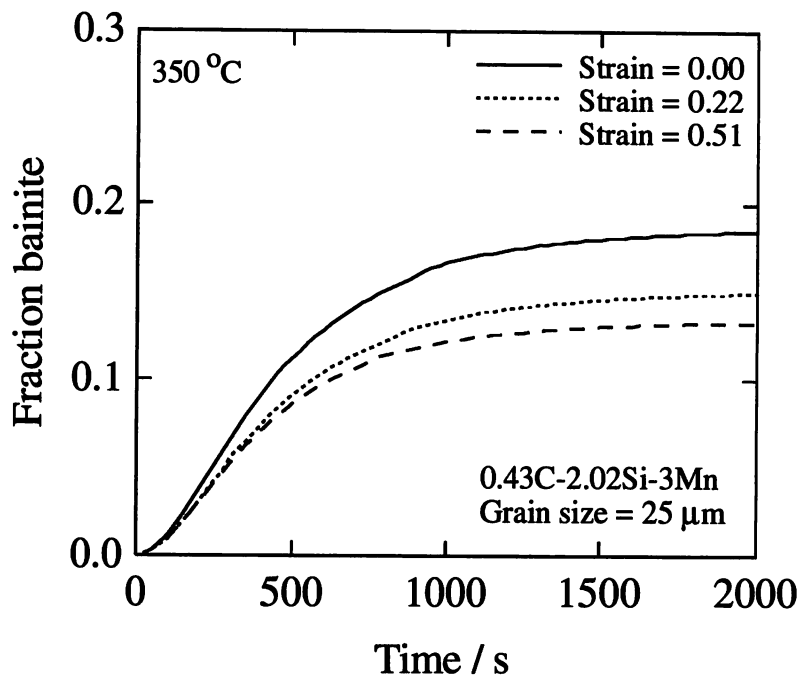


Figure 8.30: The predicted bainite transformation kinetics of the Fe-0.43C-2.02Si-3.0Mn (wt.%) steel at 350 °C. The initial austenite grain size was taken to be 25 μm for these calculations. The results compare well with the experiments of Yang *et al.* [1996].

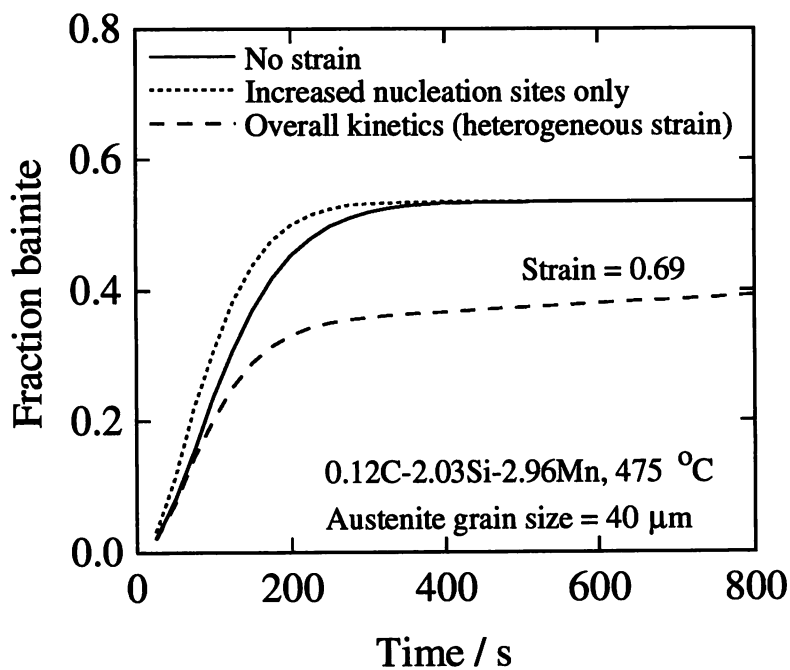


Figure 8.31: The bainite transformation curves of the Fe-0.12C-2.03Si-2.96Mn (wt.%) steel at 475 °C. The initial austenite grain size was taken to be 40 μm for these calculations.

was 21  $\mu\text{m}$  whereas it was 200  $\mu\text{m}$  in the work of Yamamoto *et al.* The deformation is expected to retard the bainite kinetics in the former case while it would accelerate the transformation in the latter.

### 8.4.3 Effect of Transformation Temperature

The calculated curves of the Fe–0.12C–2.03Si–2.96Mn (wt.%) steel for isothermal transformation at 450 °C and 500 °C are given in Figure 8.32 for strains of 0 and 0.69. The bainite plate thickness was varied with strain in a way similar to that at 475 °C. The extent of stabilisation ( $\phi_S$ ) is predicted to be almost the same at all the transformation temperatures. The experiments indicate that a smaller fraction of austenite is stabilised by deformation at a higher supercooling below the  $B_S$  temperature. At lower transformation temperatures, the driving force for growth is higher and the deformation-induced defects are less effective in restricting the plate growth. It can then be said that for a given strain, the stabilisation is manifested in a smaller volume fraction of austenite at a lower temperature. Exactly the reverse is true at a high transformation temperature. The microstructure of the samples deformed and transformed at 500 °C and 450 °C shown in Figures 8.12 and 8.16 confirms this. The calculations with  $Z = 0.75$  for 450 °C and  $Z = 0.1$  for 500 °C are shown in Figure 8.33. The predictions are now in close agreement with the experiments. The observed dilatation at 500 °C for a strain of 0.69 was negligibly small and the predicted retardation in the beginning of the reaction is consistent with the experimental results.

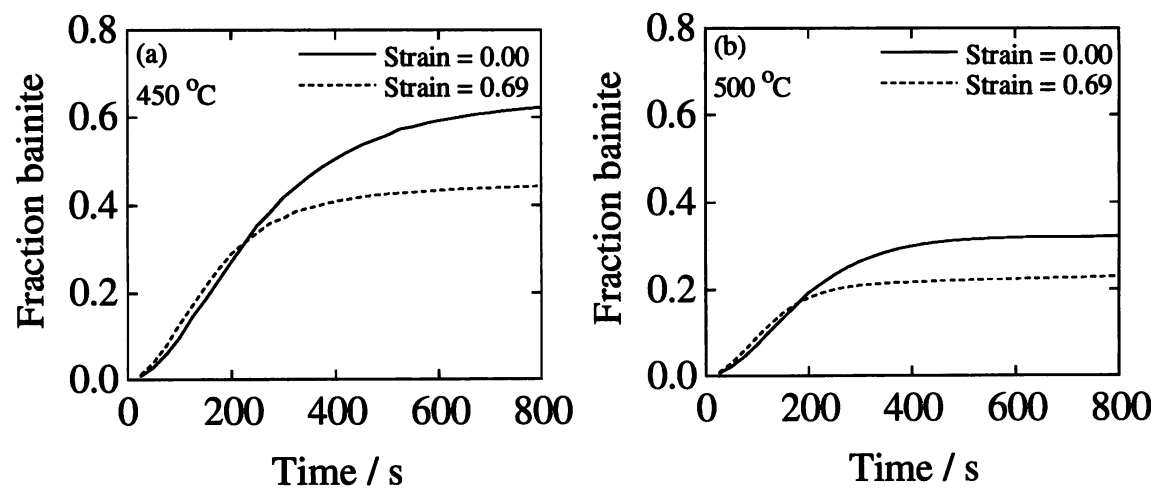


Figure 8.32: The calculated bainite kinetics after deformation. The bainite plate thickness was varied with strain as in the case of 475 °C. (a) 450 °C, with  $a'_b = 0.059 \mu\text{m}$  and (b) 500 °C, with  $a'_b = 0.067 \mu\text{m}$ . The parameter  $Z$  was taken as 0.65 for a strain of 0.69.

The above argument also explains why at the lowest transformation temperature (400 °C) deformation caused a small increase in the volume fraction of bainite (Figure 8.7). The microstructures presented in Figures 8.10b and 8.17 reveal that deformation had little effect at this temperature. The driving force at this temperature is so large that there is only a small

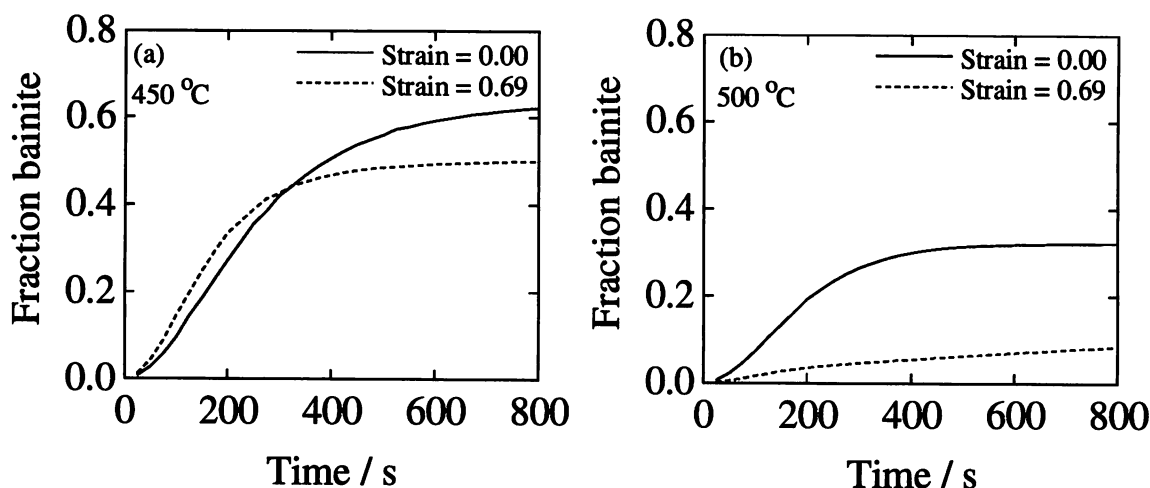


Figure 8.33: The predicted bainite transformation curves after taking into account the effect of transformation temperature on the degree of austenite stabilisation. (a) 450 °C ( $a'_b = 0.059 \mu\text{m}$ ,  $Z = 0.75$ ) and (b) 500 °C ( $a'_b = 0.067 \mu\text{m}$ ,  $Z = 0.1$ ).

effect of deformation on the plate thickness. Alternatively speaking, stabilisation is achieved in only a small fraction of austenite. This is more than compensated by an increase in the number of nucleation sites so that the net volume fraction of bainite increases.

## 8.5 Conclusions

- (1) The plastic deformation of austenite has been confirmed to stabilise it against the bainite transformation. The deformation increases the number density of nucleation sites but each nucleus then transforms to a smaller amount of bainite so that the overall extent of transformation may be reduced. The extent of stabilisation increases with prestrain and transformation temperature.
- (2) The martensite that forms from the carbon-enriched austenite is also mechanically stabilised.
- (3) A decrease in the number density of nucleation sites as the reaction progresses leads to the exhaustion of the sites. This accounts for the smaller limiting fraction of bainite in the deformed austenite.
- (4) It is found that the only way of explaining the fact that deformation at first can accelerate transformation whilst the later stages are retarded relative to undeformed austenite is to assume that the distribution of plastic strain is not homogeneous. Some regions of austenite are then stabilised whereas others are not. The model is able to explain why for a fine austenite grain size the transformation is retarded at all stages.

## Chapter Nine

# Transformation Strain Recovery During Stress-affected Cyclic Transformation

### 9.1 Introduction

The growth of Widmanstätten ferrite and bainite causes an invariant-plane strain shape deformation the shear component of which is much larger than the dilatational component [Bhadeshia, 1995]. However, when conducting stress-free transformation experiments on polycrystalline samples, the transformation shears average out on a macroscopic scale. All that is detected dilatometrically is the small change in volume. This is not the case when the microstructure is not random, *e.g.*, when an external stress favours the formation of certain variants over others. The effect of transformation shear will then be detected [Bhadeshia *et al.*, 1991; Babu and Bhadeshia, 1992; Matsuzaki *et al.*, 1994; Bhadeshia, 1995]. The purpose of the work reported in this chapter was to confirm this by some cyclic transformation experiments.

### 9.2 Experimental Method

The composition of the steel used for the study was: Fe-0.17C-0.25Si-0.88Mn-0.022P (wt.%). 8 mm diameter and 12 mm long samples were machined for testing in *Thermecmastor Z* thermomechanical simulator, the details of which were described in chapter eight.

For all the tests, the samples were heated to 1300 °C and held there for 300 seconds in order to obtain austenite. Following austenitisation, the samples were cooled and three different experiments were carried out:

- (1) Cooling was stopped at 400 °C (the transformation was found to be over before this temperature) and the sample was reheated back to 1000 °C to study the reverse transformation from bainite to austenite. The sample was finally cooled to room temperature.
- (2) The thermal cycle was the same as in 1 above. However, during cooling from 1300 °C a uniaxial compressive stress in the range of 0–40 MPa was applied at 800 °C (no transformation was detected above this temperature at the relevant cooling rate). The stress was maintained as the sample was cooled to 400 °C so that the transformation took place under the influence of stress. The stress was removed at 400 °C when reheating was started, as in cycle 1.
- (3) Repetition of cycles 1 and 2 without the reheating part to observe the development of microstructure.

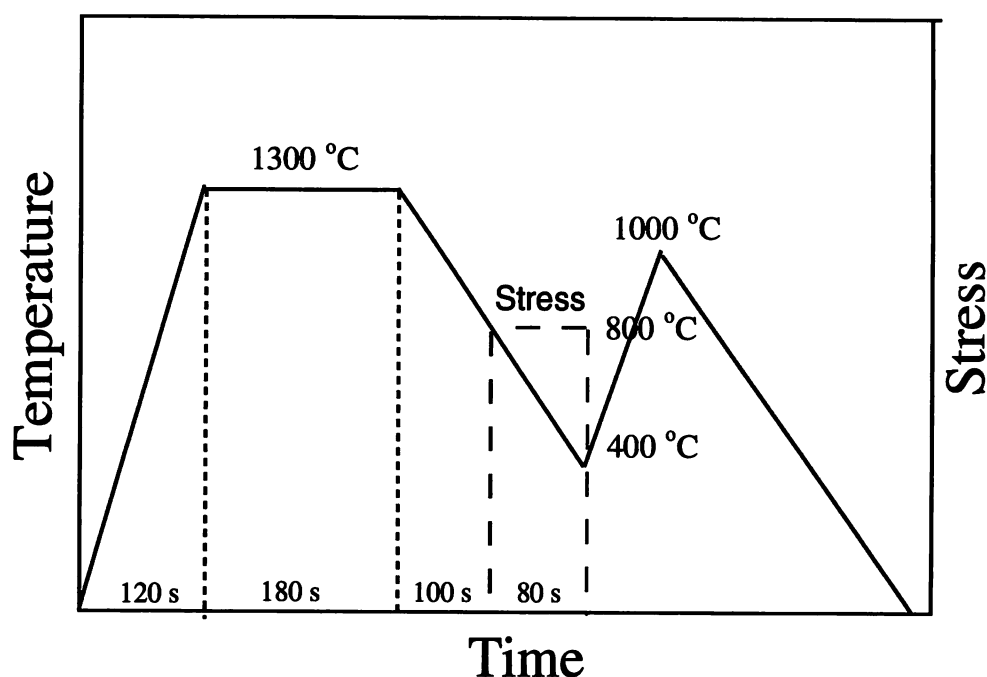


Figure 9.1: Schematic illustration of the test cycles.

All the heating and cooling rates were maintained at  $10^{\circ}\text{C s}^{-1}$  and  $5^{\circ}\text{C s}^{-1}$  respectively. The test cycle is illustrated in Figure 9.1.

### 9.3 Results and Discussions

The dilatation curves corresponding to the cycles 1 and 2 described above are presented in Figures 9.2 and 9.3 (for a stress of 40 MPa) respectively. The transformation-start and finish temperatures for a cooling rate of  $5^{\circ}\text{C s}^{-1}$  were found to be  $650^{\circ}\text{C}$  and  $500^{\circ}\text{C}$  respectively. The microstructure consisted of Widmanstätten ferrite and bainite (Figure 9.4).

Interesting results were obtained when transformation was allowed to occur under the influence of stress. A stress of 40 MPa caused a small plastic strain at  $800^{\circ}\text{C}$ . The transformation was found to start at somewhat higher temperature. Moreover, the radial transformation strain during cooling was measured to be much larger (Figure 9.3a) than that observed during cooling without the application of any stress (Figure 9.2a). They were  $10.89 \times 10^{-3}$  and  $2.13 \times 10^{-3}$  respectively. However, in both the cases during reheating, the strain due to reverse bainite to austenite transformation was observed to be the same (within the limits of experimental error) and small. It was  $1.24 \times 10^{-3}$  in the former case and  $1.42 \times 10^{-3}$  in the latter. The transformation strains were measured at the same temperature by extrapolation. The procedure of extrapolation to measure the transformation strain at a given temperature is illustrated in Figure 9.5. The reheating was performed without any stress in both the cases. The transformation of bainite or Widmanstätten ferrite to austenite takes place by a reconstructive mechanism involving a simple volume change only and an applied stress is not expected to have any significant effect.

Similar results were obtained at lower values of stress. Stresses up to 20 MPa caused little



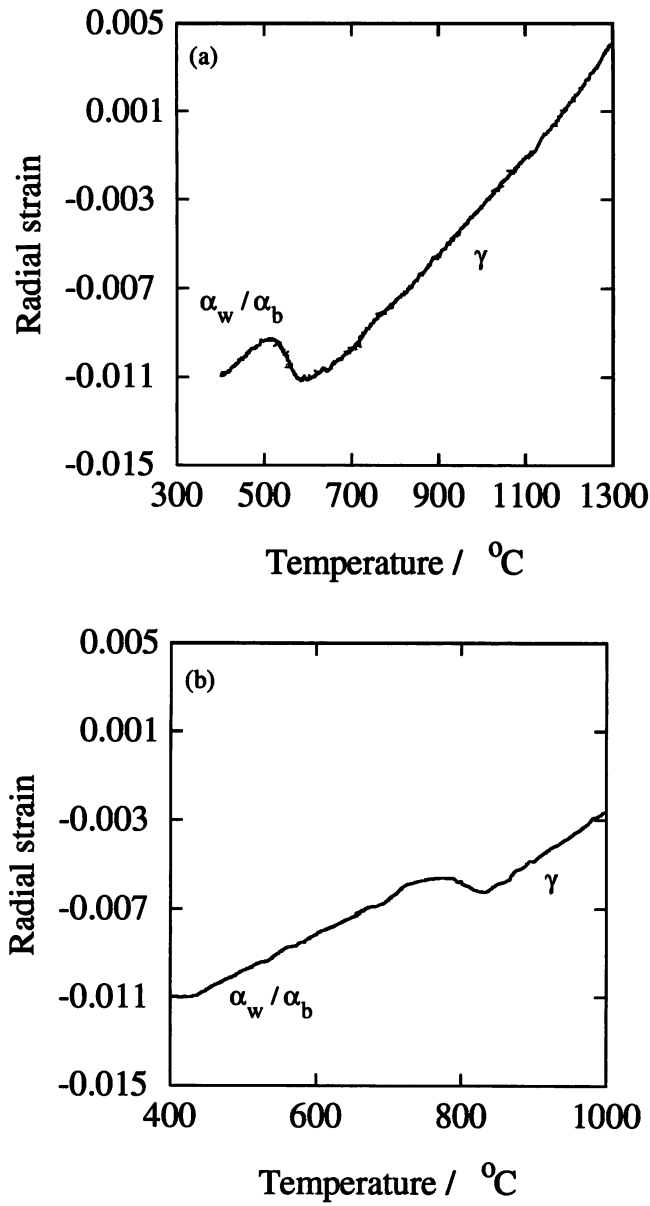


Figure 9.2: The change in radial strain corresponding to thermal cycle 1. (a) During cooling, without stress and (b) during reheating.

plastic strain. The dilatation recorded during cooling under a variety of stress is illustrated in Figure 9.6. The transformation strain increases with the applied stress during cooling while it remains constant during reheating.

The reheating results show that the amount of transformation during cooling with and without the stress was the same. Therefore, the larger transformation strain observed during cooling under the influence of stress does not reflect any increase in the extent of transformation. The explanation for this has to be found somewhere else – in the mechanism of displacive transformation.

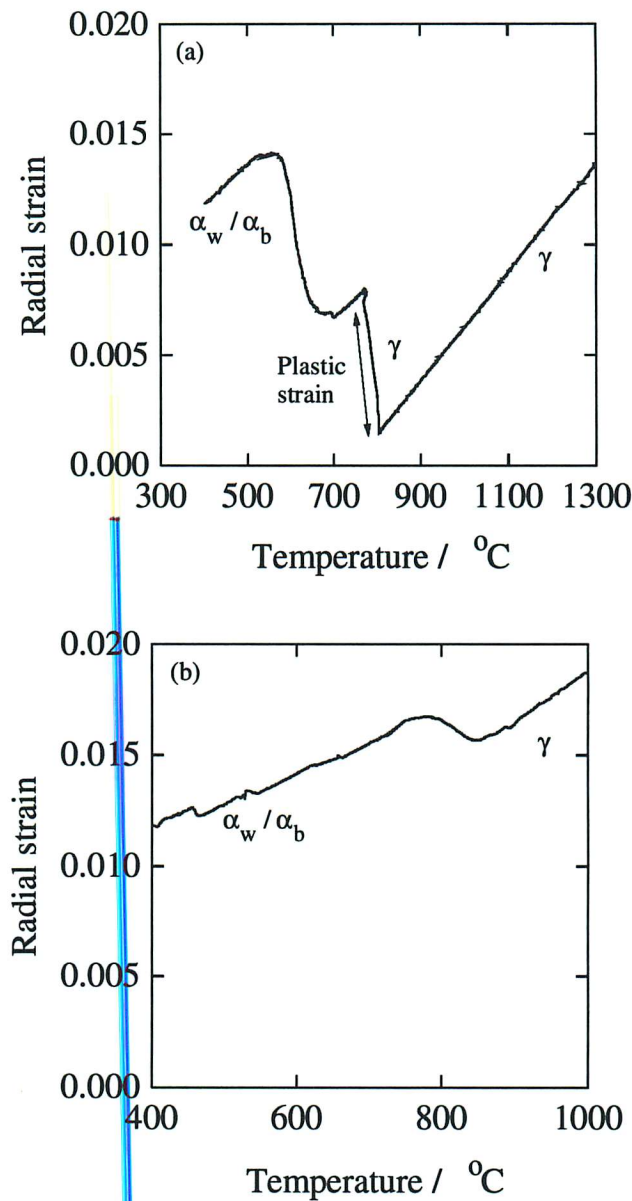


Figure 9.3: The observed radial strain corresponding to thermal cycle 2. (a) During cooling, with 40 MPa of compressive stress applied at 800 °C, before the onset of transformation and (b) during reheating.

### 9.3.1 The Transformation Strain

The growth of Widmanstätten ferrite and bainite is associated with a change in shape which is invariant-plane strain on the habit plane. The shear component of the shape deformation is much larger than the dilatational component and is directed parallel to the invariant plane whereas the dilatational component is directed along the habit plane normal [Bhadeshia, 1995]. The habit plane and the displacement vector of invariant-plane strain accompanying transformation completely describe the shape change. In general, there are 24 possible variants of this system per austenite grain. When the growth takes place in a randomly oriented polycrystalline, unstressed sample, it has a freedom to randomly choose from one of these 24 possible

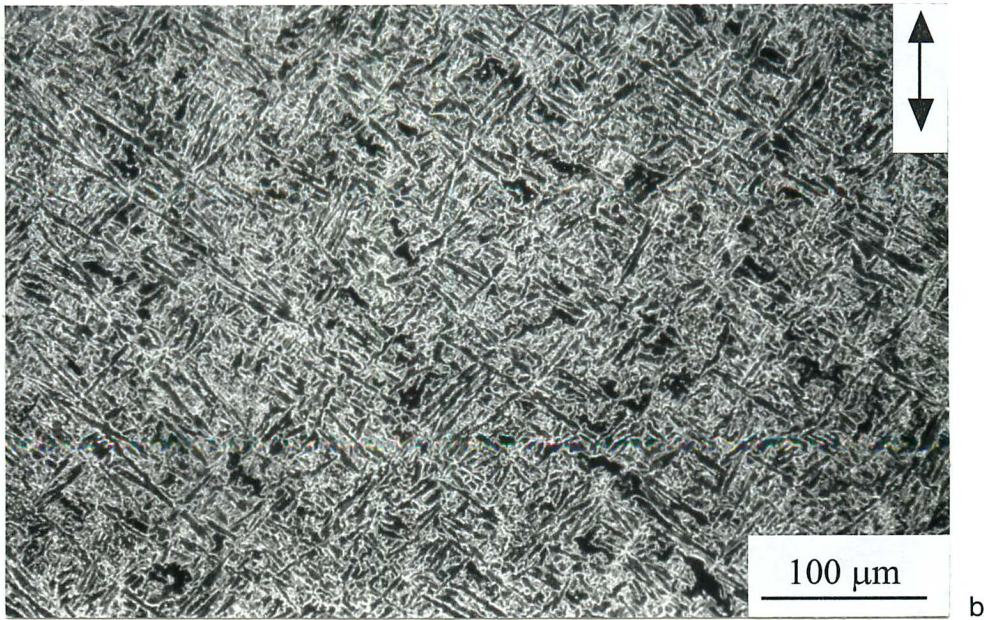


Figure 9.4: The microstructure of the samples cooled from 1300 °C (a) without stress and (b) under 40 MPa of compressive stress, the direction of the stress is shown.

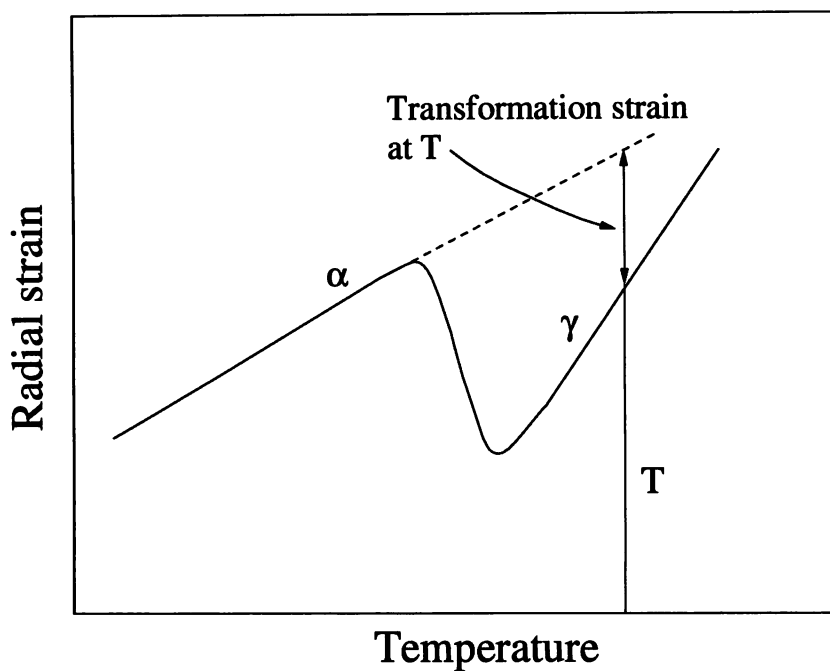


Figure 9.5: Schematic illustration of the procedure adopted for measuring the transformation strain at a given temperature by extrapolation.

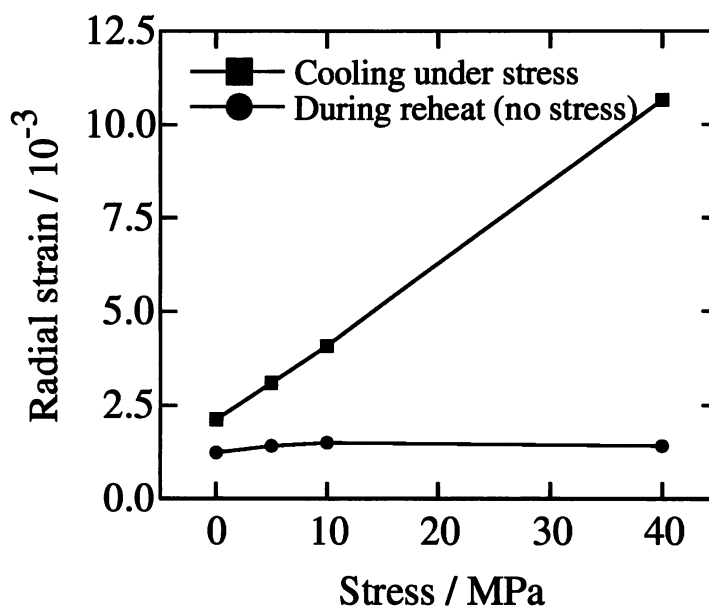


Figure 9.6: The radial strain associated with the formation of Widmanstätten ferrite and bainite when the transformation takes place under the influence of an applied stress. The corresponding strain during the reverse transformation to austenite on reheating is also shown. The transformation to austenite during reheating took place without any applied stress. It should be noted that the strain during reheating is a contraction while that during cooling is an expansion.



variants. All the variants are equally favoured. The shear components of the individual shape deformation of the large number of variants which form along any direction then average out on a macroscopic scale and we observe a small strain as in Figure 9.2a. The transformation strain in this case is isotropic [Bhadeshia *et al.*, 1991].

However, when they form under stress those variants would be preferred which comply best with the stress. The applied compressive stress resolves to give maximum shear stress on planes which are inclined  $45^\circ$  to the stress axis. The mechanical and hence the total driving force is higher for those variants which are close to the plane of maximum shear stress. Thus most plates should grow on this plane. However, since the grains are randomly oriented in an untextured, polycrystalline sample, it is only by chance that for a particular austenite grain orientation the plane of maximum shear stress coincides with one of the permitted habit planes. Nevertheless, those variants which happen to be most parallel to these planes of maximum shear stress are favoured and should form preferentially. In such a case, the probability of averaging out of shear components of individual shape deformation is correspondingly less. This is why the transformation strain was measured to be much higher when the transformation proceeded under the influence of stress. The extent of alignment increases with the applied stress. The above explanation is illustrated schematically in Figure 9.7.

The volume change due to the growth of bainite is not isotropic, the dilatational component being directed normal to the habit plane. In the absence of stress it gets averaged out on a macroscopic scale for reasons already discussed and the volume expansion appears to be isotropic. With the application of stress, the plates are expected to align approximately on planes with the maximum shear stress. However, the large magnitude of the observed radial strain cannot be explained by the dilatational component of the shape change alone. This would require that almost all the bainite sheaves have their habit plane normals parallel to the radial direction, a fact that is not corroborated by the microstructural observation and the volume change measurement along the same direction during the reheating experiment. On the other hand, the magnitude of the observed strain can easily be explained by the shear strain associated with the shape deformation.

### 9.3.2 The Microstructure

The microstructures developed after cooling from the austenite region without and with the application of stress (cycle 3) is shown in Figure 9.4. As already discussed, in the absence of stress all the variants are equally favoured and hence the resultant microstructure is fully chaotic as shown in Figure 9.4a. With the application of stress, growth of selective variants of bainite led to the development of a less chaotic microstructure (Figure 9.4b). Any large scale alignment could not be observed because of the small magnitude of the applied stress.

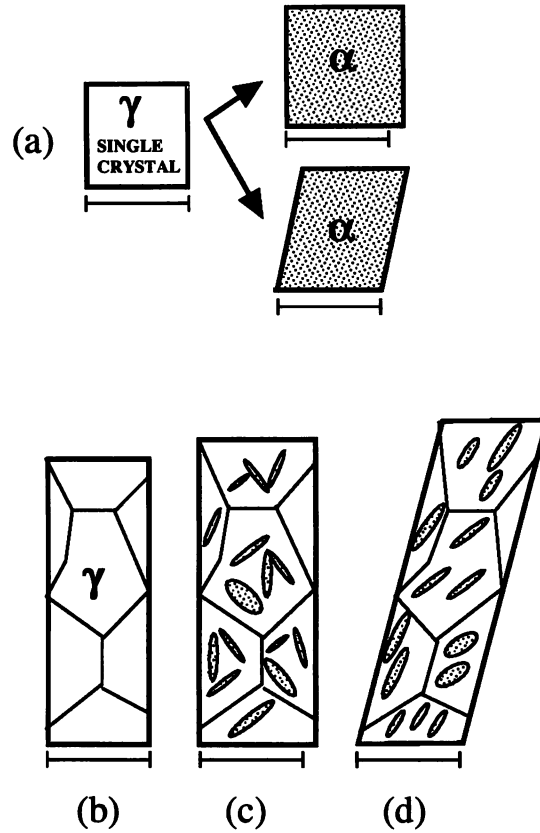


Figure 9.7: Schematic illustration of the shape change associated with phase transformations. (a) Simple isotropic expansion and invariant-plane strain shape deformation associated with reconstructive and displacive mechanisms of transformations respectively. A polycrystalline sample of austenite (b), which transforms by a displacive mechanism into a random set of plates of ferrite resulting in averaging out of the shear components (c), and into an organised set of plates where the shear components reinforce (d). After Bhadeshia [1995].

#### 9.4 Conclusions

The radial strain during transformation to Widmanstätten ferrite and bainite was measured and it was found that the magnitude of the strain was much larger when the transformation took place under the influence of stress than when it occurred in the absence of any stress. The strain associated with reverse transformation to austenite was the same in both the cases (with and without the stress) signifying that the amount of bainite formed during cooling was the same in both the cases. The results reveal the shear component of the shape deformation of displacive transformation. It is impossible to rationalise the results by a reconstructive mechanism of transformation.

## Chapter Ten

# Estimation of Bainite Plate Thickness in Low-alloy Steels

### 10.1 Introduction

The microstructure of bainite consists of fine plates of ferrite, growing in clusters known as sheaves. Within each sheaf the plates are parallel and in identical crystallographic orientation, each with a well-defined crystallographic habit plane. The fine plates within a sheaf are known as sub-units. Their thickness is typically a fraction of a micrometer. It was pointed out in chapter six that the volume of the sub-units together with their nucleation rate determines the kinetics of bainite transformation. With the assumption of a constant aspect ratio, the plate volume was shown to depend on its thickness. It is therefore important to be able to calculate the thickness for a given chemical composition and reaction temperature. Furthermore, since it is the thickness rather than the plate length which primarily determines the mean free slip distance [Daigne *et al.*, 1986], there is considerable technological interest in understanding and controlling the scale of the microstructure.

There are well established trends reported in the published literature. For example, the aspect ratio of sheaves is known to decrease with the transformation temperature but is not sensitive to the substitutional alloy content, at least for the low-alloy steels studied [Speich, 1962; Irvine and Pickering, 1965; Hawkins and Barford, 1972]. Other evidences have been reviewed by Bhadeshia [1992]; the general trend is that the sub-unit and the sheaf width increases as the transformation temperature is increased whereas the number of sub-units per sheaf decreases with increasing temperature. Similar trends have been observed for martensitic transformations [Ghosh and Raghavan, 1986].

Like martensite, the growth of bainite causes displacements which can, on a macroscopic scale, be described by an invariant-plane strain (IPS). The invariant-plane is the habit plane of the plate [Srinivasan and Wayman, 1968; Ko and Cottrell, 1952]. The strain is a large shear deformation (about 0.26) on the habit plane and a smaller dilatational strain (about 0.03) directed normal to the habit plane. The magnitude of the strain is so large that the transformation product is constrained to be in the form of a thin plate, a shape which minimises the strain energy when the plate is elastically accommodated.

The shape change is not always elastically accommodated, particularly when the martensite or bainite transformation occurs at an elevated temperature where the austenite has a low yield strength. Direct observations reveal the plastic relaxation in the austenite adjacent to a

plate of bainite, as illustrated schematically in Figure 10.1 [Swallow and Bhadeshia, 1996]. The dislocation debris associated with the plastic deformation resists the further advance of the interface, the resistance being largest when the austenite is strong. Consequently, the strength of austenite must be an important factor in controlling the ultimate thickness of bainite plates. The plates are expected to be thicker at higher temperatures when the yield strength of the austenite remains low in spite of the plastic relaxation. Dynamic recovery may also play a role but since this can only weaken the austenite, its effect will be similar to that of the temperature dependence of the yield strength.

On the other hand, if the austenite is sufficiently strong, then the plates are expected to be elastically accommodated. They may then maintain elastic equilibrium with the matrix, continuing to thicken until the strain energy balances the available free energy. If the plates are allowed to grow freely (*i.e.* without impingement) they would then be expected to be thicker at lower temperatures where the driving force is largest. Not surprisingly, this contradicts the experimental data for bainite, which certainly is not in thermoelastic equilibrium with the matrix.

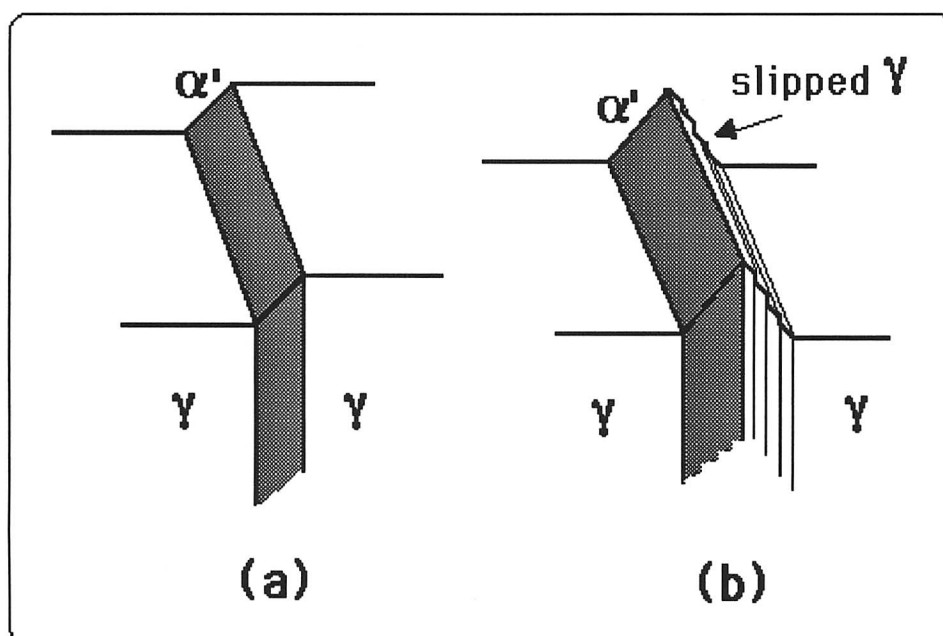


Figure 10.1: Schematic illustration of a perfect invariant-plane strain surface relief (a), and one where plastic relaxation occurs in the adjacent austenite (b) [Bhadeshia, 1992].

There is a further effect concerned with impingement between adjacent particles which might determine the size of bainite plates. A large nucleation rate must naturally refine the microstructure.

The purpose of the present work was to relate some recently published data [Chang and Bhadeshia, 1996] on the thickness of bainite sub-units to austenite strength, temperature and



the chemical driving force for nucleation which are treated as *independent* variables. The relationship was then used for the bainite kinetics model.

### 10.2 Data

The bainite sub-unit data are from a set of isothermal experiments on silicon-rich steels where the precipitation of carbides is suppressed [Chang and Bhadeshia, 1996]. The microstructure thus consists of just bainitic ferrite and austenite, together with any martensite which forms when the austenite is cooled. The alloys studied were listed in chapter two and  $\lambda_{ave}$  reproduced here in Table 10.1.

Alloy	C	Si	Mn	Ni	Cr	P	S	N
A	0.27	1.98	2.18	0.02	1.90	0.015	0.012	0.0054
C	0.46	2.10	2.15	0.02	–	0.014	0.013	0.0062
E	0.10	1.77	2.12	2.00	0.02	0.013	0.012	0.0053
F	0.26	1.85	2.10	0.02	–	0.015	0.013	0.0086
G	0.26	1.93	2.04	0.02	1.02	0.015	0.010	0.0069
H	0.10	1.63	1.99	0.03	1.97	0.013	0.011	0.0080

Table 10.1: The composition (wt.%) of the alloys used in the measurements of bainite plate thickness by Chang and Bhadeshia [1996].

The plate thicknesses are listed as a function of the transformation temperature and the other variables in Table 10.2. It should be pointed out that the measurements were stereologically corrected as described by Chang and Bhadeshia [1996]. The austenite strength calculations included in the table are based on an empirical model by Young and Bhadeshia [1994], where the yield strength is expressed as follows:

$$\sigma_y^\gamma = (1 - 0.26 \times 10^{-2} T_r + 0.47 \times 10^{-5} T_r^2 - 0.326 \times 10^{-8} T_r^3) \times 15.4(4.4 + 23w_C + 1.3w_{Si} + 0.24w_{Cr} + 0.94w_{Mo} + 32w_N) \tag{10.1}$$

where  $T_r = T - 298$ ,  $T$  is the temperature in Kelvin and  $w$  represents the concentration of the element identified by the subscript, in weight percent. The yield strength of the austenite is given in units of MPa.

The chemical free energy change (driving force) available for nucleation was calculated as prescribed by Bhadeshia [1982b].

The original data of Chang and Bhadeshia [1996] are illustrated in Figure 10.2. At a given transformation temperature, the plates are thicker when the strength of the steel is low (steels E and H). Similarly, it can be argued that the finest plate thickness is obtained for the steel with the highest strength (steel C). The plate thickness of the other steels with intermediate but similar strengths lies between these two extremes.

Alloy	Temp. °C	Free energy J mol <sup>-1</sup>	Austenite strength, MPa	Bainite plate thickness, $\mu\text{m}$
A	300	-1669	121.8	0.053
	315	-1589	119.5	0.059
	330	-1503	117.4	0.083
	350	-1392	114.8	0.110
	380	-1225	111.4	0.130
	400	-1115	109.3	0.170
C	260	-2174	167.2	0.046
	270	-2104	164.7	0.055
	305	-1855	156.9	0.059
	320	-1755	153.9	0.06
	345	-1595	149.6	0.064
	370	-1454	145.8	0.093
	400	-1285	141.8	0.115
	430	-1118	138.3	0.122
E	360	-1399	75.4	0.170
	380	-1289	73.9	0.180
	430	-1015	70.8	0.210
	460	-850	69.2	0.240
F	350	-1636	108.5	0.092
	370	-1525	106.3	0.098
	400	-1358	103.4	0.120
	430	-1193	100.8	0.190
G	330	-1647	113.5	0.070
	350	-1536	110.9	0.090
	370	-1431	108.7	0.110
	400	-1254	105.7	0.120
	430	-1088	103.1	0.150
H	380	-1316	76.0	0.220
	410	-1147	74.0	0.240
	430	-1038	72.8	0.330

Table 10.2: The chemical free energy [Bhadeshia, 1982b], the austenite strength [Young and Bhadeshia, 1994] and the bainite plate thickness at different transformation temperatures [Chang and Bhadeshia, 1996].

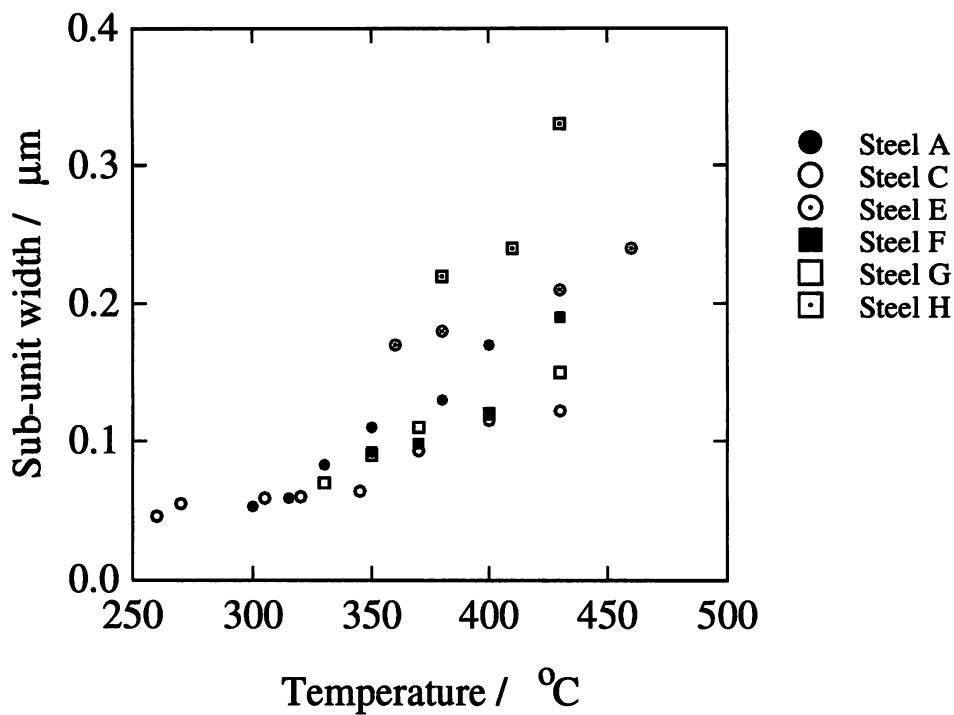


Figure 10.2: The variation in bainite plate thickness as a function of transformation temperature as reported by Chang and Bhadeshia [1996]. Note that a variation in the transformation temperature also causes a change in the austenite strength and the chemical driving force. Thus the variation illustrated is not due to the effect of temperature alone.

One difficulty is that although the strength, temperature and driving force are expected to influence the plate thickness, the explicit dependence of the thickness on these variables is not known. The usual regression methods do not help in this respect since they require an assumed relationship to begin the analysis. The regression analysis was therefore conducted with a computer based neural network method which does not require a prior choice of the relationship between the input and output variables. The technique is introduced briefly – detailed descriptions and examples can be found elsewhere [MacKay, 1992a, 1992b, 1994, 1995, 1997; Bhadeshia *et al.*, 1995; Fujii *et al.*, 1996].

### 10.3 The Technique

Neural networks are parameterised non-linear models used for empirical regression and classification modelling. Their flexibility makes them able to discover more complex relationships in data than traditional linear statistical models.

A neural network is ‘trained’ on a set of examples of input and output data. The outcome of training is a set of coefficients (called weights) and a specification of the functions which in combination with the weights relate the input to the output. The training process involves a search for the optimum non-linear relationship between the inputs and the outputs and is computer intensive. Once the network is trained, estimation of the outputs for any given inputs

is rapid.

One of the difficulties with blind data modelling is that of ‘overfitting’, in which spurious details and noise in the training data are overfitted by the model. This gives rise to solutions that generalise poorly. MacKay [1992a, 1992b, 1994, 1995, 1997] and Neal [1996] have developed a Bayesian framework for neural networks in which the appropriate model complexity is inferred from the data.

The Bayesian framework for neural networks has two further advantages. First, the significance of the input variables is automatically quantified. Consequently the model-perceived significance of each input variable can be compared against metallurgical theory. Second, the network’s predictions are accompanied by error bars which depend on the specific position in input space. These quantify the model’s certainty about its predictions.

As described earlier, the input variables considered to influence the plate thickness include (1) the transformation temperature, (2) the nucleation rate as represented by the free energy available for nucleation ( $\Delta G_m$ ) at the transformation temperature and (3) the strength of austenite at the temperature of transformation. The variation of elastic modulus over the temperature range considered here is negligible [Aaronson *et al.*, 1975].

The variables are listed in Table 10.3. The plate thickness data were available for a total of 30 combinations of temperatures and the alloys listed above. All of these were included in the analysis.

Variable	Range	Mean	Standard Deviation
Temperature, °C	260–460	368.5	50.31
$-\Delta G_m$ , J mole <sup>-1</sup>	2174–850	1418	308.6
Austenite strength, MPa	69.24–167.20	112.9	29.28
Bainite plate thickness, $\mu\text{m}$	0.046–0.33	0.13	0.069

Table 10.3: The variables used in the analysis.

### 10.4 The Analysis

Both the input and output variables are first normalised within the range  $\pm 0.5$  as follows:

$$x_j^N = \frac{x_j - x_{min}}{x_{max} - x_{min}} - 0.5 \tag{10.2}$$

where  $x_j^N$  is the normalised value of  $x_j$  which has maximum and minimum values given by  $x_{max}$  and  $x_{min}$  respectively.

Linear functions of the normalised inputs  $x_j^N$  are operated on by a hyperbolic tangent transfer function:

$$h_i = \tanh \left( \sum_j w_{ij}^{(1)} x_j^N + \theta_i^{(1)} \right) \tag{10.3}$$

so that each input contributes to every hidden unit (Figure 10.3). The bias is designated  $\theta_i^{(1)}$  and is analogous to the constant that appears in linear regression. The strength of the transfer function is in each case determined by the weight  $w_{ij}^{(1)}$ . The “output”  $y$  is, in the present case, the plate thickness normalised according to equation 10.2. It is obtained using the following linear operation:

$$y = \sum_i w_{ij}^{(2)} h_i + \theta^{(2)} \quad (10.4)$$

The specification of the network structure, together with the set of weights is a complete description of the formula relating the inputs to the output. The set of weights ( $\mathbf{w}$ ) and biases are determined by training the network over a data set  $\{x_j^m, t^m\}$ , where  $t^m$  is the target value corresponding to the inputs  $x_j^m$ . The training starts with a number of random seeds and involves minimisation of the error function:

$$E_D(\mathbf{w}) = \frac{1}{2} \sum_m [y(x_j^m; \mathbf{w}) - t^m]^2 \quad (10.5)$$

where  $y(x_j^m; \mathbf{w})$  is the predicted value of the output for the given inputs and weights  $\mathbf{w}$ .

Often, regularisation is included so that the error function to be minimised is modified to:

$$M(\mathbf{w}) = \beta_N E_D + \alpha_N E_W \quad (10.6)$$

where  $E_W = \frac{1}{2} \sum w_i^2$ . The additional term  $E_W$  favours small values of  $\mathbf{w}$  and thus encourages the model to find simpler solutions with less tendency to ‘overfit’ noise in the training data. The term  $\beta_N$  defines a noise level,  $\sigma_v^2 = 1/\beta_N$  and  $\alpha_N$  defines weight variance,  $\sigma_w^2 = 1/\alpha_N$ .  $\sigma_v$  is the framework estimate of the noise level of the data. The details of the training procedure are described elsewhere [MacKay, 1992a, 1992b, 1994, 1995, 1997; Bhadeshia *et al.*, 1995; Fujii *et al.*, 1996].

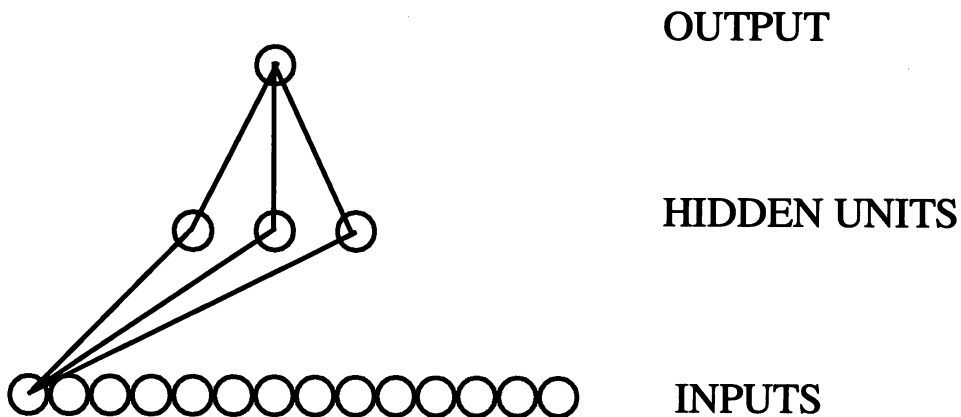


Figure 10.3: A typical network used in the analysis. Only the connections originating from one input unit are illustrated.

## 10.5 Network Training

The network consisted of 3 input nodes, a number of hidden nodes and an output node representing the bainite plate thickness (Figure 10.3). The network was trained using a randomly chosen 15 of the examples from a total of 30 available, the remaining 15 examples being kept aside at first to be used as ‘new’ experiments to test the behaviour of the trained network. This procedure helps avoid over-complex models.

The complexity of the model is controlled by the number of hidden units (Figure 10.4 and Figure 10.5), and the values of the 5 regularisation constants ( $\sigma_w$ ), one associated with each of the 3 inputs, one for biases and one for all weights connected to the output.

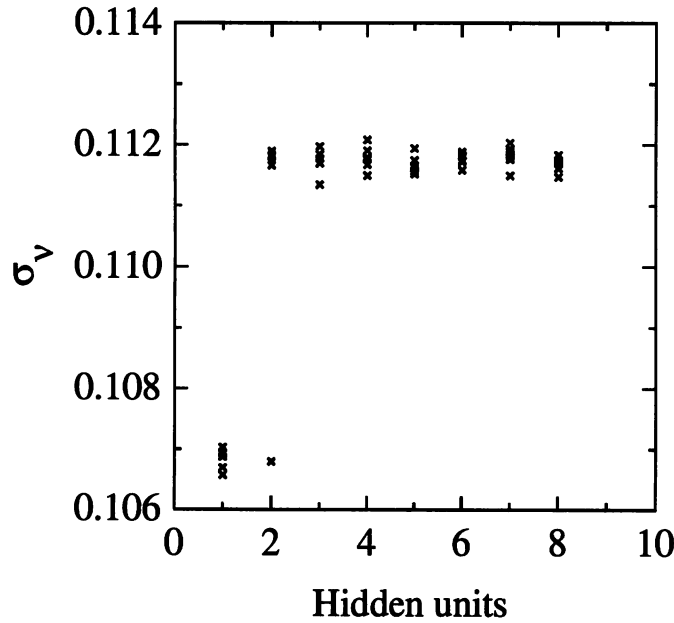


Figure 10.4: Variation in  $\sigma_v$  as a function of the number of hidden units. Several values are presented for each set of hidden units because the training for each network was started with a variety of random seeds.

The inferred noise level of the data shows little variation with the number of hidden units, Figure 10.4. This can simply be because the number of data used for the training were too few. A highly complex model with a large number of hidden units may not be justified, because the model may, in a meaningless way, attempt to fit the noise in the experimental data. The number of hidden units was set by examining the performance of the model on the unseen test data (Figure 10.5). The deviation of the predicted value from the experimental one in the test data set is represented by the test error ( $T_e$ ):

$$T_e = 0.5 \sum_n (y_n - t_n)^2 \quad (10.7)$$

where  $y_n$  is the predicted value and  $t_n$  the measured value of the output variable which is the bainite plate thickness in this case.

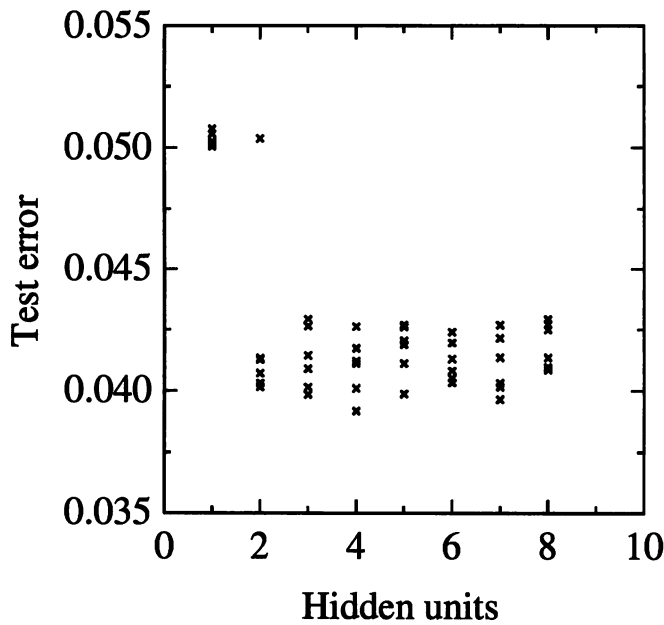


Figure 10.5: The test error as a function of the number of hidden units. Several values are presented for each set of hidden units because the training for each network was started with a variety of random seeds.

Even the test error showed only a small variation with the number of hidden units. A model with four hidden units gave the lowest test error. This model was then chosen to represent the variation in the bainite plate thickness as a function of the input variables.

The agreement between the training and the test data for the best model (4 hidden units, seed=70) is shown in Figure 10.6. The fit appears to be good and similar for both data sets, indicating again that the model is neither too simple nor too complex.

Once the optimum number of hidden units was established, the model was retrained on the entire data set to give a more accurate model. The final degree of agreement is shown in Figure 10.7. The weights which would be required for the use of equations 10.3 and 10.4 in order to calculate the bainite plate thickness are listed in Table 10.4. The inputs and outputs are used as normalised in equation 10.2, so the maximum and minimum values listed in Table 10.3 are necessary in order to normalise the inputs and then unnormalise the output. The computer program which does all these calculations is available on

<http://www.msm.cam.ac.uk/map/neural/programs/plate-b.html>

## 10.6 Application of the Model

The model described above can be used in practice to manipulate the size of bainite plates, in general by altering the alloy chemical composition. The latter influences the austenite strength, driving force and the transformation temperatures, the effects of all of which can be estimated quantitatively using the model. For the moment we use the results of the trained model to study the effect of individual variables on the plate thickness to see whether they make metallurgical sense.

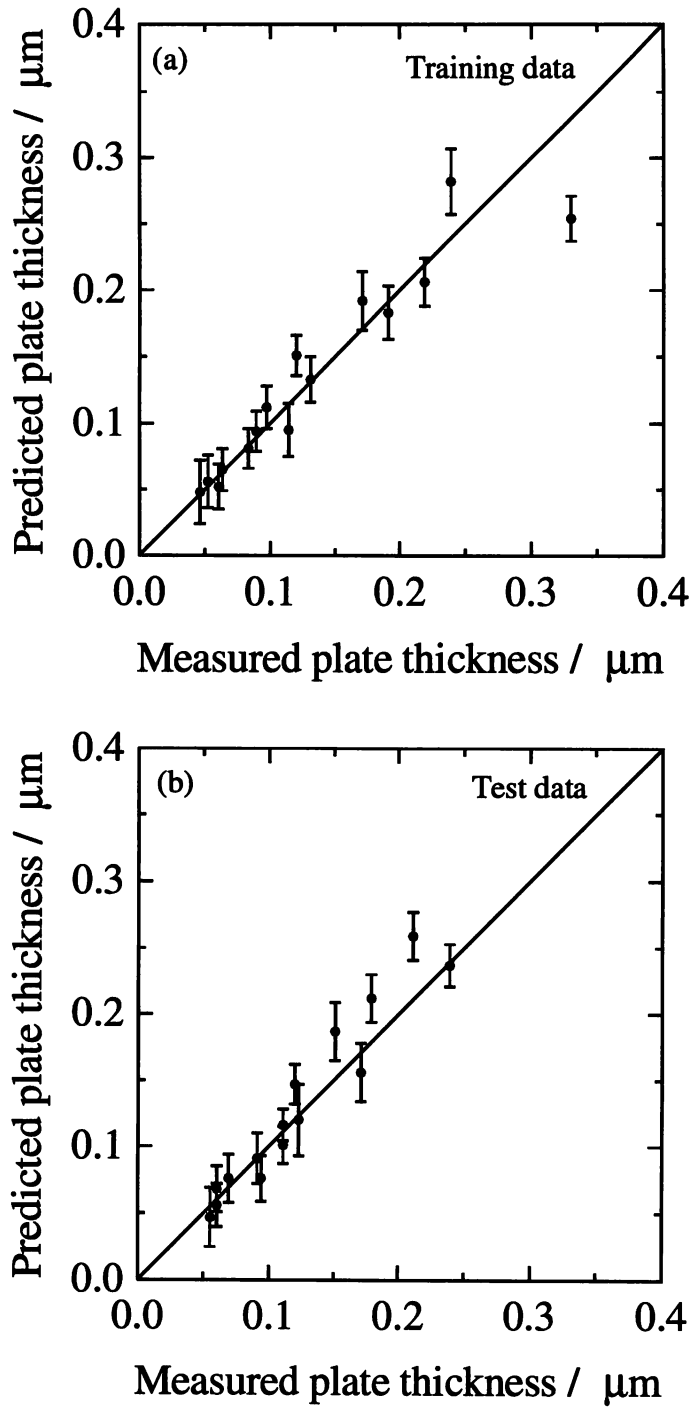


Figure 10.6: (a) Training and (b) test data for the best model. The error bars represent  $\pm 1\sigma$ .

The significance ( $\sigma_w$ ) of each of the variables, as perceived by the neural network, in influencing the plate thickness is illustrated in Figure 10.8. The significance parameter is like the partial correlation coefficient in the multiple regression analysis. A high value of  $\sigma_w$  for a given input parameter implies that this variable explains a relatively large variation in the bainite plate thickness in the data set. Thus, it is interesting to note from Figure 10.8 that



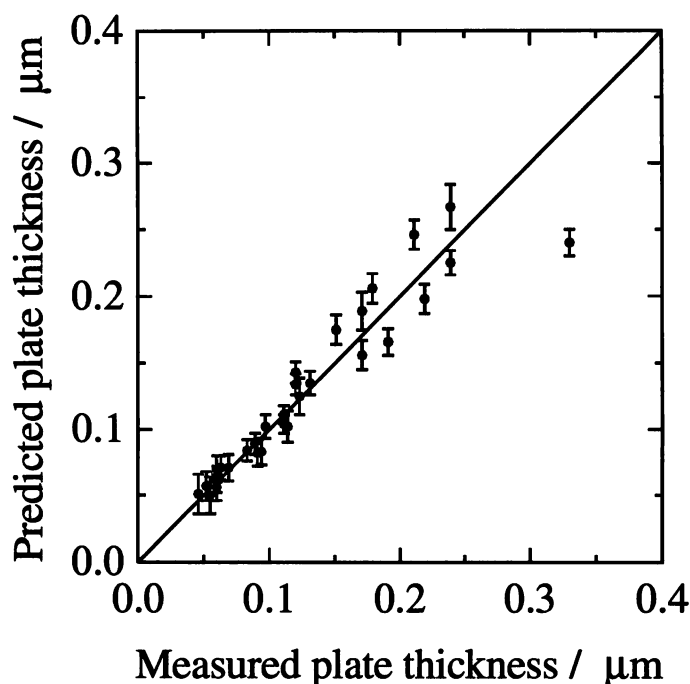


Figure 10.7: Result of training on the whole data set. The error bars represent  $\pm 1\sigma$ .

-0.00144919	-0.0024908	-0.015984	-0.0199077	0.00156831
0.00267663	0.0173535	0.0173944	-0.173165	0.0419401
0.239065	1.38359	0.431789	-0.0746111	-0.524353
1.59167	0.141247	-0.0277307	0.0298074	0.669476
-0.952923				

Table 10.4: The weights for the plate thickness model. The data are arranged in a continuous horizontal sequence in the following order:

$$\begin{aligned}
 &\theta_1^{(1)}, w_{1,1}^{(1)} \dots w_{1,3}^{(1)}, \\
 &\theta_2^{(1)}, w_{2,1}^{(1)} \dots w_{2,3}^{(1)}, \\
 &\theta_3^{(1)}, w_{3,1}^{(1)} \dots w_{3,3}^{(1)}, \\
 &\theta_4^{(1)}, w_{4,1}^{(1)} \dots w_{1,3}^{(1)}, \\
 &\theta^{(2)}, w_1^{(2)} \dots w_4^{(2)}
 \end{aligned}$$

a large part of the variation in the bainite plate thickness in the data set is explained by the variation in the austenite strength. The transformation temperature explains only a small part once the variation in austenite strength and driving force due to the change in temperature are allowed for separately.

The model could then be used to estimate the bainite plate thickness given all the input

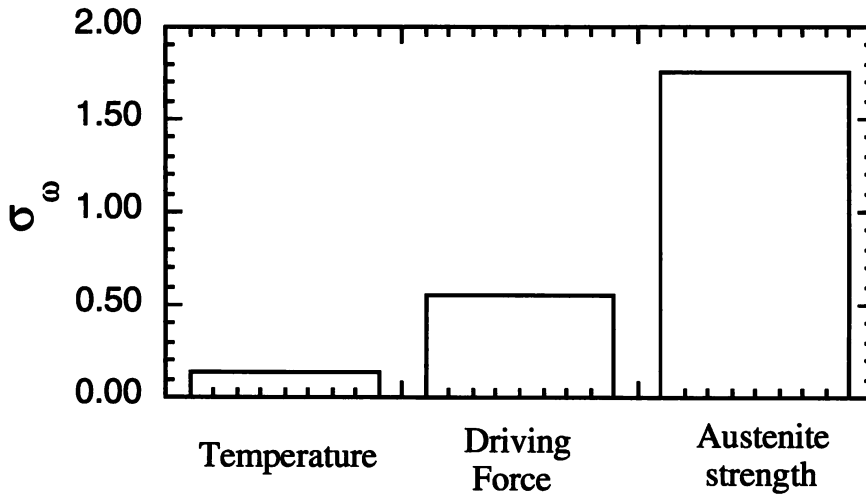


Figure 10.8: The model perceived significance of the input variables in influencing the bainite plate thickness.

variables. The effect of the individual variables is discussed below.

#### 10.6.1 Effect of Temperature

Figure 10.9 shows the effect of temperature alone on the bainite plate thickness at a fixed level of austenite strength and  $\Delta G_m$ . The plate thickness is virtually independent of the transformation temperature *per se*, once the austenite strength and driving force have been taken into account. Therefore, it appears that temperature by itself does not have much of an effect. This may be a reflection of the limited temperature range of the experimental data. For example, it might be expected that dynamic recovery effects become prominent at high temperatures in which case there would be a temperature effect which is independent of the austenite strength and the driving force.

#### 10.6.2 Effect of Driving Force

For a given alloy composition, the driving force available for nucleation of bainite increases as the supercooling below the bainite-start temperature is increased. A large nucleation rate is expected at large supercoolings (low temperatures). This must lead to a refinement of microstructure by impingement effects. Such a trend is indeed found, as illustrated in Figure 10.10. It is emphasised that the model developed is nonlinear with four hidden units, capable of capturing synergistic effects between the input variables. Thus, the slope of the curve in Figure 10.10 may be somewhat different for weaker austenite or for a different temperature.

With this result in mind, the original data of Chang and Bhadeshia [1996] is plotted once again in Figure 10.11, this time as a function of the driving force for nucleation ( $\Delta G_m$ ). The data for most of the high strength steels lie on the same straight line. Once again, at the same driving force level, the plate thicknesses of the weakest alloys are the highest.

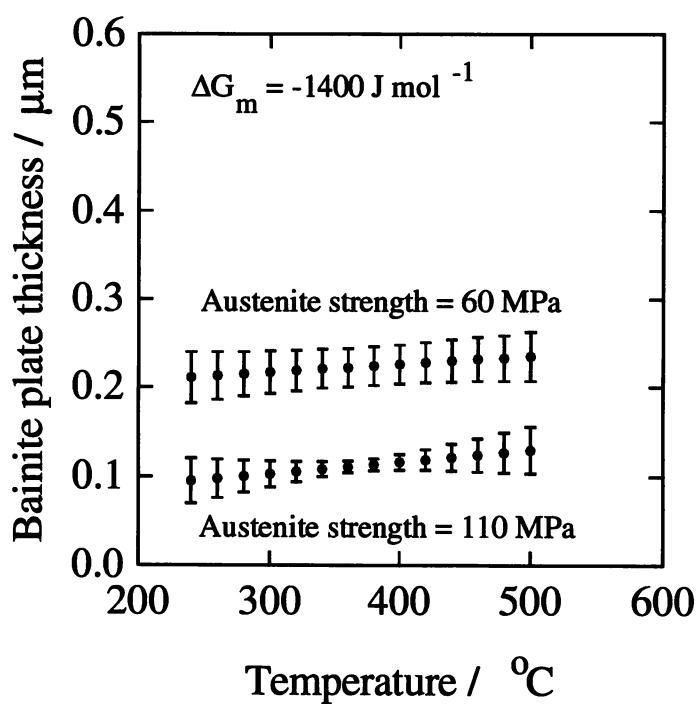
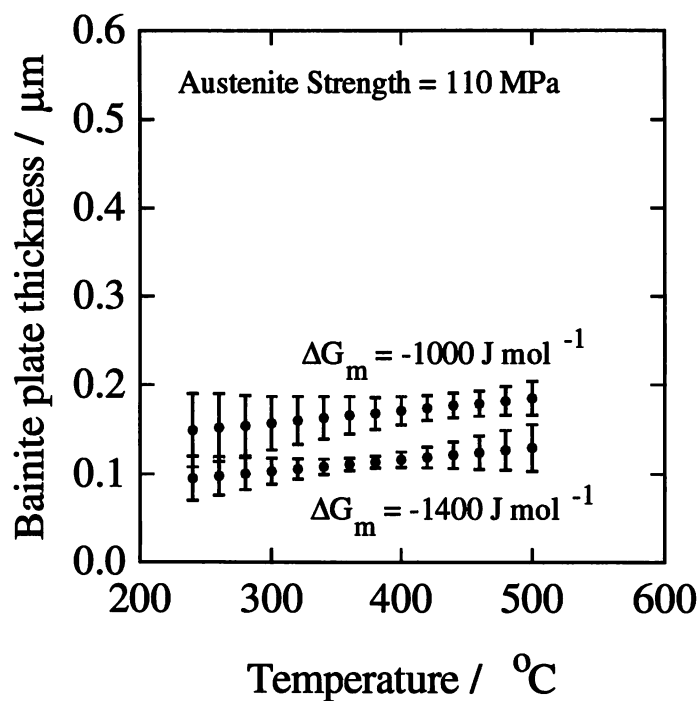


Figure 10.9: The variation of the bainite plate thickness with the transformation temperature, austenite strength and driving force. Note that unlike Figure 10.2, the temperature, strength and driving force are independent variables in this illustration. The error bounds represent  $\pm 1\sigma$  confidence limits.

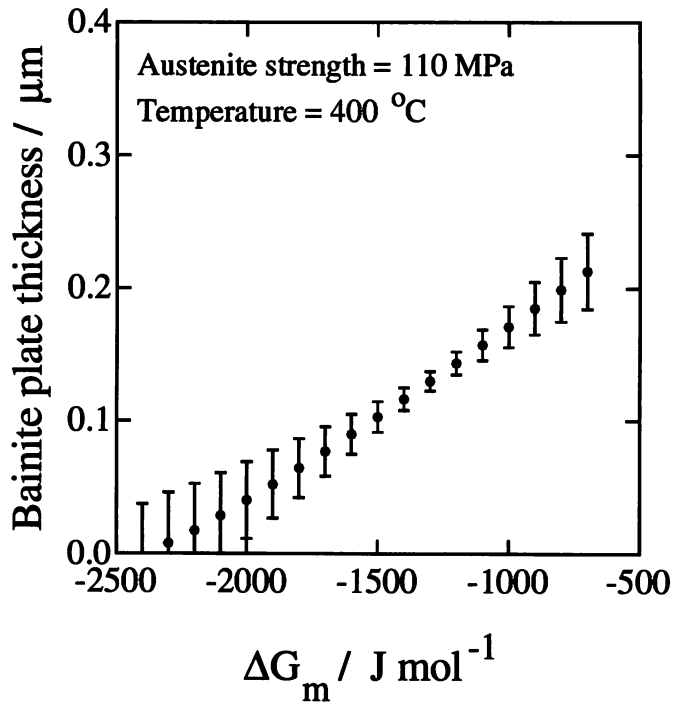


Figure 10.10: The effect of driving force for bainite nucleation on plate thickness. The error bars represent  $\pm 1\sigma$  confidence limits. Driving forces as large as  $-2500 \text{ J mol}^{-1}$  are not expected for the transformation temperature of  $400^\circ\text{C}$ , but the calculations are nevertheless presented for interest.

### 10.6.3 Effect of Austenite Strength

As described earlier, for cases where the shape deformation causes plastic relaxation, weaker austenite will present a smaller resistance to interface propagation. The plate thickness in this limit is therefore expected to decrease with increasingly strong austenite. The model perceives such a relationship, as illustrated in Figure 10.12. The fact that the error bars become very large beyond about 170 MPa is a reflection of the upper limit of the strength in the experimental database and the fact that the data set itself is limited to just thirty points.

## 10.7 Conclusions

It appears that the thickness of bainite plates in silicon-rich alloys depends primarily on the strength of the austenite at the transformation temperature, and the chemical free energy change accompanying nucleation, when these variables are treated independently. This conclusion applies specifically when the shape deformation causes plastic strain in the adjacent austenite. Strong austenite or a large driving force results in finer plates, the former because there is a larger resistance to interface motion and the latter because an increased nucleation rate leads to microstructural refinement.

Temperature does not, in its own right, seem to have a significant effect over the range  $260\text{--}460^\circ\text{C}$ , but it is possible that this situation could change should dynamic recovery effects become prominent.

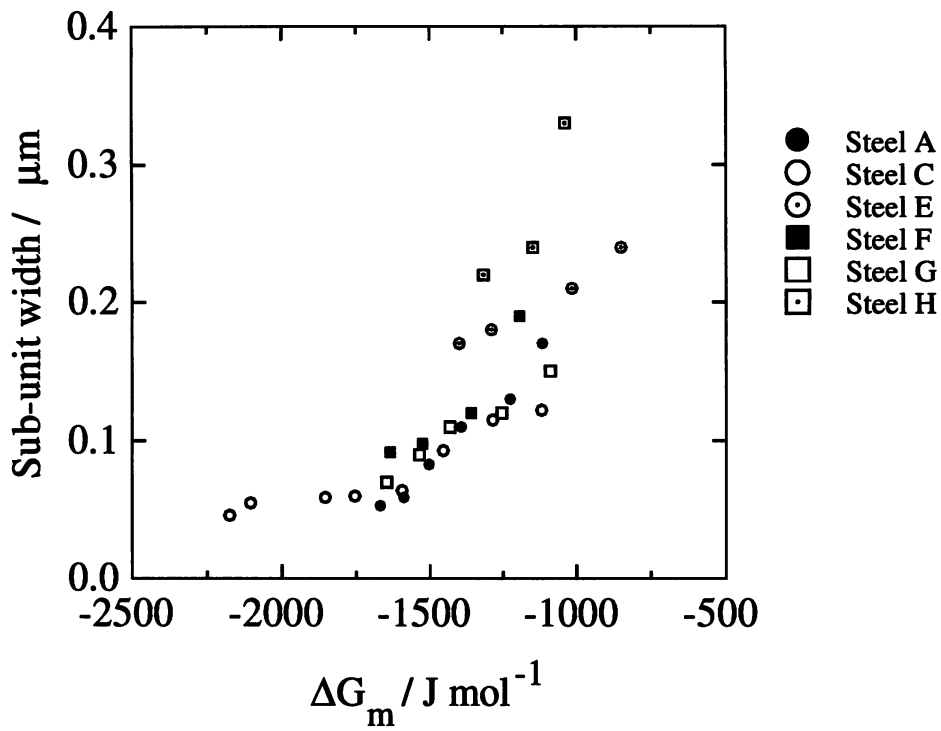


Figure 10.11: The original bainite plate thickness data of Chang and Bhadeshia [1996] replotted as a function of the driving force for nucleation ( $\Delta G_m$ ) at the transformation temperature.

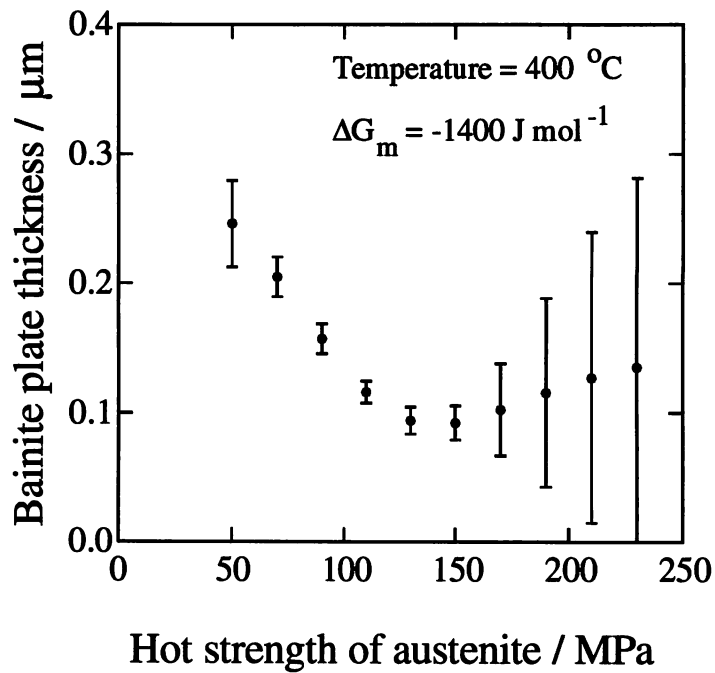


Figure 10.12: The effect of austenite strength at the transformation temperature on the bainite plate thickness. The error bounds are  $\pm 1\sigma$  confidence limits.

## Chapter Eleven

# Neural Network Analysis of Steel Plate Processing

### 11.1 Introduction

Cast steel is usually processed into usable products by severe plastic deformation, frequently using the rolling process which was described briefly in chapter three. The purpose of this deformation is to refine the cast microstructure, to produce the steel in the required shape and to achieve the optimum mechanical properties. The properties depend not only on the deformation but also on the detailed chemical composition in two respects. Firstly, the steel may contain microalloying elements which help control the austenite grain structure and in some cases provide precipitation strengthening [Gladman, 1997]. The other alloying additions such as manganese control the relative stabilities of the austenite and ferrite phases and hence the nature of the austenite transformation products.

When a hot ingot or slab enters a rolling mill, its typical dimensions are so large that it has to be reduced to the required thickness in many separate passes. The purpose of the present work was to develop a model enabling the estimation of strength as a function of a large number of rolling parameters and the chemical composition of the steel. The model is based on the neural network analysis technique with a total of 108 variables. The method was described in the chapter ten and has been dealt with in detail by MacKay [1992a, 1992b, 1994, 1995, 1997]. The variables are introduced below; the work is restricted to steels with a ferrite and pearlite microstructure.

### 11.2 The Database

The neural network method is empirical and hence requires experimental data in order to discover the relationships. The data used were obtained directly from a commercial, instrumented plate rolling mill. Given that the work is focused on a production mill, the variables have to be selected from routine records. The input variables therefore consisted of:

- (1) The slab reheating temperature, which is universally recognised to be important in determining the initial austenite grain size and the temperature of the slab as it progresses through the rolling mill.
- (2) The length of the slab which determines the timing of the rolling process.

- (3) The slab gauge; this is of vital importance in determining the total reduction required to achieve the final plate thickness.
- (4) The chemical composition, consisting of a total of fourteen different elements.
- (5) The rolling parameters, including the pass-by-pass screw settings, delay period between the passes and the time spent for an individual pass.
- (6) The “rolling condition” which is set to 0 for as-rolled plates and 1 for control-rolled or normalised-rolled plates; the latter involved rolling with water cooling, with or without a delay period.

A total of 1892 examples were available for analysis. The maximum number of rolling passes was thirty; when the number was less than thirty, the missing passes were set with zero pass-time, zero delay time and with a roll gap setting which gives zero deformation. All the variables were normalised within the range  $\pm 0.5$  (equation 10.2). The purpose of the analysis was to be able to estimate the yield and ultimate tensile strengths as a function of each one of the 108 variables. Some further information about the variables is given in Appendix two; that information is necessary in order to reproduce the present work using the trained network.

### 11.3 Network Training

#### 11.3.1 The Yield Strength

The network model for the yield strength consisted of 108 input nodes, a number of hidden nodes and an output node representing the yield strength. To help avoid over-complex model, the database was split into two equal halves. The network was trained using 946 of the examples randomly chosen from a total of 1892 available, the remaining 946 examples were used as ‘new’ experiments to test the performance of the trained network on unseen data. Various error indicators after training the models are illustrated in Figure 11.1.

Figure 11.1a shows that the inferred noise level decreases as the number of hidden units increases. However, the complexity of the model also increases with the number of hidden units. A high degree of complexity is not justified if the model attempts to fit the noise in the experimental data. The number of hidden units was therefore set by examining the performance of the model on the unseen test data (Figures 11.1b and c).

It is seen that a model with just two hidden units gives an adequate representation of the data with a minimum in the test error  $T_e$  (Figure 11.1b). Another useful measure of the performance of a model is the “log predictive error” [MacKay, 1992a, 1992b, 1994, 1995] for which the penalty for making a wild prediction is much less if the wild prediction is accompanied by an appropriately large error bar. Assuming that for each example  $n$  the model gives a prediction with error,  $(y_n, \sigma_n^2)$ , the log predictive error (LPE) is:

$$\text{LPE} = \sum_n \left[ \frac{1}{2} \left( t_n - y_n \right)^2 / \sigma_n^2 + \log(\sqrt{2\pi} \sigma_n) \right] \quad (11.1)$$

Once again, the log predictive error is minimum for a model with two hidden units (Figure 11.1c).

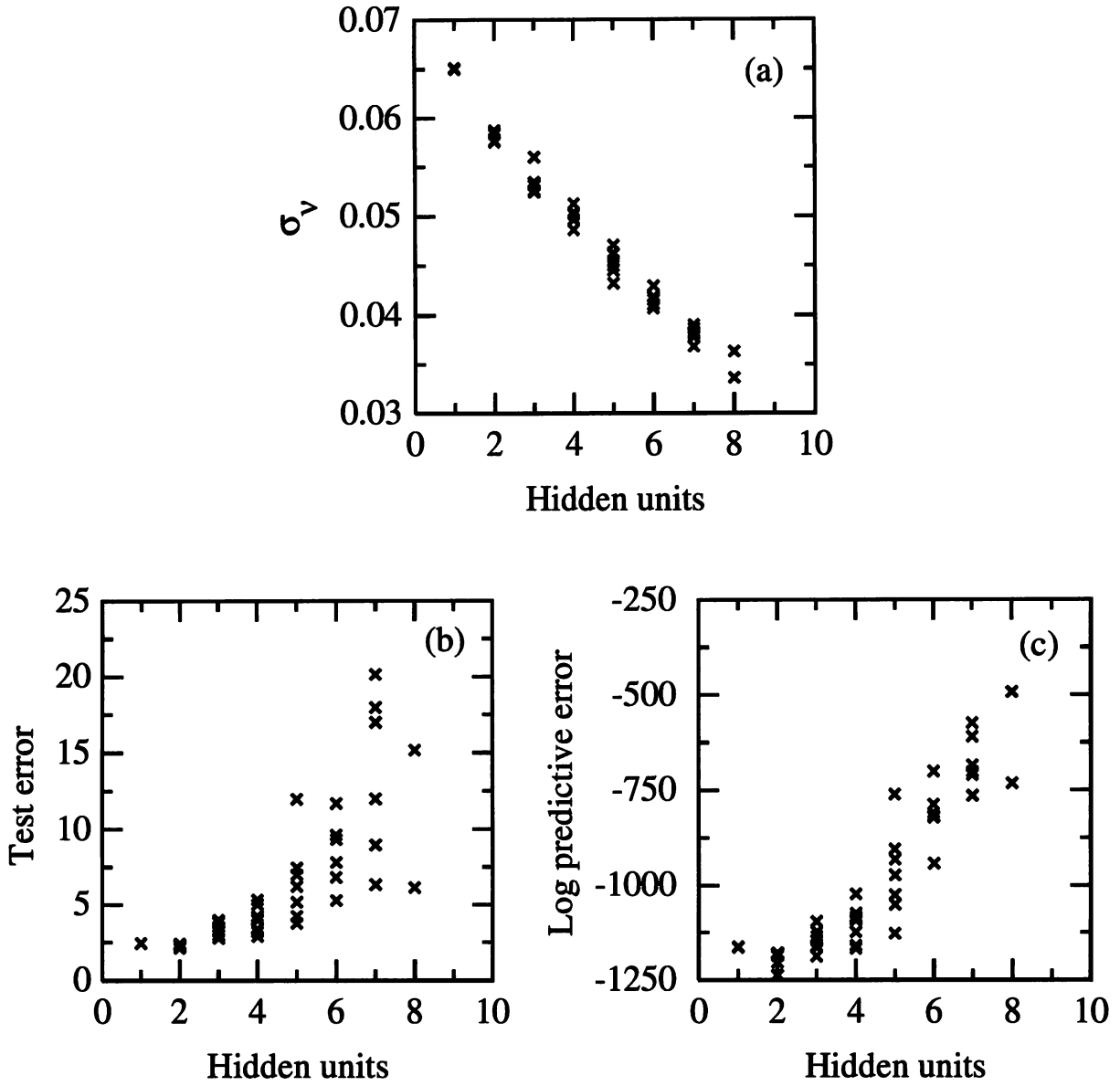


Figure 11.1: The YS model: (a) Variation in  $\sigma_v$  as a function of the number of hidden units, (b) The test error for each of the models, and (c) The log predictive error. Several values are presented for each set of hidden units because the training for each network was started with a variety of random seeds.

The behaviour of the training and test data is illustrated in Figure 11.2 which shows a similar degree of scatter in both the graphs, indicating that the complexity of this particular model is optimum. It should be noted that the test data cover a wider range of yield strength values and for a few cases at the highest yield strengths, the model underpredicts the measured values. The error bars in Figure 11.2 include the error bars on the underlying function and the inferred noise level in the data set ( $\sigma_v$ ). In all other subsequent predictions discussed below, the error bars include the former component only.

A case of over-fitting which leads to better accuracy in the prediction of training data



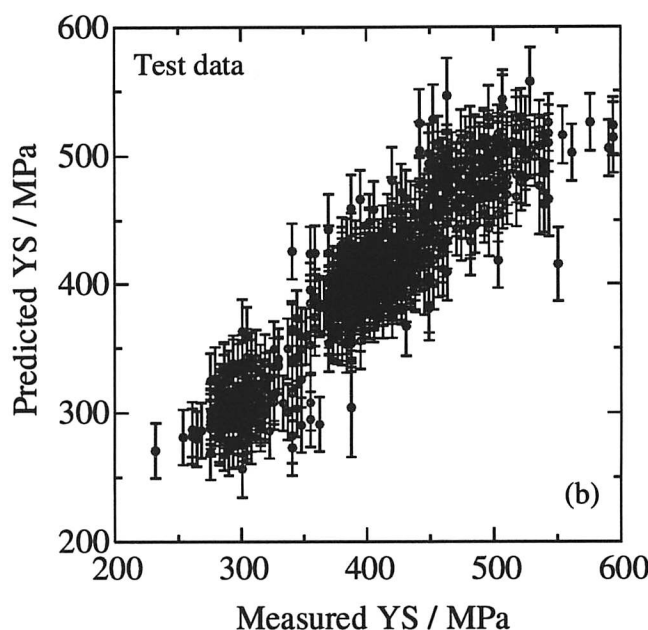
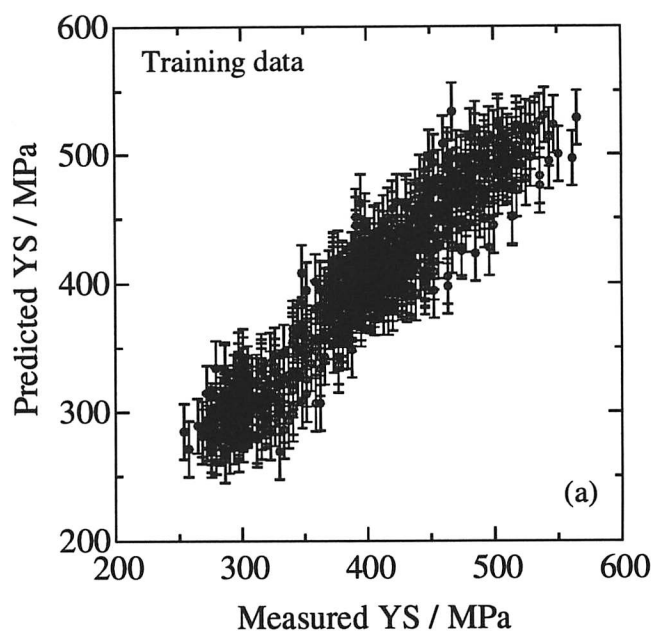


Figure 11.2: A comparison between the predicted and measured yield strengths (YS) for the best model with 2 hidden units. (a) Training and (b) test data. The error bars are set to  $\pm 1\sigma$  limits and have two components: error bar on the underlying function and the inferred noise level in the data for this model ( $\sigma_\nu$ ).

when compared with the test data is illustrated in Figure 11.3.

When making predictions, Mackay [1994] has recommended the use of multiple good models instead of just one best model. This is called 'forming a committee'. The committee

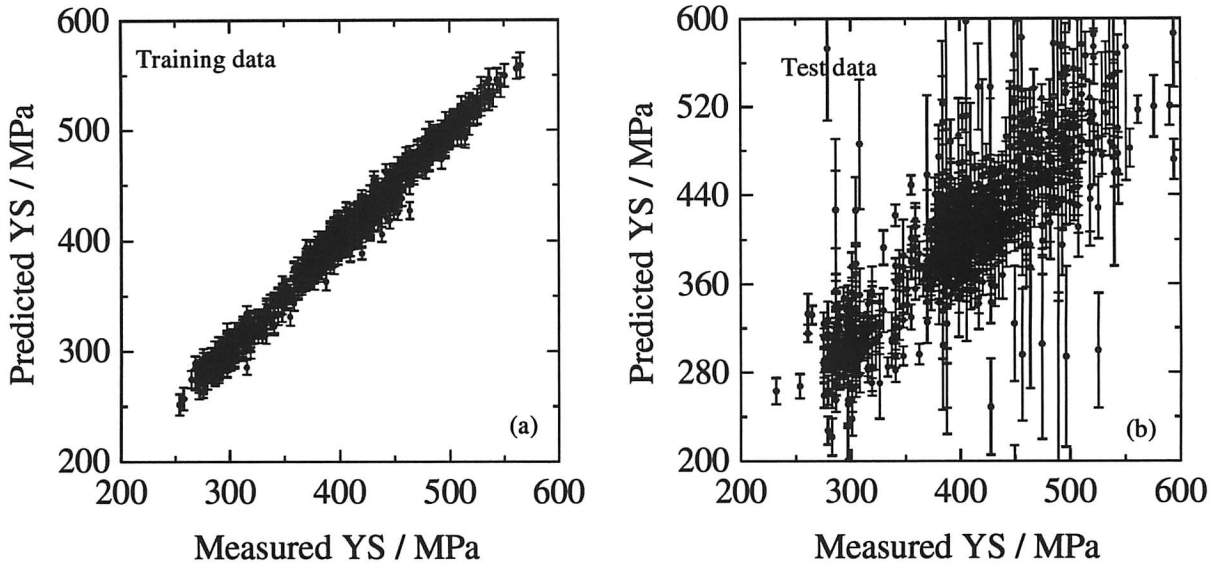


Figure 11.3: An illustration of over-fitting by a highly complex model (8 hidden units). While the model accurately fits the data in training set (a), it fails to reproduce the trend in the unseen test data set (b).

prediction,  $\bar{y}$ , is obtained using the expression:

$$\bar{y} = \frac{1}{L} \sum_i y_i \quad (11.2)$$

where  $L$  is the size of the committee and  $y_i$  is the estimate of a particular model  $i$ . The optimum size of the committee is determined from the validation error of the committee's predictions using the test data set. The test error of the predictions made by a committee is calculated by replacing the  $y_n$  in equation 10.7 with  $\bar{y}$ . In the present analysis a committee of models was used to make more reliable predictions. The models were ranked according to their log predictive errors. Committees were then formed by combining the predictions of best  $M$  models, where  $M$  gives the number of members in a given committee model. The test errors for the first 18 committees are shown in Figure 11.4.

A committee of the best four models gives the minimum error; three of these were two hidden unit models and the remaining one was a three hidden unit model. Each constituent model of the committee was therefore retrained on the entire data set beginning with the weights previously determined. Figure 11.5 shows the results from the new training. For the sake of simplicity, the error bars in Figure 11.5 include the error on the fitted function only.

### 11.3.2 The Ultimate Tensile Strength

The same procedure was used to model the ultimate tensile strength (UTS) with the same set of 108 input variables. The variation in  $\sigma_\nu$ , the test error and log predictive error with the number of hidden units is shown in Figure 11.6.

The model with two hidden units was found to be the optimum one and a committee of the nine best models led to a further reduction in the test error, as illustrated in Figure 11.7.

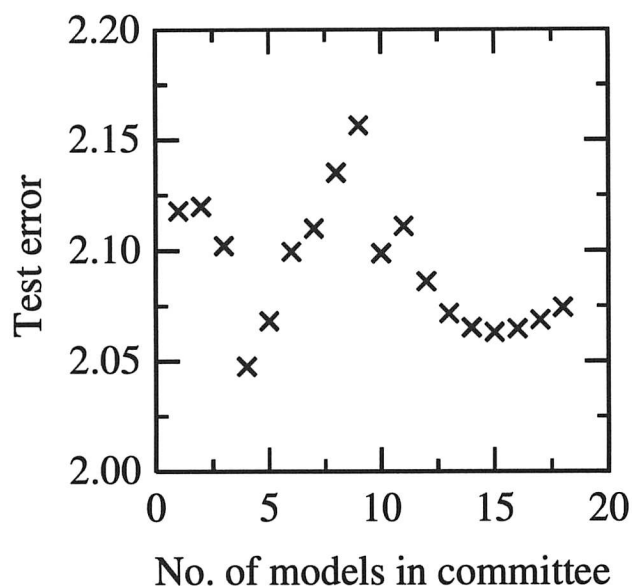


Figure 11.4 : The test error as a function of the number of members in a committee of YS models.

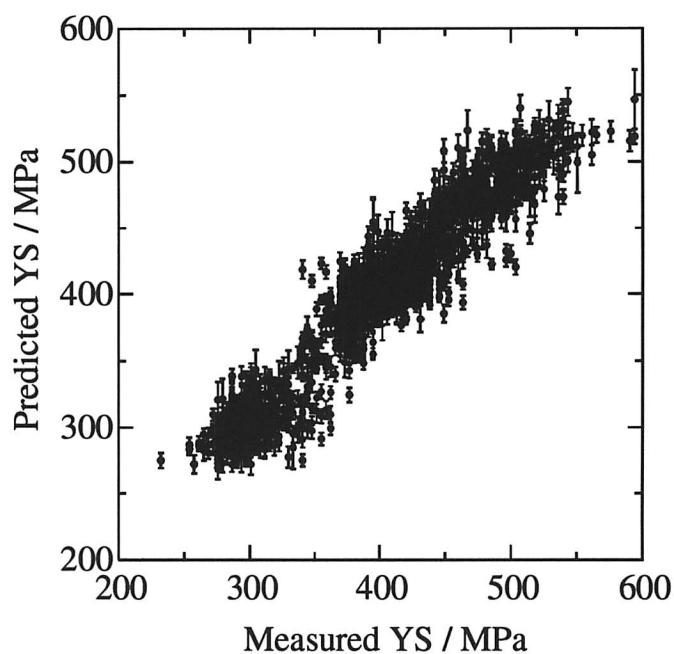


Figure 11.5: Training data for the best yield strength committee model, training was done on the whole data set. The error bars include the error in the underlying function only.

Three of the nine models in the committee were two hidden unit models, four were three hidden unit models and remaining two were four hidden unit models.

The results of the retraining of the committee model on the all of the data are illustrated in Figure 11.8.

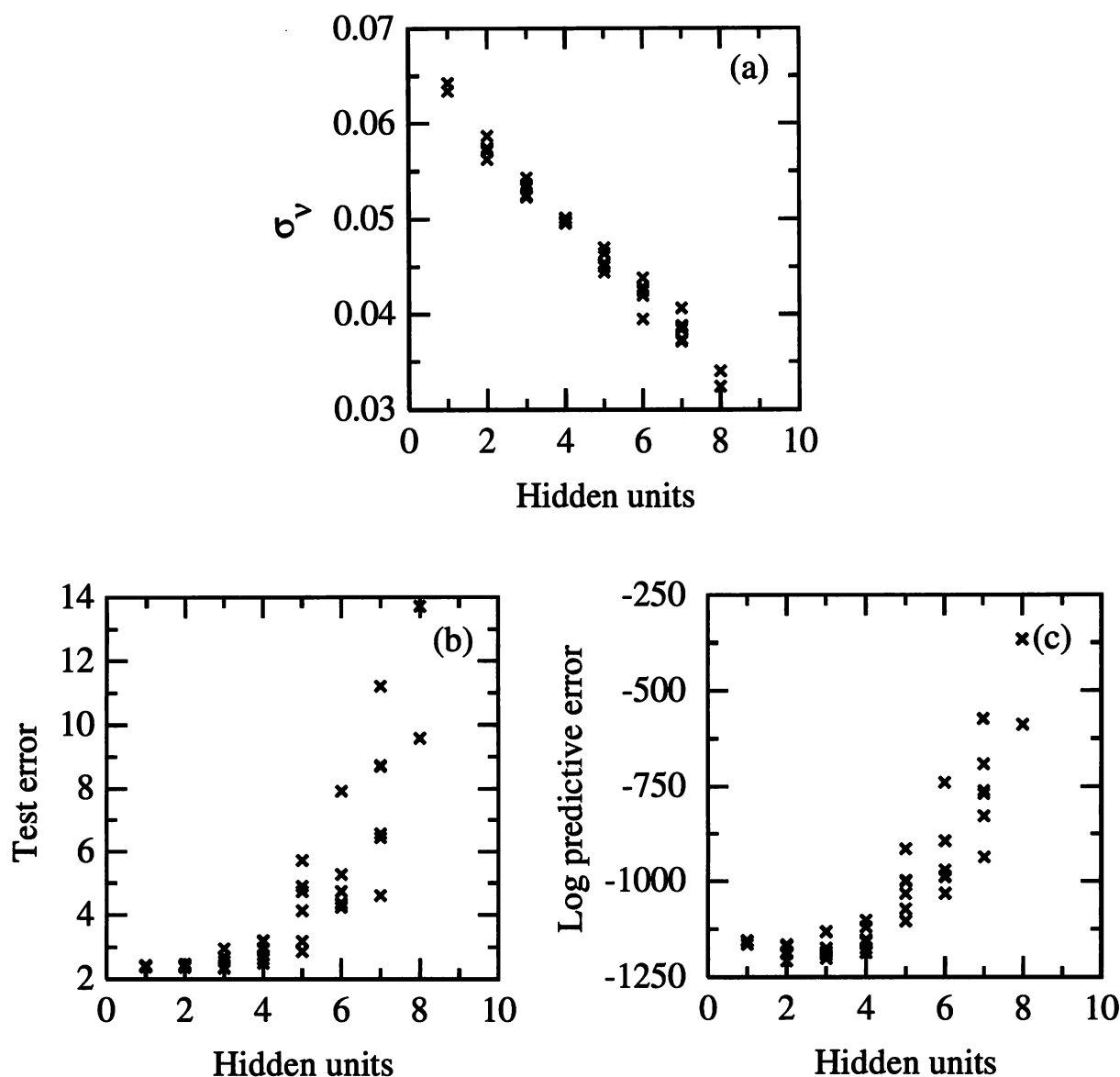


Figure 11.6: The  $\sigma_v$  and errors as a function of the number of hidden units for the UTS models. Several values are presented for each set of hidden units because the training for each network was started with a number of random seeds.

#### 11.4 Application of the Models

The optimised committee models were used to study the effect of individual variables on the yield strength and the tensile strength in order to examine whether the results are compatible with known metallurgical principles and other published data. These studies are limited to simple relationships since there are no metallurgical models which deal with all the variables incorporated in the neural network approach.

In the discussion that follows, a typical 19 pass schedule with a starting slab thickness of 200 mm and the final pass screw setting of 13.8 mm was used unless otherwise stated. The

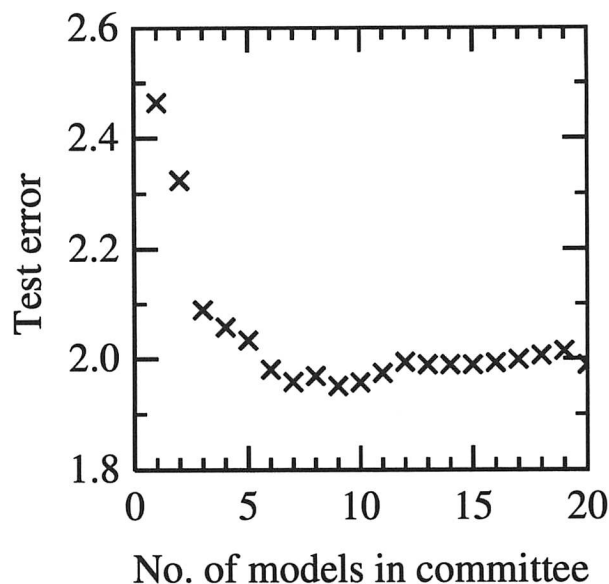


Figure 11.7: The test error as a function of the number of members in a committee of models for UTS.

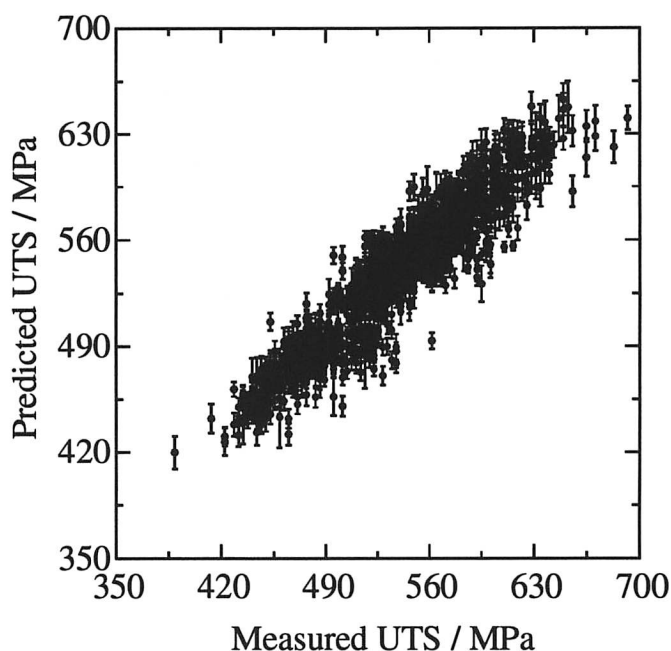


Figure 11.8: Training data for the best UTS committee model, training was done on the whole data set.

slab reheating temperature was set at 1215 °C. The chemical compositions were set at their average concentrations listed in Appendix two. A comprehensive list of the standard set of variables is presented in Table 11.1 in the precise order in which they appear in Appendix two. For example, a variation in the carbon concentration is discussed leaving all the other variables in Table 11.1 unchanged unless otherwise specified. In all the predictions below, the error bars represent the  $\pm 1\sigma$  limits on the underlying function.

1215.0	200.0	2760.0	0.140	1.260	0.320	0.007	0.015	0.031
0.030	0.003	0.025	0.037	0.005	0.023	0.009	0.002	174.0
158.0	2.0	149.6	8.0	4.0	141.3	23.0	1.0	133.6
7.0	1.0	125.9	6.0	2.0	118.3	5.0	2.0	110.0
6.0	2.0	105.1	16.0	3.0	85.1	24.0	3.0	70.7
7.0	3.0	58.6	6.0	3.0	48.7	7.0	3.0	40.1
7.0	4.0	33.0	6.0	5.0	22.9	36.0	6.0	15.8
7.0	9.0	14.9	6.0	9.0	14.1	7.0	10.0	13.8
7.0	10.0	13.8	0.0	0.0	13.8	0.0	0.0	13.8
0.0	0.0	13.8	0.0	0.0	13.8	0.0	0.0	13.8
0.0	0.0	13.8	0.0	0.0	13.8	0.0	0.0	13.8
0.0	0.0	13.8	0.0	0.0	13.8	0.0	0.0	7

Table 11.1: Table of variables used for the predictions. The variables appear in the same sequence as they appear in Appendix two.

#### 11.4.1 Carbon Concentration

It is well known that carbon forms an interstitial solid solution in iron, leading to intense solid solution strengthening. The effect is more pronounced in the case of ferritic iron because unlike austenite, the carbon atoms cause a tetragonal distortion of the lattice giving strong interactions with all kinds of dislocations [Honeycombe and Bhadeshia, 1995]. It has been estimated that 1 wt.% C in solid solution in ferrite raises the yield strength by 4600 MPa and UTS by 6800 MPa [Pickering, 1978]. However, the solubility of carbon in ferrite is extremely small so that the main effect in the context of steels with a mixed microstructure of ferrite and pearlite is to increase the fraction of the latter phase. There is also a refinement of microstructure since the temperature at which the ferrite forms is suppressed. Both the yield and tensile strengths should therefore increase with the carbon concentration and this is indeed replicated by the model (Figure 11.9); the calculations are for a steel without Nb or V additions. Note also that as must be expected, the UTS is always predicted to be higher than the yield strength even though the latter was not included as an input to the UTS model. The error bars ( $\pm 1\sigma$ ) are larger when an attempt is made to predict at concentrations beyond the range of the training data set. The yield strength increases by about 32 MPa (ignoring the error bars) when the concentration is increased from 0.025 to 0.25 wt.%. This is consistent with experimental data by Hodgson and Gibbs [1992] who found an increase in the lower yield strength by about 15 MPa for a 0.1 wt.% increase in the carbon concentration.

Consistent with experimental observations [Pickering, 1978; Shimizu *et al.*, 1986; Leslie, 1981] the UTS is predicted to be more sensitive to the carbon concentration than the yield strength (Figure 11.9). The predominant effect of carbon in the steels considered here is to

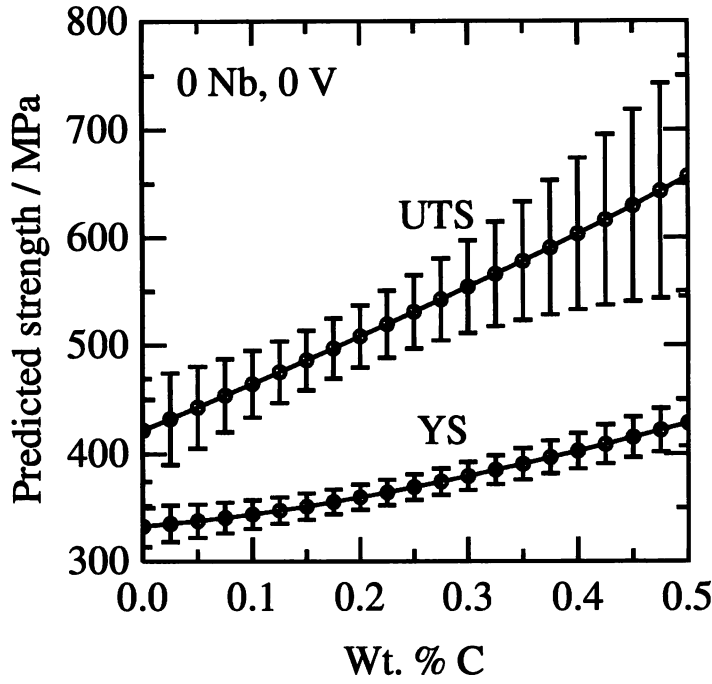


Figure 11.9: The variation of yield and ultimate tensile strength with carbon for a steel without any microalloying additions. The error bars represent  $\pm 1\sigma$  limits.

increase the pearlite fraction in the microstructure [Irvine, 1962; Honeycombe and Bhadeshia, 1995]. For carbon concentrations up to 0.3 wt.% where the pearlite fraction is relatively small, yielding begins in the softer ferrite which has to work harden before the pearlite starts to undergo plastic deformation. As a consequence, the effect of pearlite on the yield strength is smaller. On the other hand, pearlite content does affect the UTS because it is associated with large plastic strains where all phases must participate in deformation. These observations are also reflected in Pickering's [1978] regression equations for similar steels, where the quantity of pearlite features only in the UTS equation:

$$\text{YS, MPa} = 53.9 + 32.3w_{Mn} + 83.2w_{Si} + 354.2\sqrt{w_{N_f}} + 17.4(d_\alpha^{-0.5}) \quad (11.3)$$

$$\text{UTS, MPa} = 294.1 + 27.7w_{Mn} + 83.2w_{Si} + 3.85(\%\text{pearlite}) + 7.7(d_\alpha^{-0.5}) \quad (11.4)$$

where  $w_i$  represents the concentration, in weight percent, of the element identified by the subscript,  $N_f$  is the free nitrogen in weight percent and  $d_\alpha$  is the ferrite grain size in mm.

Based on a study covering a wide range of ferrite grain sizes in a number of C steels Morrison [1966] found a slightly different factor of 18.13 for the effect of ferrite grain size on the yield strength (equation 11.3).

Figure 11.10a shows calculations for a microalloyed steel with 0.03 wt.% Nb. Figure 11.10b illustrates on the same scale, the effect of increasing pearlite content on the UTS as calculated using equation 11.4 (the zero carbon result is from the neural network model). The agreement between the two is excellent and similar results have been reported by Shimizu *et al.* [1986]

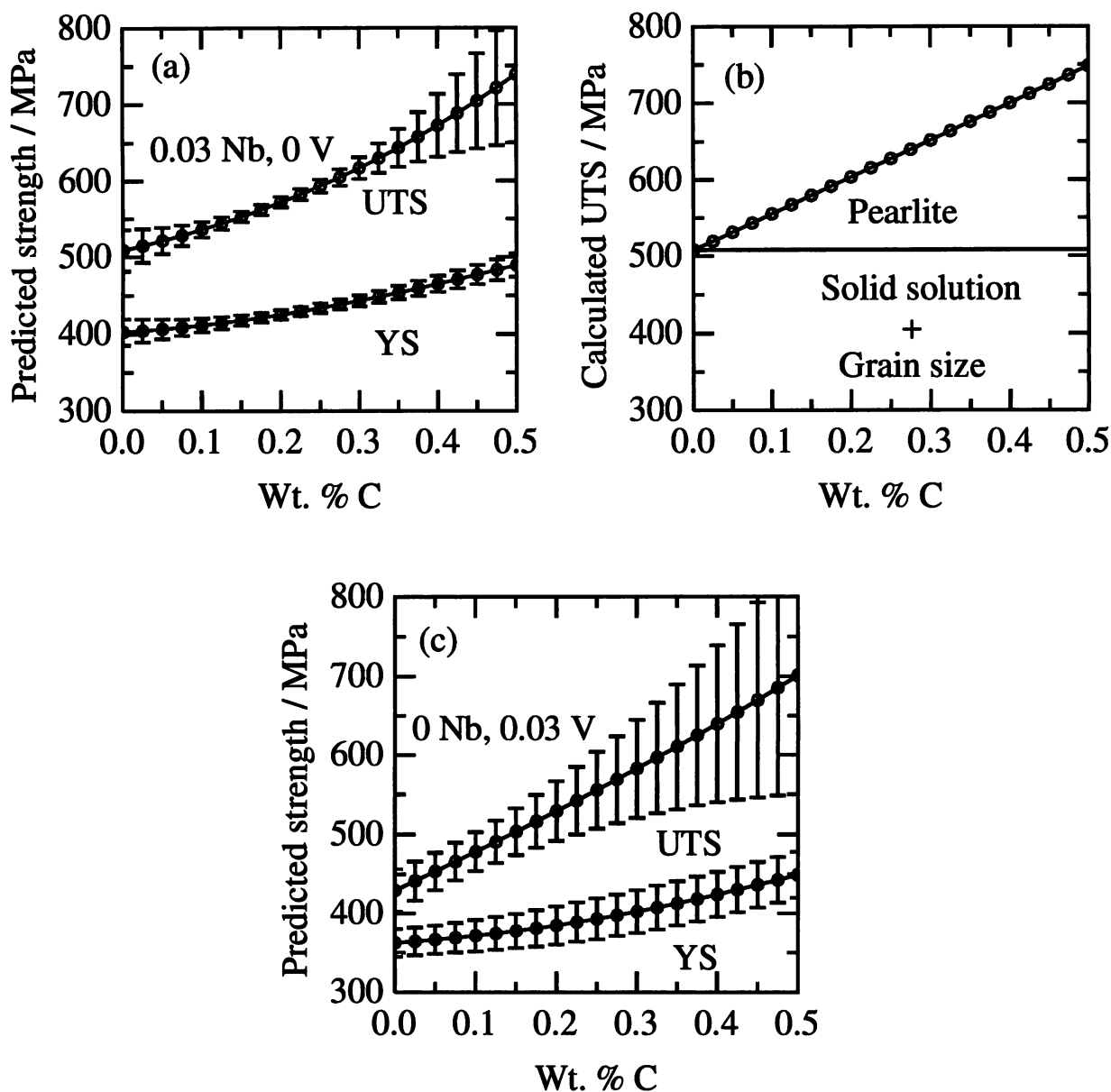


Figure 11.10: The effect of (a) carbon; (b) pearlite content on the yield and ultimate tensile strengths of a microalloyed steel containing 0.03 wt.% Nb (zero vanadium). (c) The yield and ultimate tensile strengths for a 0.03 wt.% vanadium microalloyed steel (zero niobium). Other elements were as in Table 11.1. The UTS in (b) was calculated using equation 11.4 [Pickering, 1978].

A comparison of Figure 11.9 with Figure 11.10a shows that the addition of 0.03 wt.% Nb to a plain C-Mn steel raises both the yield and ultimate tensile strengths by about 65 MPa at all carbon concentrations. A corresponding addition of 0.03 wt.% V increases the strength by only about 20 MPa (Figure 11.10c). It is well known that niobium is more effective in restricting recrystallisation than vanadium [Irvine *et al.*, 1967; Abe *et al.*, 1886]. This will be



discussed separately.

The starting slab thickness was set at 200 mm and the final plate thickness 13.8 mm in all of the above calculations. If this is changed to a 400 mm initial thickness but the rolling schedule is kept the same (*i.e.*, the same percentage pass reductions and the pass and interpass times), then the final plate thickness becomes 27.7 mm. This should lead to a reduction in the strength because the cooling rate when rolling is completed will be slower for a thicker plate and because the rolling reductions occur at relatively higher temperatures (the thicker slab spends the same time in the mill). The finish rolling temperature will be higher for 27.7 mm plate compared with 13.8 mm plate. The reduction in strength is predicted by the neural network as illustrated in Figure 11.11, although there is some uncertainty due to the large error bars for the UTS calculations. It needs to be emphasised that an initial slab thickness of 400 mm is simply used as an example here to test the model predictions. In actual practice, the initial slab thickness is typically in the range of 225–305 mm. Or alternatively, ingot of an initial thickness of 600 mm is used.

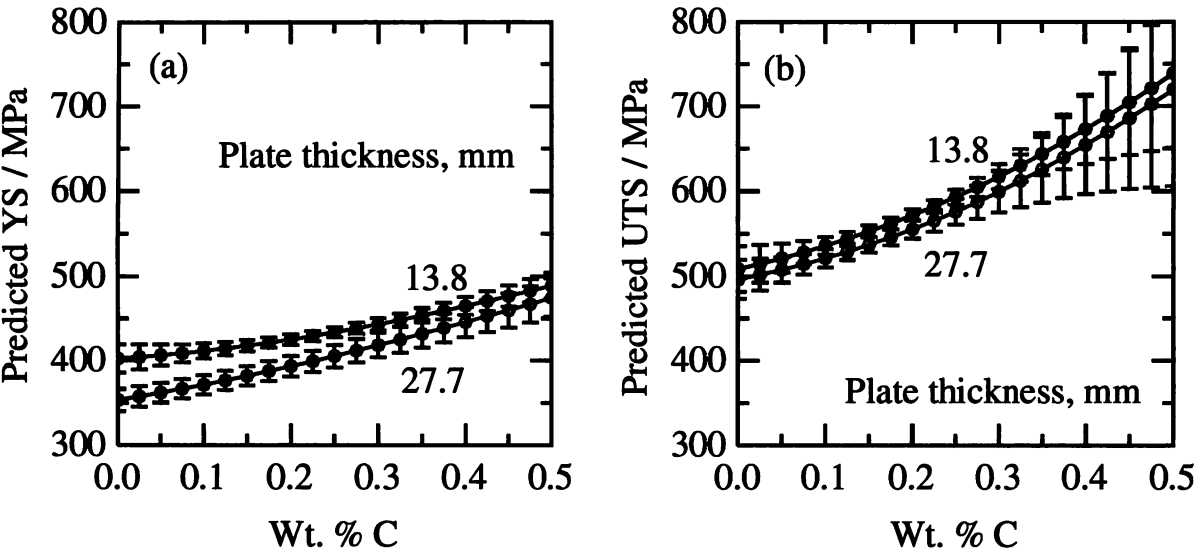


Figure 11.11: The effect of plate thickness on the yield and ultimate tensile strengths of a niobium microalloyed steel as a function of the carbon concentration.

#### 11.4.2 Manganese Concentration

Manganese not only provides solid solution strengthening but also has a strong effect on the stability of the austenite. It lowers the ferrite transformation temperature and therefore leads to a refinement of microstructure [Cohen and Hansen, 1986]. Manganese also shifts the eutectoid point to lower carbon concentrations and thus leads to an increase in the volume fraction of pearlite.

The Pickering equations given above attribute 32 and 27 MPa solid solution strengthening increment in the yield and ultimate tensile strengths respectively due to a 1 wt.% increase in the

manganese level. The predictions in Figure 11.12a, b include all the effects of manganese and hence the somewhat larger strength increment is consistent with the smaller values reported by Pickering. The results are in agreement with the work of Irvine [1962] and Irvine and Pickering [1963].

Cohen and Hansen [1986] have measured the effect of Mn on the ferrite grain size of rolled 0.03Nb, 0.05 and 0.10V (wt.%) steels. Table 11.2 compares the YS and the UTS predicted by the neural network model with those calculated according to Pickering equations for a 0.07C, 0.32Si (wt.%) steel. The ferrite grain size used in the calculations were taken from the work of Cohen and Hansen. Once again the agreement is very good.

Wt. % Mn	YS / MPa	YS / MPa	UTS / MPa	UTS / MPa
	Present	Pickering	Present	Pickering
	model	equation	model	equation
0.5	322 ± 9.8	347	484 ± 40.6	478
1.0	373 ± 7.6	396	501 ± 20.6	506
1.5	425 ± 7.9	441	531 ± 11.5	533

Table 11.2: Comparison of the YS and the UTS calculated from Pickering equations [1978] with those predicted by the present model for a 0.07C, 0.32Si (wt.%) steel. The ferrite grain size was taken from Cohen and Hansen [1986].

As with carbon, an increase in the plate thickness led to a decrease in strength (Figure 11.12c, d). The increase in thickness was achieved by doubling the slab thickness whilst keeping the same rolling schedule. The reduction in the yield strength is larger than in the UTS, presumably because the former is more sensitive to grain size (equations 11.3 and 11.4).

It is a common practice during thermomechanical processing to hold the slab at an intermediate stage during rolling for a certain length of time. This allows it to cool to a pre-determined temperature before rolling is resumed. The temperature is then sufficiently low to prevent the austenite from recrystallising during deformation. The deformation and the increase in austenite surface area per unit volume due to its pancaked shape enhances the ferrite nucleation rate, giving grain refinement and a corresponding increase in strength. This behaviour is predicted as illustrated in Figure 11.13. The delay period before the 9 th pass was increased from 24 to 700 seconds, this would have the effect of lowering both the end hold temperature and the finish rolling temperature with a consequent increase in the yield and the tensile strengths (Figure 11.13).

If the increase in the strength is assumed to be due to grain refinement then according to the Pickering regression equations 11.3 and 11.4, the increase in YS should be 17.4/7.7 times the rise in UTS. The model predictions are in excellent agreement with this. For a 1.3 wt.% Mn steel, the YS increases by 52 MPa whereas UTS increases by 23 MPa (Figure 11.13). Thus, it might be argued that a delay of 700 seconds before the 9 th pass is equivalent to an addition

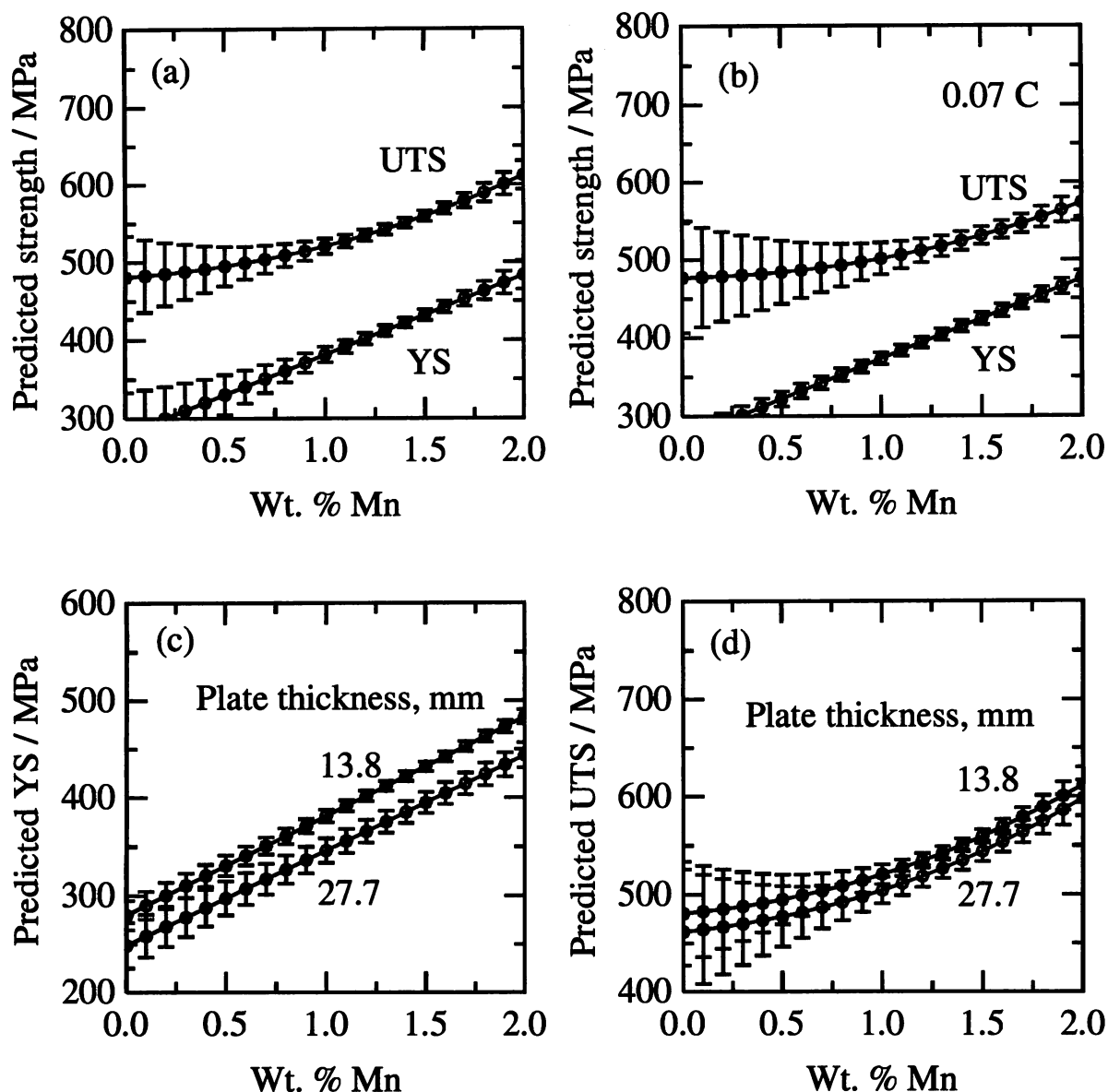


Figure 11.12: (a, b) The yield and ultimate tensile strengths as a function of the manganese content. (c, d) The effect of manganese concentration and plate thickness on strength. The thickness was increased by doubling the initial slab thickness.

of about 0.025 wt.% of costly Nb. These factors are consistent with the mill experience though in actual practice, it is the concentration of C and/or Mn which is reduced rather than that of Nb to improve the weldability and toughness. However, a hold of as large a period as 700 seconds has other commercial implications. It amounts to a total loss of production; in 700 seconds two plates can be rolled to schedules which do not involve long delay periods.

#### 11.4.3 Silicon Concentration

The effect of silicon on strength as predicted by the model is shown in Figure 11.14. It can be seen that Si has little effect on YS or UTS. Si is a ferrite stabiliser and raises the ferrite transformation temperature. This results in coarser ferrite grains [Wray, 1984]. It appears that

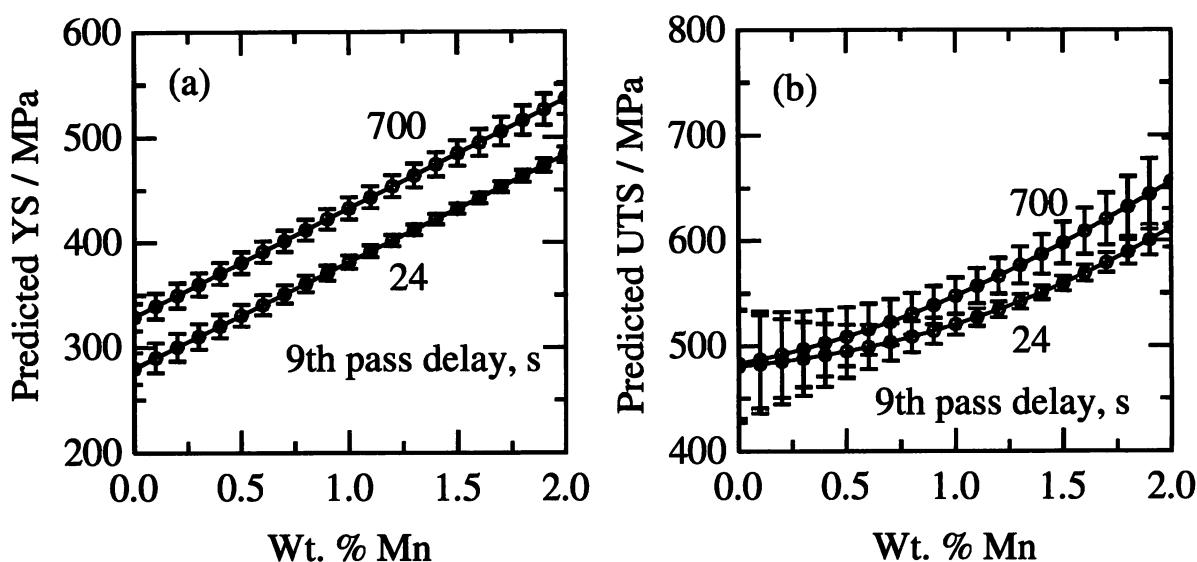


Figure 11.13: The effect of a delay period before the 9th pass on the strength for a range of manganese concentrations.

the solid solution strengthening effect of Si is neutralised by this effect. It should, however, be noted that the variation of the Si concentration in the database was very small (Appendix two) and the results might be different if a large variation is dealt with in the analysis.

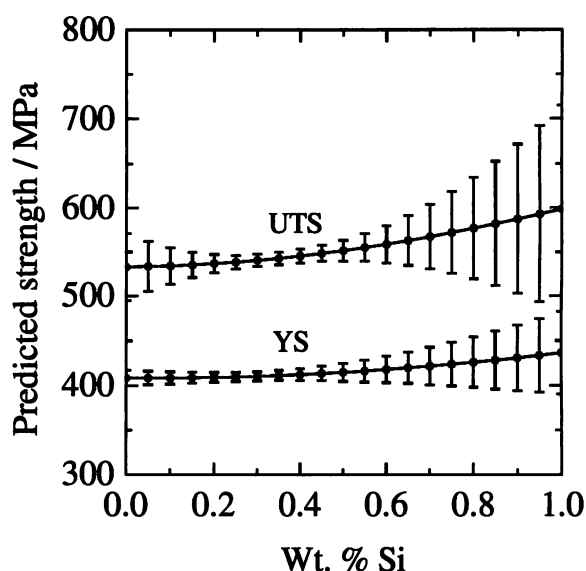


Figure 11.14: The effect of Si on the strength and elongation.

#### 11.4.4 Microalloying Additions

Niobium and vanadium carbonitrides prevent austenite grain coarsening during reheating [Amin and Pickering, 1982a]. They also help refine the austenite grain structure during hot-rolling by pinning the grain boundaries and retarding recrystallisation [Amin and Pickering,

1982a]. Nb is the most effective microalloying addition for suppressing the recrystallisation, Figure 11.15 [Cuddy, 1982]. This is also evident from the regression equation proposed by Boratto *et al.* [1988]:

$$\begin{aligned}
 T_{nr} = & 887 + 464w_C + (6445w_{Nb} - 644\sqrt{w_{Nb}}) + (732w_V - 230\sqrt{w_V}) + \\
 & 890w_{Ti} + 363w_{Al} - 357w_{Si}
 \end{aligned}
 \tag{11.5}$$

where  $T_{nr}$  is the no recrystallisation temperature *i.e.*, the temperature below which recrystallisation is very sluggish and  $w_i$  is the concentration, in weight percent, of the element  $i$ .

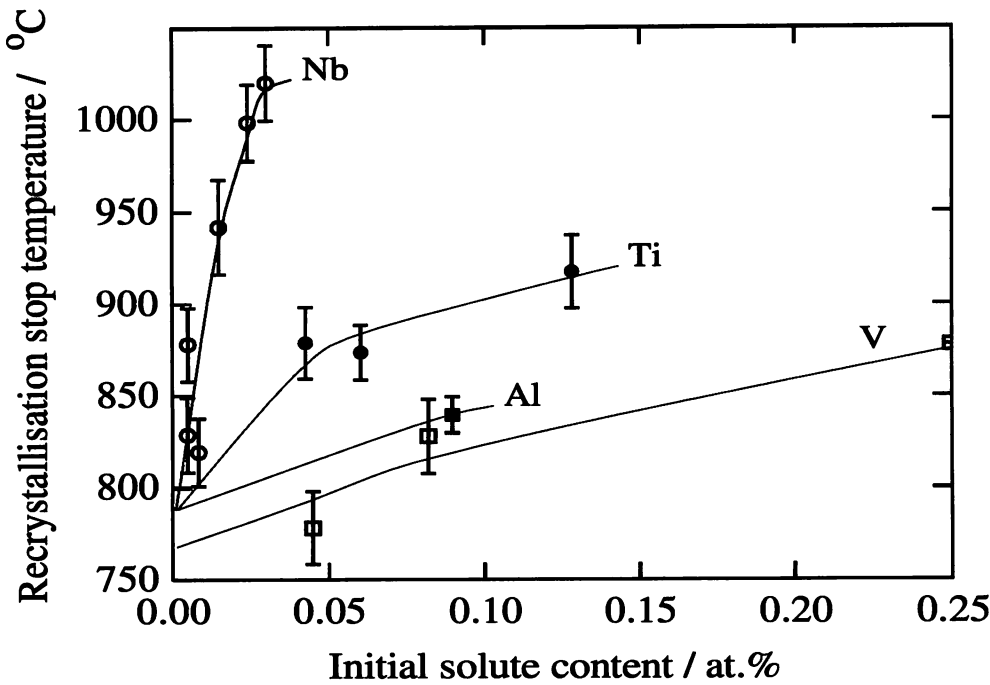


Figure 11.15: The effects of microalloying elements on the recrystallisation temperature of austenite in a low carbon steel [Cuddy, 1982].

By suppressing recrystallisation, they allow a higher fraction of the strain to be retained in austenite. This increases the ferrite nucleation rate during subsequent cooling and a finer ferrite grain size is obtained. Nb is more effective than V in refining the grains. Irvine *et al.* [1967] and Abe *et al.* [1986] have observed a finer ferrite grain size in niobium steel than in comparable vanadium steel. A larger concentration of vanadium is required to achieve the same effect as niobium [Irvine *et al.*, 1967]. Interphase precipitation also causes grain refinement by hindering the ferrite grain growth [Amin and Pickering, 1982b].

At the same grain size microalloyed steels have higher strengths than the plain C-Mn steels, and this has been attributed to the presence of fine precipitates of carbides and nitrides of the microalloying elements [Irvine *et al.*, 1967]. In this respect V is more effective than Nb particularly at higher nitrogen contents [Irvine and Pickering, 1963].

Both Nb and V also increase the hardenability and reduce the ferrite transformation temperature [Abe *et al.*, 1986; Amin and Pickering, 1982b].

These characteristics are predicted using the neural network model as shown in Figure 11.16. A 0.02 wt.% increase in Nb, in the region in which the error bars are small, increases the yield strength by about 40 MPa and the tensile strength by 25 MPa whilst the same amount of V increases both the YS and the UTS by only 15 MPa. The experimental results reported in literature more or less confirm these model predictions [Irvine *et al.*, 1967; Shimizu *et al.*, 1986; Abe *et al.*, 1986; Cohen and Hansen, 1986; Lessells, 1986].

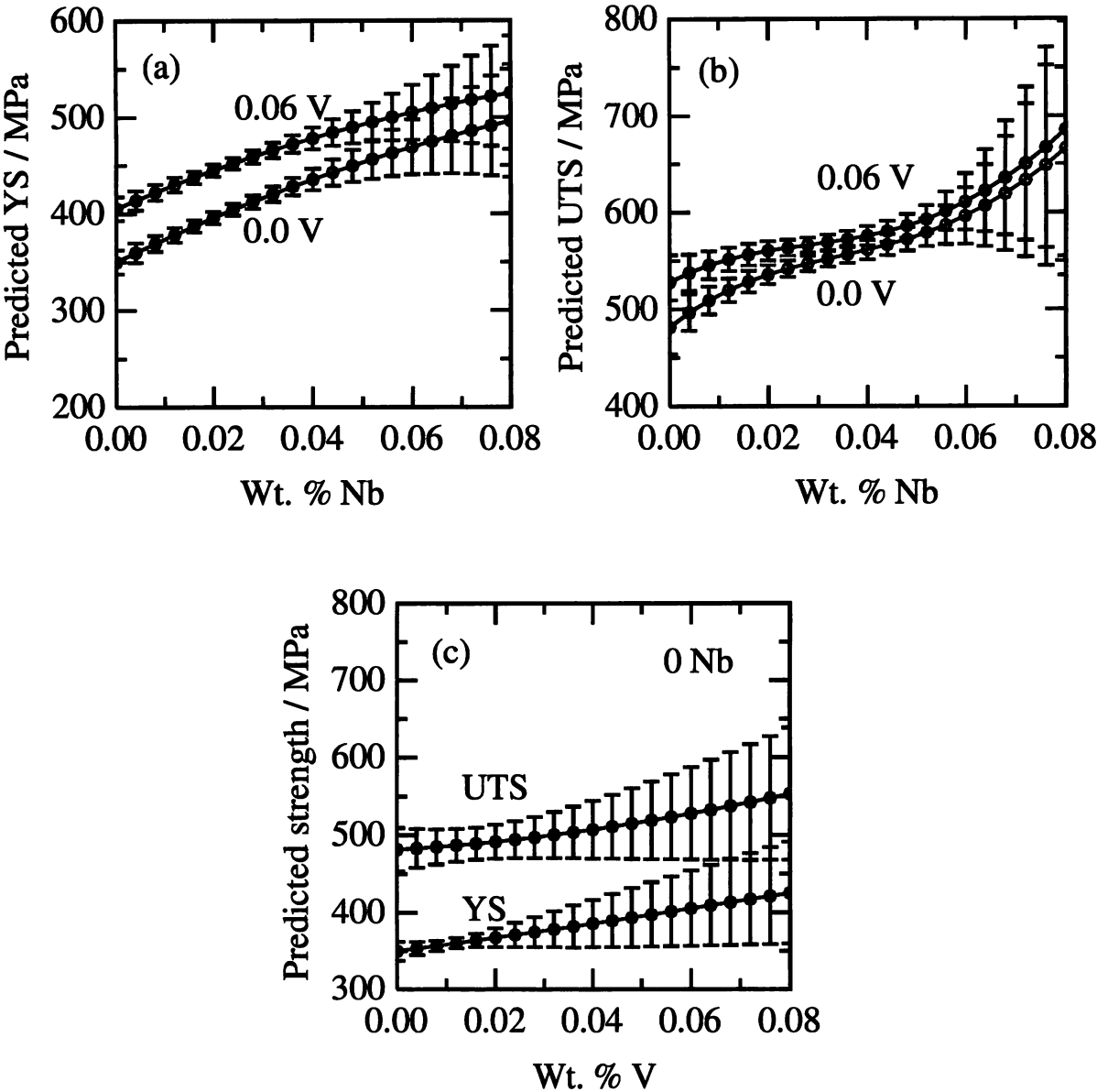


Figure 11.16: The effect of niobium and vanadium on the yield and tensile properties. Normally V is not added alone but is combined with Nb. The calculations are presented here for illustration only.

Figure 11.16 also highlights the fact that a combined addition of V and Nb enhances the strengthening effects, consistent with the experimental results reported by Irvine *et al.* [1967]. They found that an addition of 0.06 wt.% of V to a Nb microalloyed steel raises the yield strength by about 40 MPa and the UTS by a smaller increment of 15 MPa.

#### 11.4.5 Rolling Parameters

Figure 11.17 shows the effect of 1 st pass reduction on the yield and ultimate tensile strengths; both increase as the pass reduction is increased with the yield strength showing a greater variation. Figure 11.17 is an extrapolation over the normal rolling practice. Usually the first pass reduction is less than 10% and in some cases it may be preceded by a few unrecorded cogging passes. It should also be noted that the effect shown in Figure 11.17 is not of the pass reduction alone. Other factors need to be taken into account. The percentage reduction in all other passes were kept constant so that for a given slab thickness, a higher 1 st pass reduction meant a lower gauge at all other stages of rolling and hence a thinner final plate gauge. It follows that with increasing 1 st pass reduction all other subsequent passes are executed at lower temperatures due to the thinner gauge.

The effect of increasing (1) the initial slab thickness to 400 mm and (2) the 9 th pass delay time (delay before 9 th pass) to 500 s from 24 s is also included in Figure 11.17. A slab thickness of 400 mm is used here as an example only.

The effect of increasing the slab thickness to 400 mm without changing the pass reductions is to lower the strength, which is reasonable. For reasons already discussed, the introduction of a delay period of 500 seconds before the 9 th pass raises the strength.

In the above discussion, the percent reduction of only one pass was systematically varied. This has the effect of changing the final plate thickness. We now present some calculations where the reductions for two or more passes were simultaneously varied in such a way that the final plate thickness is not altered. The slab thickness, the delay times and the pass times were not changed and the reductions for the other passes are the same as in Table 11.1. Figure 11.18a shows the lack of variation in strength for a case where the 1 st pass reduction was increased together with a corresponding decrease in the 19 th (the last) pass reduction which left the final plate thickness unaltered at 8.1 mm for a 200 mm starting slab. This is because a small first pass reduction leads to a higher temperature for all subsequent passes including the last pass with a high reduction since none of the delay times is altered, so that the strength does not increase. When the 1 st pass reduction is large, the later passes occur at a lower temperature but the last pass reduction is small. It is suggested that the resultant of these two effects is that the strength does not vary.

Similar results were obtained when the schedule given in Table 11.1 was modified. The 15 th and the 16 th pass strain were set to zero but the 4 th and the 5 th pass strains were increased equally so that the final plate thickness remained 13.8 mm. The effect of this change in schedule on the variation of YS and UTS with carbon is illustrated in Figure 11.18b. A comparison with Figure 11.10a makes it obvious that the change in schedule has not made any significant difference to the properties.

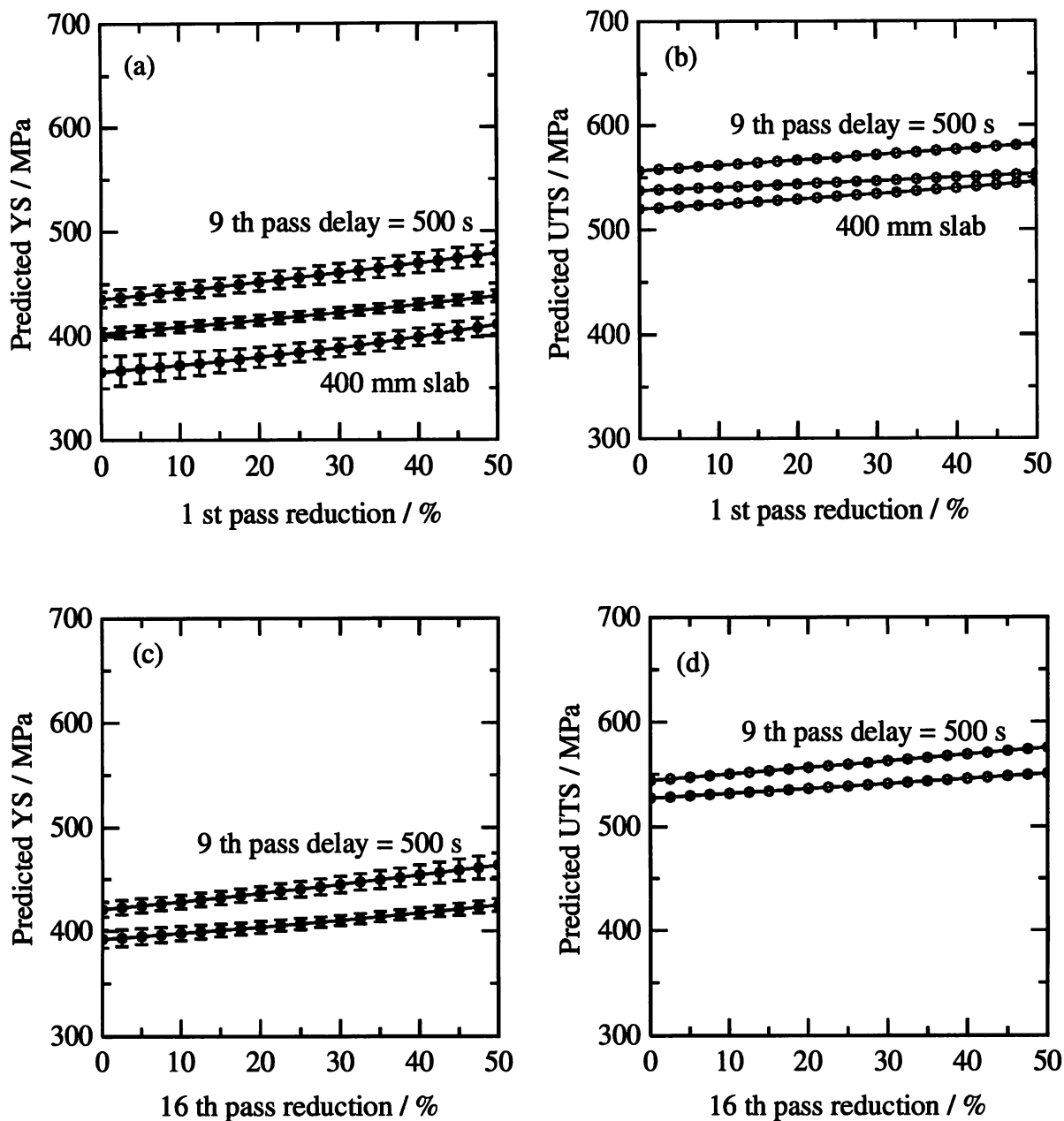


Figure 11.17: (a, b) The effect of 1 st pass reduction on the yield and ultimate tensile strengths. (c, d) The corresponding effects as a function of the 16 th pass reduction.

We have already seen that the introduction of a delay time can have an effect on the final mechanical properties if it leads to grain refinement. Naturally, this can only be significant at the late stages of rolling and this is reflected in the results presented in Figure 11.19.

#### 11.4.6 Optimisation of YS/UTS Ratio

The YS/UTS ratio is an important design criterion for many fail-safe applications where a low value is desired. Examples include earthquake resistant steels and cases where a good fatigue resistance is required [Bhadeshia, 1992].



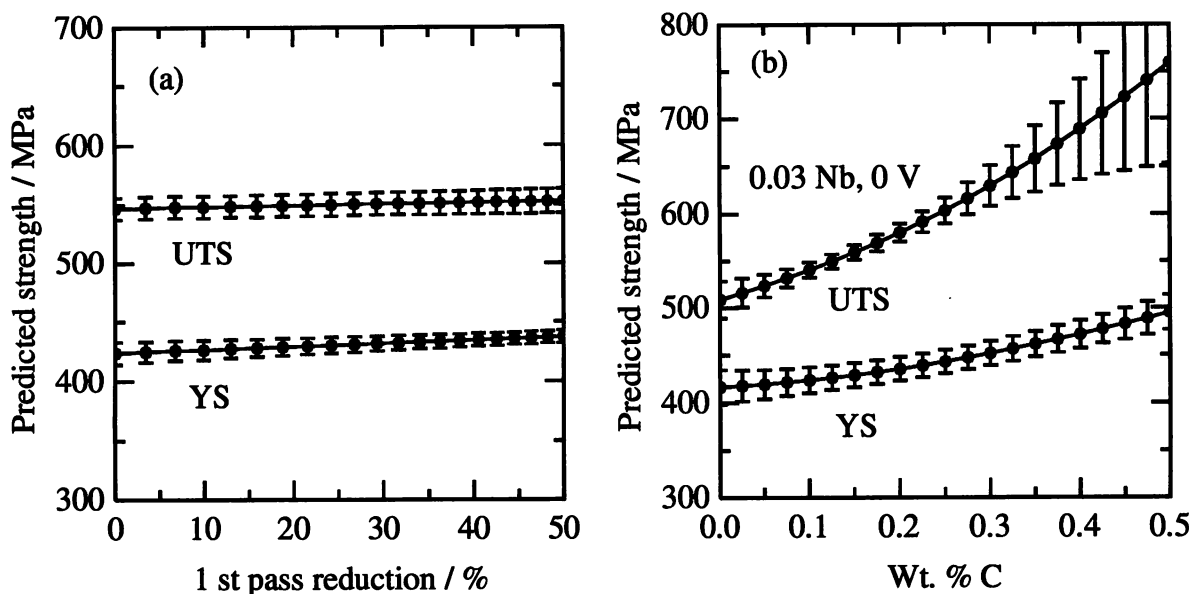


Figure 11.18: (a) Effect of a simultaneous variation of first and last pass strain keeping the final plate thickness constant. (b) The effect of a modification of the schedule given in Table 11.1 in such a way that the final plate thickness was the same.

The present model was used to explore the possibility of designing such a steel. The effect of variations in the carbon and manganese concentrations on the ratio are summarised in Figure 11.20.

The ratio decreased with increasing C concentration. As argued earlier, this is because the pearlite content increases with C which affects UTS more than the YS. However, a very high carbon is not acceptable because of its adverse effect on weldability and toughness. Low C will not give adequate strength. Mn raises the ratio mainly due to its influence on ferrite grain size which raises the YS more than the UTS. Other factors which affect the YS/UTS ratio are the delay period and the plate thickness. These have already been discussed.

#### 11.4.7 Other Published Data

Irvine *et al.* [1967] have systematically studied the effect of chemical composition on the final properties of steel in the as-rolled and normalised conditions (Table 11.3). The present model was tested against their results. In their experiments the samples were reheated to 1200 °C and the finish rolling temperature was about 900 °C. They have not reported the details of rolling schedule employed and for the present calculation it has been assumed that they are similar to the standard conditions used here. It is clear that the model predicts the data rather well (Figure 11.21 and Table 11.4).

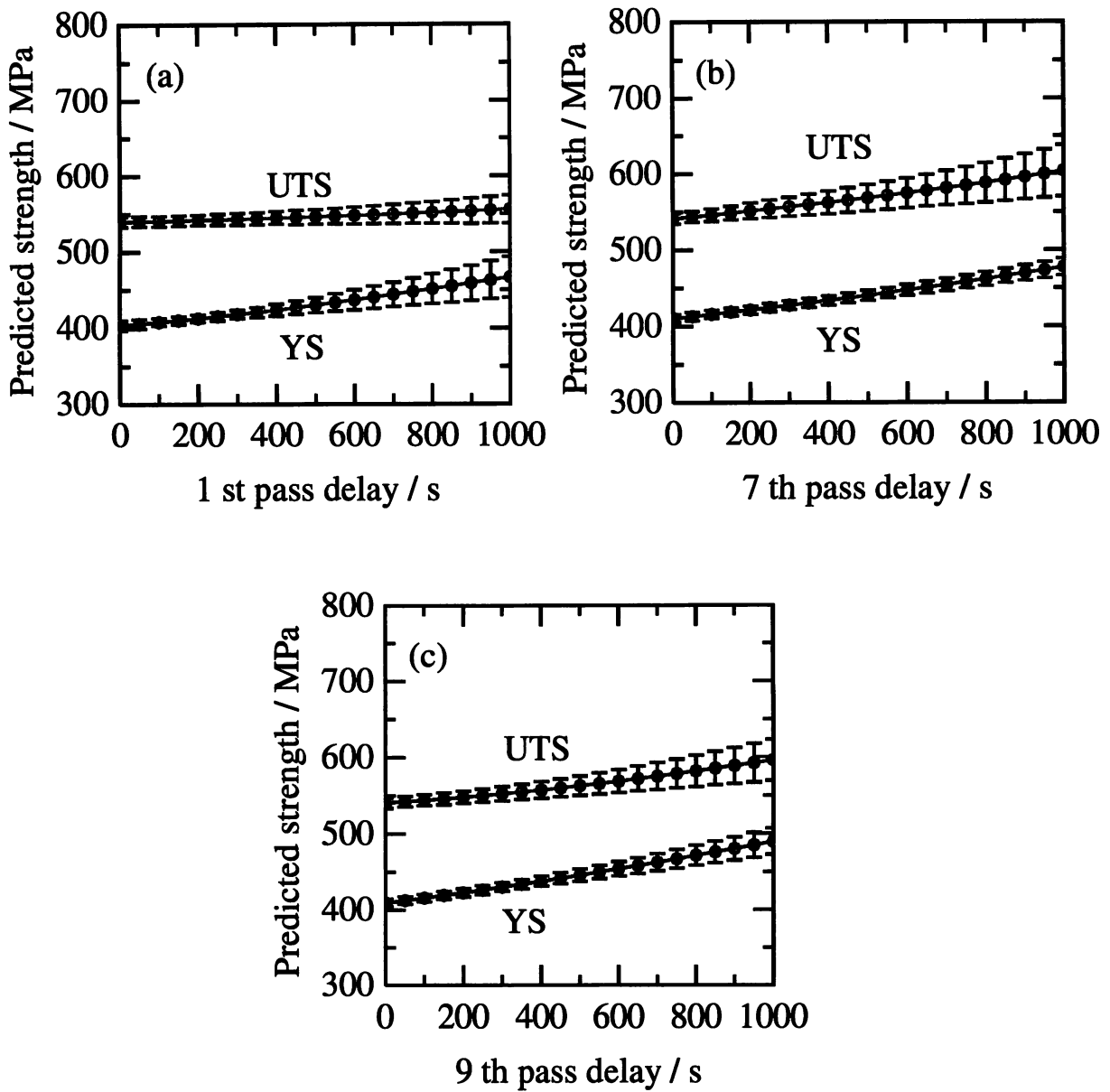


Figure 11.19: Effect of delay time on yield and tensile strengths.

### 11.5 Conclusions

A neural network model capable of predicting the yield and tensile strengths of steel plates as a function of composition and rolling parameters has been trained and tested. The model has been shown to be consistent with established metallurgical trends and can, for example, be used to study the effect of each variable in isolation. There are interesting results on the yield to tensile strength ratio whose value can be altered systematically by controlling the carbon and manganese concentrations.

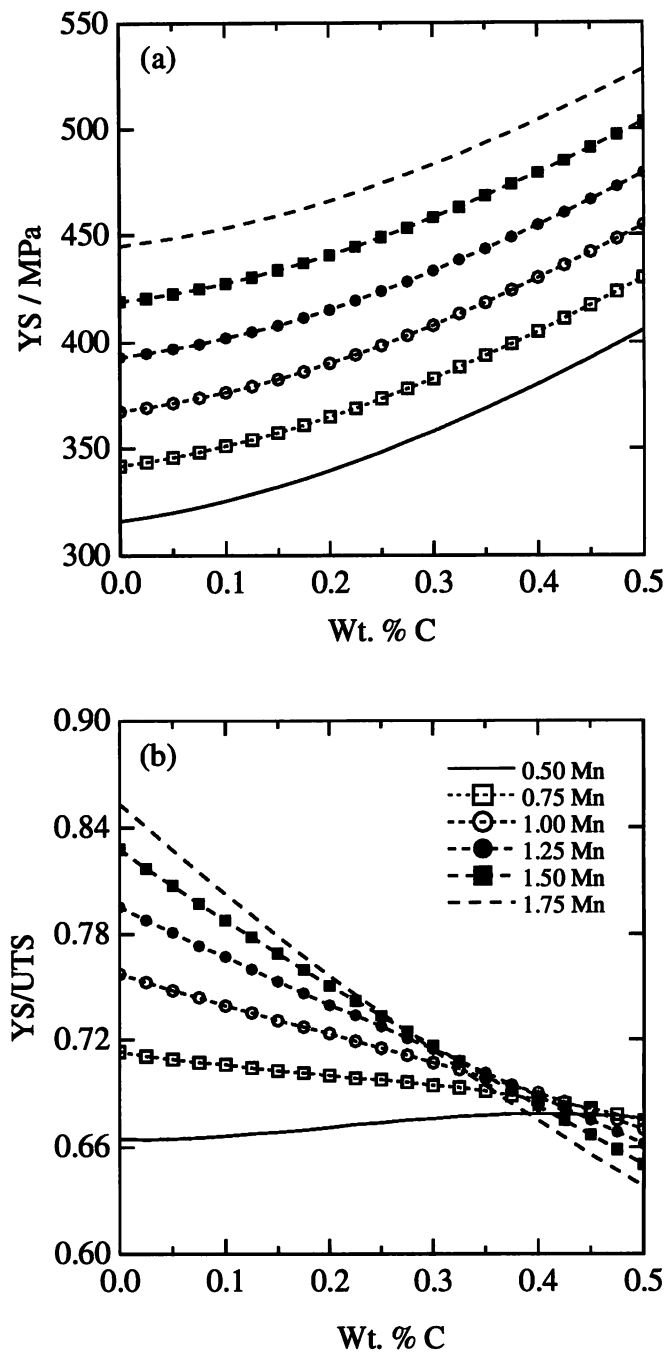


Figure 11.20: The effect of carbon and manganese on the yield strength and the YS/UTS ratio.

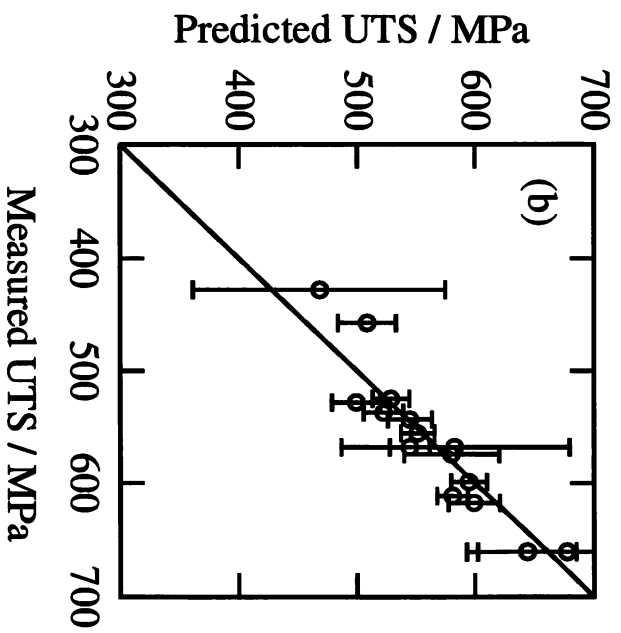
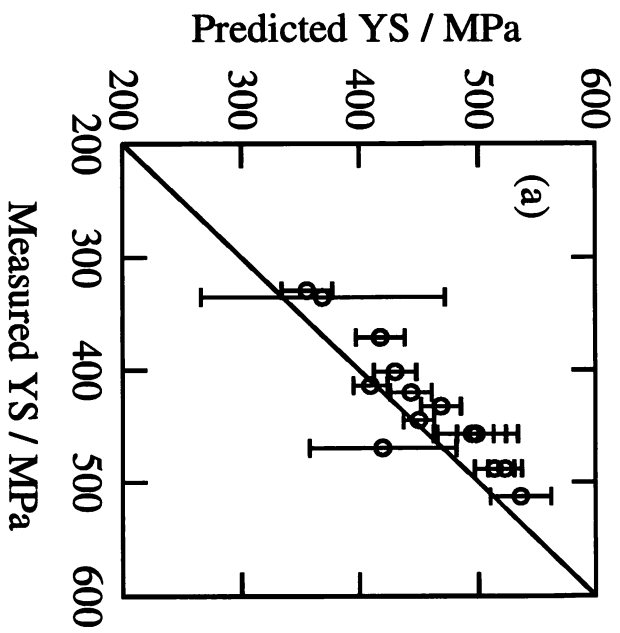


Figure 11.21: Comparison of the predicted YS and UTS with experiments reported in literature [Irvine *et al.*, 1967]. Please note that these experiments were not included in the training database.

Steel	C	Mn	Si	Al	N	Nb	V
1	0.10	0.60	0.41	–	–	0.08	–
2	0.10	0.50	0.1	–	0.013	–	0.095
3	0.15	1.39	0.22	0.039	0.015	–	–
4	0.05	1.30	0.09	–	0.0072	0.037	–
5	0.044	1.42	0.24	–	0.0088	0.048	0.058
6	0.099	1.35	0.26	–	0.0076	0.044	–
7	0.104	1.43	0.27	–	0.0080	0.047	0.075
8	0.151	1.48	0.27	–	0.0080	0.047	–
9	0.149	1.49	0.32	–	0.0088	0.049	0.070
10	0.046	1.40	0.27	–	0.0138	0.037	–
11	0.040	1.31	0.26	–	0.0172	0.043	0.072
12	0.083	1.32	0.16	–	0.016	0.03	–
13	0.085	1.36	0.13	–	0.0154	0.04	0.070
14	0.148	1.43	0.23	–	0.0142	0.04	–
15	0.144	1.48	0.22	–	0.0144	0.05	0.08

Table 11.3: Chemical composition of the steels studied by Irvine *et al.* [1967].  
The concentrations are in wt.%.

Steel	Measured YS / MPa	Predicted YS / MP	Measured UTS / MPa	Predicted UTS / MPa
1	469.5	419.5	568.2	582.9
2	335.0	368.7	427.7	468.4
3	328.9	355.4	528.0	499.2
4	370.7	417.7	457.0	508.7
5	457.2	497.3	568.2	545.0
6	420.0	443.4	555.8	551.7
7	488.0	513.6	617.6	599.2
8	432.4	468.4	599.1	595.0
9	488.0	522.7	660.8	643.8
10	401.5	430.0	524.9	528.9
11	457.1	494.4	543.5	545.0
12	413.9	409.4	537.3	522.6
13	457.1	498.0	574.4	580.2
14	444.8	449.5	611.4	581.4
15	512.8	536.1	660.8	677.1

Table 11.4: Comparison of the predicted yield and tensile strengths with those reported in literature [Irvine *et al.*, 1967]

## Chapter Twelve

# Control–Rolled Bainitic Steels

### 12.1 Introduction

Conventional high–strength bainitic steels have not been very successful due to the presence of coarse cementite particles which are detrimental to toughness. The carbides can be avoided by increasing the silicon concentration. In carbide–free bainitic steels the carbon is partitioned into austenite which is then retained in the microstructure. However, large blocky regions of austenite can transform to untempered, high carbon martensite under the influence of stress, thus rendering the steel susceptible to brittle failure. Phase transformation theory can be used to design alloys in which the fraction of blocky austenite is greatly reduced [Bhadeshia, 1998]. The advantage of such a microstructure is that the ferrite is in the form of fine, submicrometer plates which enhance both strength and toughness; the ferrite plates are separated by films of ductile austenite which are also conducive to good toughness.

It was shown in chapter eight that the deformation of austenite refines bainite because the plate growth is stifled to a smaller limiting size. Thus, it should be possible to improve the strength and toughness of bainitic steels by transforming from “cold–deformed” austenite, rather like the controlled rolling of ferrite–pearlite steels. A contribution to strength also comes from the dislocations in the deformed austenite, which, because of the displacive transformation mechanism, are inherited by bainite [Dulieu and Irani, 1969; Edward and Kennon, 1978]. Conventional bainite sheaves are disrupted when they form from deformed austenite. In normal bainite, the sub–units within a sheaf have identical orientation so cracks can propagate undeflected across the sub–unit boundaries, particularly in low alloy steels where the amount of interplate–phases like cementite, martensite or retained austenite is so small that the plates touch each other over large areas [Pickering, 1967; Bhadeshia, 1992]. The effect of transforming from deformed austenite is to produce a more chaotic microstructure which frequently deflects propagating cracks.

To exploit these potential advantages of transformation from deformed austenite, three bainitic steels were designed and rolled in an experimental rolling mill.

The work was carried out in two parts and accordingly it is reported here in two sections. Two Si–Mn–Mo ingots with compositions similar to the one described in chapter eight were rolled first and tested. After analysing the results, two more steels, microalloyed bainitic steel (MABS) and boron alloyed bainitic steel (BABS) were designed which are described in the second section.

## Part One: Si-Mn-Mo Steels

The nominal composition of the steel was: Fe-0.12C-2.0Si-3.0Mn-0.25Mo (wt.%). This is similar to the steel of chapter eight to which 0.25 weight percent of molybdenum is added to counter the possible temper embrittlement effects arising from the inevitable presence of phosphorus in commercial steels. The calculated phase diagram and the TTT diagram of the steel is shown in Figure 12.1 [Bhadeshia and Edmonds, 1980; Bhadeshia, 1982b]. The  $B_S$  and  $M_S$  temperatures were calculated to be 515 and 382 °C respectively. The maximum fraction of bainite that can form at  $M_S$  was found to be 0.76.

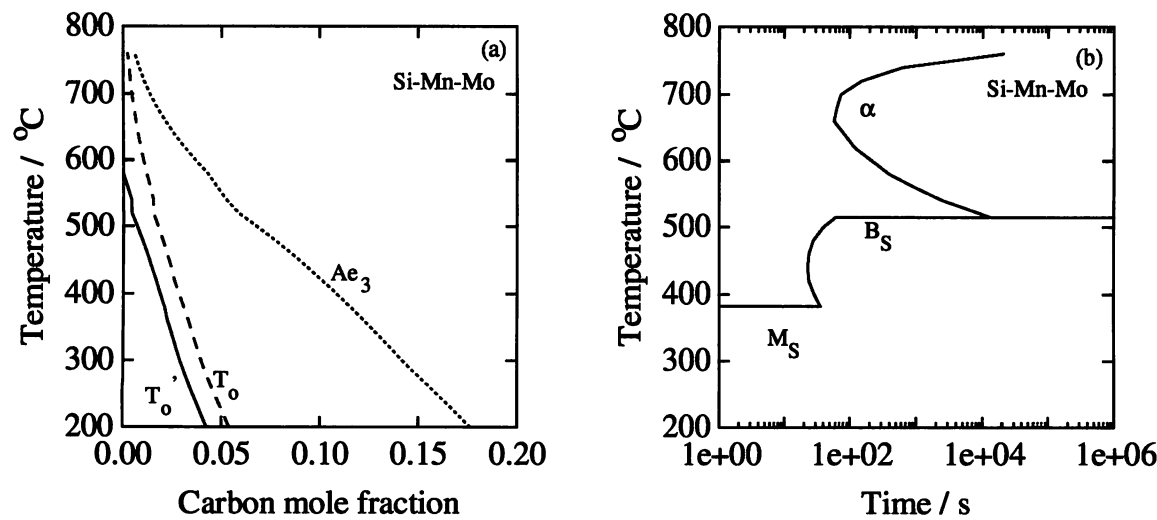


Figure 12.1: The calculated (a) phase diagram and (b) TTT diagrams of Si-Mn-Mo steel [Bhadeshia and Edmonds, 1980; Bhadeshia, 1982b].

### 12.2 Experiments

The alloys were made in a vacuum induction furnace and cast as ingots. The actual ingot compositions are given in Table 12.1.

Alloy	C	Si	Mn	P	S	Ni	Cr	Mo	Al	Nb	B	N
Si-Mn-Mo, 1	0.11	1.95	3.01	0.010	0.005	0.0	0.0	0.26	0.031	0.00	0.0010	0.0052
Si-Mn-Mo, 2	0.13	1.96	2.99	0.010	0.005	0.0	0.0	0.26	0.030	0.00	0.0005	0.0053

Table 12.1: The actual chemical compositions (wt.%) of the Si-Mn-Mo ingots.

The ingots were austenitised at 1200 °C before rolling which was carried out in a pilot rolling mill. One of the ingots was control-rolled. The first few reduction passes were given at relatively high temperatures. The rolling was suspended at 925 °C. The temperature is



referred to as the start hold-temperature (SHT). The rolling was resumed at the end of the ‘delay’ or the ‘hold’ period when the temperature of the work piece reached about 720 °C. This temperature is referred to as the end hold-temperature (EHT). The temperatures were measured using an optical pyrometer. The total reduction after the hold period amounted to 50%. To minimise allotriomorphic ferrite formation, an attempt was made to complete the rolling above the temperature at which the rate of allotriomorphic ferrite formation is maximum. The actual finish rolling temperature (FRT) was below 700 °C. The other ingot (Si-Mn-Mo, 1) was rolled without the delay period (“as-rolled” plate). The FRT in this case was 843 °C. Various rolling parameters are summarised in Table 12.2. The final plate thickness was 20 mm. After rolling, the plates were allowed to cool in air.

Steel	SHT °C	EHT °C	FRT °C
Si-Mn-Mo, 1	–	–	843
Si-Mn-Mo, 2	925	716	688

Table 12.2: The rolling parameters for Si-Mn-Mo steels.

### 12.2.1 Testing

Longitudinal tensile and standard Charpy impact samples were machined from the plates and tested. The fractured samples were examined using a scanning electron microscope.

### 12.3 Results

The measured tensile properties of the rolled plates given in Table 12.3 show that the control-rolled Si-Mn-Mo steel is stronger than the as-rolled one.

Steel	0.2% PS MPa	UTS MPa	Elongation %	Reduction of area / %
Si-Mn-Mo, 1	671	1109	14	45.5
Si-Mn-Mo, 2	796	1240	13	40.5

Table 12.3: The measured tensile properties of the experimental rolled Si-Mn-Mo steels (PS=proof stress).

The results of the Charpy impact tests are shown in Figure 12.2. In spite of its higher strength, the control-rolled Si-Mn-Mo steel was tougher than the as-rolled steel at all temperatures. Thus, control-rolling of bainitic steel with a low FRT improves both the strength and the toughness simultaneously.

The control-rolled Si-Mn-Mo steel showed ductile fracture at 0 °C (Figure 12.3) while the as-rolled steel failed by cleavage in a brittle manner.

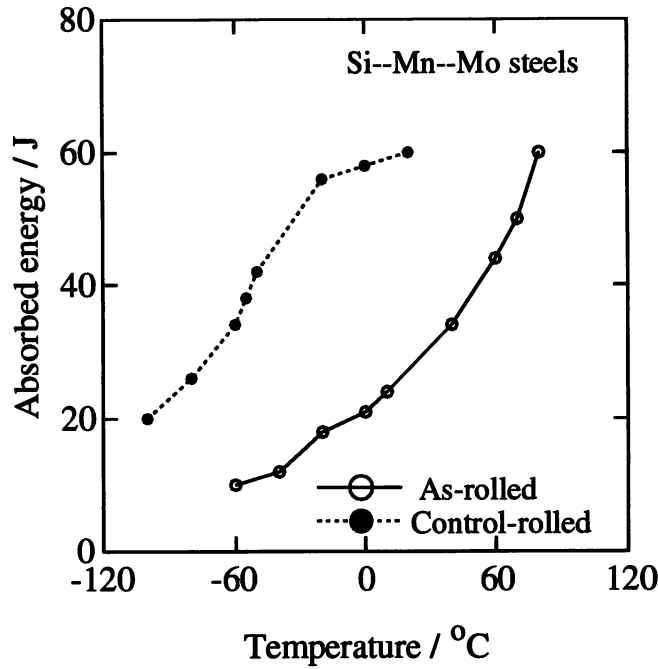
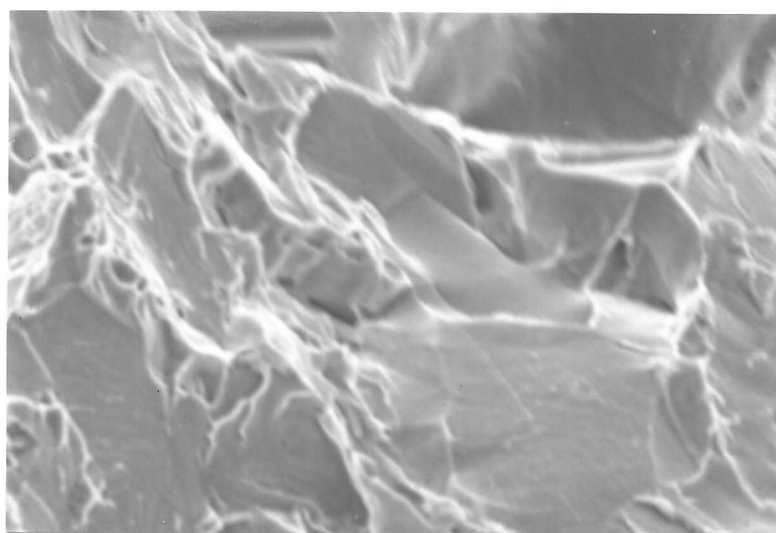


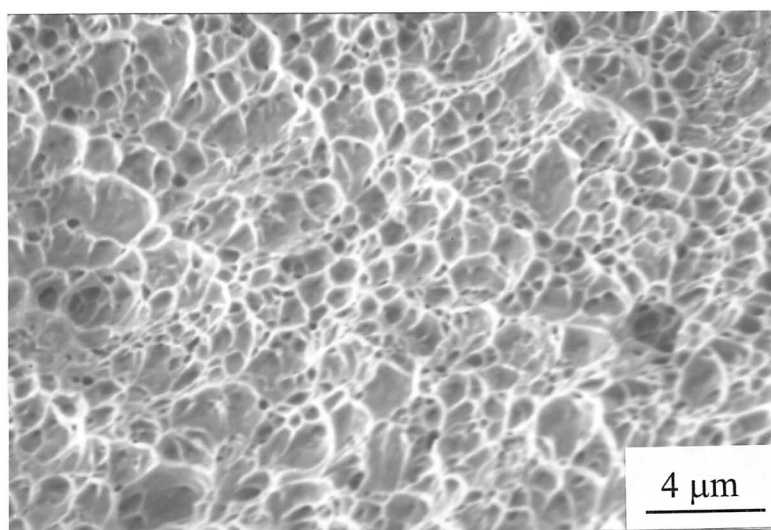
Figure 12.2: The impact transition curves of the two Si-Mn-Mo steels.

The microstructures of the as-rolled and control-rolled Si-Mn-Mo steels are shown in Figures 12.4 and 12.5 respectively. These consist essentially of bainitic ferrite and retained austenite plus some possible martensite in both the cases. A small amount of allotriomorphic ferrite was also observed. Of the two plates, the microstructure was more refined in the control-rolled steel which gave it better strength and toughness. Severe banding was observed in both the steel plates (Figures 12.4a and 12.5a). It is thought that banding also contributed to inferior toughness of the as-rolled plate. This<sup>is</sup> reflected in the fractured tensile specimen where the as-rolled sample showed unusual flaking, Figure 12.6.

The experience gained from above experiments was used to design two new steels. It was decided to reduce the Mn content to minimise banding. Banding can also be avoided by homogenising the ingot before rolling. It was thought that microalloying (Nb) addition can be used to suppress recrystallisation so that a higher amount of strain is retained in austenite. Allotriomorphic ferrite transformation can be retarded by addition of a small amount of boron [Irvine *et al.*, 1957; Pickering, 1978].



a



b

Figure 12.3: Fracture surface of the Charpy samples tested at 0 °C. (a) As-rolled and (b) control-rolled.

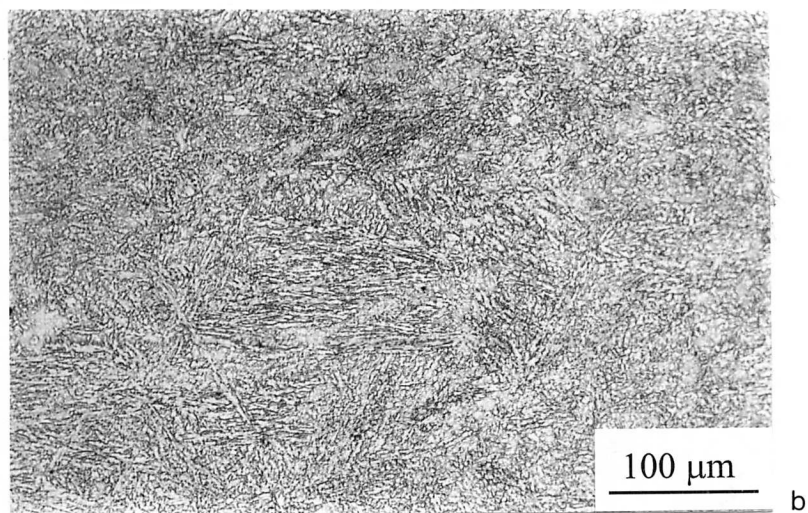
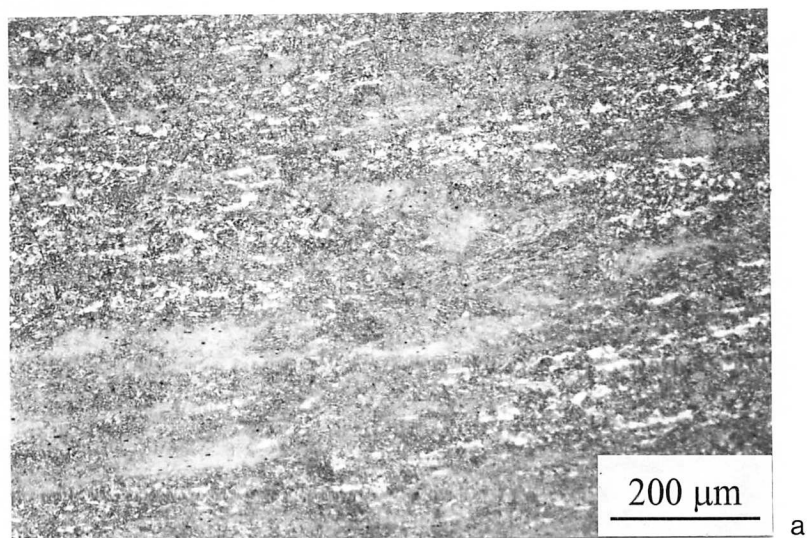


Figure 12.4: Microstructure of the as-rolled Si-Mn-Mo steels. Micrograph in (a) shows banding.

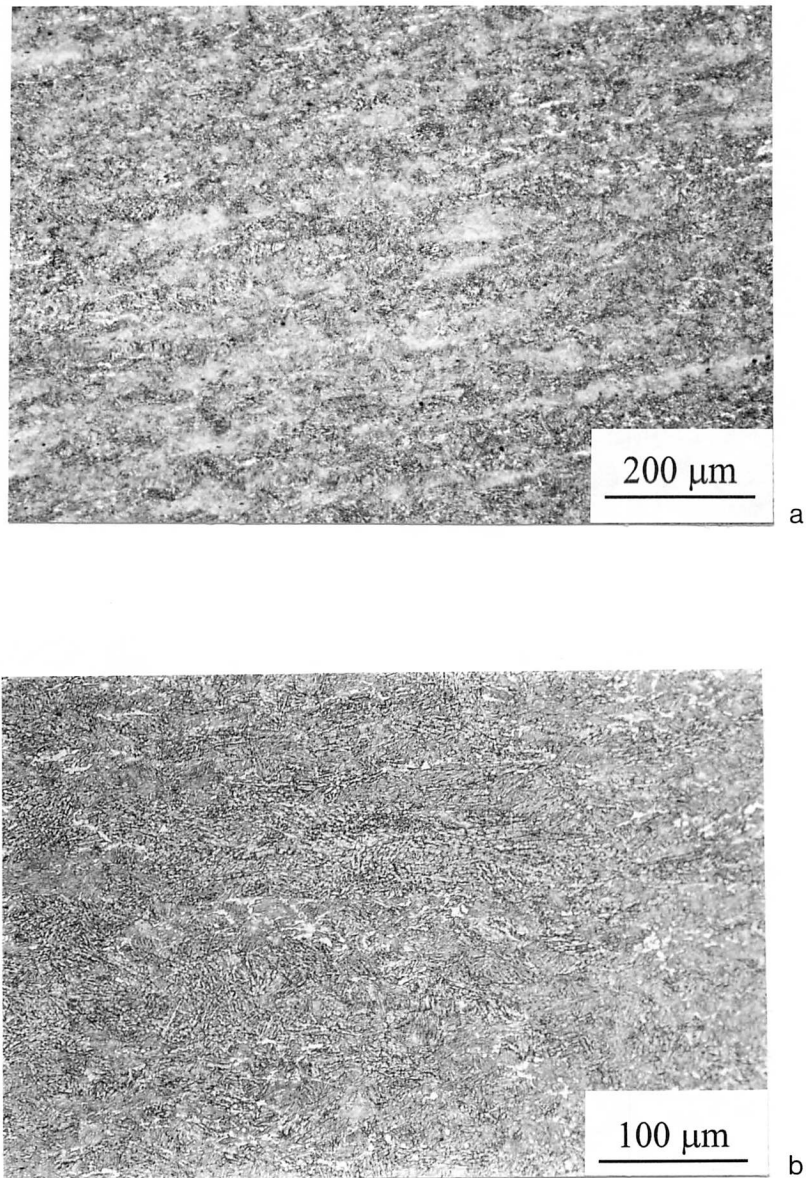


Figure 12.5: Microstructure of the control-rolled Si-Mn-Mo steels. (a) shows banding

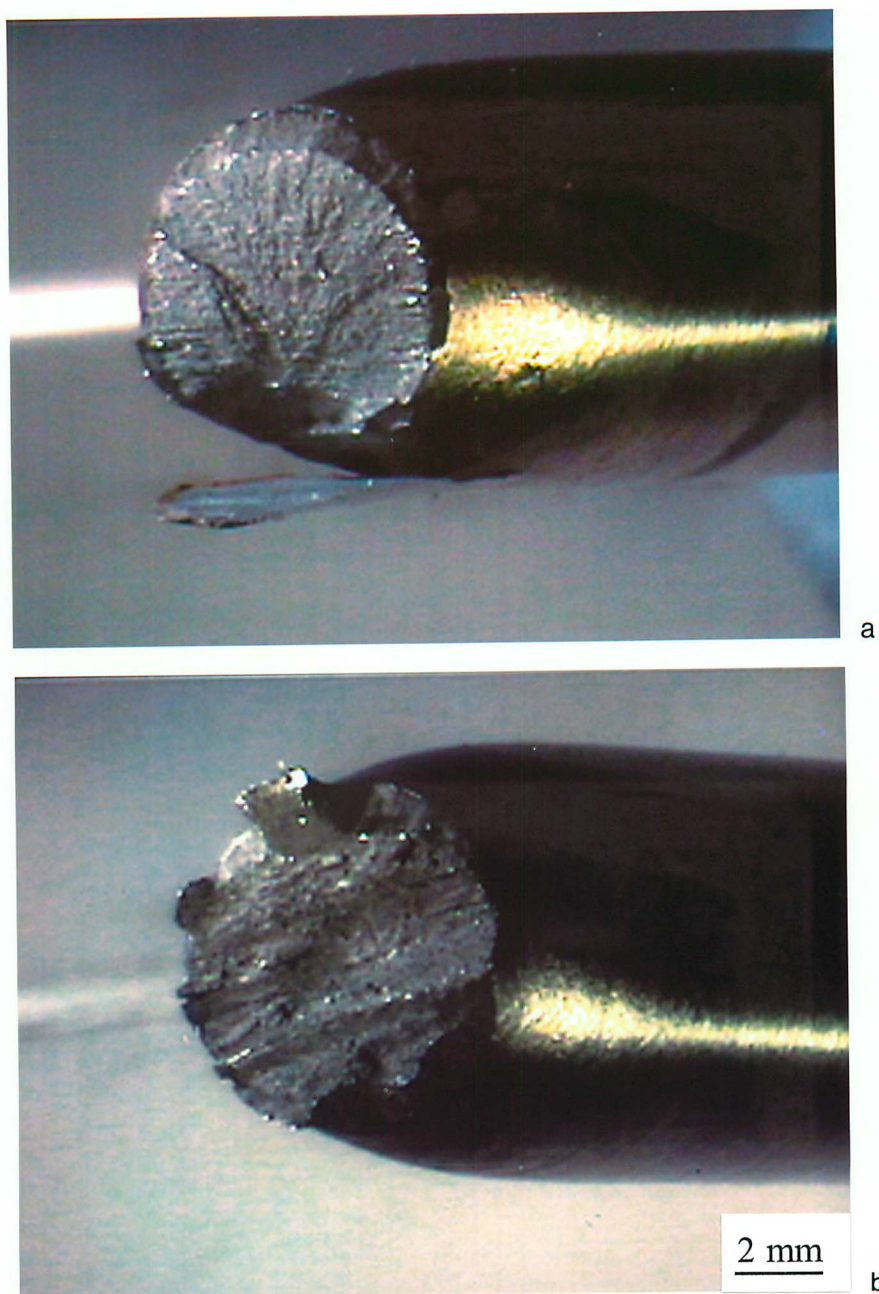


Figure 12.6: The fracture surface of the Si-Mn-Mo steels after tensile test. (a) As-rolled and (b) control-rolled. The tensile specimen from the as-rolled plate shows abnormal failure.

The first part of the report deals with the general situation of the country. It is a very interesting and informative study of the country's development. The author has done a great deal of research and has gathered a wealth of material. The report is well written and is a valuable contribution to the study of the country.

The second part of the report deals with the economic situation. It is a very detailed and thorough study of the country's economy. The author has done a great deal of research and has gathered a wealth of material. The report is well written and is a valuable contribution to the study of the country's economy.

The third part of the report deals with the social situation. It is a very detailed and thorough study of the country's social conditions. The author has done a great deal of research and has gathered a wealth of material. The report is well written and is a valuable contribution to the study of the country's social conditions.

The fourth part of the report deals with the political situation. It is a very detailed and thorough study of the country's political conditions. The author has done a great deal of research and has gathered a wealth of material. The report is well written and is a valuable contribution to the study of the country's political conditions.

The fifth part of the report deals with the cultural situation. It is a very detailed and thorough study of the country's cultural conditions. The author has done a great deal of research and has gathered a wealth of material. The report is well written and is a valuable contribution to the study of the country's cultural conditions.

The sixth part of the report deals with the future of the country. It is a very detailed and thorough study of the country's future. The author has done a great deal of research and has gathered a wealth of material. The report is well written and is a valuable contribution to the study of the country's future.

The seventh part of the report deals with the conclusion. It is a very detailed and thorough study of the country's conclusion. The author has done a great deal of research and has gathered a wealth of material. The report is well written and is a valuable contribution to the study of the country's conclusion.

The eighth part of the report deals with the appendix. It is a very detailed and thorough study of the country's appendix. The author has done a great deal of research and has gathered a wealth of material. The report is well written and is a valuable contribution to the study of the country's appendix.

The ninth part of the report deals with the bibliography. It is a very detailed and thorough study of the country's bibliography. The author has done a great deal of research and has gathered a wealth of material. The report is well written and is a valuable contribution to the study of the country's bibliography.

## Part Two: MABS and BABS

### 12.4 Alloy Design

Two approaches were adopted in the design procedure, one based on phase transformation theory and the other on a neural network model.

The alloy should naturally have sufficient hardenability with respect to bainite in order to avoid the formation of allotriomorphic ferrite even when the austenite is in a deformed state. The composition must nevertheless be such that a high fraction of bainitic ferrite can be obtained so that most of the austenite is consumed before the martensite transformation sets in. This would leave only a small fraction of high carbon austenite, ideally retained as films between the bainite sub-units.

Based on these considerations together with the effect of the alloying elements on the mechanical properties (discussed in the next section), two compositions were selected which are given in Table 12.4. The steels have small additions of Nb or B and are called microalloyed bainitic steel (MABS) and boron alloyed bainitic steel (BABS) respectively. Nb was added to suppress the recrystallisation and grain growth of austenite during hot-rolling following well established practice in the control-rolling of commercial steels [Cuddy, 1982]. Nb is also known to retard the formation of allotriomorphic ferrite [Abe *et al.*, 1986; Huang *et al.*, 1993]. Boron was added to exploit its ability to retard the formation of allotriomorphic ferrite without significantly affecting the bainite transformation [Irvine *et al.*, 1957; Pickering, 1978]. It was hoped that the use of a lower concentration of Mn in both MABS and BABS (permitted by addition of Nb or B) would reduce the incidence of banding in the microstructure. As in the Si-Mn-Mo steel, both MABS and BABS had 0.25 weight percent of Mo to avoid temper embrittlement.

Alloy	C	Si	Mn	Ni	Cr	Mo	Nb	B
MABS	0.12	1.75	2.00	2.00	0.00	0.25	0.01	0.00
BABS	0.13	1.75	2.5	0.00	1.2	0.30	0.00	0.001

Table 12.4: The chemical composition (wt.%) of the bainitic steels for control-rolling.

The calculated phase diagrams and the TTT curves of the steels are shown in Figure 12.7 [Bhadeshia and Edmonds, 1980; Bhadeshia, 1982b]. The calculations do not take into account Nb or B or the deformed state of austenite. The phase boundaries of both the steels follow similar trajectories as those for the Si-Mn-Mo steel described earlier. Both the alloys are seen to have sufficient hardenability to prevent the formation of allotriomorphic ferrite on cooling from the rolling temperature. These data were used to estimate the rolling temperatures, especially the temperature at which to finish the rolling. The calculated bainite and the



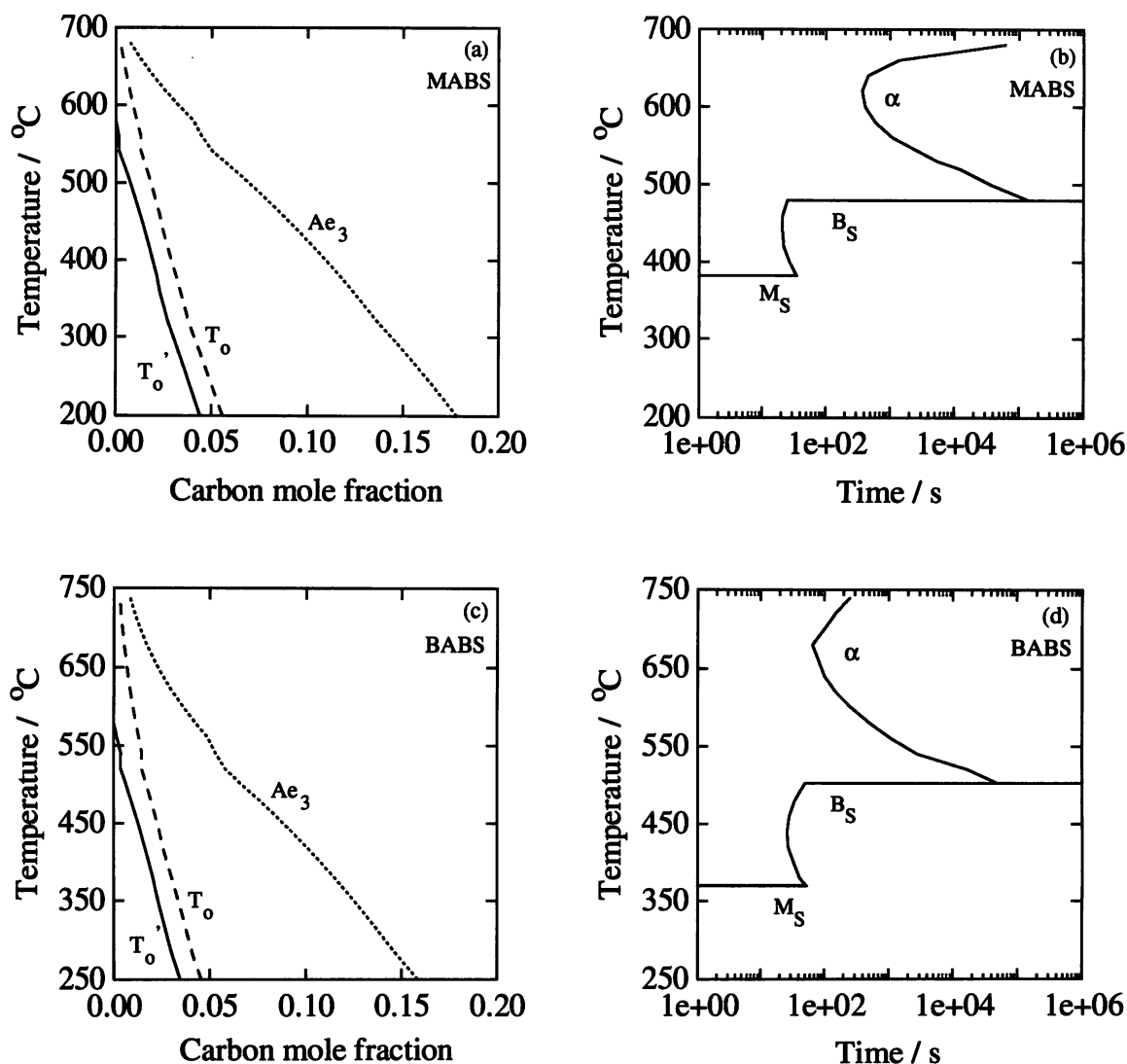


Figure 12.7: The calculated phase diagrams and the TTT diagrams (for the initiation of transformation) of the two bainitic steels. (a and b) Microalloyed bainitic steel (MABS) and (c and d) boron added bainitic steel (BABS) [Bhadeshia and Edmonds, 1980; Bhadeshia, 1982b].

martensite-start temperatures and the maximum fraction of the bainite just above the  $M_S$  temperature calculated from the  $T'_0$  lines for the two alloys are given in Table 12.5.

It was intended to roll the plates to a thickness of 20 mm. The total cooling time from 500 °C to 400 °C (the approximate bainite transformation range for these steels) for this thickness was estimated to be around 300 seconds [Straatmann *et al.*, 1988]. The calculated isothermal kinetics of bainite at  $T = B_S - 50$  °C are shown in Figure 12.8. The rate of the reaction is fast enough so that it should be possible to obtain as much bainite as is thermodynamically feasible, even though the steels are cooled continuously. These calculations were done for undeformed austenite, assuming an initial austenite grain size of 30  $\mu\text{m}$ . The calculations are likely to provide no more than a guide to designing alloys which are able to transform to

Alloy	Calculated $B_S$ / °C	Calculated $M_S$ / °C	Maximum fraction of bainite at $M_S$
MABS	480	382	0.76
BABS	503	371	0.74

Table 12.5: The calculated bainite and the martensite–start temperatures and the maximum fraction of the bainite that can form at a temperature just above  $M_S$ .

predominantly bainitic microstructures, thereby avoiding the formation of excessive quantities of martensite during cooling to ambient temperature.

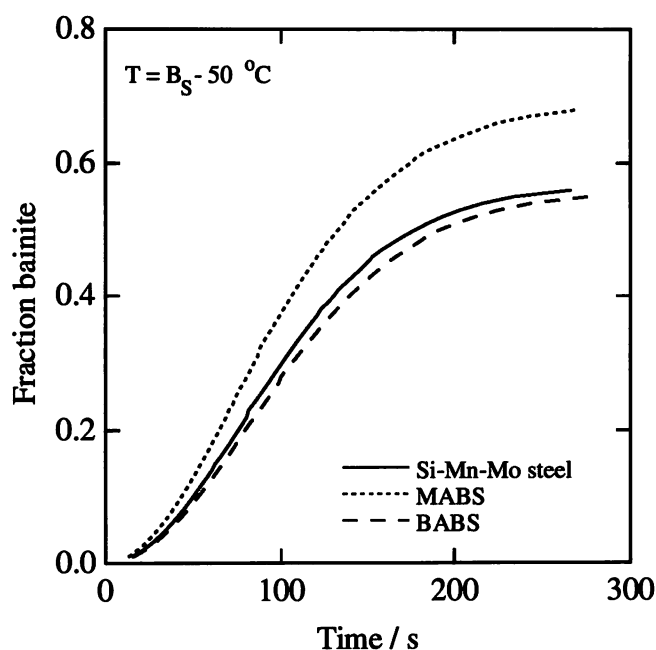


Figure 12.8: The calculated transformation kinetics of bainite at a supercooling of 50 °C below the  $B_S$  temperature. The calculation for the Si–Mn–Mo steel is also presented for comparison.

#### 12.4.1 Neural Network Analysis of Rolled Bainitic Steel Plates

The microstructure calculations are very useful in estimating the hardenability and in optimising the fraction of bainite but they do not give a quantitative estimate of the mechanical properties. A neural network model was therefore used for the purpose. Such models for the yield and the tensile strengths of ferrite–pearlite steels were discussed in chapter eleven. A similar but simpler model was developed and tested on a limited data set for high Si bainitic steels. The details of the technique are not repeated here; only the relevant results are discussed.

The input variables for the analysis included the chemical composition and the finish rolling temperature (FRT) for the yield and the tensile strength models. Bainitic steels undergo

continuous yielding so the elastic limit is generally specified by a 0.2% proof stress (PS). For the Charpy toughness model, the input variables included the yield and the tensile strengths as well. Data from 90 bainitic plates rolled in British Steel constituted the training database. The range, mean and the standard deviation of the input and the output variables are given in Table 12.6. Since the database was small, elements such as sulphur and phosphorus were not considered. The database also included the results of the two plates of the Si-Mn-Mo alloy described in part one.

Variable	Range	Mean	Standard deviation
C	0.1–0.46	0.23	0.077
Si	0.29–2.13	1.75	0.47
Mn	1.06–3.01	2.02	0.32
Ni	0.00–2.07	0.13	0.47
Cr	0.00–2.5	1.11	0.81
Mo	0.00–1.31	0.39	0.38
Nb	0.00–0.054	0.004	0.014
B	0.00–0.0031	0.0014	0.0012
FRT, °C	688–1035	940	934
YS, MPa	503–1411	835	200
UTS, MPa	820–1869	1299	209
Room temp. Charpy, J	4–61	21.5	13

Table 12.6: The variables used in the neural network analysis of bainitic steels. The compositions are in wt.%.

As usual, the training was first performed by randomly splitting the database into two equal halves, one for training and the other for testing to establish the best model for each output. Two hidden unit models gave the best results (minimum test and log predictive error) for the yield and the tensile strength models whereas a one hidden unit model was found to be the best for the room temperature Charpy model. The simplicity of the models is almost certainly a reflection of the limited data set used. These models were then retrained over the entire data set. The comparisons between the measured and the predicted values after retraining the three models are shown in Figure 12.9.

#### 12.4.2 Testing the Models

The optimum models were tested to check whether they reproduce expected metallurgical behaviour. The effect of individual variables on the predicted properties was studied. Unless

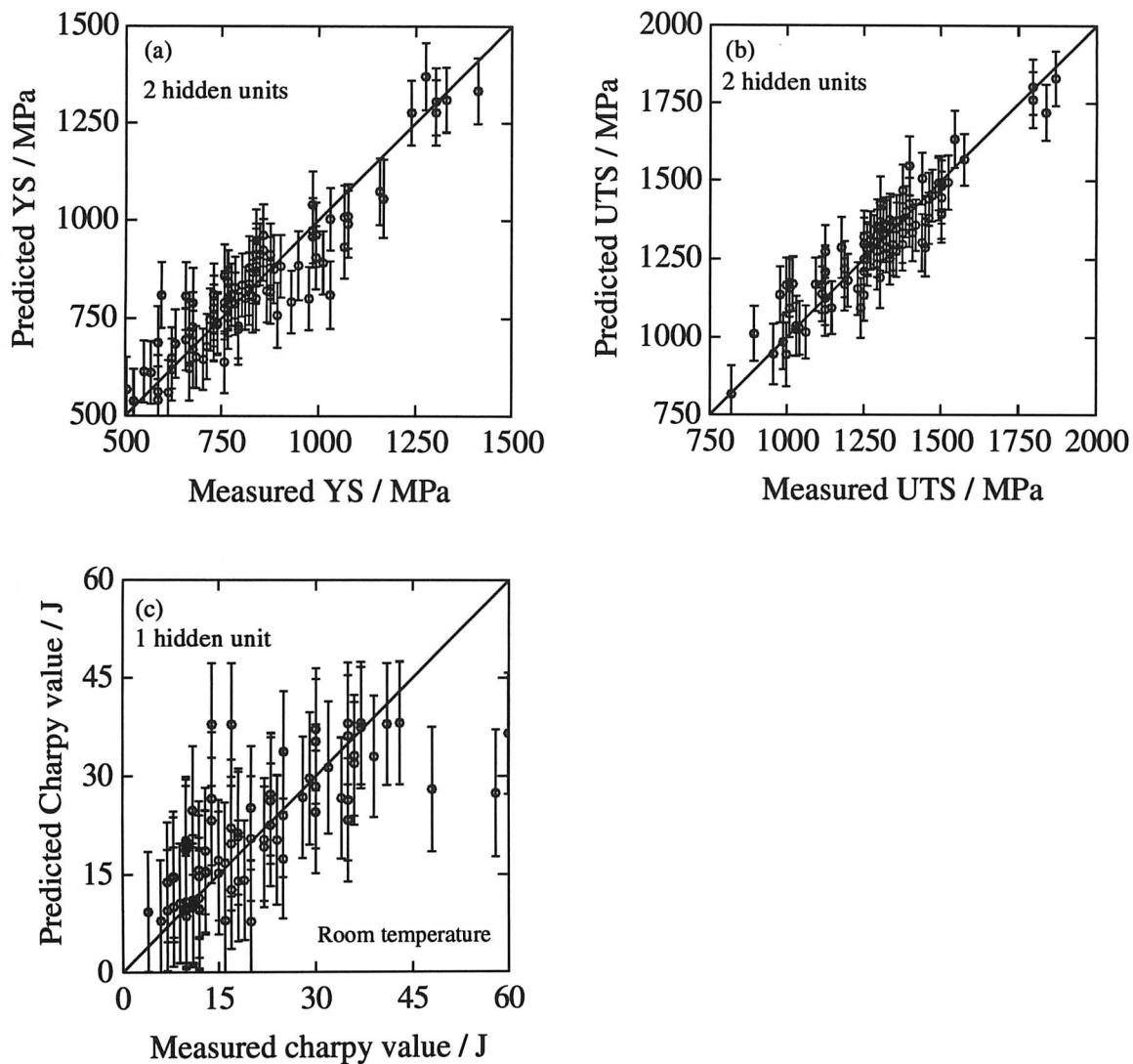


Figure 12.9: The comparison between the measured and the predicted values of (a) Yield strength, (b) ultimate tensile strength and (c) room temperature Charpy impact energy for the optimum retrained models. The error bars represent the  $\pm 1\sigma$  limit and include the inferred noise level of the data and the error bar on the fitted function.

otherwise specified, the variables were set to 0.22C, 1.78Si, 2.0Mn, 0.11Ni, 1.15Cr, 0.35Mo, 0.0035Nb, 0.0013B (all wt.%) with a finish rolling temperature of 948 °C. Only those variables which had an appreciable influence on the properties are discussed. In all the predictions below, the error bars specify  $\pm 1\sigma$  limits and has two components, the error associated with the fitting of the mathematical function and the perceived level of noise in the data.

#### 12.4.2.1 The Yield and the Tensile Strength Models

For low carbon bainitic steels, Irvine and Pickering [1957] have shown that the strength increases linearly as  $T_m$ , the temperature at which the rate of bainite transformation is at a maximum, decreases. This is because the bainite plates become more refined and the disloca-

tion density increases as the transformation temperature drops. Most of the commonly used alloying elements lower the  $B_S$  temperature and should therefore raise the yield and tensile strength. The model predictions are consistent with this for C, Mn and Cr (Figure 12.10), but the variation of yield (proof stress) and tensile strengths with Ni shows odd results. For Ni concentrations less than 1.5 wt.%, the ultimate tensile strength (UTS) decreases with concentration but the yield strength is hardly affected. For larger concentrations both the yield and the tensile strengths increase. There is no obvious explanation for the initial drop in UTS. Nickel does cause a decrease in the bainite transformation temperature, though the effect is much smaller than that of manganese. The trend recognised may be anomalous because there were only six Ni containing steels in a ninety strong database, five of which had 2 wt.% of Ni and one had 1 wt.%.

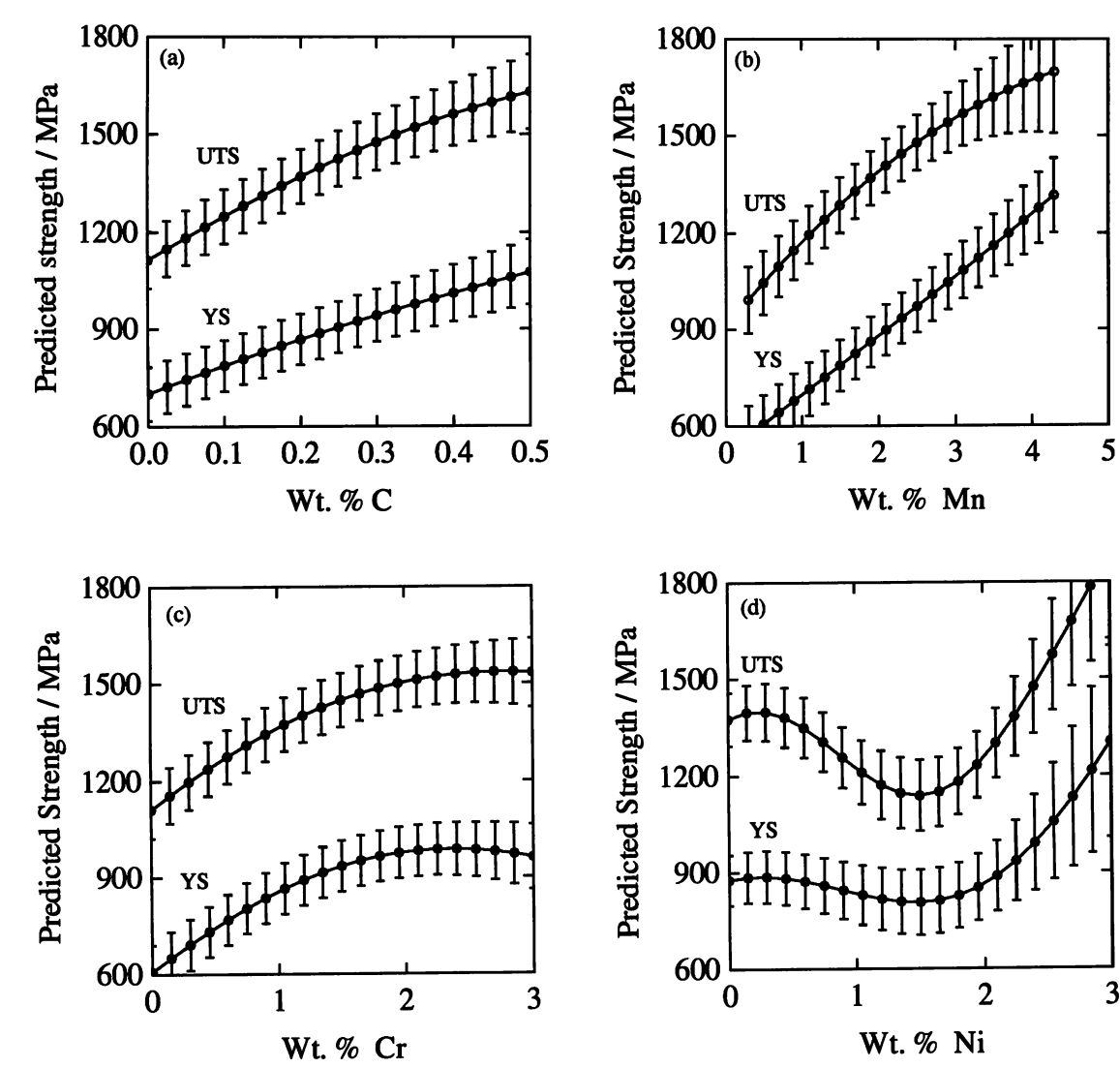


Figure 12.10: The variation in the predicted yield and the tensile strengths of bainitic steels with the concentration of alloying elements. The error bars specify  $\pm 1\sigma$  limits as explained in the text.

Irvine and Pickering [1957] have derived the following empirical relationship between the UTS and the composition of the bainitic alloys:

$$\text{UTS, MPa} = 246.4 + 1925w_C + 231(w_{Mn} + w_{Cr}) + 184.8w_{Mo} + 123.2w_{Ni} + 385(w_V + w_{Ti}) \quad (12.1)$$

where  $w_i$  is the concentration of element  $i$  in wt.%. It was also observed that the yield stress (YS) increased linearly with UTS:

$$\text{YS, MPa} = 0.67 + 0.55 \text{ UTS, MPa} \quad (12.2)$$

The yield and the tensile strength values calculated from the above equations are compared with those predicted by the present neural network model in Figure 12.11. The agreement is good even though equations 12.1 and 12.2 were derived for low Si steels.

Consistent with the equations given above, the effect of the other elements like Si and Nb on the strength properties was relatively small. Mo was predicted to have a strong effect, Figure 12.12. For most of the plates in the database, the finish rolling temperature (FRT) was in the range of 950–1000 °C and the neural network model did not predict any significant variation in strength with the FRT.

#### 12.4.2.2 The Charpy Toughness

Only the room temperature Charpy impact behaviour could be modelled due to lack of data for other temperatures. Besides the variables used in the strength models, the calculated yield and tensile strengths were included as input variables. The change in the room temperature Charpy energy with some of the solute elements is shown in Figure 12.13. The effect of other variables was predicted to be insignificant.

The effect of solutes elements on toughness is two fold. They cause solid solution strengthening which leads to a deterioration in toughness. The solutes also change the microstructure, thereby affecting the toughness. Thus an increase in the concentration of carbon is predicted to reduce the toughness in Figure 12.13a, though the effect is small. Carbon has a strong solid solution strengthening effect and also increases the amount of martensite in the microstructure. Manganese, on the other hand, is beneficial to toughness (Figure 12.13b) because it has a strong effect on hardenability and hence prevents the formation of detrimental phases such as allotriomorphic ferrite.

The unusual effect of nickel on the predicted strength was discussed earlier. Figure 12.13c shows that the toughness predictions are consistent with the predictions of the strength model in that the toughness improves as the strength drops.

Molybdenum is known to improve the toughness by minimising the grain boundary segregation of phosphorus. The model recognises such an effect, as shown in Figure 12.13d. Addition of up to 1 wt.% is predicted to improve the toughness in spite of an increase in the strength.

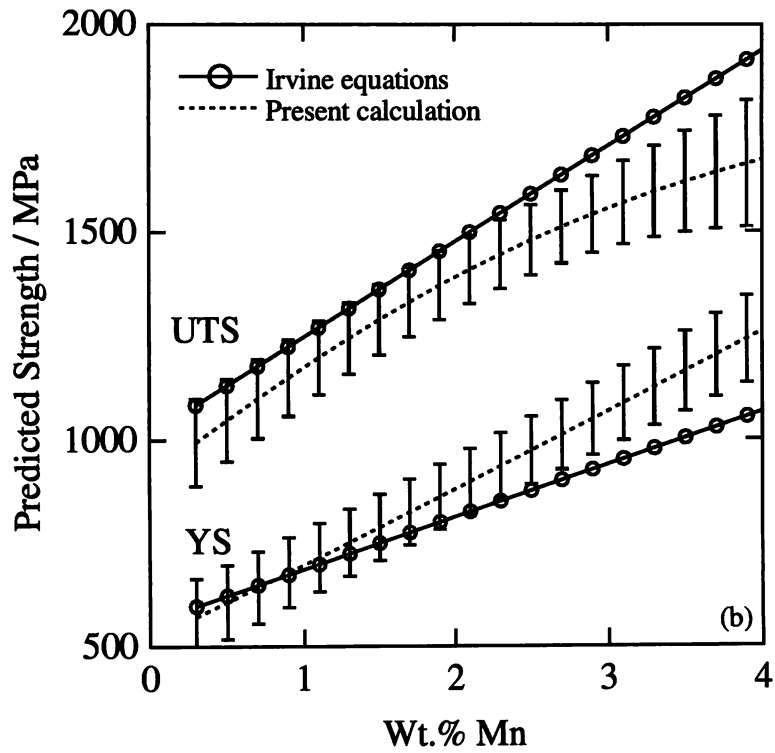
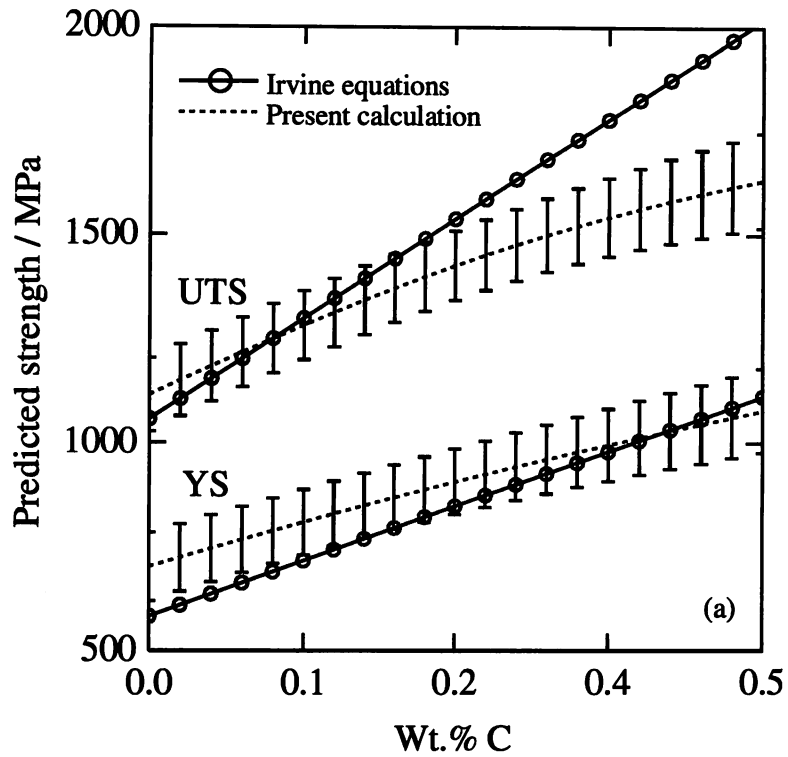


Figure 12.11: Comparison of the yield and the tensile strengths predicted by the present model with those calculated according to the Irvine and Pickering equations [1957]. The base composition for these calculations was 0.22C, 1.78Si, 2.0Mn, 0.11Ni, 1.15Cr, 0.35Mo (wt.%).

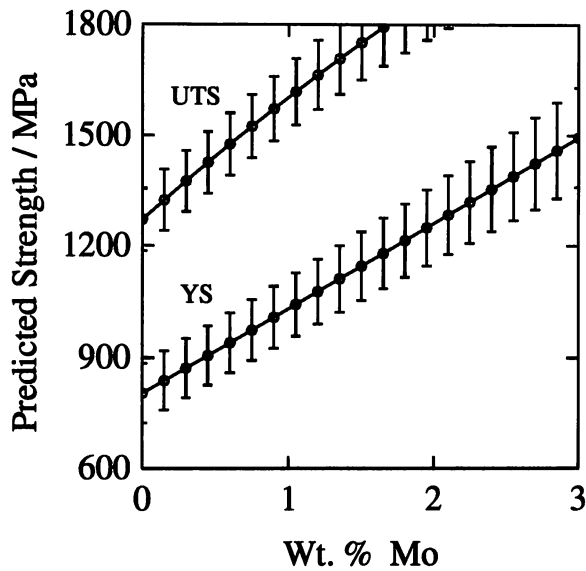


Figure 12.12: The variation of yield and the tensile strength with Mo concentration as predicted by the neural network model.

## 12.5 Rolling and Testing

The actual ingot compositions of MABS and BABS are given in Table 12.7. BABS had slightly higher concentration of aluminium to combine with nitrogen; this leaves free boron available for segregation to the austenite grain boundaries. In an attempt to reduce banding which was observed in both the Si-Mn-Mo plates, the ingots of MABS and BABS were given a homogenisation treatment at 1200 °C for one day. The ingots were then control-rolled to 20 mm plates; other details are given in Table 12.8. Usual tensile and Charpy impact tests were carried out.

Alloy	C	Si	Mn	P	S	Ni	Cr	Mo	Al	Nb	B	N
MABS	0.13	1.72	2.01	0.011	0.006	2.0	0.0	0.25	0.041	0.013	0.0007	0.0042
BABS	0.14	1.70	2.50	0.011	0.007	0.0	1.2	0.30	0.056	0.00	0.0016	0.0059

Table 12.7: The actual chemical compositions (wt.%) of MABS and BABS.

Steel	SHT °C	EHT °C	FRT °C
MABS	1013	720	682
BABS	1003	715	675

Table 12.8: Rolling parameters for MABS and BABS.



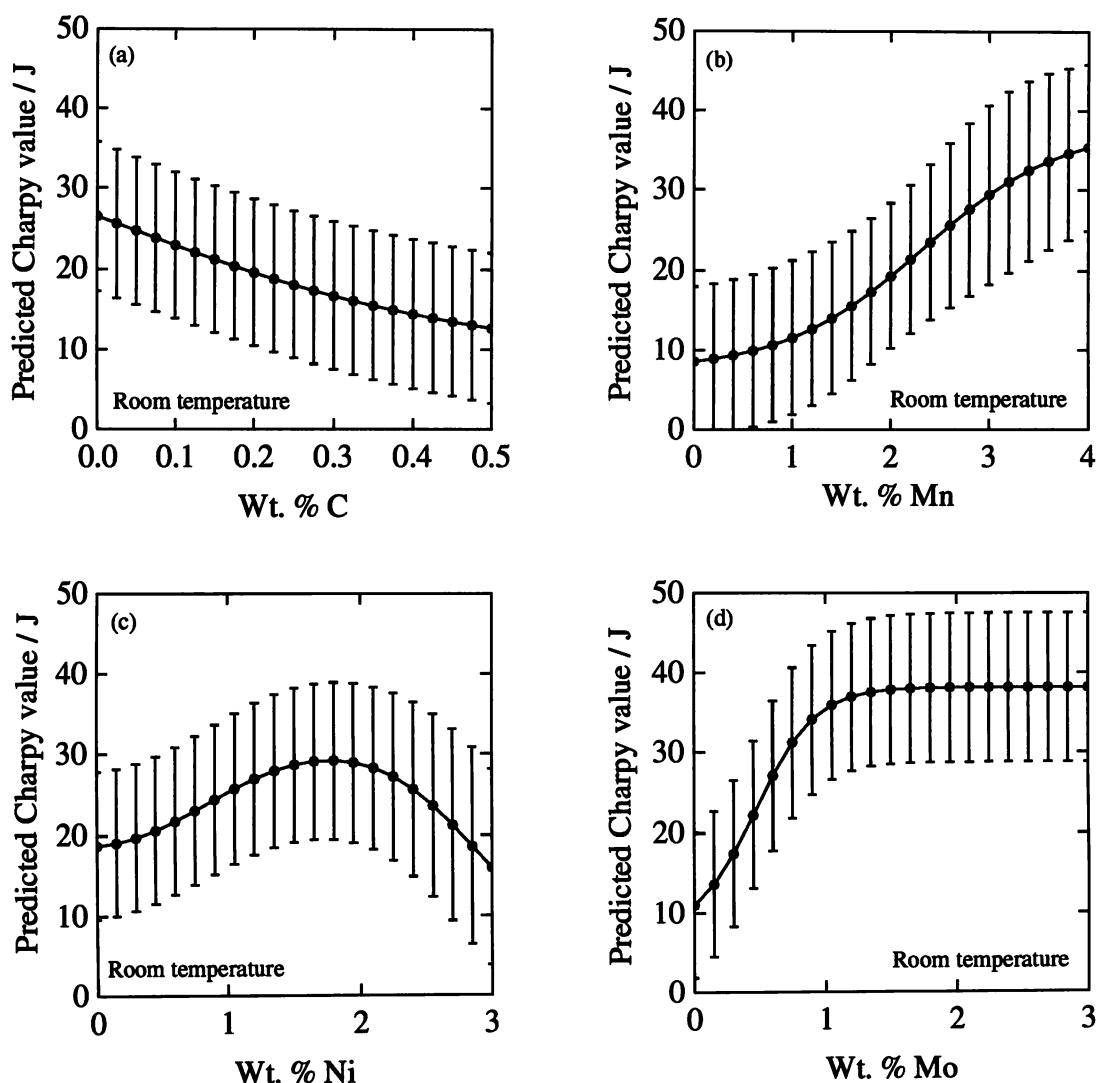


Figure 12.13: The predicted room temperature Charpy impact energy of bainitic steels. The input for the calculations included the predicted yield and the tensile strength for these variables. The error bars specify  $\pm 1\sigma$  limit and has two components.

## 12.6 Results

The measured tensile properties of the two rolled plates are given in Table 12.9. For comparison, the proof and the tensile strengths estimated using the neural network model are also given in Table 12.9. It can be seen that the agreement with the experimental data is very good.

The impact transition curves of the two steels are shown in Figure 12.14. MABS had better toughness than BABS. This could simply be because of the lower strength of MABS which allows it to absorb more energy by the process of plastic deformation. The measured values of the energies absorbed by MABS and BABS during the room temperature Charpy test are compared with the predicted values in Table 12.10. In both the cases, the model underestimates the experimental value, possibly because it cannot account for the effect of a

Steel	0.2% PS MPa	Predicted PS MPa	UTS MPa	Predicted UTS MPa	Elongation %	Reduction of area, %
MABS	749	795 ±91	1199	1106 ±93	14	45
BABS	828	884 ±83	1308	1274 ±88	11	31

Table 12.9: Comparison between the measured and calculated strengths of MABS and BABS. The error bars represent  $\pm 1\sigma$  limits.

Steel	Measured absorbed energy, J	Predicted absorbed energy, J
MABS	50	25 ±10
BABS	42	31 ±9

Table 12.10: Comparison of the measured and predicted Charpy impact energies of MABS and BABS. The error represents  $\pm 1\sigma$  limits.

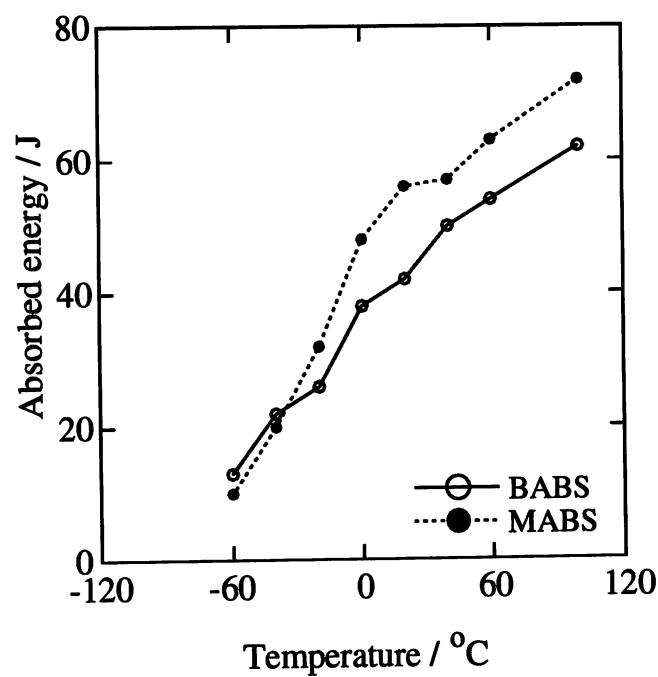


Figure 12.14: The impact transition curves of MABS and BABS.

low FRT. Both the steels showed a ductile fracture at 0 °C, Figure 12.15.

Figure 12.16 shows the toughness (room temperature Charpy value) of a number of as-rolled bainitic steels as a function of their respective tensile strengths. They were rolled to a high finishing temperature (~ 1000 °C in most cases). Containing high Si and up to 0.4 wt.% Mo, these steels were otherwise similar to the ones studied here. The Mo concentration is important because of its direct influence on toughness [Chang, 1995]. The toughness of the steels control-rolled as part of this study is also shown in Figure 12.16. Clearly, at the same

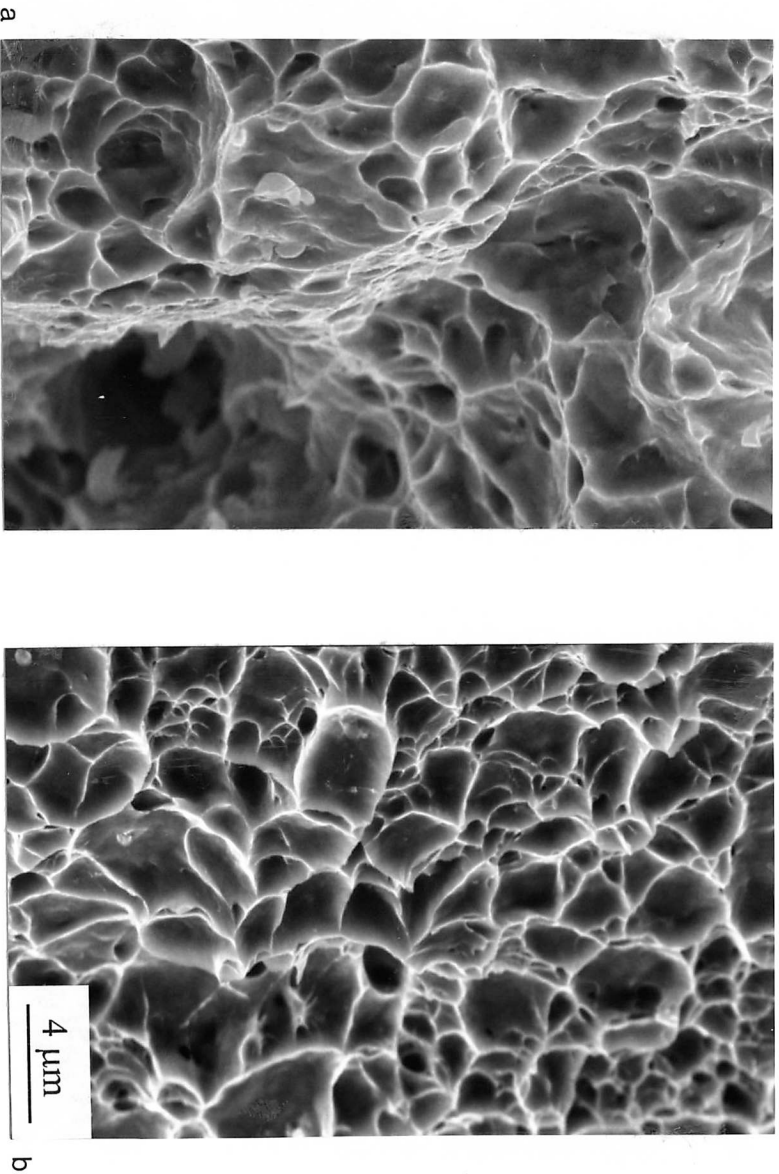


Figure 12.15: SEM fractographs of the Charpy samples tested at 0 °C. (a) MABS and (b) BABS.

strength level, the present control-rolled steels have better toughness than the as-rolled ones.

The microstructure of the two steels is shown in Figures 12.17 and 12.18. In the case of MABS, it was possible to avoid the formation of allotriomorphic ferrite. Despite the homogenization treatment, banding was observed in MABS and BABS, though it was far more severe in MABS.

### 12.7 Conclusions

Three bainitic steels have been designed, rolled and tested. It is possible to achieve a good combination of strength and toughness by ensuring that  $T_o$  condition occurs at high carbon concentrations and by control-rolling. Controlled rolling of bainitic steels can improve the strength and toughness simultaneously.

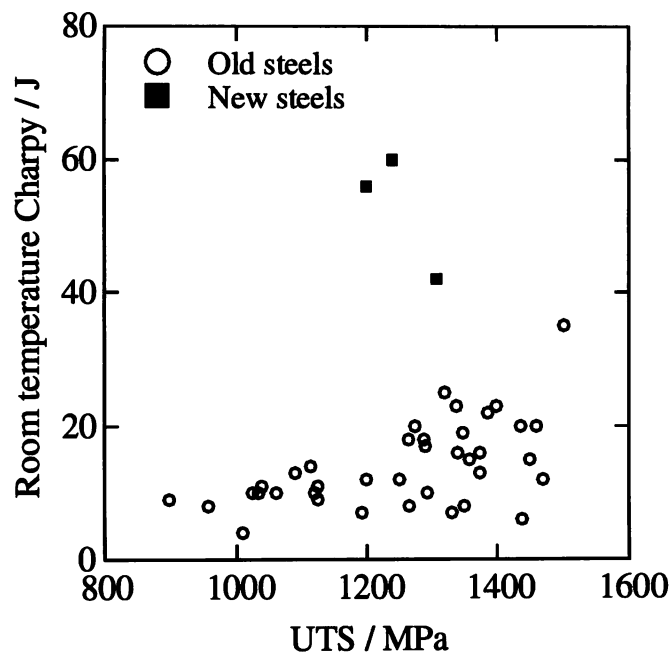


Figure 12.16: The comparison of the toughness of the control-rolled steels with the as-rolled steels at their respective tensile strength.

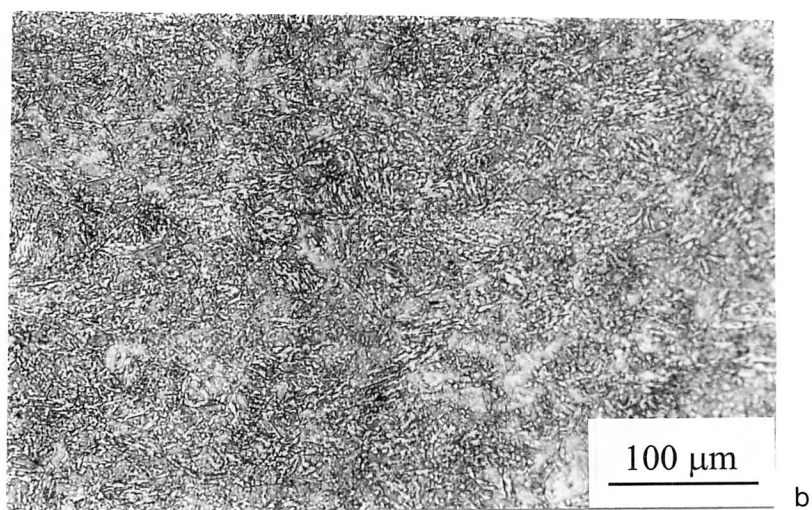
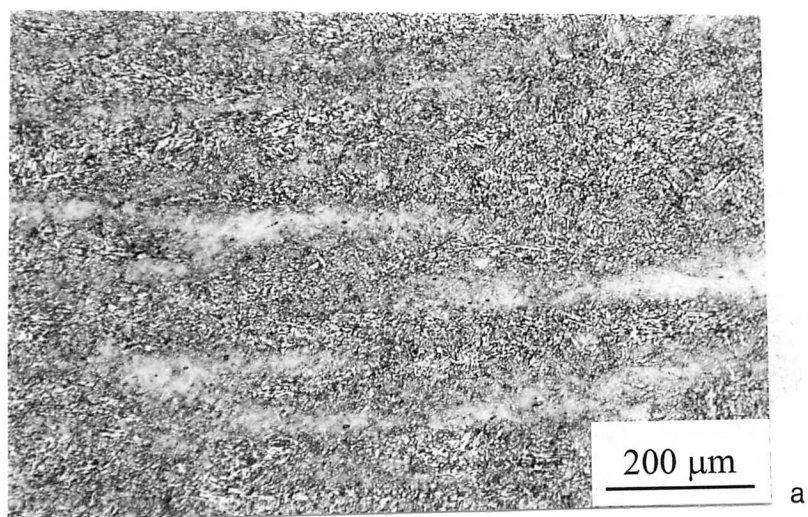


Figure 12.17: The optical microstructure of MABS. (a) shows banding.

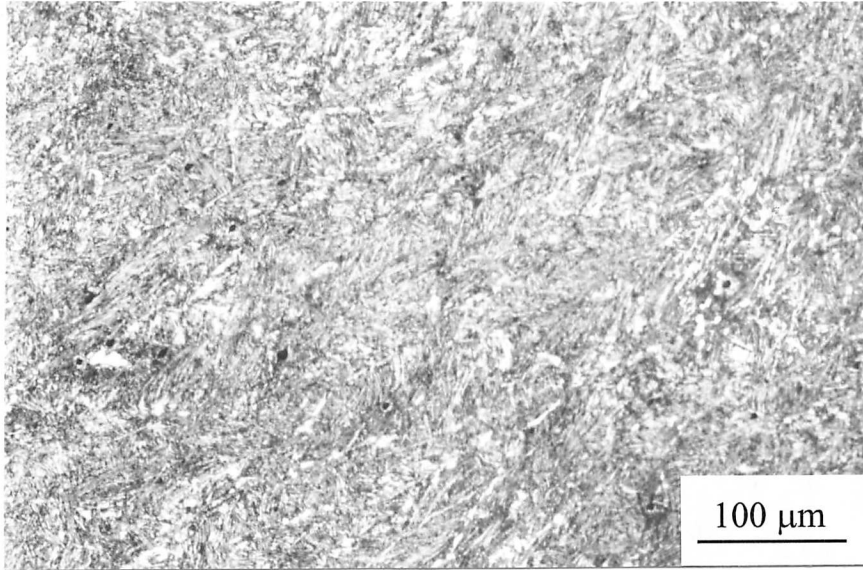


Figure 12.18: The optical microstructure BABS.

## Chapter Thirteen

# Conclusions and Suggestions

The deformation of austenite below its recrystallisation temperature alters its structural state which in turn affects its transformation behaviour. Deformation increases the defect density of austenite in two respects, the total grain boundary surface per unit volume increases and so does the density of the other defects such as dislocations, deformation bands *etc.* This results in an increase in the nucleation site density and overall stored energy of the austenite. All of these have consequences on the subsequent transformation of austenite, the details depending on the mechanism of phase change. The work presented in the thesis has been an attempt to understand and express quantitatively the kinetics of transformation from deformed austenite and to use this knowledge in the design of better steels.

The change in grain topology due to rolling and wire drawing operations has been calculated by applying the appropriate deformation matrix to austenite grains represented by tetrakaidecahedra. It has been possible for the first time to estimate accurately not only the change in the specific grain surface area, but also the increase in the grain edge length as a function of orientation relative to the principal deformation axes.

The calculated increase in the grain boundary surface area compared well with a few measured values reported in literature. Further comparison can be done as and when the data become available.

The increase in the nucleation site density in deformed austenite accelerates the allotriomorphic ferrite transformation. The formation of ferrite is stimulated not only at the austenite grain boundaries but also in the neighbouring regions around the grain boundaries. It is thought that this is due to strain gradient and the resultant concentration of strain near the grain boundaries. The effect has not yet been modelled; even the concept of strain gradient is ill-defined and needs to be clearly understood. Some direct observations are called for.

The early stages of both the allotriomorphic ferrite and bainite transformations are accelerated in the deformed austenite because of the increase in the nucleation site density. However, the subsequent development of the ferrite and bainite reactions is different owing to their growth mechanisms.

Allotriomorphic ferrite forms by a reconstructive mechanism. The transformation is analogous to recrystallisation but with an accompanying change in the crystal structure. The elimination of the stored energy of deformation provides driving force for recrystallisation. Similarly, the growth of allotriomorphic ferrite into the deformed austenite eliminates the defects of the parent phase thereby providing additional driving force for the transformation which

is accelerated as a result. Thus, the austenite becomes less stable because of deformation.

Bainite forms by a displacive mechanism; the change in crystal structure is achieved by a homogeneous deformation. The displacive mechanism of transformation means that defects in the austenite are inherited by the bainite so that the energy stored in austenite due to deformation does not contribute to the driving force for transformation. The parent/product interface consists of dislocations which leave the interface glissile. The motion of any glissile interface is hindered by the presence of defects such as dislocations. The deformation-induced defects restrict the growth of bainite plates. This leads to *mechanical stabilisation* which is akin to work hardening during ordinary plastic deformation where the movement of dislocations is made more difficult by the presence of other dislocations. The stabilisation of the parent phase is unique to displacive transformation and is a *fundamental* way of distinguishing it from the reconstructive transformation. Nevertheless, as pointed out earlier, the stabilisation may be preceded by an acceleration of transformation in the initial stages because of the enhanced nucleation effect.

Building on previous work, a model for bainite transformation with fewer empirical assumptions was developed. The model uses the results of a neural network analysis to estimate the bainite plate thickness as a function of the alloy composition and the reaction temperature. The autocatalytic nucleation of sub-units is treated in a manner which is consistent with the observed sheaf microstructure. The model gave better agreement with experimental data than any previous work.

It is possible that a further improvement can be achieved by considering the variation of aspect ratio of the bainite plates as a function of transformation temperature, although at this point in time this is mere speculation. The model is limited to carbide-free upper bainite so an effort is required to model the precipitation of carbides and hence to generalise the theory to all steels.

Consistent with the theory of bainite transformation, it has been shown that the  $B_S$  temperature may depend on the austenite grain size. Experiments have been conducted which prove such an effect. As a consequence, the so-called universal nucleation function  $G_N$  has been modified and it has been possible to reduce the number of empirical constants in the kinetic theory.

It has been demonstrated for the first time that the kinetic model described above can explain all the experimentally observed features of the mechanical stabilisation phenomenon. However, it is necessary to assume that the distribution of plastic strain is not homogeneous on a microscopic level. Finally, the model has been able to rationalise apparently conflicting published data on mechanical stabilisation on the basis of austenite grain size effect.

The effect of austenite prestrain on the bainite plate thickness is an important input to the stabilisation model. This has not been studied quantitatively. Any work in this direction will be useful. The inhomogeneous nature of the strain distribution also needs to be studied and understood in greater depth. The model predictions regarding the effect of grain size on bainite kinetics in deformed and undeformed austenite should be further verified experimentally. The effect of deformation temperature on stabilisation may also be studied systematically.



The published data on bainite plate thickness of silicon-rich steels have been analysed using neural network technique. It has been shown that the thickness depends primarily on the strength of the austenite at the transformation temperature, and the chemical free energy change accompanying nucleation. It has been argued that a stronger austenite offers a larger resistance to the motion of the transformation interface and this results in finer plates. A high nucleation rate because of a large driving force also leads to microstructural refinement. Temperature *per se* did not have any effect on the plate thickness, its effect is via the austenite strength and the driving force.

The inference of the neural network model that the bainite plate thickness depends strongly on the strength of austenite is consistent with many experiments on martensite and demonstrates the power of a neural network in recognising patterns in complex data.

This is also illustrated by neural network models for estimating the yield and the tensile strengths of structural steels as a function of the rolling process parameters and the chemical composition. The models have been tested to ensure that they conform to the metallurgical principles. The models can quantify the contribution of the individual variables to the strength properties. These are in agreement with several published relationships for simple circumstances.

The network with 108 inputs was trained with a set of 1892 data. For both the yield and the tensile strengths, 2 hidden unit models were found to give the best representation of the data. It is thought that more complex and accurate relationships can be found once a larger number of example data are included in the database. The results of the model can be used to design alloys and to set the optimum rolling conditions to achieve a given strength. This would provide further validation of the model. Similar models can be attempted for elongation and toughness when reliable data become available.

Three bainitic steels were developed using the theory of bainite transformation and the neural network technique. They gave a better set of strength and toughness properties than any existing bainitic steels.

A thorough microstructural characterisation of the new bainitic steels is required. This will help in understanding the role of microstructure in determining the mechanical properties.

The possibility of replacing the conventional bainitic steels with the control-rolled alloys should be explored. This can, at first, be done for specific applications, for example, for rail steels which are currently under development. This may require evaluation of other properties such as fatigue and wear.

## Appendix One

# MAP Documentation

The Materials Algorithms Project (MAP) provides a perpetual FORTRAN library of complete programs, elementary subroutines and functions relevant to materials science and metallurgy. The MAP FORTRAN library is available at:

<http://www.msm.cam.ac.uk/map/mapmain.html>

The program for calculating bainite transformation kinetics is documented below in a format consistent with MAP.

### A.1 Program MAP\_STEEL\_SPEEDNEW

#### A.1.1 Provenance of Source Code

S. B. Singh and H. K. D .H. Bhadeshia, Phase Transformations Group, Department of Materials Science and Metallurgy, Pembroke Street, Cambridge, CB2 3QZ, UK.

#### A.1.2 Purpose

To calculate the isothermal transformation kinetics of upper bainite in steels.

#### A.1.3 Specification

```
PROGRAM MAP_STEEL_SPEEDNEW
IMPLICIT DOUBLE PRECISION (A-H, K-Z), INTEGER (I, J)
DOUBLE PRECISION CNT(4), C(8), K(8), CEN(8), KEN(8), AV(100)
DOUBLE PRECISION ACTEMP(100), AU(100), AXTO(100), AXTO400(100), X(15)
DOUBLE PRECISION W1(4, 14), W2(4), THETA1(14), H(4), AMIN(15), AMAX(15)
```

#### A.1.4 Description

The program uses a new and more rational model than an earlier version [2] to predict the bainite transformation kinetics. The sub-unit thickness is calculated as a function of alloy composition and reaction temperature using the results of a neural network analysis [4]. The model treats the autocatalytic nucleation of sub-units in a more realistic way (chapter six). The maximum volume fraction of bainite at any temperature is calculated using the  $T'_o$  line.

### A.1.5 References

1. Bhadeshia, H. K. D. H., *Journal de Physique*, **43(2-C4)**, (1982), 443-448.
2. Rees, G. I. and Bhadeshia, H. K. D. H., *Materials Science and Technology*, **8**, (1992), 985-993.
3. Singh, S. B., *Ph. D. Thesis*, University of Cambridge, 1998.
4. Singh, S. B. and Bhadeshia, H. K. D. H., *Materials Science and Engineering A*, **245A**, (1998), 72-79.

### A.1.6 Parameters

#### A.1.6.1 Input parameters

K – real array of dimension 8

K contains the composition of the steel in wt.%, corresponding to the alloying elements C, Si, Mn, Ni, Mo, Cr, V, Fe (Fe not entered, is assumed to be the remainder).

TEMP – real

TEMP is the isothermal temperature in °C.

ND – real

ND is the grain size of the parent austenite in micrometers.

CNT – real array of dimension 4

CNT contains the four optimised constants for the bainite transformation model. The values are:

CNT(1) = 0.3854701D-24

CNT(2) = 0.4931922D+01

CNT(3) = 0.3804845D+05

CNT(4) = 0.4515832D+02

ANS – real

ANS is the answer for whether there is intercritical annealing or not.

Yes: ANS = 1, NO: ANS = 0.

VPRIOR – real

VPRIOR is the volume fraction of prior ferrite formed during the intercritical annealing, needed if ANS = 1.

TEMPI – real

TEMPI is the intercritical annealing temperature in °C, only needed if ANS = 1.

IN – integer

IN is the choice of calculation mode:

Isothermal, all volume fractions: IN = 1

Isothermal, one volume fraction: IN = 2.

VOL – real

VOL is the volume fraction if IN = 2.

W1 – real array of dimension (4, 14)

W1 contains the weights required for the neural network computation of the bainite plate thickness, read in from file "WEIGHTS". Weights W1 specify the relationship between the input units and the hidden units of the network [4].

W2 – real array of dimension 4

W2 contains weights for the neural network calculation of the bainite plate thickness, read in from file "WEIGHTS". Weights W2 are for the connection between the hidden units and the output unit [4].

THETA1 – real array of dimension 14

THETA1 contains biases for the neural network computation of the bainite plate thickness, read in from file "WEIGHTS".

AMIN - real array of dimension 15

AMIN contains the minimum value of the variables in the experimental data set used to develop the neural network model for bainite plate thickness, read in from file "WEIGHTS".

AMAX - real array of dimension 15

AMAX contains the maximum value of the variables in the experimental data set used to develop the neural network model for bainite plate thickness, read in from file "WEIGHTS".

#### **A.1.6.2 Output parameters**

The program gives the time, in seconds, required to form a certain volume fraction of bainite at the input temperature. If IN=1, reaction time is calculated for all possible volume fractions at intervals of 0.01. For IN=2, reaction time is calculated for the input fraction VOL. The program also calculates the bainite plate thickness in micrometer. The results of the calculations are written to file "out" and to the screen.

#### **A.1.7 Error Indicators**

#### **A.1.8 Accuracy**

#### **A.1.9 Further Comments**

The calculations are limited to steels where there is no carbide precipitation during transformation.

#### **A.1.10 Example**

##### **A.1.10.1 Program Text**

Complete program.

##### **A.1.10.2 Program Data**

K(1)	=	0.12
K(2)	=	2.03
K(3)	=	2.96
K(4)	=	0
K(5)	=	0
K(6)	=	0
K(7)	=	0
TEMP	=	475
ND	=	135
ANS	=	0
VPRIOR	=	0
TEMPI	=	800

IN = 1

**A.1.10.3 Program Results**

Fraction	Seconds	Micron
0.01	30.6	0.270
0.02	42.7	0.270
0.03	53.1	0.270
0.04	62.0	0.270
0.05	69.8	0.270
0.06	77.0	0.270
0.07	83.7	0.270
0.08	90.1	0.270
0.09	96.2	0.270
0.10	102.0	0.270
0.11	107.7	0.270
0.12	111.0	0.270
0.13	117.0	0.270
0.14	122.8	0.270
0.15	128.4	0.270
0.16	133.9	0.270
0.17	139.2	0.270
0.18	144.5	0.270
0.19	149.7	0.270
0.20	154.9	0.270
0.21	160.1	0.270
0.22	165.3	0.270
0.23	170.5	0.270
0.24	175.8	0.270
0.25	181.1	0.270
0.26	186.4	0.270
0.27	191.8	0.270
0.28	197.3	0.270
0.29	202.8	0.270
0.30	208.5	0.270
0.31	214.2	0.270
0.32	220.2	0.270
0.33	224.7	0.270
0.34	232.0	0.270
0.35	238.8	0.270
0.36	245.5	0.270
0.37	252.4	0.270
0.38	259.6	0.270
0.39	262.5	0.270
0.40	272.1	0.270
0.41	281.4	0.270
0.42	290.8	0.270
0.43	300.4	0.270
0.44	310.6	0.270
0.45	321.4	0.270
0.46	333.2	0.270
0.47	346.1	0.270

Fraction	Seconds	Micron
0.48	360.7	0.270
0.49	377.5	0.270
0.50	397.5	0.270
0.51	422.1	0.270
0.52	448.3	0.270
0.53	526.7	0.270

#### **A.1.11 Auxiliary Routines**

MAP\_STEEL\_AFEG  
MAP\_STEEL\_ATM  
MAP\_STEEL\_AXTO  
MAP\_STEEL\_BOUND  
MAP\_STEEL.CG  
MAP\_STEEL\_ENERGY  
MAP\_STEEL\_FINE  
MAP\_STEEL\_FTO1  
MAP\_STEEL.GMAAX  
MAP\_STEEL.G91  
MAP\_STEEL.INTAN  
MAP\_STEEL.ISO  
MAP\_STEEL.MUCG  
MAP\_STEEL.MUCGREAD  
MAP\_STEEL.MV  
MAP\_STEEL.NEWF  
MAP\_STEEL.OMEGA  
MAP\_STEEL.REED  
MAP\_STEEL.REEDI  
MAP\_STEEL.ROUGH  
MAP\_STEEL.STRAUS  
MAP\_STEEL.THICK  
MAP\_STEEL.WEIGH  
MAP\_STEEL.XALPH.

#### **A.1.12 Keywords**

Isothermal bainite kinetics, bainite plate thickness.

Appendix Two

Data for Neural Network Analysis  
of Steel Plate Processing

Variable	Range	Mean	Standard deviation
Reheat temp., °C	993–1373	1212	22.98
Slab gauge, mm	161–600	245.1	36.25
Slab length, mm	915–4080	2828	700.6
C	0.076–0.25	0.14	0.036
Mn	0.7–1.54	1.29	0.24
Si	0.14–0.46	0.32	0.07
S	0.001–0.019	0.006	0.004
P	0.008–0.027	0.015	0.003
Ni	0.014–0.56	0.038	0.045
Cr	0.01–0.53	0.028	0.047
Mo	0.001–0.017	0.003	0.0014
Cu	0.004–0.296	0.032	0.049
Al	0–0.058	0.036	0.008
N	0–0.011	0.005	0.002
Nb	0–0.043	0.024	0.014
V	0.001–0.063	0.009	0.016
Ti	0–0.033	0.0019	0.0017
S(1)	91.0–354.9	190.3	40.67
D(1)	47.0–736.0	144.3	58.05
T(1)	1.0–3.0	1.5	0.51

*contd...*



Variable	Range	Mean	Standard deviation
S(2)	80.1–343.1	175.4	39.75
D(2)	5.0–39.0	7.3	1.77
T(2)	1.0–5.0	2.2	0.92
S(3)	66.1–328.1	161.1	38.44
D(3)	5.0–105.0	14.4	10.34
T(3)	1.0–25.0	1.5	0.75
S(4)	64.5–311.2	150.0	37.02
D(4)	4.0–198.0	12.16	6.58
T(4)	1.0–6.0	2.4	1.19
S(5)	46.0–288.6	130.6	36.43
D(5)	5.0–1163.0	48.4	160.24
T(5)	1.0–9.0	2.0	0.80
S(6)	34.4–268.0	119.1	36.66
D(6)	3.0–263.0	10.0	8.24
T(6)	1.0–9.0	2.6	0.87
S(7)	26.8–249.1	103.9	35.99
D(7)	5.0–986.0	72.1	181.24
T(7)	1.0–5.0	2.5	0.91
S(8)	21.3–232.1	92.2	35.66
D(8)	4.0–43.0	8.0	3.66
T(8)	1.0–7.0	3.1	1.03
S(9)	15.7–216.9	79.3	33.20
D(9)	0.0–894.0	102.1	218.45
T(9)	0.0–48.0	3.4	1.67
S(10)	12.9–203.5	69.3	31.32
D(10)	0.0–170.0	6.7	5.28
T(10)	0.0–19.0	4.0	1.71

*contd...*

Variable	Range	Mean	Standard deviation
S(11)	11.1–192.0	60.3	28.94
D(11)	0.0–910.0	41.8	128.62
T(11)	0.0–16.0	4.4	1.81
S(12)	8.8–182.4	53.5	26.97
D(12)	0.0–660.0	7.0	17.71
T(12)	0.0–20.0	4.9	2.19
S(13)	8.0–174.0	47.9	24.65
D(13)	0.0–735.0	24.0	84.84
T(13)	0.0–15.0	5.0	2.41
S(14)	5.8–167.2	43.7	22.85
D(14)	0.0–163.0	6.3	6.03
T(14)	0.0–28.0	5.3	2.98
S(15)	7.0–161.6	40.5	20.75
D(15)	0.0–790.0	20.6	84.70
T(15)	0.0–15.0	4.7	3.04
S(16)	5.3–157.1	38.0	19.33
D(16)	0.0–163.0	5.9	8.02
T(16)	0.0–26.0	5.0	3.62
S(17)	7.7–153.8	36.3	17.91
D(17)	0.0–497.0	6.5	19.64
T(17)	0.0–17.0	3.9	3.42
S(18)	7.9–151.3	34.9	16.98
D(18)	0.0–111.0	4.9	7.43
T(18)	0.0–21.0	4.2	4.12
S(19)	7.9–150.2	33.9	16.17
D(19)	0.0–193.0	4.3	8.14
T(19)	0.0–17.0	3.1	3.72

*contd...*

Variable	Range	Mean	Standard deviation
S(20)	7.9–150.2	33.1	15.57
D(20)	0.0–86.0	4.1	7.74
T(20)	0.0–27.0	3.1	4.02
S(21)	7.9–150.2	32.5	15.16
D(21)	0.0–183.0	4.2	14.35
T(21)	0.0–15.0	2.4	3.66
S(22)	7.6–150.2	32.1	14.87
D(22)	0.0–142.0	3.4	8.78
T(22)	0.0–19.0	2.4	3.78
S(23)	7.6–150.2	31.8	14.72
D(23)	0.0–172.0	4.4	16.45
T(23)	0.0–16.0	1.8	3.40
S(24)	7.9–150.2	31.5	14.60
D(24)	0.0–121.0	2.2	6.60
T(24)	0.0–14.0	1.7	3.35
S(25)	7.9–150.2	31.4	14.45
D(25)	0.0–295.0	2.9	15.97
T(25)	0.0–13.0	1.2	2.81
S(26)	7.9–50.2	31.3	14.38
D(26)	0.0–107.0	1.6	6.19
T(26)	0.0–15.0	1.2	3.12
S(27)	7.9–150.2	31.2	14.30
D(27)	0.0–112.0	1.1	5.60
T(27)	0.0–13.0	0.7	2.21
S(28)	6.7–150.2	31.2	14.29
D(28)	0.0–136.0	1.3	7.50
T(28)	0.0–15.0	0.5	2.05

*contd...*

Variable	Range	Mean	Standard deviation
S(29)	7.9–150.2	31.2	14.25
D(29)	0.0–40.0	0.4	2.02
T(29)	0.0–12.0	0.2	1.05
S(30)	7.2–150.2	31.1	14.25
D(30)	0.0–64.0	0.5	4.57
T(30)	0.0–10.0	0.1	0.92
Condition	0 or 1	—	—
YS, MPa	232.0–594.0	398.5	66.64
UTS, MPa	389–692	537.5	44.07

Table A2.1: The variables used in the neural network analysis of steel plate processing (chapter eleven). The concentrations are stated in wt.%. S(J)=screw setting, in mm, for J th pass; D(J)= delay time, in seconds, before J th pass and T(J)=J th pass time in seconds. Condition 0 refers to as-rolled plates whereas 1 refers to control-rolled plates which involved rolling with water cooling with or without a delay period.

# References

- Aaronson, H. I., Hall, M. G., Barnett, D. M. and Kinsman, K. R., *Scripta Metallurgica*, **9** (1975) 705–712.
- Abe, T., Tsukada, K. and Kozasu, I., *HSLA Steels: Metallurgy and Applications*, eds. Gray, M., Ko, T., Shouhua, Z., Baorong, W. and Xishan, X., ASM International, Metals Park, OH, U. S. A., (1986) 103–111.
- Abe, T., Tsukada, K. and Kozasu, I., *Tetsu-to-Hagane*, **74** (1988) 505–512.
- Ali, A., *Widmanstätten Ferrite and Bainite in Ultra High Strength Steels*, Ph. D. Thesis, University of Cambridge, (1991).
- Ali, A. and Bhadeshia, H. K. D. H., *Materials Science and Technology*, **5** (1989) 398–402.
- Ali, A. and Bhadeshia, H. K. D. H., *Materials Science and Technology*, **6** (1989) 781–784.
- Amano, K., Matomura, T., Koda, M., Shiga, C. and Tanaka, T., *Accelerated Cooling of Rolled Steels*, ed. Southwick, P. D., TMS-AIME, Warrendale, PA, U. S. A., (1986) 349–365.
- Amin, R. K. and Pickering, F. B., *Thermomechanical Processing of Microalloyed Austenite*, eds. DeArdo, A. J., Ratz, G. A. and Wray, P. J., TMS-AIME, Warrendale, PA, U. S. A., (1982a) 1–31.
- Amin, R. K. and Pickering, F. B., *Thermomechanical Processing of Microalloyed Austenite*, eds. DeArdo, A. J., Ratz, G. A. and Wray, P. J., TMS-AIME, Warrendale, PA, U. S. A., (1982b) 377–402.
- Avrami, M., *Journal of Chemical Physics*, **7** (1939) 1103–1112.
- Babu, S. S., and Bhadeshia, H. K. D. H., *Materials Science and Engineering A*, **156A** (1992) 1–9.
- Bai, D. Q., Yue, S., Maccagno, T. M. and Jonas, J. J., *ISIJ International*, **38** (1998) 371–379.
- Barford, J. and Owen, W. S., *Journal of the Iron and Steel Institute*, **197** (1961) 146–151.
- Bay, B. and Hansen, N., *Recrystallisation and Grain Growth of Multi-Phase and Particle Containing Materials*, eds. Hansen, N., Jones, A. R. and Leffers, T., Risø National Laboratory, Roskilde, Denmark, (1980) 51–56.
- Bhadeshia, H. K. D. H., *Acta Metallurgica*, **29** (1981) 1117–1130.
- Bhadeshia, H. K. D. H., *Journal de Physique*, **43(2–C4)** (1982a) 443–448.
- Bhadeshia, H. K. D. H., *Metal Science*, **16** (1982b) 159–165.
- Bhadeshia, H. K. D. H., *Phase Transformations in Ferrous Alloys*, eds. Marder, A. R. and Goldstein, J. I., TMS-AIME, Warrendale, PA, U. S. A., (1984) 335–340.
- Bhadeshia, H. K. D. H., *Progress in Materials Science*, **29** (1985) 321–386.

- Bhadeshia, H. K. D. H., *Worked Examples in the Geometry of Crystals*, The Institute of Metals, London, U. K., (1987) 1–100.
- Bhadeshia, H. K. D. H., *Bainite in Steels*, Institute of Materials, London, U. K., (1992).
- Bhadeshia, H. K. D. H., *Mathematical Modelling of Weld Phenomena II*, eds. Cerjak, H. and Bhadeshia, H. K. D. H., Institute of Materials, London, U. K., (1995) 71–118.
- Bhadeshia, H. K. D. H., *Displacive Phase Transformations and Their Applications in Materials Engineering*, eds. Inoue, K., Mukherjee, K., Otsuka, K. and Chen, H., TMS, Warrendale, PA, U. S. A., (1998) 69–78.
- Bhadeshia, H. K. D. H. and Edmonds, D. V., *Metallurgical Transactions A*, **10A** (1979) 895–907.
- Bhadeshia, H. K. D. H. and Edmonds, D. V., *Acta Metallurgica*, **28** (1980) 1265–1273.
- Bhadeshia, H. K. D. H. and Waugh A. R., *Acta Metallurgica*, **30** (1982) 775–784.
- Bhadeshia, H. K. D. H., Svensson, L. -E. and Grefott, B., *Welding Metallurgy of Structural Steels*, ed. Y. Koo, TMS-AIME, Warrendale, PA, U. S. A., (1987) 517–530.
- Bhadeshia, H. K. D. H. and Christian, J. W., *Metallurgical Transactions A*, **21A** (1990) 767–797.
- Bhadeshia, H. K. D. H., David, S. A., Vitek, J. M. and Reed, R. W., *Materials Science and Technology*, **7** (1991) 686–698.
- Bhadeshia, H. K. D. H., MacKay, D. J. C. and Svensson, L. -E., *Materials Science and Technology*, **11** (1995) 1046–1051.
- Bhattacharya, S. and Kehl, G. L., *Trans. ASM*, **47** (1955) 351–379.
- Boratto, F., Barbosa, R., Yue, S. and Jonas, J. J., *International Conference on Physical Metallurgy of Thermomechanical Processing of Steel and Other Metals (Thermec-88)*, ed. Tamura, I., ISIJ, Tokyo, Japan, (1988) 383.
- Cahn, J. ., *Acta Metallurgica*, **4** (1956) 449–459.
- Chang, L. C., *Transformation and Novel Bainitic Rail Steels*, Ph. D. Thesis, University of Cambridge, (1995).
- Chang, L. C. and Bhadeshia, H. K. D. H., *Materials Science and Technology*, **11** (1996) 874–881.
- Christian, J. W., *Decomposition of Austenite by Diffusional Processes*, eds. Zackay, V. F. and Aaronson, H. I., Interscience Publishers, NY, U. S. A., (1962) 387–546.
- Christian, J. W., *Theory of Transformations in Metals and Alloys*, Part 1, 2nd edition, Pergamon Press, Oxford, U. K., (1975).
- Christian, J. W. and Edmonds, D. V., *Phase Transformations in Ferrous Alloys*, eds. Marder, A. R. and Goldstein, J. I., TMS-AIME, Warrendale, PA, U. S. A., (1984) 293–325.
- Christian, J. W., *Metallurgical and Materials Transactions A*, **25A** (1994) 1821–1839.
- Christian, J. W., *Progress in Materials Science*, **42** (1997) 101–108.
- Coates, D. E., *Metallurgical Transactions*, **4** (1973) 2313–2325.
- Cohen, M. and Hansen, S. S., *HSLA Steels: Metallurgy and Applications*, eds. Gray, M.,

- Ko, T., Shouhua, Z., Baorong, W. and Xishan, X., ASM International, Metals Park, OH, U. S. A., (1986) 61–71.
- Collins, L. E., Shehata, M. T. and Boyd, J. D., *Phase Transformations '87*, ed. Lorimer, G. W., The Institute of Metals, London, U. K., (1988) 530–533.
- Cottrell, A. H., *Journal of the Iron and Steel Institute*, **151** (1945) 93P–104P.
- Cottrell, A. H., *Dislocations and Plastic Flow in Crystals*, Oxford University Press, London, U. K., (1961).
- Cuddy, L. J., *Thermomechanical Processing of Microalloyed Austenite*, eds. DeArdo, A. J., Ratz, G. A. and Wray, P. J., TMS–AIME, Warrendale, PA, U. S. A., (1982) 129–140.
- Daigne, J., Guttman, M. and Naylor, J. P., *Materials Science and Engineering*, **56** (1982) 1–10.
- Davenport, A. T., *The Hot Deformation of Austenite*, ed. Ballance, J. B., TMS–AIME, NY, U. S. A., (1977) 517–536.
- Davenport, E. S., Grange, R. A. and Hafsten, R. J., *Trans. AIME*, **145** (1941) 301.
- Drozдов, B. Y., Rogan, L. I. and Entin, R. I., *Physics of Metals and Metallography*, **13** (1962) 135–138.
- Dulieu, D. and Irani, J. J., *Journal of the Iron and Steel Institute*, **207** (1969) 308–318.
- Dyson, D. J., Holmes, B., *Journal of Iron and Steel Institute*, (1970) 469–474.
- Edwards, R. H. and Kennon, N. F., *Journal of the Australian Institute of Metals*, **19** (1974) 45–50.
- Edwards, R. H. and Kennon, N. F., *Metallurgical Transactions A*, **9A** (1978) 1801–1809.
- Ericsson, C. E., Bhat, M. S., Parker, E. R. and Zackay, V. F., *Metallurgical Transactions A*, **7A** (1976) 1800–1803.
- Essadiqi, E., and Jonas, J. J., *Metallurgical Transactions A*, **20A** (1989) 987–998.
- Feng, B., Dunne, D. P. and Chandra, T., *Materials Forum*, **14** (1990) 264–269.
- Fiedler, H. C., Averbach, B. L. and Cohen, M., *Trans. ASM*, **47** (1955) 267–290.
- Freiwillig, R., Kurdman, J. and Chraska, P., *Metallurgical Transactions A*, **7A** (1976) 1091–1097.
- Fujii, H., Bhadeshia, H. K. D. H. and MacKay, D. J. C., *ISIJ International*, **36** (1996) 1373–1382.
- Fujiwara, K., Okaguchi, S. and Ohtani, H., *ISIJ International*, **35** (1995) 1006–1012.
- Ghosh, G. and Raghavan, V., *Materials Science and Engineering A*, **79A** (1986) 223–231.
- Gladman, T., *The Physical Metallurgy of Microalloyed Steels*, The Institute of Materials, London, U. K., (1997).
- Graham, L. W. and Axon, H. J., *Journal of the Iron and Steel Institute*, **191** (1959) 361–365.
- Hawkins, M. J. and Barford, J., *Journal of the Iron and Steel Institute*, **210** (1972) 97–105.
- Hehemann, R. F., *Phase Transformations*, ASM, Metals Park, OH, U. S. A., (1970) 397–432.

- Hillert, M., *Acta Metallurgica*, **1** (1953) 764–766.
- Hodgson, P. D. and Gibbs, R. K., *ISIJ International*, **32** (1992) 1329–1338.
- Honeycombe, R. W. K. and Bhadeshia, H. K. D. H., *Steels Microstructure and Properties*, Edward Arnold, London, U. K., (1995).
- Howard, R. T. and Cohen, M., *Trans. AIMME*, **176** (1948) 384–400.
- Huang, C. Y., Yang, J. R. and Wang, S. C., *Materials Transactions, JIM*, **34** (1993) 658–668.
- Hutchinson, W. B., *Metal Science*, **8** (1974) 185–196.
- Inagaki, H., *Zeitschrift fur Metallkunde*, **77** (1986) 36–42.
- Irani, J. J., British Iron and Steel Research Association Report No. MG/A/60/67, BISRA, London, U. K., (1967).
- Irvine, K. J., *Journal of the Iron and Steel Institute*, **200** (1962) 820–836.
- Irvine, K. J., Pickering, F. B., Heselwood, W. C. and Atkins, M., *Journal of the Iron and Steel Institute*, **186** (1957) 54–67.
- Irvine, K. J. and Pickering, F. B., *Journal of the Iron and Steel Institute*, **187** (1957) 292–309.
- Irvine, K. J. and Pickering, F. B., *Journal of the Iron and Steel Institute*, **201** (1963) 944–959.
- Irvine, K. J. and Pickering, F. B., *Physical Properties of Martensite and Bainite*, Iron and Steel Institute Special Report 93, London, U. K., (1965) 110–125.
- Irvine, K. J., Pickering, F. B. and Gladman, T., *Journal of the Iron and Steel Institute*, **210** (1967) 161–182.
- Jung, Y., Ueno, H., Ohtsubo, H., Nakai, K. and Ohmori, Y., *ISIJ International*, **35** (1995) 1001–1005.
- Kalish, D., Kulin, S. A. and Cohen, M., *Journal of Metals*, **17** (1965) 157–164.
- Kasper, R., Lotter, U. and Biegus, C., *Steel Research*, **65** (1994) 242–246.
- Khlestov, V. M., Konopleva, E. V. and McQueen, H. J., *Canadian Metallurgical Quarterly*, **35** (1996) 169–180.
- Kirkaldy, J. S., *Canadian Journal of Physics*, **36** (1958) 899–925.
- Ko, T. and Cottrell, S. A., *Journal of the Iron and Steel Institute*, **172** (1952) 307–313.
- Konopleva, E. V. and McQueen, H. J., *Hot Workability of Steels and Light Alloys–Composites*, eds. McQueen, H. J., Konopleva, E. V. and Ryan, N. D., Canadian Institute of Mining, Metallurgy and Petroleum, Montreal, Canada, (1996) 557–568.
- Kozasu, I., Ouchi, C., Sampei, K. and Okita, T., *Microalloying '75* ed. Korchynsky, M., Union Carbide Corporation, NY, U. S. A., (1976) 120–135.
- Kumar, R., *Physical Metallurgy of Iron and Steel*, Asia Publishing House, London, U. K., (1968).
- Lee, J. K. and Aaronson, H. I., *Acta Metallurgica*, **23** (1975) 799–808 and 809–820.
- Leslie, W. C., *The Physical Metallurgy of Steels*, McGraw–Hill Book Company, (1981).



- Lessells, J., *HSLA Steels: Metallurgy and Applications*, eds. Gray, M., Ko, T., Shouhua, Z., Baorong, W. and Xishan, X., ASM International, Metals Park, OH, U. S. A., (1986) 613–626.
- Liu, X., Solberg, J. K. and Gjengedal, R., *Materials Science and Engineering A*, **194A** (1995) L15–L18.
- Liu, X., Solberg, J. K. and Gjengedal, R., *Materials Science and Technology*, **12** (1996) 345–350.
- Liu, X. D. and Karjalainen, P., *Mechanical Working and Steel Processing*, Iron and Steel Society, **33** (1996) 769–774.
- MacKay, D. J. C., *Neural Computation*, **4** (1992a) 415–447.
- MacKay, D. J. C., *Neural Computation*, **4** (1992b) 448–472.
- MacKay, D. J. C., *ASHRAE (American Society of Heating, Refrigerating and Air-conditioning Engineers) Transactions*, **100**, pt. **2** (1994) 1053–1062.
- MacKay, D. J. C., *Network: Computation in Neural Systems*, **6** (1995) 469–505.
- MacKay, D. J. C., *Mathematical Modelling of Weld Phenomena III*, eds. Cerjack, H., Buchmayer, B. and Bhadeshia, H. K. D. H., Institute of Materials, London, U. K., (1997) 359–389.
- Magee, C. L., *Phase Transformations*, ASM, Metals Park, OH, U. S. A., (1970) 115–156.
- Matsumara, Y. and Yada, H., *Transactions of the Iron and Steel Institute of Japan*, **27** (1987) 492–498.
- Matsuzaki, A., Bhadeshia, H. K. D. H. and Harada, H., *Acta Metallurgica et Materialia*, **42** (1994) 1081–1090.
- Mehl, R. F. and Hagel, W. C., *Progress in Metal Physics*, **6** (1956) 74–134.
- Morrison, W. B., *Journal of the Iron and Steel Institute*, **201** (1963) 317–325.
- Morrison, W. B., *Trans. ASM*, **59** (1966) 824–846.
- Morrison, W. B. and Chapman, J. A., *Proc. Rosenhain Centenary Conference on The Contribution of Physical Metallurgy to Engineering Practice*, eds. Baker, R. G. and Kelly, A., The Royal Society, London, U. K., (1976) 289–303.
- Mukherjee, A. K., *Plastic Deformation of Metals*, Treatise on Materials Science and Technology, Vol. 6, ed. Arsenault, R. J., Academic Press, NY, U. S. A., (1975) 187.
- Mutiu, T. A., Kinderman, A. J. and Bernstein, I. M., *The Hot Deformation of Austenite*, ed. Ballance, J. B., TMS–AIME, NY, U. S. A., (1977) 410–427.
- Neal, R. M., *Bayesian Learning for Neural Networks*, Springer, (1996).
- Oblak, J. M. and Hehemann, R. F., *Transformation and Hardenability in Steels*, Climax Molybdenum Company, Ann Arbor, MI, U. S. A., (1967) 15–30.
- Ohmori, Y., Ohtani, H. and Kunitake, T., *Transactions of the Iron and Steel Institute of Japan*, **11** (1971) 250–259.
- Olson, G. B. and Cohen M., *Metallurgical Transactions A*, **7A** (1976) 1897–1904, 1905–1914 and 1915–1923.
- Ouchi, C., Sampei, T. and Kozasu, I., *Transactions of the Iron and Steel Institute of Japan*,

22 (1982) 214–222.

- Parker, S. V., *Modelling of Phase Transformations in Hot-Rolled Steels*, Ph. D. Thesis, University of Cambridge, (1997).
- Patel, J. R. and Cohen, M., *Acta Metallurgica*, **1** (1953) 531–538.
- Pickering, F. B., *Transformation and Hardenability in Steels*, Climax Molybdenum Company, Ann Arbor, MI, U. S. A., (1967) 109–132.
- Pickering, F. B., *Physical Metallurgy and the Design of Steels*, Allied Science Publishers, London, U. K., (1978).
- Priestner, R., *Revue de Metallurgie*, **72** (1975) 285–292.
- Raghavan, V., *Martensite, a Tribute to Morris Cohen*, eds. Olson, G. B. and Owen, W. S., ASM International, Materials Park, OH, U. S. A., (1992) 197–226.
- Raghavan, V. and Cohen, M., *Metallurgical Transactions*, **2** (1971) 2409–2418.
- Reed, R. C. and Bhadeshia, H. K. D. H., *Materials Science and Technology*, **8** (1992) 421–435.
- Rees, G. I. and Bhadeshia, H. K. D. H., *Materials Science and Technology*, **8** (1992) 985–993.
- Roberts, W., Lidefelt, H. and Sandberg, A., *Hot-Working and Forming Processes*, eds. Sellars, C. M. and Davies, G. J., The Metals Society, London, U. K., (1980) 38–42.
- Sandberg, A. and Roberts, W., *Thermomechanical Processing of Microalloyed Austenite*, eds. DeArdo, A. J., Ratz, G. A. and Wray, P. J., TMS-AIME, Warrendale, PA, U. S. A., (1982) 405–430.
- Sandvik, B. P. J. and Nevalainen, H. P., *Metals Technology*, **8** (1981) 213–220.
- Santella, M. L. and DeArdo, A. J., *Thermomechanical Processing of Microalloyed Austenite*, eds. DeArdo, A. J., Ratz, G. A. and Wray, P. J., TMS-AIME, Warrendale, PA, U. S. A., (1982) 83–99.
- Shimizu, M., Hiromatsu, M., Takashima, S., Kaji, H. and Kano, M., *HSLA Steels: Metallurgy and Applications*, eds. Gray, M., Ko, T., Shouhua, Z., Baorong, W. and Xishan, X., ASM International, Metals Park, OH, U. S. A., (1986) 591–598.
- Shipway, P. H. and Bhadeshia, H. K. D. H., *Materials Science and Technology*, **11** (1995a) 1116–1128.
- Shipway, P. H. and Bhadeshia, H. K. D. H., *Materials Science and Engineering A*, **201A** (1995b) 143–149.
- Shipway, P. H. and Bhadeshia, H. K. D. H., *Materials Science and Engineering A*, **223A** (1997) 179–185.
- Smith, Y. E. and Siebert, C. A., *Metallurgical Transactions*, **2** (1971) 1711–1725.
- Speich, G. R., *Decomposition of Austenite by Diffusional Processes*, eds. Zackay, V. F. and Aaronson, H. I., Interscience, NY, U. S. A., (1962) 353–386.
- Speich, G. R., Cuddy, L. J., Gordon, C. R. and DeArdo, A. J., *Phase Transformations in Ferrous Alloys*, eds. Marder, A. R. and Goldstein, J. I., TMS-AIME, Warrendale, PA, U. S. A., (1984) 341–390.
- Srinivasan, G. R. and Wayman, C. M., *Acta Metallurgica*, **16** (1968) 621–636.

- Steven, W. and Haynes, A. J., *Journal of the Iron and Steel Institute*, **183** (1956) 349–359.
- Straatmann, J. A., Doane, D. V. and Park, Y. J., *Processing, Microstructure and properties of HSLA Steels*, ed. DeArdo, A. J., TMS-AIME, Warrendale, PA, U. S. A., (1988) 287–303.
- Swallow, E. and Bhadeshia, H. K. D. H., *Materials Science and Technology*, **12** (1996) 121–125.
- Tanaka, T., Enami, T., Kimura, M., Saito, Y. and Hatomura, T., *Thermomechanical Processing of Microalloyed Austenite*, eds. DeArdo, A. J., Ratz, G. A. and Wray, P. J., TMS-AIME, Warrendale, PA, U. S. A., (1982) 195–215.
- Tanaka, T., *Microalloying '95*, Iron and Steel Society, Pittsburg, U. S. A., (1995) 165–181.
- Thomas, M. H. and Michal, G. M., *Proc. of Int. Conf. on Solid → Solid Phase Transformations*, eds. Aaronson, H. I., Laughlin, D. E., Sekerka, R. F. and Wayman, C. M., TMS-AIME, Warrendale, PA, U. S. A., (1982) 469–473.
- Tsuzaki, K., Ueda, T., Fujiwara, K. and Maki, T., *New Materials and Processes for the Future*, 1st Japan International SAMPE Symposium and Exhibition, Society for Advancement of Material and Process Engineering, Chiba, Japan, (1989) 799–804.
- Umemoto, M., Ohtsuka H. and Tamura, I., *Transactions of the Iron and Steel Institute of Japan*, **23** (1983) 775–784.
- Umemoto, M. and Tamura, I., *HSLA Steels: Metallurgy and Applications*, eds. Gray, M., Ko, T., Shouhua, Z., Baorong, W. and Xishan, X., ASM International, Metals Park, OH, U. S. A., (1986) 373–382.
- Umemoto, M., Bando, S., Tamura, I., *Proc. Int. Conf. on Martensitic Transformations (ICOMAT '86)*, Japan Institute of Metals, Kyoto, Japan, (1986) 595–600.
- Underwood, E. E., *Quantitative Microscopy*, eds. DeHoff, R. T. and Rhines, F. N., McGraw Hill, (1968) 77–127.
- Vlad, C. M., *Accelerated Cooling of Rolled Steels*, ed. Southwick, P. D., TMS-AIME, Warrendale, PA, U. S. A., (1986) 435–448.
- Walker, D. J., and Honeycombe, R. W. K., *Metal Science*, **12** (1978) 445–452.
- Wayman, C. M. and Bhadeshia, H. K. D. H., *Physical Metallurgy, Volume 2*, eds. Cahn, R. W. and Haasen, P., Elsevier, Amsterdam, Holland, (1996) 1507–1554.
- Yada, H., Matsumura, Y. and Senuma, T., *Proc. Int. Conf. on Martensitic Transformations (ICOMAT '86)*, Japan Institute of Metals, Kyoto, Japan, (1986) 515–520.
- Yamamoto, S., Yokomaya, H., Yamada, K. and Nikura, M., *ISIJ International*, **35** (1995) 1020–1026.
- Yang, J. R., Huang, C. Y., Huang, C. F. and Aoh, J. H., *Journal of Materials Science*, **30** (1995) 5036–5041.
- Yang, J. R., Huang, C. Y., Hsieh, W. H. and Chiou, C. S., *Materials Transactions, JIM*, **37** (1996) 579–585.

- Yoshie, A., Morikawa, H., Onoe, Y. and Itoh, K., *Transactions of the Iron and Steel Institute of Japan*, **27** (1987) 425–431.
- Young, C. H. and Bhadeshia, H. K. D. H., *Materials Science and Technology*, **10** (1994) 209–214.
- Zhang, F. and Boyd, J. D., *Hot Workability of Steels and Light Alloys–Composites* eds. McQueen, H. J., Konopleva, E. V. and Ryan, N. D., Canadian Institute of Mining, Metallurgy and Petroleum, Montreal, Canada, (1996) 585–592.